Prototyping lead-free $Na_{0.5}Bi_{0.5}TiO_3$-based multilayer ceramic capacitors

Zur Erlangung des akademischen Grades Doktor-Ingenieur (Dr.-Ing.)
Genehmigte Dissertation von Maximilian Gehringer aus Erlenbach a.Main
Tag der Einreichung: 30. Oktober 2023, Tag der Prüfung: 6. Dezember 2023

1. Gutachten: Dr. Till Frömling
2. Gutachten: Prof. Dr. Andreas Klein
Darmstadt, Technische Universität Darmstadt

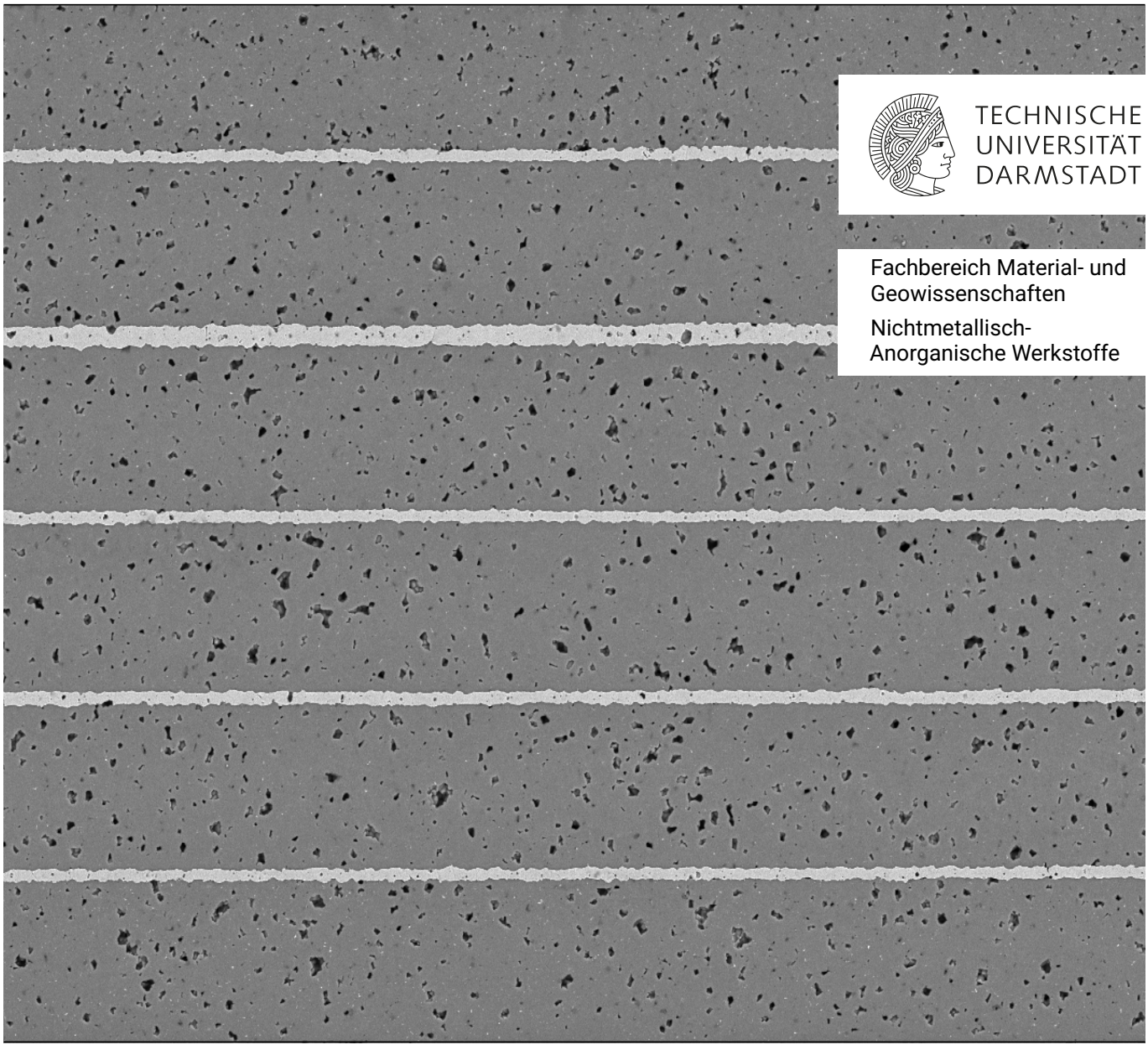

TECHNISCHE UNIVERSITÄT DARMSTADT

Fachbereich Material- und Geowissenschaften

Nichtmetallisch-Anorganische Werkstoffe

Prototyping lead-free $Na_{0.5}Bi_{0.5}TiO_3$-based multilayer ceramic capacitors

Accepted doctoral thesis by Maximilian Gehringer

Date of submission: 30. Oktober 2023
Date of thesis defense: 6. Dezember 2023

Darmstadt, Technische Universität Darmstadt

Erklärungen laut Promotionsordnung

§ 8 Abs. 1 lit. c PromO

Ich versichere hiermit, dass die elektronische Version meiner Dissertation mit der schriftlichen Version übereinstimmt.

§ 8 Abs. 1 lit. d PromO

Ich versichere hiermit, dass zu einem vorherigen Zeitpunkt noch keine Promotion versucht wurde. In diesem Fall sind nähere Angaben über Zeitpunkt, Hochschule, Dissertationsthema und Ergebnis dieses Versuchs mitzuteilen.

§ 9 Abs. 1 PromO

Ich versichere hiermit, dass die vorliegende Dissertation selbstständig und nur unter Verwendung der angegebenen Quellen verfasst wurde.

§ 9 Abs. 2 PromO

Die Arbeit hat bisher noch nicht zu Prüfungszwecken gedient.

Darmstadt, 30. Oktober 2023

M. Gehringer

Abstract

Multilayer ceramic capacitors (MLCCs) that can withstand high temperatures and voltages are urgently needed for upcoming high-temperature (HT) power electronics applications like renewable energies, power conversion, and electric vehicles. While environmental conditions usually do not exceed 300 °C, voltage requirements and limits for capacitors under operation are often uncertain. Thus, the stability of electrical properties in a broad range of operating conditions is required. Lead zirconate titanate (PZT)-based capacitors cannot be utilized due to the toxicity of lead and environmental concerns. Commercial lead-free $BaTiO_3$ (BT)-based ceramic capacitors are limited to 190 °C.

Capacitor materials based on $Na_{0.5}Bi_{0.5}TiO_3$ (NBT) are promising contenders, but their complex defect chemistry has to be assessed. Especially since oxygen vacancy migration during operation is one of the most critical aspects. In MLCCs that operate under temperature and voltage stress, additional migration of the inner electrode material into the dielectric needs to be considered. This well-known issue in lead-based components with silver-palladium (Ag/Pd) electrodes can cause severe electrodegradation and lower reliability. While similar effects are expected for NBT-based MLCCs, the actual mechanism for this complex electrodegradation is investigated.

Capacitors are prepared using the MLCC fabrication route, comprised of slurry preparation, tape casting, shaping processes, and thermal treatment of green bodies. This work aims to provide an integral approach to optimizing the manufacturing processes of NBT-based MLCCs co-fired with Ag/Pd electrodes. Four key influencing factors are evaluated: slurry composition, shaping processes, sintering conditions, and electrode material.

Ultimately, the prepared prototype MLCCs exhibit a homogeneous microstructure with low porosity and excellent lamination of individual layers and electrodes. They feature an exceptional operational window regarding temperature (-67 to 375 °C) and voltage (up to 1.5 kV), with only a slight variation of capacitance ($\leq \pm 10\%$). Voltage ratings do not have to be specified due to this high voltage insensitivity. The prototype MLCCs with Ag/Pd electrodes exhibit greater resilience against enhanced degradation. Moreover, a novel indentation method was conceptualized to evaluate the dielectric breakdown strength (DBS), excluding extrinsic effects and identifying areas with electric field concentrations. Here, NBT-based MLCCs are more limited by the component's design than by the dielectric strength of the ceramic.

This work demonstrates the remarkable stability of NBT-based prototype MLCCs against high temperatures and voltages, making them strong candidates for future high-temperature and power electronics applications.

Zusammenfassung

Keramik-Vielschichtkondensatoren, engl. multilayer ceramic capacitors (MLCCs), die hohe Temperaturen und Spannungen aushalten müssen, werden dringend für zukünftige Anwendungen in der Hochtemperatur-Leistungselektronik benötigt. Dazu gehören beispielsweise Systeme in erneuerbaren Energien, der Leistungsübertragung und elektrischen Fahrzeugen. Während die Umgebungsbedingungen normalerweise 300 °C nicht überschreiten, sind die Spannungsanforderungen und -grenzen für Kondensatoren unter Last oft nicht genau bekannt. Daher ist die Stabilität der elektrischen Eigenschaften über einen großen Einsatzbereich erforderlich. Da Blei giftig ist und die Umweltbedenken bei Verwendung von bleihaltigen Materialien groß sind, können Kondensatoren auf Blei-Zirkonat-Titanat (PZT)-Basis nicht verwendet werden. Handelsübliche bleifreie Bariumtitanat (BT)-Keramikkondensatoren sind auf 190 °C begrenzt.

Kondensatormaterialien auf Basis von Natrium-Bismut-Titanat (NBT) sind vielversprechende Dielektrika, aber ihre komplexe Defektchemie muss evaluiert werden, insbesondere da die Migration von Sauerstofffleerstellen während des Betriebs eines der kritischsten Aspekte ist. In MLCCs, die unter Temperatur- und Spannungsbelastung betrieben werden, muss auch die zusätzliche Migration des Innenelektrodenmaterials in das Dielektrikum berücksichtigt werden. Dieses bekannte Problem bei bleihaltigen Bauteilen mit Silber-Palladium (Ag/Pd)-Elektroden kann zu schwerwiegender Degradation und geringerer Zuverlässigkeit führen. Während ähnliche Effekte bei NBT-basierten MLCCs erwartet werden, wird der tatsächliche Mechanismus für diese komplexe Degradation untersucht.

Die Kondensatoren werden nach dem MLCC-Herstellungsverfahren hergestellt. Es beinhaltet die Herstellung des Schlickers, das Gießen von Grünfolien, Formgebungsprozesse und die thermische Behandlung der Grünkörper.

Diese Arbeit zielt darauf ab, einen ganzheitlichen Ansatz zur Optimierung der Herstellungsprozesse von NBT-basierten MLCCs, die zusammen mit Ag/Pd-Elektroden gebrannt werden, zu bieten. Vier Einflussfaktoren werden untersucht: Schlickerzusammensetzung, Formgebungsprozesse, Brennbedingungen und Elektrodenmaterial.

Letztendlich zeigen die hergestellten Prototyp-MLCCs eine homogene Mikrostruktur mit geringer Porosität und eine ausgezeichnete Laminierung der Schichten und Elektroden. Sie verfügen über ein außergewöhnlichen Einsatzbereich in Bezug auf Temperatur (-67 bis 375 °C) und Spannung (bis zu 1,5 kV). Dabei treten nur kleine Veränderungen der Kapazität von $\leq \pm 10\%$ auf. Die Nennspannungen müssen aufgrund der geringen Empfindlichkeit gegenüber hohen Spannungen nicht spezifiziert werden.

Die Kondensatorprototypen mit Ag/Pd-Elektroden zeigen einen größeren Widerstand gegen Degrada-

tion. Darüber hinaus wurde eine neue Eindringmethode konzipiert, um die Durchschlagfestigkeit des Dielektrikums zu bewerten, wobei extrinsische Effekte ausgeschlossen und Bereiche mit elektrischen Feldkonzentrationen lokalisiert werden. Hier sind NBT-basierte MLCCs mehr durch das Bauteildesign als durch die Durchschlagfestigkeit der Keramik begrenzt.
Diese Arbeit zeigt die bemerkenswerte Stabilität der NBT-basierten Kondensatorprototypen gegenüber hohen Temperaturen und Spannungen und macht die Kondensatoren zu vielversprechenden Kandidaten für zukünftige Anwendungen in der Hochtemperatur- und Leistungselektronik.

Contents

List of Figures

List of Tables

List of Abbreviations

AC	Alternating current
AFE	Antiferroelectric
Ag/Pd	Silver-palladium
ATBC	Acetyltributylcitrate
BA	Bismuth aluminate
BCT	Barium calcium titanate
BME	Base metal electrode
BSE	Backscattered electron
BT	$BaTiO_3$
CPE	Constant phase element
CTE	Coefficient of thermal expansion
CZ	Calcium zirconate
DAISY-MAT	Darmstadt integrated system for materials research
DBS	Dielectric breakdown strength
DC	Direct current
DF	Dissipation factor
DSC	Differential scanning calorimetry
ECIA	Electronic Components Industry Association
EDX	Energy-dispersive X-ray spectroscopy
EPC	Electric field permittivity coefficient
ER	Ergodic relaxor
ESL	Equivalent series inductance
ESR	Equivalent series resistance
FE	Ferroelectric

GB	Grain boundary
HT	High-temperature
HT-PNR	High-temperature polar nano region
HV	High-voltage
IS	Impedance spectroscopy
LT-PNR	Low-temperature polar nano region
MEK	Methyl ethyl ketone
MLCC	Multilayer ceramic capacitor
MPB	Morphotropic phase boundary
$NB_{0.501}T$-Fe	$Na_{0.5}Bi_{0.501}Fe_xTi_{1-x}O_3$
$NB_{0.501}T$	$Na_{0.5}Bi_{0.501}TiO_3$
NBT	Sodium bismuth titanate
NBT-BT-CZ	$Na_{0.5}Bi_{0.5}TiO_3$-$BaTiO_3$-$CaZrO_3$
NBT-BT-KNN	$Na_{0.5}Bi_{0.5}TiO_3$-$BaTiO_3$-$K_{0.5}Na_{0.5}NbO_3$
NBT-BT	$Na_{0.5}Bi_{0.5}TiO_3$-$BaTiO_3$
NBT-BT-CZ-BA	$Na_{0.5}Bi_{0.5}TiO_3$-$BaTiO_3$-$CaZrO_3$-$BiAlO_3$
P-E	Polarization-electric field
PCB	Printed circuit board
PEG	Polyethylene glycol
PET	Polyethylene terephthalate
PLZT	Lead lanthanum zirconate titanate
PME	Precious metal electrode
PMN	Lead magnesium niobate
PNR	Polar nano region
PVB	Polyvinyl butyral
PZT	Lead zirconate titanate
RFE	Relaxor ferroelectric
RMS	Root mean square
RoHS	Restriction of Hazardous Substances
RT	Room temperature

SE	Secondary electron
SEM	Scanning electron microscopy
SiC	Silicon carbide
SRF	Self-resonant frequency
STO	Strontium titanate
TCC	Temperature coefficient of capacitance
TGA	Thermogravimetric analysis
VCC	Voltage coefficient of capacitance
XPS	X-ray photoelectron spectroscopy
YSZ	Yttria-stabilized zirconia

List of Symbols

A	Active area
C	Capacitance
C_0	Vacuum capacitance
C_R	Rated capacitance
C_T	Capacitance at given temperature
C_α	Constant phase element parameter
C_{nom}	Nominal capacitance
D	Dielectric displacement
E	Electric field
E_{bd}	Breakdown field
$I^*(\omega)$	Complex electric current
I_0	Peak current
J	Current density
M^*	Complex modulus
P_D	Power dissipation
P_{max}	Maximum polarization
Q	Quality factor
R	Resistance
R_p	Insulation resistance
S^*	Complex elastance
T	Temperature
T_B	Burns temperature
T_C	Transition temperature
T_g	Glass transition temperature
T_m	Temperature of maximum permittivity
T_{F-R}	Ferroelectric-relaxor phase transition temperature
T_{max}	Maximum temperature
$T_{range}(\eta \geq 80\%)$	Temperature range with efficiency at least 80%
$T_{range}(\tan\delta \leq 0.02)$	Temperature range with dielectric loss smaller or equal to 2%
$T_{range}(\varepsilon_r' \pm 15\%)$	Temperature range with permittivity deviations less than 15% from $\varepsilon_r'(150\,°C)$

U	Voltage
$U^*(\omega)$	Complex voltage
U_0	Peak voltage
U_R	Rated voltage
U_{max}	Maximum voltage
U_{op}	Operating voltage
U_{rms}	Effective voltage
V	Volume
W	Stored energy
W_{loss}	Energy loss density
W_{rec}	Recoverable energy density
W_{total}	Total energy density
X	Reactance
X_C	Capacitive reactance
X_L	Inductive reactance
Y^*	Complex admittance
Y_C^*	Complex admittance of a capacitor
Y_R^*	Complex admittance of a resistor
Z	Impedance
$Z''(\omega)$	Imaginary part of complex impedance
$Z'(\omega)$	Real part of complex impedance
$Z^*(\omega)$	Complex impedance
Z_C^*	Complex impedance of a capacitor
Z_L^*	Complex impedance of an inductor
Z_R^*	Complex impedance of a resistor
Z_{CPE}^*	Impedance of a capacitive constant phase element
Z_{total}^*	Total complex impedance of a RC-circuit
$\Delta T(\varepsilon_r' \pm 15\%; \tan\delta \leq 0.02)$	Overlapping temperature range of stable permittivity and low dielectric loss
α	Width parameter
α_c	Temperature coefficient of capacitance
η	Energy storage efficiency
$\eta(T_{max})$	Efficiency at the maximum temperature
ω	Angular frequency
ω_{max}	Peak frequency
σ	Electrical conductivity
ε_0	Vacuum permittivity
ε_{E0}	Zero-field permittivity

ε_E	Permittivity at applied electric field
ε_r	Relative permittivity
ε_r'	Real part of the relative permittivity
$\varepsilon_r'(150\,°C)$	Relative permittivity at 150 °C
$\varepsilon_r'(\max)$	Maximum relative permittivity
ε_r''	Imaginary part of the relative permittivity
ε_r^*	Complex relative permittivity
φ	Phase shift angle
φ_I	Current phase angle
φ_U	Voltage phase angle
d	distance between two electrodes; thickness of the dielectric
f_{SRF}	Self-resonant frequency
q	Electric charge

1 Introduction

The demand for energy from clean and renewable sources and the need for efficient power conversion and storage have become increasingly prominent.[1] Evidently, fossil energy is not an unlimited resource, and its consumption contributes to climate change and environmental pollution.[2] This pivotal moment leads to a change of requirements for power systems and electronics.[3,4] It may have started with deep earth drilling for fossil fuels, which can be regarded as one of the oldest applications for HT electronics.[5] Such electronics are also needed for power systems like internal combustion engines and jet engines. The shift towards replacing conventional mechanical and hydraulic systems in vehicles and avionics with electromechanical or mechatronic systems creates further demand for high-temperature power electronics. This is due to the need for power electronics converters to be located close to the components with high ambient temperatures.[6] Both fields are merging together more and more due to renewable energy conversion and electrically powered vehicles. Nowadays, HT power electronics are inevitable in a variety of different applications, including renewable energy systems for power conversion and storage, electric vehicle transportation, space exploration, and aviation.[7–9] Temperatures can range from -55 °C to more than 300 °C with huge variations during operation.[10] The industry and manufacturers are calling for electronics being able to be operated in harsh environments reliably.[8,9,11] Sharp increases in temperature or electric fields must not bring them out of their operational range; high temperatures are particularly intricate. Cooling sometimes may not be possible due to cost or the risk of failure of an additional cooling system. Ideally, the industry wants reliable high-temperature power electronics that defy high temperatures and fields on their own.[5] It is essential to understand that not only passive components are subject of intensive research. All components of such electronic systems need to be adjusted to harsh conditions.[12] For example, in HT power electronics converters, semiconductors, magnetic components, other passive components (resistors), gate drivers, signal circuits, and printed circuit boards (PCBs) are integrated.[5] It can be concluded that tackling that issue is not a problem of a single component of the system but a system problem.[5,13]

Among the passive components in these systems, capacitors play a crucial role, yet they are often the least reliable.[13,14] As indicated by industry experts for the reliability of power electronics systems, improving the reliability of capacitors is one of the most urgent topics for future research.[9] Capacitors are needed for different types of power conversion and direct current (DC)-link applications:[7,15] DC-DC converters, (power) inverters (DC-alternating current (AC)), rectifiers (AC-DC), and transformers or voltage converters (AC/AC). As DC-link, filter, or smoothing capacitors, they can filter or smooth the input signals in, e.g., full wave rectifiers.[16,17] In DC-AC inverters, the capacitors reduce voltage spikes

and function as snubber capacitors. Especially the power conversion in renewable energies or electric vehicles is critical regarding voltage peaks. Passive components need to withstand high voltages and maintain constant properties during operation.[15]

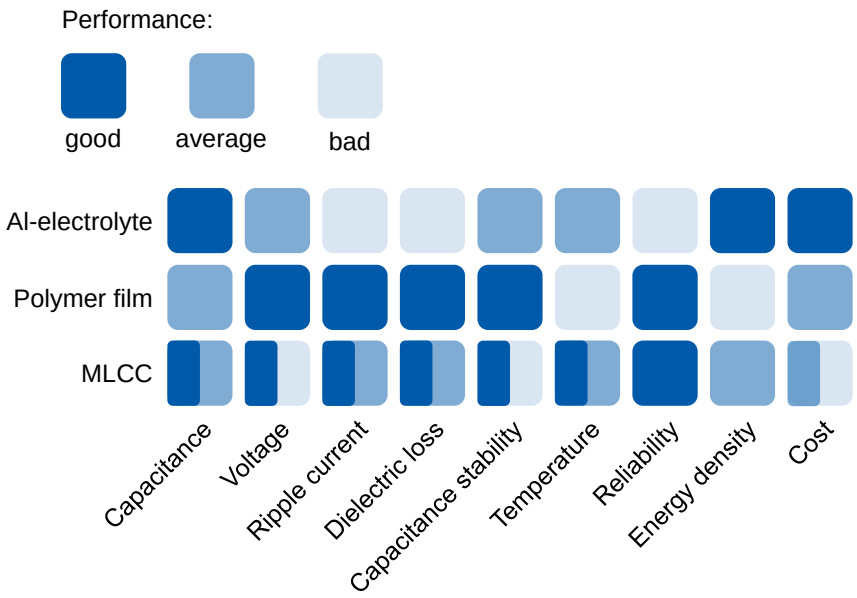

Figure 1.1: Performance comparison of key parameters of capacitors for DC-link applications, adapted from Wang and Blaabjerg.[15]

Besides ceramic capacitors, a large variety of capacitor materials exist for applications with lower requirements. Non-ceramic capacitors include polymer film capacitors, aluminum electrolytic (Al-electrolyte) capacitors, tantalum electrolytic capacitors, and mica paper capacitors. Three main groups of capacitors for DC-link applications were stated by Wang and Blaabjerg:[15] Al-electrolyte, polymer film, and MLCCs. A performance comparison of key parameters of these capacitors for DC-link applications, visualized in Figure 1.1, shows their individual benefits and shortcomings. For capacitors in general, temperature ripple and voltage ripple have been identified as main stresses leading to failure.[9,18] Al-electrolyte capacitors suffer from electrolyte vaporization, accelerated at high temperatures and ripple currents. In polymer film capacitors, temperature, ripple current, and humidity stress lead to dielectric loss. MLCCs suffer from oxygen vacancy migration and resistance degradation under the same stress influences and vibration.[9,19] The overall performance of polymer film capacitors regarding applied voltages, ripple current, dielectric loss, and capacitance stability is remarkable. Such capacitors are relatively cheap. Conversely, aluminum electrolyte capacitors exhibit a huge capacitance or energy density and are affordable. What's most striking, however, is the missing temperature stability of both capacitor types. The maximum temperature of about 150 °C for Al-electrolyte and 220 °C for polymer film capacitors is very limiting.[20,21] They simply cannot be used for upcoming high-temperature and power electronics applications with upper limits of over 300 °C. This is where MLCCs come into play. Commercially available ceramic capacitors, mainly made of BT or BT-based dielectric materials, are, however, limited to operating temperatures below

190 °C.[22] Lead-based capacitors indeed have excellent properties.[16,23] Due to the toxicity of lead, however, the Restriction of Hazardous Substances (RoHS) is strictly limiting the use of lead-based electronics. The urge to replace lead-based capacitor materials with lead-free materials has not yet been greater.[3,24–26] With regards to exceptional temperature and electric field requirements, no material has been proven to be suitable. One of the objectives of this thesis is a systematic improvement of key characteristics of lead-free MLCCs, including capacitance, voltage, ripple current, dielectric loss, capacitance and temperature stability, and cost. Sodium bismuth titanate (NBT)-based relaxor materials have an outstanding large temperature window of stable dielectric properties.[27–29] They also can feature an extraordinarily high permittivity.[30] Hence, NBT-based materials are perfect contenders as dielectric material for HT power electronics capacitors. NBT and relaxors, in general, are a complex topic, though.[31–33] Compared to BT, they are not well understood. Especially in terms of their application, risk profiles, reliability assessment, electrical fatigue, degradation, and failure modes of the material and the related components have to be established.

The material system $Na_{0.5}Bi_{0.5}TiO_3$-$BaTiO_3$-$CaZrO_3$-$BiAlO_3$ (NBT-BT-CZ-BA) has demonstrated to be one of the most promising candidates for lead-free capacitor materials. It was developed within this working group over the recent years.[34,35] Furthermore, Hoang et al. showed that (1-x)[0.8(0.94$Na_{0.5}Bi_{0.5}TiO_3$-0.06$BaTiO_3$)-0.2$CaZrO_3$]-x$BiAlO_3$ (NBT-BT-CZ-xBA) features encouraging stable dielectric properties as bulk samples.[29] This material system will be used to manufacture lead-free prototype MLCCs for high-temperature and power electronics applications. However, NBT-based perovskite materials are very complex systems. Observed effects are different from lead-based perovskites and are often caused by a sensitivity to non-stoichiometry in NBT-based materials.[36–39] In pure NBT, small deviations in the Bi content from the stoichiometric compound can result in a high ionic conductivity.[40–42] Evaporation of Bi_2O_3 can cause a bismuth depletion in the ceramic, which is compensated by mobile oxygen vacancies that contribute to the conductivity. Solid solutions like $Na_{0.5}Bi_{0.5}TiO_3$-$BaTiO_3$ (NBT-BT) are less prone to the evaporation; the changed stoichiometry of the ceramic, however, can still affect the dielectric properties.[43] Rather recently, it was found that the amount of defect concentration (vacancies, acceptor dopants, and defect complexes) plays a crucial role for the electrical properties.[44,45] The ionic conductivity changes by several orders of magnitude with only a small change in acceptor concentration.[46] Therefore, the defect chemistry of the NBT-based material has to be known for a successful utilization as high-temperature and power electronics capacitors.

For the preparation of MLCCs, metallic inner electrodes are necessary, which are co-fired with the ceramic. The co-firing process can be quite intricate since melting or oxidizing the electrode material must be inhibited. According to Hoang et al., the material system NBT-BT-CZ-BA is sintered at around 1100 °C, as most lead-free ceramics.[29] At such high temperatures, only precious metal electrode (PME) materials like Pt or certain Ag/Pd alloys are feasible. This includes the commonly used 70/30 Ag/Pd ratio, which has a melting point of around 1160-1170 °C.[47,48] Utilizing sintering aids such as CuO, Bi_2O_3, Li_2CO_3, ZnO, and B_2O_3 could severely lower the sintering temperature, enabling the use of base metal electrode (BME) materials like Ni or Cu.[49–52] For instance, Engel reported the manufacturing of lead-based MLCCs with copper inner electrodes.[16] However, this is likely linked to a change in sintering temperature, as

well as defect chemistry. Sintering aids could migrate and diffuse into the ceramic matrix and act as dopants. It may cause unexpected consequences and alter the dielectric properties.[49] Likewise, the sintering atmosphere is limited by the choice of electrode material. For instance, nickel and copper BMEs need reducing atmosphere to avoid oxidization.[53] The oxygen partial pressure necessary to prevent the oxidization of nickel makes it incompatible with NBT-based material.[52] A low oxygen partial pressure of $6 \cdot 10^{-8}$ atm is required not to oxidize copper.[52] Low oxygen partial pressure, however, could lead to the formation of oxygen vacancies, which would contribute to the dielectric loss at elevated temperatures.[54,55] To this end, only 70/30 Ag/Pd electrode material will be used for the manufacture of MLCCs.

Another consequence of co-firing ceramics with metal electrodes is the interaction between the metals and the ceramic matrix. In the case of $Pb(Zr_xTi_{1-x})O_3$ (PZT) ceramics with Ag/Pd inner electrodes, a complex electromigration mechanism of Ag into the ceramic was the reason for enhanced resistance degradation.[56–58] This is very detrimental with respect to the application of capacitors for high-temperature and power electronics. Compared to PZT, the knowledge about the interaction of Ag in lead-free materials is rather limited. Ag is soluble in NBT-based ceramics to at least 1%,[47,59] possibly acting as an acceptor dopant. Actuators out of an NBT-based ceramic with 70/30 Ag/Pd electrodes exhibited reduced stability during operation, which could at least be attributed to the migration.[60] Nevertheless, Ag/Pd electrodes are compatible with NBT-based materials.

The choice of electrode material also tremendously affects the economical fabrication of MLCCs. The majority of the material costs are defined by the electrode material. In general, BMEs are significantly cheaper than PMEs, as depicted in Figure 1.2, with the price evolution of Pt, Pd, 70/30 Ag/Pd, and Cu electrode materials. Before 2018, 70/30 Ag/Pd (blue) was inevitably cheaper than platinum (gray). The rapid price increase of Pd (red) starting in 2018 is claimed to be related to the Dieselgate.[61] In recent years, prices for Pt and Ag/Pd have strongly converged. Nevertheless, around 2023, a decline in Pd prices led again to significantly lower prices compared to pure platinum. In October 2023, 1 kg of Ag/Pd is expected to be approximately 12,500 EUR, while 1 kg platinum is priced at around 29,000 EUR, making Pt more than twice as expensive as 70/30 Ag/Pd. In comparison, 1 kg copper (brown) is exceptionally cheap, costing about 8 EUR. In terms of pricing, PMEs still fall behind the cost-effective alternatives Cu and other BME materials, as evidenced from Figure 1.2.

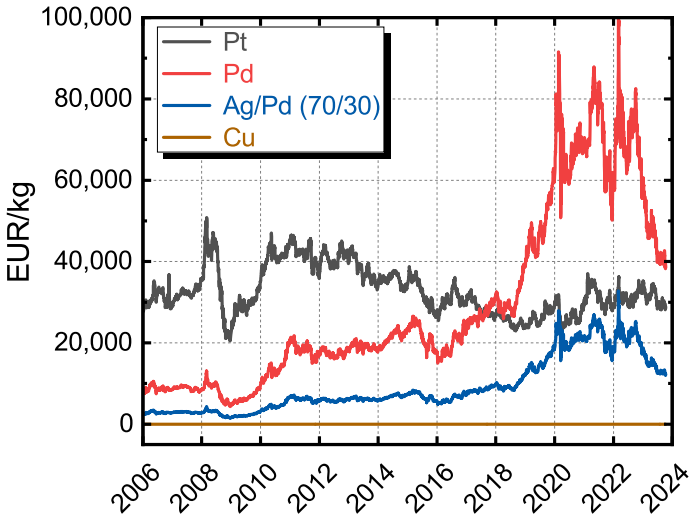

Figure 1.2: Evolution of prices for potential electrode materials in EUR per kg. Prices were extracted from 2006 until October 2023.[62,63]

An important part and key challenge of this thesis involves adapting the conventional processing route for NBT-based dielectric bulk samples to an MLCC fabrication route, while maintaining suitable properties for high-temperature and power electronics applications. Essential for the MLCC fabrication, and tape casting thin ceramic layers, is a well-adjusted slurry with various organic additives.[64] However, additional components to the slurry need to be carefully selected to avoid detrimental interference with the final properties of the MLCC. Different processing equipment and conditions are used to prepare green stacks, including cutting, screen printing, stacking, and pressing equipment. Additionally, the thermal treatment needs to be adapted, in order to remove organic additives prior sintering, as well as appropriate firing atmospheres for a complete decomposition of organic components. Appropriate firing atmosphere are required for a complete decomposition of organics.[65,66] Otherwise, residuals could also affect the final dielectric properties of the capacitors.
Obviously, a huge variety of aspects contribute to a successful and feasible manufacture of prototype lead-free NBT-based MLCCs for high-temperature and power electronics applications. Not only the dielectric material and electrode material has to be investigated and optimized, equal emphasis has to be put on the processing and different processing techniques. Thus, the next section serves as a guideline for this thesis, presenting its concept, objectives, as wells as most important steps and tasks.

1.1 Concept and Objectives

Lead-free ceramic capacitors capable of maintaining their dielectric properties although being subjected to high temperatures above 190 °C and high voltages are not available on the market.[9,22] These highly stable capacitors could be used in a wide operational window in terms of surrounding temperature and applied voltages with only small performance losses. Thereby, stability of capacitance and low

dielectric losses against high temperatures and voltages are vital. The ceramic material NBT-BT-CZ-BA is quite sophisticated given its complex defect behavior. This defect chemistry of the dielectric material, in combination with the electrode material can severely hamper a successful fabrication of MLCCs.[47] Attention should be focused on possible migration of oxygen vacancies through the materials and electrode material into the NBT matrix during operation. This would cause substantial degradation and impair the reliability of MLCCs.[9]

An integral approach will be elaborated to shed light on all facets of the MLCC fabrication route. A proof of concept of the preparation of lead-free NBT-based MLCCs with Ag/Pd inner electrodes will be established. In the beginning, MLCCs will be fabricated and characterized. Based on this state, optimization will be systematically conducted. Four key influencing factors emerged throughout the manufacturing of MLCCs, including the slurry composition, shaping processes, sintering conditions, and the electrode material. This is represented in Figure 1.3 and indicates that the influencing factors itself are interconnected.

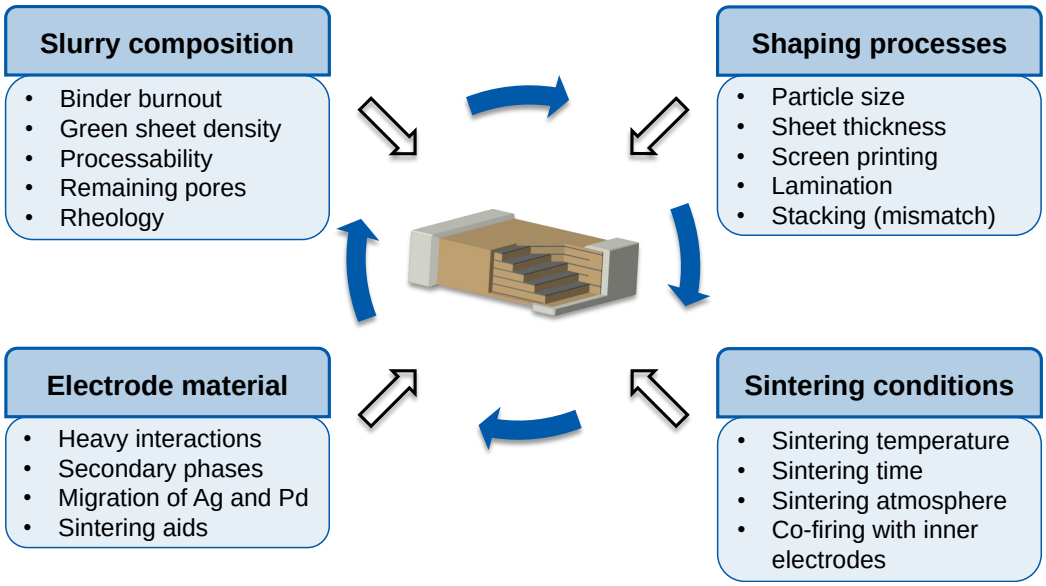

Figure 1.3: influencing factors during MLCC fabrication.

The first influencing factor is the slurry composition. The choice and ratio of ingredients for the slurry are crucial in determining the final properties of the capacitor component. For instance, a high number of remaining pores after the binder burnout affects the mechanisms of the subsequent sintering step, possibly resulting in a highly porous structure.[67] Therefore, the objective for the slurry is selecting ingredients that lead to superior final properties of the MLCC and keep up the processability of the green sheets and stacks.

The MLCC fabrication route contains a multitude of different steps with multiple influencing factors. They will be explained later in detail in Figure 2.21. All of them affect the processability and also the final properties of the capacitor.[65] It is of high concern to find suitable parameters during tape casting, sheet cutting, screen printing, lamination, and stacking.

The main objective of investigating the sintering conditions is to find an optimal temperature, dwell

time, and atmosphere for the co-firing process. It involves adapting the solid-state processing route for NBT-based bulk samples to the MLCC fabrication route, as described in Section 2.5, while maintaining dielectric properties.
This is closely related to the last influencing factor of electrode material and sintering aids. Depending on the sintering conditions, diffusion of Ag or Pd of the electrode material into the dielectric can occur. It is possible for the electrode material to segregate so that secondary phases are formed.[47] Therefore, the effect of sintering aids to lower sintering temperatures and inhibit partial melting of the electrode material will be discussed. Diffusion of sintering aids into the NBT lattice could also alter the defect chemistry of the components.[68,69] Regarding the electrode material, the task is to suppress migration of ions and the formation of secondary phases. These aspects, and the incorporation of ions in the host lattice in particular, can impair the reliability and enhance degradation of the MLCCs during operation.[58,70,71]

Evidently, each of the influencing factors are mutually correlated with the overall goal to adjust the final properties of the MLCCs with respect to high-temperature and power electronics applications. In order to help the reader to follow the investigation process of the influencing factors, conclusions will be drawn after each factor, including an outlook on further possible improvements regarding properties and microstructure of the prototype capacitors. Overall, this thesis does not only entail deep engineering insights about prototyping MLCCs, but also integrates profound knowledge about solid-state chemistry of ceramics and polymer chemistry. It can be regarded as a guideline for further development.
After establishing a proper fabrication route with improved manufacturing parameters, a in-depth characterization of NBT-based capacitors is followed. This will include a comprehensive evaluation concerning their applicability as high-temperature and power electronics capacitors.[72] Besides microstructural investigations, the temperature stability, stability of dielectric properties, energy storage properties, high voltage stability, and impedance data will be considered. To gauge the performance of prototype MLCCs, they will be compared to commercially available CeraLink capacitors from TDK Electronics AG.[23]
Finally, a thorough study on reliability and electrical fatigue behavior is presented and will contribute to the understanding of electrodegradation and the dielectric breakdown of NBT-based materials and the prototype capacitors. Investigations on bulk NBT(-BT) under high voltages and elevated temperatures will help to identify the most critical aspects affecting the reliability of MLCCs. As MLCCs suffer most from oxygen vacancy migration and resistance degradation under temperature and voltage stress, special emphasis has to be given to improve reliability upon utilization.[9,19] A novel and viable solution presented by Gehringer et al. will be used in this work to first evaluate manufacturing of curved indentations into a green stereotype ceramic, $BaTiO_3$.[73] Corroborated by further electrical investigations of the effects of thickness, active volume, and voltage ramp, which allow for assessing the robustness of the novel indentation method, the results will be transferred to the actual capacitors. Obtaining knowledge about high voltage limits of NBT-based MLCCs aims to further increase the reliability.
All of the latter investigations may unburden a considerable amount of industrial validation efforts. By investigating the NBT-based ceramic material and MLCCs with respect to electrical fatigue and failure upon temperature and voltage stress, key information can be obtained to develop prevention strategies

and predict reliability. This work will ultimately answer the question whether prototype NBT-based MLCCs are viable for upcoming high-temperature and power electronics applications. This work aims to present a capacitor which is highly versatile and can be utilized in a broad range of operating conditions instead of exhibiting record-high relative permittivities or energy storage densities.

2 Theoretical Background

The following chapter entails the fundamental background of multilayer ceramic capacitors. A general overview of the physics of single- or multilayer capacitors and their classification will be provided. Key parameters deduced from academic research and industry are listed. This information will be conveyed towards high-temperature and power electronics materials, which will be elucidated subsequently. The main characteristics of the material itself and its dielectric properties are explained. Particular emphasis will be given to the NBT-BT-CZ-BA material system and its defect chemistry. Reliability and electrical fatigue are other crucial topics covered concerning electromigration and dielectric breakdown strength. Furthermore, the basics of impedance spectroscopy are expressed as this is a beneficial tool regarding the characterization of high-temperature and power electronics materials and MLCCs but also regarding application-related properties. Since the MLCC fabrication route was relatively new within this research group, a brief overview of MLCC prototyping is concluding the theoretical background. It will later help to evaluate the findings obtained during this work.

2.1 Multilayer Ceramic Capacitors

There are plenty of different types of capacitors being used for innumerable fields of applications. However, in this work, the focus will be put on MLCCs with emphasis on the dielectric material. In Figure 2.1 such a prototypical MLCC is depicted. Unlike simple plate capacitors, see Figure 2.2, MLCCs consist of a particular amount n of alternatively stacked inner electrodes. Alternative stacking allows for creating parallel pathways considering equivalent circuit diagrams. Hence, every dielectric layer between two alternative inner electrodes (dark gray) can be regarded as an active area A with distinct thickness d. Every stacked active area will, in turn, add up to the net capacitance of the device. Furthermore, the overlap between those alternative electrodes confines the active area. To test the components, outer electrodes or terminations (light gray) need to be applied. Please note that terminations consist of more than one material. A combination of different materials can serve as a barrier layer and passivation.[74] Within this work, only one material is used for the termination.
The choice of each material is highly significant for the performance of the capacitor but also regarding profitability, among others.

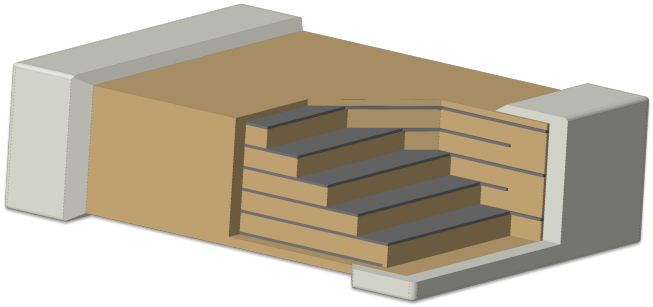

Figure 2.1: Schematic representation of a multilayer ceramic capacitor. The component comprises the dielectric material (brown), a particular amount n of inner electrodes (dark gray), and terminations (light gray).

2.1.1 Classification and Parameters

The classification of capacitors with respect to temperature and tolerance of capacitance will be explained first. This is followed by a set of the most important parameters of capacitors for high-temperature and power electronics applications. The following section is based on the textbooks of Reisch[75], Stiny[76], and the Technical Guide 2021 for CeraLink capacitors[77].
Ceramic capacitors are categorized into four different groups depending on their specific application. A guideline is provided by the Electronic Components Industry Association (ECIA) that defines the four classes as follows:[78]

Class I:

Ceramic capacitors exhibiting very high capacitance stability and low temperature, voltage, and frequency variation. However, permittivity is very low and low losses. Those components are suitable for resonant circuits, filtering, smoothing in high-frequency, and coupling/decoupling applications.

Class II:

Ceramic capacitors with a non-linear temperature- and voltage-dependence of capacitance but high permittivity and high volumetric efficiency. They also feature larger losses compared to Class I capacitors. The main applications are smoothing, snubber, by-pass, smoothing, DC-link, and coupling/decoupling.

Class III:

Similar to Class II capacitors but with even higher variation in capacitance and high volumetric efficiency. The field of application is comparable to Class II capacitors, but where the tolerance of capacitance is less important.

Class IV:

Ceramic capacitors with very high permittivities which serve as barrier layer capacitors. There

is essentially no standardization anymore. Additionally, other electrical characteristics are worse compared to the classes above.

A variety of different capacitor materials exist besides ceramic dielectrics, including electrolytic (Al, Ta, Nb) capacitors, polymer film, and mica paper capacitors, among others. Some of them, on the one side, can maintain relatively stable properties at elevated temperatures of up to 220 °C, whereas on the other side, capacitors with high capacitance are available. However, none of the latter types can combine high values of capacitance, high-temperature and high-field stability, high volumetric efficiency, low dielectric losses, and low production cost at once.[13,79,80] Class II capacitors may be the only class eligible to fulfill most requirements. However, their rather low temperature stability seems to be a major issue. In recent years, it has been focused on improving Class II dielectric materials to their high-temperature applicability and stability of capacitance.[10] Therefore, a classification scheme by the ECIA helps to render different dielectric materials. It is based on a three-digit-system as shown in Table 2.1. The first digit is a letter corresponding to the lower operating temperature, whereas the second digit, a number, expresses the upper operating temperature. The last digit, again a letter, characterizes the tolerance of capacitance.[10,76,78]

Table 2.1: Classification scheme for Class II dielectric capacitor materials.[10,76,78]

First digit		**Second digit**		**Third digit**	
Symbol	Lower temperature limit (°C)	Symbol	Upper temperature limit (°C)	Symbol	Tolerance of capacitance (%)
Z	+10	4	+65	A	±1
Y	-30	5	+85	B	±1.5
X	-55	6	+105	C	±2.2
		7	+125	D	±3.3
		8	+150	E	±4.7
		9	+200	F	±7.5
				P	±10
				R	±15
				S	±22

Example: An X7R dielectric can be used in a temperature window ranging from -55 to +125 °C with a ±15% tolerance of capacitance. The most well-known material for X7R capacitors is $BaTiO_3$.[10,22,76,81] Notwithstanding, very recent lead-free NBT-based material systems have been demonstrated to be among the most promising candidates for Class II dielectrics that could operate over wide temperature ranges and to over 300 °C.[29,82–85] This will later be seen in Subsection 2.2.3.

It needs to be highlighted that the above classification only takes into consideration the tolerance of capacitance in terms of a temperature range. There is no definition by ECIA or else about tolerances of capacitance when applying voltages. Additionally, manufacturers are not obligated to disclose it in data sheets.[86] There are still key parameters to rank and compare different material-related properties and other capacitor materials. They will be elucidated in the following:

Capacitance:

The parallel-plate capacitor consists of two conductor plates or electrodes, respectively, clamping

the dielectric material with relative permittivity ε_r in between, as schematically depicted in Figure 2.2. After applying an external voltage U, the dielectric will get polarized, and, hence, positive and negative charges will accumulate, with equal amounts, on both plates. This process continues until the electric potential in the dielectric has reached the value of applied voltage U. The electric field E can be expressed as

$$E = \frac{U}{d} \tag{2.1}$$

with the d the distance between two electrodes or thickness of the dielectric, respectively.

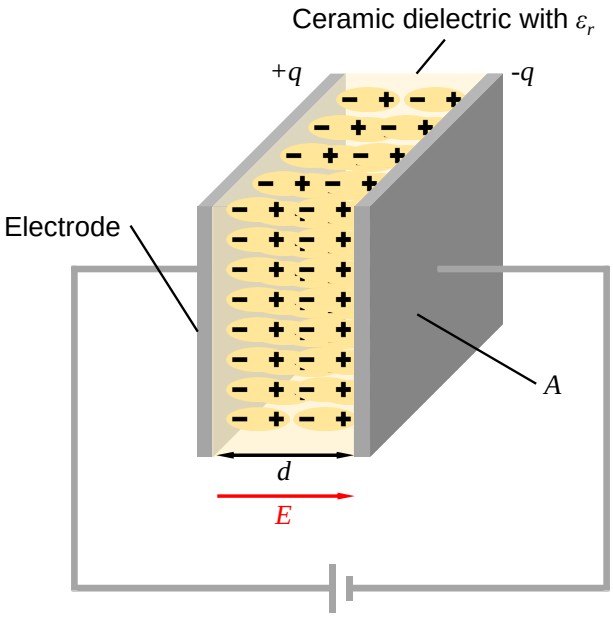

Figure 2.2: Schematic representation of a parallel-plate capacitor under application of an electric field.

Capacitors are capable of storing energy, which is expressed by the capacitance C. The capacitance is defined as

$$C = \frac{q}{U} \tag{2.2}$$

with the electric charge q. The capacitance can likewise be determined by employing the relative permittivity of the dielectric and the geometry of the capacitor:

$$C = \varepsilon_r \cdot \varepsilon_0 \cdot \frac{A}{d} \tag{2.3}$$

where A denotes the active area of a single layer and ε_0 the vacuum permittivity. As stacked multilayers are investigated (see Figure 2.1), the amount of inner electrodes n are parallel-connected. To calculate the capacitance of an MLCC, $n-1$ simple plate capacitors have to be considered. The capacitance is now expressed as:

$$C = (n-1)\,\varepsilon_r \varepsilon_0 \frac{A}{d} \tag{2.4}$$

In data sheets, the nominal capacitance C_{nom} or rated capacitance C_R of the capacitor is specified.[77] It is most often referred to the value at room temperature and is measured at the operating voltage U_{op}. Important capacitance tolerances from C_{nom} can be taken from Table 2.1. It essentially categorizes permitted tolerances of capacitances within a specified lower and upper operating temperature range.

Operating voltage:

The operating voltage U_{op} is the actual voltage applied during operation for the corresponding component. For instance, U_{op} is in the range of 80-90% of U_R, which also implies that saturation polarization does not have to be reached.[77]

Rated voltage:

The rated voltage U_R is defined as the maximum DC voltage at RT and is related to C_{nom}. The voltage rating gives the maximum safe potential difference between two adjacent inner electrodes the component can handle. Up to this voltage, the capacitor is supposed to be operable without dielectric failure or breakdown, respectively. When AC voltages are applied, the volt root mean square (RMS) U_{rms} must not be greater than U_R.
The rated voltage can also be denoted as the value reaching saturation polarization of the dielectric.[77]

Energy density:

For power electronics, the energy storage density is another key parameter, expressed with the help of the energy W stored in a capacitor

$$W = \frac{1}{2} C U^2 \tag{2.5}$$

as it follows:

$$\frac{W}{V} = \frac{\varepsilon_r \varepsilon_0 \cdot U^2}{2d^2} \tag{2.6}$$

with the volume V.

Volumetric efficiency:

The miniaturization of electronic devices, especially ceramic-based multilayer devices, is gaining attention.[10,87] Like the energy density, which expresses the stored energy per unit volume, the volumetric efficiency defines the capacitance per unit volume:

$$\frac{C}{V} = \frac{\varepsilon_r \varepsilon_0}{d^2} \tag{2.7}$$

Electric field-permittivity coefficient:

At high fields and temperatures dielectric, capacitors with pronounced permittivity behave somewhat non-linearly. Bias-field stability is an important issue to be able to operate the components within a broad range of electric fields without considerable losses of capacitance. The electric field permittivity coefficient (EPC) highlights deviations from a reference zero-field permittivity value

ε_{E0} and is defined by:[11,84]

$$EPC = \frac{\varepsilon_E - \varepsilon_{E0}}{\varepsilon_{E0}} \cdot 100 \tag{2.8}$$

with permittivity ε_E given at a certain electric field. The EPC can be used as a figure of merit for a simple comparison between different capacitors.
Like the EPC, the so-called voltage coefficient of capacitance (VCC) expresses the DC voltage dependence of the capacitance.

Temperature coefficient of capacitance:

Denoted as the temperature coefficient of capacitance (TCC), it indicates the change of capacitance with temperature relative to the room temperature. It can likewise be named α_c and is expressed by the subsequent equation:[88,89]

$$TCC = \alpha_c = \frac{C_T - C_0}{C_0 \cdot (T - RT)} \cdot 10^6 \tag{2.9}$$

with capacitance C_T at given temperature T. The TCC is denoted in ppm/°C or 10^{-6}/K. It is more relevant to Class I capacitors. However, since prepared MLCCs will be tested for temperature stability, it will also be considered.

Dielectric breakdown strength:

The DBS or simple dielectric strength is the most important parameter regarding failure modes of capacitors.[90,91] It is denoted as the electric field at which the conductivity of an insulator or dielectric rapidly increases by several orders of magnitude.[92] The DBS is most often given in kV/mm or MV/m but can also be expressed as the breakdown field $E_{bd} = \frac{U_{bd}}{d}$. A detailed description is followed in Section 2.3.2.

Loss factor:

The loss factor has several synonyms. It can likewise be called dissipation factor (DF) and dielectric loss and always refers to $\tan\delta$ with the loss angle δ. However, a common expression is also given by the subsequent equation where the real part of the relative permittivity ε_r' is related to the polarization of a system and the imaginary part of the relative permittivity ε_r'' is related to energy losses. This quotient yields the dielectric loss:

$$\tan\delta = \frac{\varepsilon_r''}{\varepsilon_r'} \tag{2.10}$$

with ($\delta = 90° - |\varphi|$) and φ as the phase angle.[93] Dielectric loss is typically specified at 1 kHz and RT.[94] Ideal capacitors do not have any losses. Every real capacitor, however, exhibits losses dependent on several aspects: contact resistance of the dielectric, inner electrodes, and terminations; dimension of (inner) electrodes and terminations; material of (inner) electrodes and terminations; and, of course, the dielectric material itself.[75,76,94] Different intrinsic and extrinsic contributions can occur depending on the existing polarization mechanisms, which are comprehensively described in

the work of Liu et al.[95] and Uchino et al.[38] In general, the loss factor quantifies all contributing losses under DC bias, which typically dissipate as heat and can be described as:

$$P_D = \omega \cdot C \cdot U^2 \cdot \tan\delta \tag{2.11}$$

with the power dissipation P_D and the angular frequency ω. The loss factor will again be discussed in Subsection 2.4.1.

ESR and ESL:

The equivalent series resistance (ESR) characterizes the effective ohmic resistance of the capacitor in series.[76] It includes all losses from above and is related to the dielectric loss by the following equation:

$$\tan\delta = \frac{ESR}{X_C} = \frac{1}{Q} \tag{2.12}$$

with the quality factor Q and the capacitive reactance X_C. For instance, capacitors in DC-to-DC converters need to have a low ESR to maintain good efficiency. Manufacturers often state ESR values at rated voltages, specific frequencies, and RT.

Besides the resistive part of the impedance, real capacitors have an inductive part. It is called equivalent series inductance (ESL), plays a role at higher frequencies, and may be neglected far below the self-resonant frequency (SRF).[96,97] It can be calculated at the SRF and is expressed by:

$$ESL = \frac{1}{\omega^2 C} \tag{2.13}$$

Specification in data sheets is even more sparse, and only the ESL value is occasionally given. ESR and ESL will again be discussed in Subsection 2.4.1.

Leakage current:

Lastly, the leakage current or insulation resistance R_p is another critical parameter. High insulation resistance corresponds to low leakage currents. Dielectrics with low leakage currents are desired to withstand high electric fields.[22] Regarding ceramic dielectrics, the leakage currents are mostly negligible. Albeit, during storage or under extreme conditions with respect to degradation, the capacitors may suffer from considerable leakage currents.

2.2 High-temperature and Power Electronics Materials

This section will briefly describe the physics of the materials being suitable for high-temperature and power electronics applications. A comprehensive description of other dielectric materials and their response to applied electric fields can be found in the textbooks of Moulson and Herbert[98], Waser and Böttger[99], Jaffe and Cook[100], Bain and Chand[101], and Newnham[102]. A comparison between relaxor ferroelectric and ferroelectric materials with respect to temperature and electric field will be provided. Further, fundamental knowledge about dielectric energy storage will be elucidated. This is accompanied by a literature review of the most promising and up-to-date capacitors and capacitor materials and will be contrasted concerning high-temperature and power electronics applications. Lastly, the material system NBT-BT-CZ-BA will be reviewed regarding defect chemical considerations, high-temperature, and energy storage properties.

2.2.1 Relaxor Ferroelectrics

Within this work, the relaxor ferroelectric material NBT-BT-CZ-BA will be utilized for prototyping multilayer ceramic capacitors. Investigating the physical principle behind relaxors is not part of this work. Relaxor ferroelectric (RFE) materials are closely related yet significantly different from conventional ferroelectrics. Ferroelectric materials are a subgroup of pyroelectric, piezoelectric, and dielectric materials, as depicted in Figure 2.3.

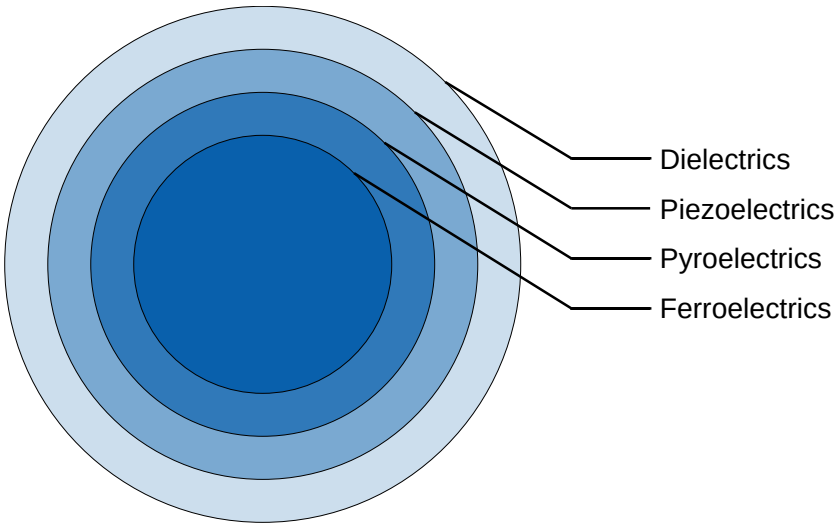

Figure 2.3: Corresponding subgroups of the group of dielectric materials including piezoelectrics, pyroelectrics, and ferroelectrics.[70]

Although discovered around 70 years ago, the conceptual mechanisms behind relaxor ferroelectrics have not yet been fully understood. Comprehensive reviews of the proposed models are published by Bokov and Ye[103], Cowley et al.[104], and Ahn et al.[105] The characteristic compositional order-disorder greatly affects relaxor properties, as suggested by multiple authors.[31,105,106] Both ferroelectric (FE) and RFE

materials will display a paraelectric, cubic structure at correspondingly high temperatures. Upon cooling, material properties start to deviate. In classic FEs, the spontaneous polarization will start to be present at the transition temperature T_C, accompanied by a phase transition. This also involves peaking of the relative permittivity. In RFEs, however, there is no real phase transition. It was thought that a diffuse phase transition into FE would take place, but no change of crystal structure on the macro- or mesoscopic scale could be detected.[103] Below the Burns temperature T_B, relaxors transition from the paraelectric into the ergodic relaxor (ER) state. One of the key features of relaxors starts to appear, the so-called polar nano regions (PNRs). At temperatures close to the T_B, these localized polarization clusters are dynamic. They are also capable of aligning in applied electric fields. Upon further cooling below T_B, PNRs are formed, but they also grow in size. It happens due to the increasing polarizability of the matrix with decreasing temperature. Since not every PNR is growing in the same manner, a broad size distribution is prevailing, associated with a broad dispersion of relaxation times.[32,107] Additionally, interactions with other polar regions will enhance the dispersion even more. Consequently, a frequency-dependent maximum of relative permittivity T_m emerges. A comparison between a regular FE and RFE material is depicted in Figure 2.4. In Figure 2.4(a) and 2.4(c), the temperature-dependent polarization and permittivity of FE materials are opposed to the behavior of RFE materials (Figure 2.4(b) and 2.4(d)). A distinct transition temperature is missing for relaxor materials. Instead, they show the latter-mentioned frequency-dependent maximum of relative permittivity. This frequency dispersion is one of the key features of PNRs and is unique compared to common ferroelectrics.[31]

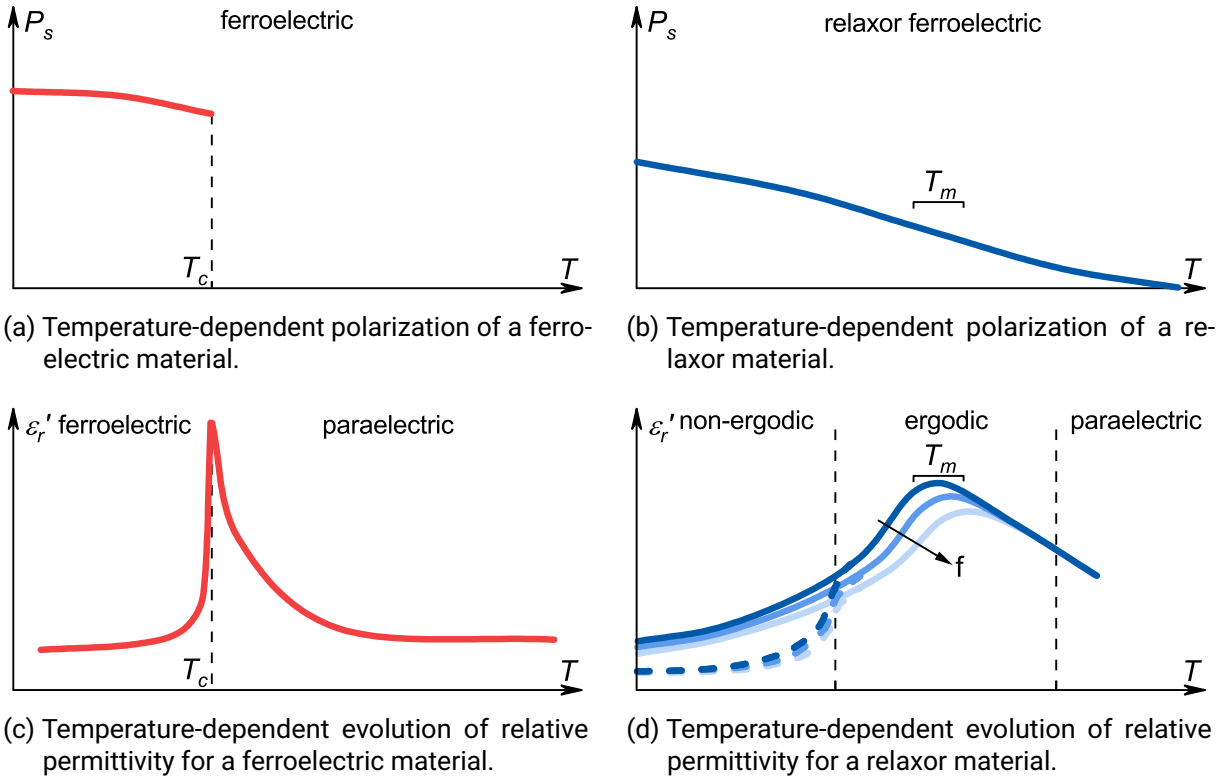

(a) Temperature-dependent polarization of a ferroelectric material.

(b) Temperature-dependent polarization of a relaxor material.

(c) Temperature-dependent evolution of relative permittivity for a ferroelectric material.

(d) Temperature-dependent evolution of relative permittivity for a relaxor material.

Figure 2.4: Comparison of FE and RFE materials detailing the spontaneous polarizations (a) and (b) for FE and RFE, respectively, accompanied by temperature-dependent phase transitions and the permittivity response at various temperatures (c) and (d) for FE and RFE, respectively, adapted from Samara.[31]

Going a bit further towards the material under investigation, another phenomenon can be perceived in certain relaxor materials. There is a differentiation between so-called high-temperature polar nano regions (HT-PNRs) and low-temperature polar nano regions (LT-PNRs). This was evidenced by Zang et al. who investigated a $Na_{0.5}Bi_{0.5}TiO_3$-$BaTiO_3$-$K_{0.5}Na_{0.5}NbO_3$ (NBT-BT-KNN) material system with impedance spectroscopy, which is depicted in Figure 2.5.[108,109] In Figure 2.5(a) the thermal evolution of PNRs at 0KNN or 18KNN is represented by the dielectric response. For different amounts of KNN, different types of PNRs appeared to be present. At T_m a transition from the low-temperature state to the high-temperature state occurs. Different polarizabilities, along with a distinct change in crystal structure between the two types of PNRs, are characteristic and were also shown in the system $Na_{0.5}Bi_{0.5}TiO_3$-$BaTiO_3$-$CaZrO_3$ (NBT-BT-CZ).[35] Likewise, the Burns and freezing temperature are shifted according to different amounts of KNN. The modulus plot in Figure 2.5(b) at 300 °C and varying 18KNN-xCZ content was helpful regarding the detection of a second response (shoulder), which could be attributed to the contribution of transforming PNRs. However, it is still a matter of debate where the second response is coming from. By impedance spectroscopy-derived elastance data from model calculations, Frömling et al. rationalized that parallel electrical pathways also can contribute to such a response, as highlighted later in Section 2.4.[110]

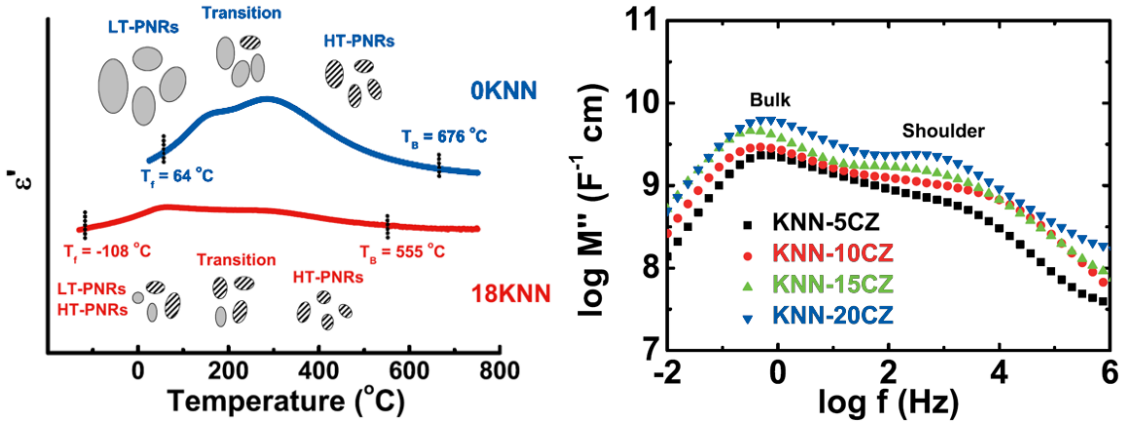

(a) Thermal evolution of PNRs expressed by the dielectric response with 0KNN and 18KNN. Each phase between T_f and T_B is marked correspondingly, adapted from Zang et al.[108]

(b) Modulus representation of 18KNN samples at 300 °C and varying CZ content for the detection of a second PNR response (shoulder), adapted from Zang et al.[109]

Figure 2.5: Thermal evolution of PNRs expressed by the dielectric response and modulus representation at 300 °C with varying CZ content.

As demonstrated by Figure 2.5, relaxor materials exhibit exclusive features regarding their response due to their temperature-dependent frequency dispersion. The dispersion of relaxation times, exceptionally high values of permittivity, and the lack of an abrupt T_C make them attractive for high-temperature applications by broadening the temperature-stable permittivity plateau. The plateau allows for stable properties within a specific temperature range, which is vital for capacitors being operated in a wide temperature window. Another key difference to regular ferroelectrics is situated in the polarization-electric field (P-E) behavior. It will be explained in combination with the fundamentals of dielectric energy storage in the following section.

2.2.2 Dielectric Energy Storage

The dielectric energy storage of dielectric materials is a crucial representative when it comes to the utilization of such materials, e.g., as capacitors. The total energy density W_{total} is related to the accumulated charges and can subsequently be described by the following equation:[98,111]

$$W_{total} = \int_0^q U dq = \int_0^{P_{max}} E(P) dP = W_{rec} + W_{loss} \tag{2.14}$$

with the maximum polarization P_{max}. The area between the y-axis and the corresponding hysteresis loop is the recoverable energy density W_{rec}, while the energy loss W_{loss} corresponds to the area within the loop. Further, W_{rec} is expressed as

$$W_{rec} = \int_{P_R}^{P_{max}} E(P) dP. \tag{2.15}$$

The ratio between W_{rec} and the sum $W_{rec} + W_{loss}$ yields the energy storage efficiency η:

$$\eta = \frac{W_{rec}}{W_{rec} + W_{loss}} \cdot 100\%. \tag{2.16}$$

An exemplary visualization of characteristic hysteresis loops for both RFE and FE but also linear dielectric and antiferroelectric materials is provided in Figure 2.6. The red area marks the energy storage density W_{rec}, and the gray one denotes the energy loss density W_{loss}. Relaxor materials (Figure 2.6(b)) typically show very slim hysteresis loops accompanied by a low remanent polarization P_R. The loops do not possess a typical hysteresis; the nonlinearity, however, is associated with PNRs and its reorientation of polarization.[112] This behavior is governed by the electric field response of the PNRs inside the relaxor material. After releasing the electric field, the PNRs tend to return to their random equilibrium orientation. This is reflected in a low net remanent polarization at zero field and low energy loss, too. Regarding FE materials, however, their behavior is entirely different.

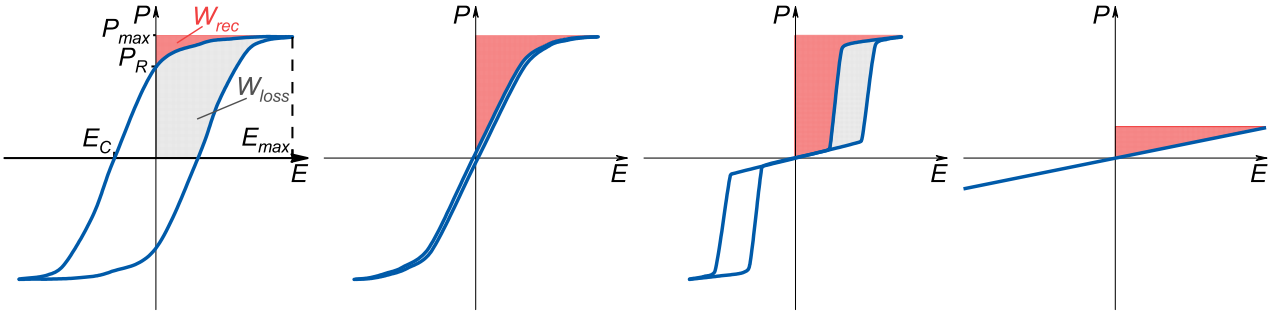

(a) Ferroelectric (b) Relaxor ferroelectric (c) Antiferroelectric (d) Linear dielectric

Figure 2.6: Comparison of characteristic polarization-electric field loops of dielectric materials and its most important subgroups. The red area in (a) corresponds to the recoverable energy density W_{rec}, whereas the gray one denotes the energy loss density W_{loss}. Marked is also the maximum polarization P_{max}, remanent polarization P_R, coercive field E_C and the maximum field E_{max}.

As shown in Figure 2.6(a), the loop features a sizeable remanent polarization. A large P_R implies a significant energy loss, which can also be seen in the increased area of the loss compared to RFE materials. Another two exciting materials are antiferroelectric (AFE) (Figure 2.6(c)) and linear dielectric (Figure 2.6(d)) materials. Opposed to classical ferroelectrics, in antiferroelectrics the polarization is stable when half of the dipoles are oriented in one direction and their adjacent dipoles in the other direction.[112] As a result, there is a lack of macroscopic net polarization. Typical for antiferroelectric materials is the double hysteresis loop.[111] A sudden increase in polarization only starts beyond a particular phase transition field. Before, it appeared to behave linearly. High maximum polarizations can be achieved. They are, dependent on the phase transition field, accompanied by rather high losses. It can be recognized by the large area within the loops. However, high maximum polarizations also imply high recoverable energy densities. These characteristics make AFE materials also extremely interesting for energy storage applications.[23,113,114] In contrast, the maximum polarization of linear dielectrics is much lower compared

to the other three types. The energy loss is, nevertheless, also negligible.
For the search for capacitor materials, it is beneficial to choose ceramics with a high recoverable energy storage density paired with excellent energy efficiency. Therefore, capacitors should withstand high electric fields and exhibit a low remanent polarization. Ferroelectrics, relaxors, and antiferroelectrics display a saturation of polarization with increasing electric field. The slope of the curves, which is related to the dielectric constant, at low fields is steeper than the slope at higher fields since the macroscopic polarization is already aligned along the direction of the electric field.[112] This implies that a linear increase would be most suitable for finding a versatile capacitor (material) that can be operated in a wide range of temperatures and electric fields. This requirement also implies another disadvantage of AFE materials since they only show a significant polarization beyond the switching field. It could highly limit the operational window in terms of applied electric fields.

2.2.3 Literature Review

In particular, sectors such as renewable energies, electric vehicles, power conversion, and power electronics require capacitors that can withstand challenging temperature conditions and high electric fields. Although capacitors have specific applications such as snubber, DC-link, smoothing (full wave rectifier), and filters, there is a lack of comprehensive information regarding component requirements, specifications, standards, voltage ratings, and energy density properties.[7,16,17] Only rough temperature ranges from -50 to $\leq$300 °C are specified, including limits of the TCC.[10,35,78,85] Dielectric losses are likewise arbitrarily chosen. These losses should be below 2-2.5% for high-temperature applications. It is crucial to establish standards and encourage manufacturers and industries to provide transparent disclosure of such data. Consequently, it is not logical to focus solely on finding the broadest temperature range for stable dielectric properties nor to pursue a capacitor material that emphasizes exceptional energy storage properties without real-world applications. Anyways, this subsection entails a systematic comparison between two sides of the coin, namely stable dielectric properties over a wide temperature range and capacitor materials exhibiting excellent energy efficiencies at high applied voltages. Figure 2.7 compares a variety of lead-free (NBT-, BCT-, and BT-based) capacitor materials and MLCCs regarding TCC $\leq$15%, dielectric loss (tan δ $\leq$2%), and maximum permittivity ε_r'. Numerous capacitor materials exist, yet only a limited selection is utilized in actual MLCCs with platinum electrodes, and even fewer incorporate more cost-effective silver palladium inner electrodes.[115–117] It accentuates the challenges of successfully preparing NBT-based MLCCs with Ag/Pd inner electrodes. Figure 2.8 contrasts the energy efficiency and the maximum voltage applied U_{max} of NBT- and BT-based ceramic capacitors in blue and gray, respectively. Solid symbols represent Ag/Pd inner electrodes, while half-up symbols correspond to Pt inner electrodes. Most of the MLCCs in this figure either consist of BT-based dielectric materials or are manufactured with Pt inner electrodes. Rather than promoting specific properties, this representation aims to highlight the versatility of the capacitor, such as its stability when exposed to high voltages. It can be deduced that NBT-based MLCCs with Ag/Pd inner electrodes are quite rare, and those withstanding high voltages are even rarer.

Currently, commercially available BT-based capacitors are unable to meet high-temperature requirements. They can only function reliably without severely deteriorating dielectric properties below 200 °C. This is due to their ferroelectric nature.[10] Taking power converters as an example, there is a systematic issue that parts of the power electronics converters can be operated at temperatures even higher than 500 °C.[5,7] Silicon carbide (SiC)-based devices can go to temperatures up to 500 °C while capacitors and other passive components are limited to much lower temperatures. Even for packaging design, the soldering does not allow to go beyond 225-250 °C. Engagement is needed for the systematic improvement of each component of power converters for high temperatures. Ultimately, the stability at high temperatures cannot be ignored, although the emphasis is often solely on finding the best and highest energy densities with the best efficiency. Another issue of commercial MLCCs, such as the lead-based AFE CeraLink capacitor, is their lack of temperature and capacitance stability over a broad range of applied fields or voltage.[114,118,119] In recent years, lead-free relaxor ferroelectric and NBT-based solid solutions have emerged as promising candidates for MLCCs in high-temperature and power electronics applications.[34,35,85,120] The question remains, however, why are NBT-based materials highly suitable for high-temperature and power electronics applications?

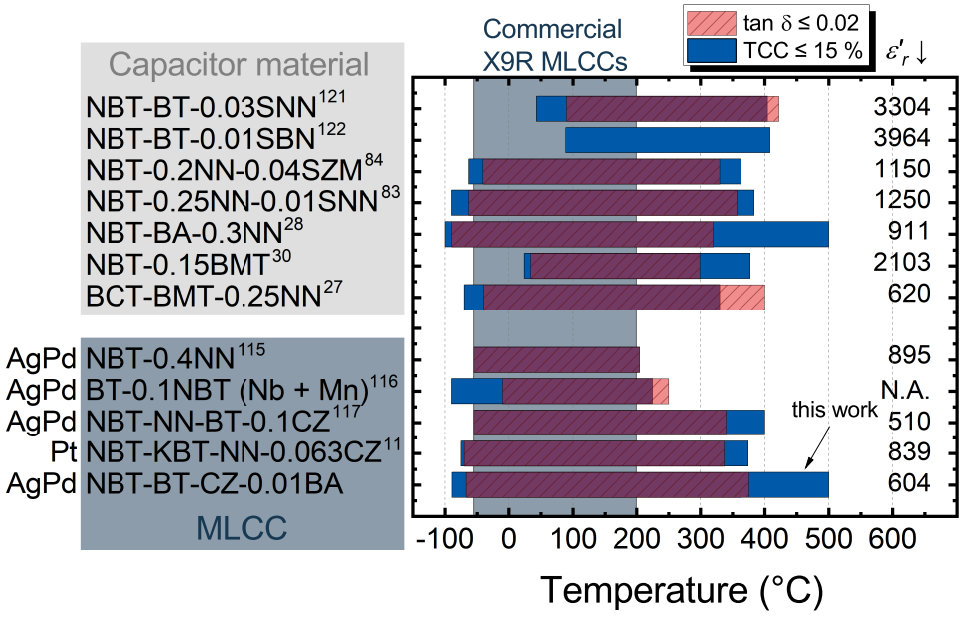

Figure 2.7: Comparison of temperature-related operational windows of lead-free NBT-, BCT-, and BT-based capacitor materials and MLCCs with respect to TCC ≤15%, dielectric loss (tan δ ≤2%), and maximum permittivity ε'_r.

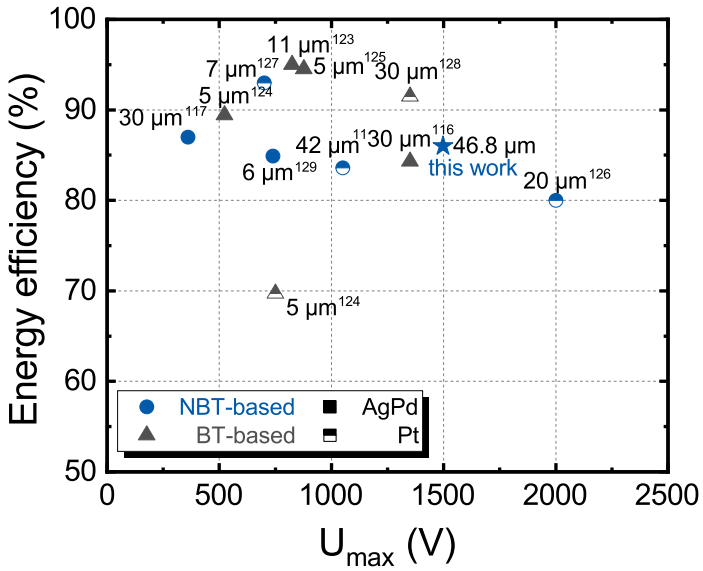

Figure 2.8: Comparison of the energy efficiency and the maximum voltage applied U_{max} of NBT- and BT-based ceramic capacitors in blue and gray, respectively.

2.2.4 Material Systems

Before NBT-BT-CZ-BA is discussed in more detail and with respect to key parameters considering high-temperature and power electronics applications, NBT and its solid solution NBT-BT will be reviewed regarding the defect chemistry. Both were already comprehensively described by the works of Steiner[121] and Dittmer.[122] However, it is vital to know the impact of high temperatures and the application of electric fields on the defect chemistry of NBT-based MLCCs.

2.2.4.1 Defect Chemistry of NBT and its Solid Solution NBT-BT

The material NBT was first investigated by Smolenskii et al. in 1961.[123] Zvirgzds et al. first observed the well-known frequency dispersion during temperature-dependent permittivity measurements.[124] The temperature of maximum permittivity T_m was reported not to be linked to a structural phase transition, though. They proposed that NBT shares similarities to lead lanthanum zirconate titanate (PLZT) and lead magnesium niobate (PMN) relaxors. X-ray and neutron diffraction investigations showed that PNRs growing with decreasing temperatures supported this claim.[125] Furthermore, the frequency-dependent evolution of permittivity was ascribed to the presence of PNR.[126] The maximum permittivity of sodium bismuth titanate was reported to be close to 3000 at T_m, depending on the applied frequency.[127,128] This substantial dielectric constant is caused by electric field-induced phase transitions. Besides this, pure NBT is not very useful for high-temperature power electronics since they require stable properties over an extensive temperature range and electric fields. Furthermore, sizeable temperature-dependent leakage currents were observed.[24] This is, of course, extremely detrimental to the capacitors' application.
With regards to dielectric properties, Mishra et al. demonstrated that high dielectric loss and leakage

current result in a considerable oxygen vacancy concentration already at room temperature.[129] For lead-free bismuth-based perovskites like NBT, it can be expected that oxygen vacancies are induced by either acceptor doping or bismuth nonstoichiometry by bismuth evaporation.[39,130] Both can be expressed with the help of the Kröger-Vink notation.[131] It denotes relative electric charges of lattice sites with respect to a distinct crystal structure and is denoted as S_P^c. The letter S defines the species, which could either be atoms (Na, Bi, Ti, etc.), vacancies indicated by V, electrons (e), or holes (h). The subscript character defines the lattice site occupied by the species S and is either indicated by the atomic symbol or i for an interstitial site. The superscript letter c displays the relative electric charge. Negative charges are characterized by a prime symbol($'$), positive charges by a bullet symbol($\bullet$), and neutral charges by an x. Positive and negative charges can also be piled up, e.g., a twofold negative charge ($''$). With the help of the Kröger-Vink notation, defect reactions can be formulated which comply with charge neutrality and mass and lattice site conservation. When doping aliovalent ions, the doped atoms are referred to as acceptor or donor doping. Going back to increasing the amount of oxygen vacancies by either Fe acceptor doping or bismuth evaporation, the resulting equations are:

$$Fe_2O_3 \rightarrow 2Fe_{Ti}^{'} + V_O^{\bullet\bullet} + 3O_O^x \tag{2.17}$$

$$2Bi_{Bi}^x + 3O_O^x \rightarrow 2V_{Bi}^{'''} + 3V_O^{\bullet\bullet} + Bi_2O_3 \uparrow \tag{2.18}$$

Fe substitutes the B-site Ti, and an additional oxygen vacancy is created.[44] Both can have a substantial impact on the dielectric properties of NBT-based capacitors.[41] Similarly, adding sintering aids to bismuth-based perovskites can also be regarded as doping under the migration of the corresponding additives into the matrix lattice. Adding the sintering additive CuO, for example, may be comparable to acceptor doping, as the following equation illustrates:

$$CuO \rightarrow Cu_{Ti}^{''} + O_O^x + V_O^{\bullet\bullet} \tag{2.19}$$

Not surprisingly, it was shown that adding CuO to the system lowers the sintering temperature of the investigated material system.[50,68] However, the influence of induced oxygen vacancies on dielectric properties cannot be neglected. They can drastically increase dielectric losses at high temperatures.[49,68] It is known that doping of FE materials, like lead zirconate titanate (PZT) and BT, causes a hardening effect, restricting the mobility of ferroelectric domain walls.[36,132] The Ti^{4+} on the B-site is claimed to be occupied by an acceptor dopant like Fe^{3+}. This is related to the formation of defect dipoles. The driving force for such defect associates may be the relaxation of strain energy, electrostatic interactions, or a combination of both.[45] Lambeck and Jonker already revealed the formation of defect complexes of an acceptor and oxygen vacancy in a BT-based system.[133] Defect complexes are formed based on the following example with a divalent acceptor dopant:[46]

$$A_B^{''} + V_O^{\bullet\bullet} \leftrightharpoons (A_B^{''}V_O^{\bullet\bullet})^x \tag{2.20}$$

In the case of Fe-doped perovskites, the defect complex $(Fe'_{Ti} - V_O^{\bullet\bullet})^{\bullet}$ is formed and immobilizes the adjacent oxygen vacancy.[44] Regarding adding CuO as a sintering aid, the resulting defect complex was $(Cu''_{Ti} - V_O^{\bullet\bullet})^{x}$.[68] However, observed effects in NBT are different compared to lead-based PZT. NBT, in general, is very complex regarding its defect chemistry.[46] Although it is highly resistive and electronically conductive at low temperatures, at high temperatures, it can behave completely different. Acceptor doping in NBT can lead to unexpectedly high ionic conductivities. This is depicted in the Arrhenius plot of pure and Fe-doped NBT in Figure 2.9(a).

As it was found that Ag can segregate from Ag/Pd inner electrodes and can be incorporated on an A-site in NBT-based perovskites, this is very concerning regarding capacitor applications.[47] In PZT ceramic stacks with Ag/Pd electrodes, it was indicated that Ag acts as an acceptor dopant and impairs the stability of the component.[55,56] Eventually, it could also result in the formation of defect dipoles. However, evidence was provided that this complex formation in NBT is highly dependent on the dopant concentration or oxygen vacancy concentration, respectively.[39] It can be expected that the dependence of defect dipole formation on vacancy concentration is nonlinear.[46] The ionic conductivity changes by orders of magnitude with only small changes in acceptor concentration. For NBT, the conductivity changes from low intrinsic electronic conductivity to orders of magnitude higher ionically dominated conductivity with a low amount of acceptor doping over a wide temperature range.

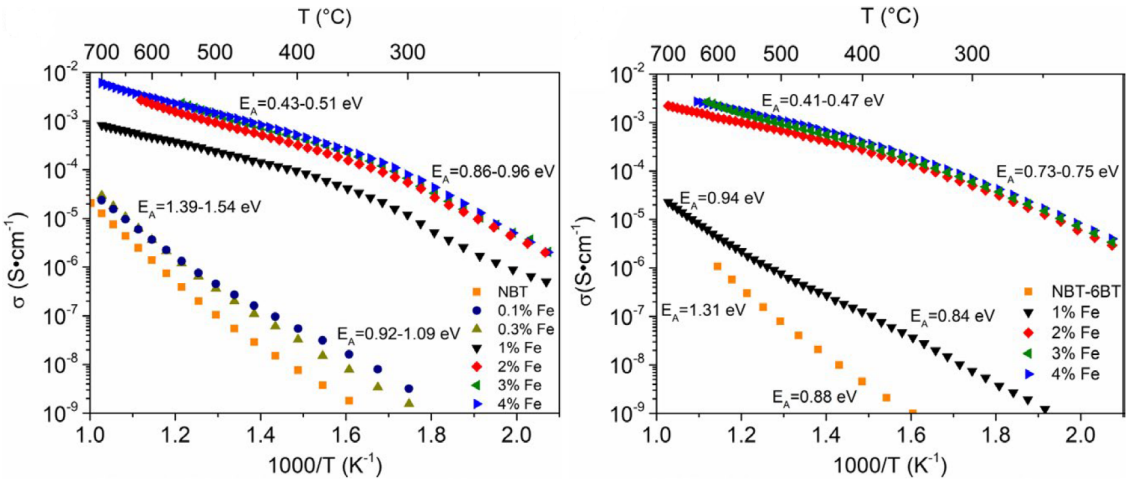

(a) Pure NBT and doped NBT up to 4 mol% Fe. (b) Pure NBT-6BT and doped NBT-6BT up to 4 mol% Fe.

Figure 2.9: Arrhenius plots of undoped and Fe doped bulk samples of NBT and NBT-6BT, adapted from Steiner et al.[44]

For ferroelectric applications, pure NBT is less relevant. The solid solution NBT-6BT, at the morphotropic phase boundary (MPB), exhibits superior FE properties.[134,135] By performing dielectric measurements, PNRs and the relaxor nature were still claimed to be evident around the MPB, i.e., in the rhombohedral and tetragonal phase.[136] Moreover, it was demonstrated that the extent of ferroelectric hardening was reduced compared to pure NBT.[137] Steiner provided evidence that NBT-6BT still exhibits low, mostly intrinsic electronic conductivity at 1 mol% acceptor doping.[44] This is reflected in Figure 2.9(b). The

question arises as to whether NBT-based solid solutions need to be treated differently when applying high temperatures and electric fields. Höfling et al. investigated NBT-BT-CZ with Bi excess on the A-site and found a noticeable positive effect on dielectric loss.[35] The addition of calcium zirconate (CZ) to NBT-6BT is based on the findings by Acosta et al., who created a viable contender for high-temperature applications.[34] By having 1 mol% Bi excess, a temperature-stable permittivity plateau in the range of -67 to 362 °C could be maintained. The ε_r' at 150 °C was still at 623. This increased extent of stable dielectric properties with low dielectric loss was justified by the additional bismuth. It significantly reduces the oxygen vacancy or mobile defect concentration, respectively.[35]

2.2.4.2 NBT-BT-CZ-BA

In a recent study to further control the defect mechanisms and influence of oxygen vacancies, Hoang et al. modified the composition with bismuth aluminate (BA) to reduce the dielectric loss at high temperatures, making the capacitor material even more suitable for its applications.[29]
Polycrystalline ceramics of (1-x) [0.8(0.94$Na_{0.5}Bi_{0.5}TiO_3$-0.06$BaTiO_3$)-0.2$CaZrO_3$]-x$BiAlO_3$ with different amounts of BA in the range of x = 0.5, 1, 1.5, 2, 4, and 8 mol% were prepared. For the study of the most encouraging material composition regarding high-temperature and high-field applications, only the compositions with 0.5 and 1 mol% will be elucidated in more detail. In general, Bi-rich secondary phases could be identified within this study. This is, of course, adverse as it will limit the high-temperature stability due to bismuth segregation and evaporation, as demonstrated by Equation 2.18. The vacancies are more mobile at elevated temperatures, resulting in enhanced losses. It was also confirmed by a recent study of a similar material system conducted by Schulz et al.[85] By using manganese as a dopant, they could validate a compensation mechanism that Mn is compensating oxygen vacancies as $Mn_{Ti}^{''}$. In the work by Hoang et al., BA was introduced to decrease the oxygen ionic conductivity and stabilize the dielectric properties over a broad temperature range, particularly in the high-temperature regime.[29] Suppression of oxygen ionic conductivity was similarly reported by Yang et al.[130] Adding BA to NBT could enhance the temperature range of stable permittivity by proposed trapping of oxygen vacancies by Al^{3+}. Bismuth aluminate is supposed to form a solid solution with NBT, as expressed in Equation 2.21:[29]

$$2BiAlO_3 \xrightarrow{\text{NBT-lattice}} Bi_A^{\bullet\bullet} + Bi_A^x + 2Al_{Ti}^{'} + 6O_O^x \tag{2.21}$$

Doping acceptors would imply compensation by a distinct amount of oxygen vacancies. However, doping aluminum for the B-site titanium is balanced by the additional A-site Bi. Under the circumstance of $V_O^{\bullet\bullet}$ being present due to bismuth evaporation during processing, the defect dipole $(Al_{Ti}^{'} - V_O^{\bullet\bullet})^{\bullet}$ is trapping and immobilizing the oxygen vacancy, diminishing thereby dielectric loss.[121,138]
Besides secondary phases, core-shell structures were observed in NBT-BT-CZ(-BA). They could also be the reason for the superb dielectric properties of this material system.[29,35] However, whether core-shell structures or PNRs are the course of the dielectric response needs further investigation but is out of the scope of this work. It needs to be noted that evidence for dynamic PNRs was found due to the frequency dispersion of dielectric permittivity and loss, as Figure 2.10 features. At low temperatures of about

-100 °C, a peak in tan δ was attributed to a nonergodic-ergodic phase transition at which rhombohedral LT-PNRs are formed.[135] This is indicated by the left arrow in Figure2.10c). A second peak (right arrow) in dielectric loss and a shift of T_m of relative permittivity with increasing frequency at around 200 °C could be associated with the transition of rhombohedral LT-PNRs towards HT-PNRs, which are comprised of both rhombohedral and tetragonal fractions.[139]

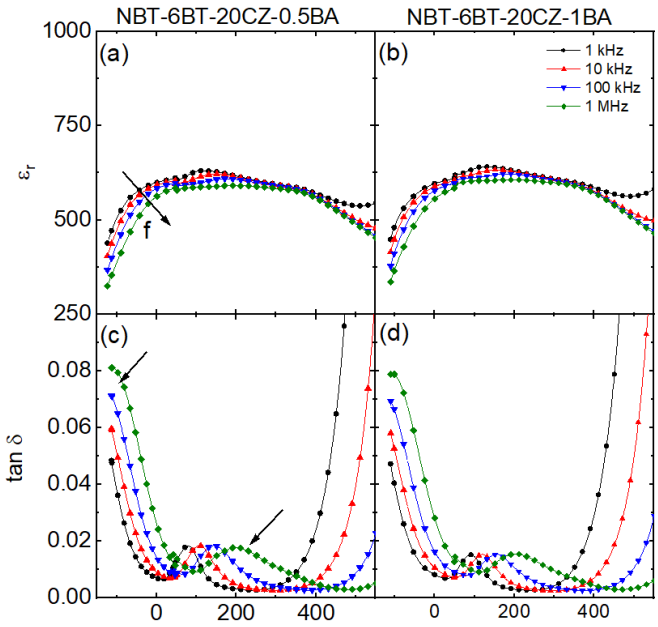

Figure 2.10: Relative permittivity (a and b) and dielectric loss (c and d) of NBT-6BT-20CZ-xBA compositions with x = 0.5 and 1%, adapted from Hoang et al.[29]

The following Table 2.2 summarizes the characteristic parameters obtained for the 0.5BA and 1BA addition to NBT-6BT-20CZ and is extracted from the work by Hoang et al.[29] The importance of each parameter was explained in Subsection 2.1.1, which is key to finding a competitive material system for high-temperature applications and power electronics. Nevertheless, with both compositions, i.e., 0.5BA and 1BA addition to NBT-6BT-20CZ, noteworthy characteristics and, in particular, an extended temperature-stable permittivity plateau could be observed. Both compositions feature a ε_r' of about 630-641, whereas at 150 °C and 1 kHz, the permittivity is still in that range. Furthermore, the relative permittivity and dielectric loss were recorded with variations ≤15% and ≤0.02, respectively, in a record-high 459 °C window. This is already an encouraging starting point for the fabrication of MLCCs with this material system as the dielectric.

Table 2.2: Characteristic parameters obtained at 1 kHz for NBT-6BT-20CZ-0.5BA and -1BA

Composition	ε_r'(max)	ε_r'(150 °C; 1 kHz)	$\Delta T(\varepsilon_r' \pm 15\%)$ (°C)	$\Delta T(\tan\delta \leq 0.02)$ (°C)	$\Delta T(\varepsilon_r' \pm 15\%; \tan\delta \leq 0.02)$ (°C)
0.5BA	630	628	-83 - 550	-68 - 391	459
1BA	641	640	-75 - 550	-71 - 381	452

Nonetheless, dielectric energy storage properties are almost equally important as latter high-temperature characteristics. The starting point, again, was given by Hoang et al. within their work, which also featured temperature-dependent polarization vs. electric field measurements, displayed in Figure 2.11.[29]

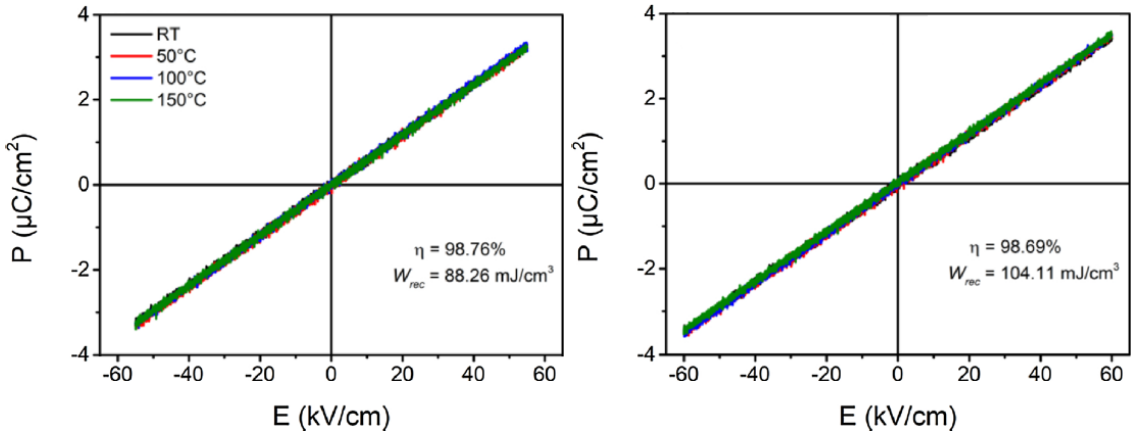

(a) NBT-6BT-20CZ-0.5BA (b) NBT-6BT-20CZ-1BA

Figure 2.11: Temperature-dependent polarization-electric field loops of NBT-6BT-20CZ-0.5BA and -1BA marked with energy efficiency and recoverable energy density, adapted from Hoang et al.[29]

For both compositions, an electric field of 60 kV/cm at 1 Hz was applied and investigated from room temperature (RT) to 150 °C. Both responses are linear. Due to the relaxor behavior of the material system, non-linear P-E loops are expected. This suggests that applied electric fields are too low to detect any saturation of the polarization loops. Much higher electric fields are needed in high-temperature and power applications like snubber and DC-link capacitors, among others.[16] Nevertheless, a recoverable energy density of 88.26 and 104.11 mJ/cm³ could be reached at 60 kV/cm for the 0.5BA and 1BA, respectively. Obviously, a paramount energy storage efficiency η of 99% for both systems was recorded. Applying much higher electric fields than 60 kV/cm at elevated temperatures can be critical regarding NBT-based MLCCs. In the previous study, only the bulk material was investigated. Within this work, Ag/Pd inner electrodes will be utilized for the MLCCs. The segregation and migration of the Ag can feature a significant drawback regarding the high voltage application at elevated temperatures, as discussed before. Thus, the effect of electromigration will be evaluated in the next section. The material system, nevertheless, serves as a basis for this work, will be utilized for the preparation of MLCCs, and is the reference material system for comparison of obtained MLCC-related data.

2.3 Reliability and Electrical Fatigue

In this section, the failure and electrical fatigue behavior of capacitor materials under specific conditions will be briefly reviewed. The application-related impact of electroformation of NBT-based materials is followed by an approach to properly determine and evaluate the dielectric breakdown behavior and strength of the capacitor material and related MLCCs as one of the most critical failure modes.

Reliability and electrical fatigue are crucial considerations in the field of passive components. When designing and manufacturing components, ensuring their long-term performance and durability is decisive.[13] Reliability refers to the ability of a material or component to consistently perform its intended function without failure over a specified period.[5,15] Most failures of ceramic capacitors are caused either by degradation of insulation resistance over time under simultaneous temperature and DC field stress, resulting in high leakage currents, or by dielectric breakdown, which is characterized by a catastrophic failure of the component.[140–143] Electrical fatigue pertains to the degradation and failure of materials or components over time due to repetitive loading, cyclic, or electric field stress.[70,144] A dielectric breakdown, on the other hand, is denoted as an instantaneous decrease of high insulation resistance caused by exceeding the dielectric strength of the material or component.[140] Both failures often occur due to defects, including oxygen vacancies, pores, voids, delaminations, or cracks.[9,131]

2.3.1 Electroformation

As explained, resistance degradation can occur during operation under applied electric fields and elevated temperatures. However, there is no real stress limit. It may even occur at electric fields and temperatures far below the critical onset values for dielectric breakdown.[140] Degradation can be represented as a typical wear-out process and the limiting factor for the lifetime of MLCCs.
Research conducted in the 1980s in Germany focused on the resistance degradation of electroceramics such as BT and STO.[71,140,145–147] In recent years, the attention has shifted towards the resistance degradation of lead-based PZT.[55,56,58] For instance, silver dendrites were found after applying electric fields of up to 1.25 kV/cm (80 µm layer thickness) at temperatures up to 520 °C caused by severe resistance degradation of PZT actuator stacks with Ag/Pd inner electrodes.[57] To ensure a high reliability and long lifetime, severe degradation of NBT-based MLCCs for high-temperature and power electronics has to be suppressed. The cause of observed resistance changes is induced by the modification of the electroceramics' defect chemistry.[148] The incorporation and extraction of oxygen at electrode interfaces play a crucial role and can lead to reduction or oxidation in the surrounding area, depending on the experimental conditions. Such circumstances may result in stoichiometry polarization when both the incorporation and removal of oxygen are hindered.[147,149] Under biased conditions, the transport of oxygen vacancies is promoted, leading to the development of oxygen vacancy concentration gradients due to the absence of oxygen exchange at electrode interfaces. This phenomenon, known as electroformation, causes an electronically inhomogeneous electroactive material with locally shifted ionic defect concentrations upon applying of

an electric field. Enhanced oxygen vacancy concentration regions experience electronic compensation, while vacancy-deficient regions exhibit hole enrichment.[150] The mechanisms of electroformation have not been fully understood, and evidence suggests that it is also temperature-dependent, as observed in the benchmark material strontium titanate (STO).[151] The induction of electroformation increases with higher temperatures, which is particularly important for components and ferroelectric capacitors in high-temperature and power electronics since temperatures can exceed 300 °C. The complex defect chemistry of NBT was already demonstrated in the previous Subsection 2.2.4. Electroformation or resistance degradation, respectively, needs to be suppressed to prevent detrimental effects on ferroelectric properties.[25] In Figure 2.9 NBT-based materials exhibit high resistivity and intrinsic electronic conductivity at very low defect concentrations but orders of magnitude higher ionically dominated conductivity at 1-2 mol% Fe. The ionic conductivity increases non-linearly with higher concentrations of acceptor defects (bismuth vacancies and dopants) or oxygen vacancies.[44] Similarly, Figure 2.12 displays two Nyquist plots: one for NBT (Figure 2.12(a)) and the other for NBT-6BT (Figure 2.12(b)) at 500°C, ranging from undoped to doped with different concentrations of Fe (up to 4 mol%). Pure NBT and NBT-6BT, as well as NBT-6BT with Fe concentrations up to 1%, still exhibit highly resistive behavior. NBT becomes ionically conductive at 1 mol%, while NBT-6BT shows ionically conductive behavior above 1 mol%.[44]

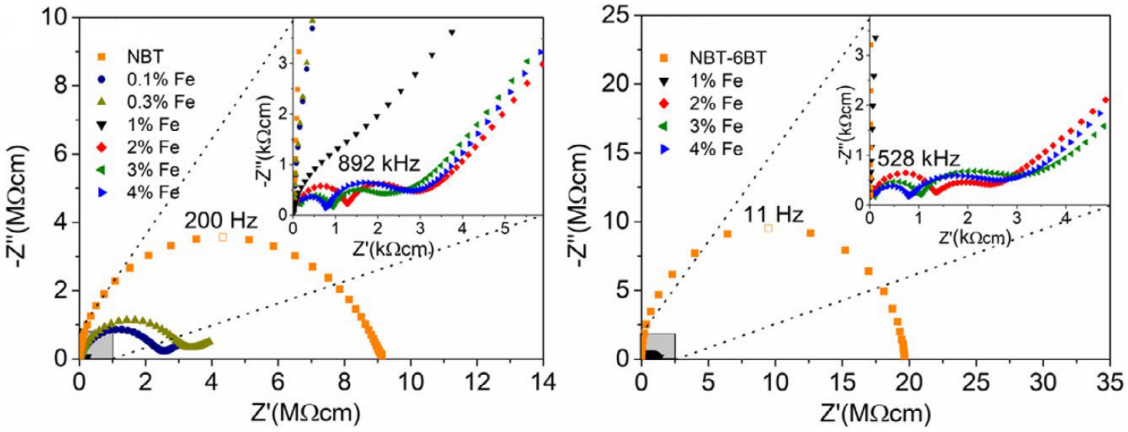

(a) Pure NBT and doped NBT up to 4 mol% Fe. (b) Pure NBT-6BT and doped NBT-6BT up to 4 mol% Fe.

Figure 2.12: Nyquist plots of NBT and NBT-6BT at 500 °C undoped and doped with different concentrations of Fe, adapted from Steiner et al.[44]

The non-linear dependence of ionic conductivity on the defect concentration was already rationalized by considering defect complexes (Equation 2.20). It is, hence, vital to address the question of whether electrical properties are dependent on acceptor dopant concentrations under high voltages and elevated temperatures. Moreover, the influence of the inner electrode material cannot be disregarded. As mentioned, Ag can be incorporated into the NBT host lattice, acting as an acceptor dopant.[47] During the operation of the prepared MLCCs, the temperatures and electric field stress can substantially contribute to enhanced resistance degradation or electroformation, respectively. The obtained results will contribute to the identification of degradation mechanisms in NBT-based ceramics and MLCC components. Likewise,

the reliability of capacitor components can be assessed by qualitative and quantitative descriptions. This will, ultimately, reduce efforts for manufacturers and industry with regard to qualification and validation significantly.

2.3.2 Dielectric Breakdown Strength

Closely related to resistance degradation, the dielectric breakdown is another, yet crucial, failure mode of electroceramics. For energy storage materials, there is an inherent driving force to operate the devices under higher voltages and electric fields, respectively, to gain the best performance. This was already outlined in Subsection 2.2.3. As this is another characteristic of the reliability and electrical fatigue behavior of a passive component, capacitor manufacturers and industry are highly interested in reliability tests of the components being used in the respective electronic circuit. This shall not imply that the components are supposed to be operated at maximum voltages or fields. It is, however, essential to know the failure behavior. For MLCCs in particular, not only the dielectric but also the design of it is vulnerable to the electric field.[22,152] Assessing the dielectric breakdown behavior is very much needed in order to ensure the longevity of such devices. This section will briefly introduce the theory behind the dielectric breakdown and highlights essential information about properly testing and evaluating the DBS of electroceramic materials.

Under the application of externally applied electric fields, insulating properties of a material may degrade due to the transport of charge carriers like free electrons, space charges, or even dissipation of thermal energy in the material.[153] A sufficiently high electric field can supply enough energy to promote electrons into the conduction band immediately. The characteristic field strength needed to cause dielectric breakdown is called dielectric breakdown strength.[101] At or beyond this parameter of dielectric materials, the conductivity increases by several orders of magnitude.[92] Upon this critical field, the local chemistry of the ceramic material can be altered abruptly. In consequence, a breakdown channel will be formed and local conductivity will rapidly increase by several orders of magnitude. It is to be distinguished between two different phenomena, i.e., between an intrinsic and extrinsic breakdown mechanism governed by different types of defects. Even further, prevailing breakdown mechanisms are strongly influenced by the nature and type of involved charge carriers. Without the effect of any kind of defect, the breakdown event is considered to be intrinsic, whereas in the case of pores, atomic inclusions, and inhomogeneities among others, the breakdown will likely be of extrinsic nature. Three main mechanisms of dielectric breakdown exist in solids, including the intrinsic, thermal, and discharge breakdown.[90,92] It is expected that a real breakdown may involve all of these or in combination. Perhaps in the case of conventionally processed ceramics, the underlying breakdown mechanisms are rather dominated by remaining porosity or any other surface asperity present in the material and not by bulk characteristics.

Intrinsic breakdown:

In 1937, von Hippel[154] and Fröhlich[155] postulated that an intrinsic breakdown occurs when the gain of energy of an electron by an electric field is higher than the loss of energy to the lattice, more specifically to phonons. Independent of the material's conductivity, upon a steadily increased

voltage that is applied to the material, a well-defined current will flow. Beyond a certain saturation level, the current will increase rapidly (in the range of 10^{-8} s), initiating a breakdown event. This intrinsic DBS is solely dependent on the material's properties and temperature. It clearly exhibits an electronic character. Such critical fields are in the range of 10-1000 kV/mm.[91] The surge in current or gain of electrons contributing to conduction may arise from impact ionization of conduction electrons, emission from bulk impurity centers, or field emission from the electrodes. Independent of the prevailing mechanism, an electron avalanche and subsequent breakdown failure is the consequence.

Thermal breakdown:

The flow of current is always accompanied by losses. Internal heat generated via Joule heating or other dielectric losses will eventually be higher and reach a rate exceeding the heat that escapes the material by radiation, conduction, or convection. As a result, a thermal „run-away" effect occurs, denoting a thermal breakdown or thermal failure. An increase in temperature also increases dielectric loss and, in most situations, the conductivity. Hence, the thermal conductivity of the material is a key factor when determining the likelihood of a thermal breakdown since thermal conductivity regulates heat generation and dissipation.

Discharge breakdown:

Ceramic materials can be considered as more or less porous materials with heterogeneous microstructures. It has been found that the presence of these defects highly affects breakdown characteristics and are regarded as extrinsic effects.[156–158] This is in close analogy with mechanical strength. The breakdown strength and mechanical strength, therefore, may be evaluated utilizing failure type statistical methods like Weibull analysis. The actual breakdown strength is dependent on many (extrinsic) factors. For example, specimen size and especially thickness play an important role. This is rationalized by the fact that a thinner volume statistically will have fewer critical defects. The chances for the electric field „finding" such a defect that would initiate the breakdown is lowered. The mechanism of how the material breaks down is still under debate but may involve the hypothesis of propagating conduction filaments.[159–161] The filaments progress from defect to defect under the influence of electric field concentrations via conventional conduction routes. It is very similar to the manner of lightning. One of the filaments eventually reaches a critical length, followed by the discharge.

All breakdown events involve local heating of the microstructure, which will also contribute to the breakdown event as described earlier. Nevertheless, ferroelectric ceramics possess high permittivities, and local temperatures may rise to 1000-1600 °C.[92,162]

The breakdown behavior of ceramic materials is influenced by numerous extrinsic factors. For a brief overview of external influences of the DBS, the work by Gehringer et al. will be considered.[73] First of all, the design of the specimen or capacitor is of outright importance because there is a relation between the

dielectric breakdown strength, or breakdown field E_{bd}, of dielectric materials, which is:

$$E_{bd} = \frac{1}{\sqrt{d}} \tag{2.22}$$

This well-known thickness dependence has been validated and analyzed in numerous studies.[161,163,164] Figure 2.13 displays the thickness dependence of different technical ceramics.

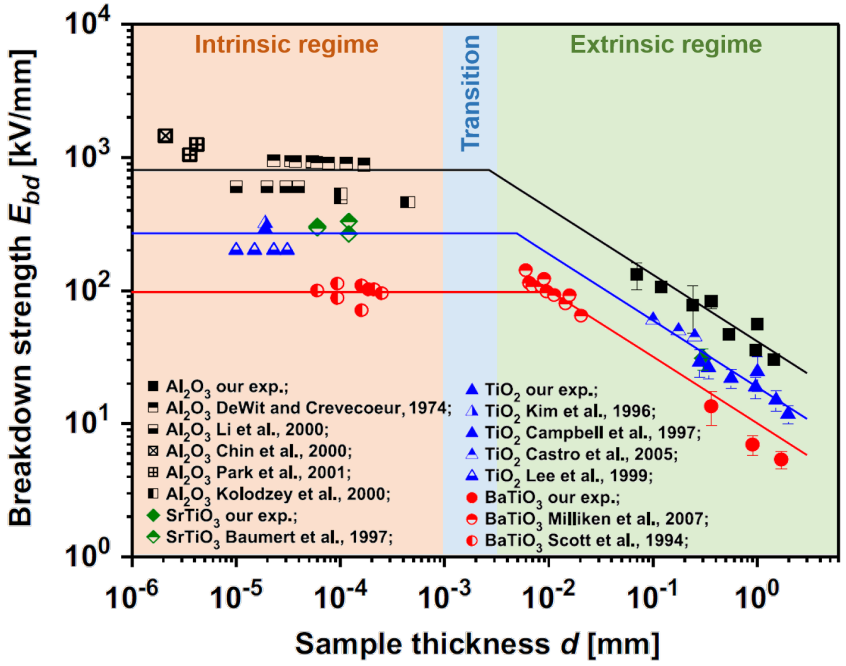

Figure 2.13: Thickness dependence of the dielectric breakdown strength with extrinsic (green) and intrinsic (red) regimes, adapted from Neusel et al.[161] Marked is also the transition regime (blue) in the range of 1-20 µm for ceramic materials.

The extrinsic (green) and intrinsic (red) breakdown strength of different technical ceramics, including Al_2O_3, $SrTiO_3$, TiO_2, and $BaTiO_3$[163,165–175], are illustrated in the figure above. In between is a transition regime in the range of 1-20 µm for ceramic materials. This coincides well with nowadays thicknesses of layered ceramic structures for high-temperature and power electronic materials; hence, it can be considered a quite important regime. Transition to a rather intrinsic breakdown value presumably will boost the reliability of the components. However, not only the thickness will affect the DBS. In addition to the spacing of electrodes, the type, size, shape, and material of the electrodes alter the distribution of the applied electric field.[4,157,176–178] This will, in turn, affect the dielectric breakdown strength of the sample under investigation. For instance, Stark et al. found that electrode edges have a significant influence on the dielectric strength by investigating disk-shaped samples with electrodes covering the surface only partially.[179] As a result, not only the electric field but also mechanical stresses are concentrated at electrode edges, leading to cracking at the electrode edges of the ferroelectric materials.[180,181] Compared to the nominal electric field, the field at electrode edges may be multiple times higher. Hence, the

formation of a breakdown channel in its vicinity is promoted by this increase of electric field.[179] A feasible approach to suppress electrode edge effects is using arched indentations. These indentations are obtained mainly by mechanical post-processing of already sintered samples by punching or drilling.[180,182] Since mechanically prepared indentations are prone to residual stresses, mechanical stress concentrations also promote electric field concentrations.[160] Subsequently, premature dielectric breakdown may be induced. Eliminating residual stresses with respect to evaluating the DBS is key to obtaining rather intrinsic materials' properties that are not masked by extrinsic parameters. Nevertheless, other extrinsic parameters, e.g., temperature and humidity[183], will also manipulate the dielectric strength. The experimental procedure, like voltage ramp during the measurement and electrode configuration, has a pronounced effect, too.[176,184] Further, permittivity, grain size, porosity, and texturing of the dielectric materials were shown to have a distinct effect on the DBS.[156,178,185,186] Pores in the bulk and the largest pores inside the bulk, in particular, are presumed to be the weakest link.[187,188] They induce high concentrations of electrical and mechanical stresses around them, leading to premature failure or breakdown.[189]
Obtaining truly intrinsic materials' effects on the behavior of dielectric breakdown would greatly benefit from arched and stress-free recesses in the material. This would narrow down the study of DBS by eliminating external effects. Moreover, to gauge the reliability of NBT-based MLCCs for high-temperature and power electronics applications, this failure mode needs to be investigated in a standardized manner. Subsequently, transferring these findings towards NBT-based materials can facilitate a proper determination of the dielectric strength of prepared MLCCs. A further contribution to an integral understanding of the failure and degradation behavior of NBT-based MLCCs can be expected.

2.4 Impedance Spectroscopy

During this work, the utilization of impedance spectroscopy (IS) has demonstrated how powerful this measurement technique is regarding the characterization of electrical material properties. Therefore, this section introduces the basics of impedance spectroscopy and outlines its application regarding ceramic capacitor components.

As a non-destructive investigation method, IS is amongst the most versatile and powerful techniques with respect to electrical testing of materials for energy storage applications like capacitors and batteries. Over the last years, it has been demonstrated that by impedance spectroscopy, the rather complex and unique electrical response of NBT and NBT-based solid solutions could be revealed more and more.[44,108–110,121,148] Different charge transport mechanisms and electrochemical reactions within the material or dielectric under AC bias need to be differentiated. Due to frequency-dependent material-related processes, particularly the dispersion of relaxation times, this characterization technique allows for discriminating between the involved processes and investigating them separately. Thus, the microstructure of the dielectric can be separated into each contributing component, namely the intragranular part (grain), the intergranular part or grain boundary (GB), and electrode interfaces. Likewise, observing frequency-dependent dielectric response, such as resistance, capacitance, and conductivity, is viable. It enables a very helpful and detailed insight into electroceramics.[190] This also includes the distinction and contribution of PNRs, as it will be discussed later in this section.[108,110]

In general, the impedance can be considered as the AC resistance of a certain component within an electric circuit. Regarding a DC bias, the electric current can easily be calculated based on Ohm's law:

$$I = \frac{U}{R} \Rightarrow R = \frac{U}{I} \tag{2.23}$$

with the resistance R. Hence, R is directly and inversely proportional to the applied voltage and electric current, respectively. Under AC conditions, however, the behavior is different. The impedance of a resistor is independent of frequency, whereas the impedance of a capacitor (and an inductor) is dependent on frequency. It is called reactance and will be derived subsequently. AC electric current and voltage can be expressed with the help of trigonometric functions:

$$U(t) = U_0 \cos(\omega t + \varphi_U) \tag{2.24}$$

and

$$I(t) = I_0 \cos(\omega t + \varphi_I) \tag{2.25}$$

with U_0 and I_0 representing the peak voltage and current, respectively, and φ_U and φ_I representing the voltage and current phase angle, respectively. The phase shift angle is defined by the difference between voltage and current phase angle:

$$\varphi = \varphi_U - \varphi_I \tag{2.26}$$

By defining $\varphi_U = 0$ voltage and current can written as:

$$U(t) = U_0 \cos(\omega t) \tag{2.27}$$

and

$$I(t) = I_0 \cos(\omega t - \varphi) \tag{2.28}$$

Continuous time-dependent functions for AC conditions, which are non-periodic or differ from sine or cosine functions, would result in quite complicated differential equations. To simplify the calculations a Fourier transformation can be conducted. By transforming time-dependent real functions into the complex frequency-dependent space, the evaluation of complex impedance data is facilitated.[191] With further help of Euler's formula, a fundamental relationship between the trigonometric and complex exponential expression of harmonic alternating voltages and currents can be deduced:[192]

$$U^*(\omega) = U_0 \cdot e^{j\omega t} = U_0 [\cos(\omega t) + j \sin(\omega t)] \tag{2.29}$$

$$I^*(\omega) = I_0 \cdot e^{j(\omega t - \varphi)} = I_0 [\cos(\omega t - \varphi) + j \sin(\omega t - \varphi)] \tag{2.30}$$

with $U^*(\omega)$ and $I^*(\omega)$ as complex voltage and electric current, respectively. Division of Equation 2.29 and Equation 2.30 yields the frequency-dependent complex impedance $Z^*(\omega)$:

$$Z^*(\omega) = \frac{U^*(\omega)}{I^*(\omega)} = \frac{U_0 \cdot e^{j\omega t}}{I_0 \cdot e^{j(\omega t - \varphi)}} = \frac{U_0}{I_0} \cdot e^{j[\omega t - (\omega t - \varphi)]} = \frac{U_0}{I_0} \cdot e^{j\varphi} = Z e^{j\varphi} \tag{2.31}$$

with the impedance Z. The subsequent derivations are all related to a simple RCL circuit, as depicted in Figure 2.14a):

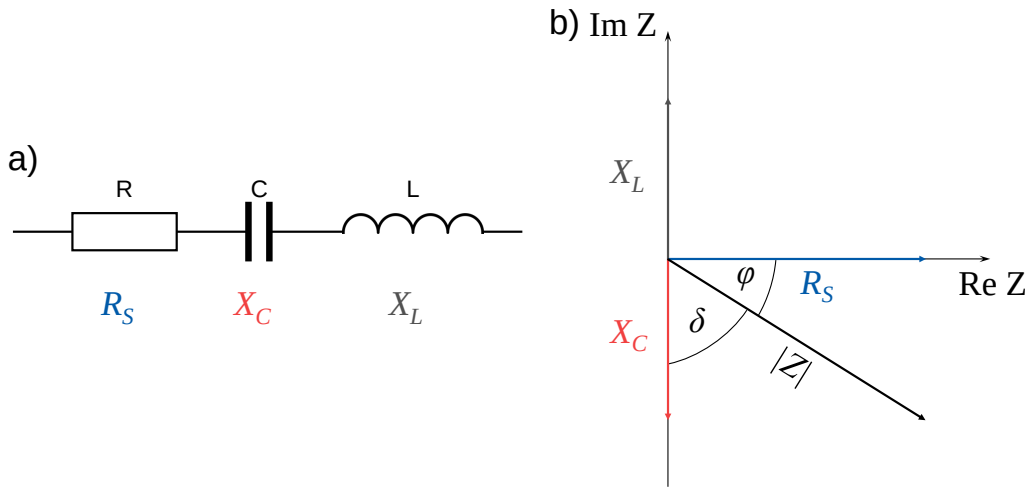

Figure 2.14: a) Schematic representation of a RCL equivalent circuit with b) corresponding complex plane diagram of impedance and reactance.

$Z^*(\omega)$ can equally be illustrated with the real part $Z'(\omega)$ and imaginary part $Z''(\omega)$ of complex impedance:

$$Z^*(\omega) = Z'(\omega) + jZ''(\omega) \tag{2.32}$$

with the reactance X. Ultimately, it can be concluded that the complex frequency-dependent impedance comprises a real, in phase, and an imaginary, out of phase, part. The above-mentioned mathematical expressions can now be applied to resistors, capacitors, and inductors. For the sake of simplicity, the three components will be considered ideal first. Real application-related systems will be described later in Section 2.4.1. The complex impedance of a resistor Z_R^* can be characterized by:

$$Z_R^* = \frac{U^*}{I^*} \cdot e^{j \cdot 0} = R \tag{2.33}$$

which is a simple ohmic resistance since the phase shift angle equals zero because current and voltage are in phase. The complex impedance of a capacitor Z_C^* can be derived as well. With the help of Equation 2.2 the complex voltage can be written as

$$U^* = \frac{1}{C} \int I^* dt = \frac{1}{j\omega C} I_0 e^{j(\omega t - \varphi)} = \frac{1}{j\omega C} I^* \Rightarrow Z_C^* = \frac{1}{j\omega C} = -\frac{j}{\omega C} \tag{2.34}$$

and transformed into the complex impedance of a capacitor Z_C^*. Additionally, $\varphi_C = -\frac{\pi}{2}$ since the Euler relationship of $e^{-j\frac{\pi}{2}} = -j$. In other words, the current leads the voltage by 90°. The impedance of a capacitor can be expressed as the capacitive reactance X_C:

$$Z_C = X_C = \frac{1}{\omega C} \tag{2.35}$$

The complex impedance of an inductor Z_L^* is deduced similarly based on the complex voltage:

$$U^* = L\frac{dI^*}{dt} = L\frac{d}{dt} I_0 e^{j(\omega t - \varphi)} = j\omega L I^* \Rightarrow Z_L^* = j\omega L \tag{2.36}$$

The impedance of an inductor is now formulated as the inductive reactance X_L:

$$Z_L = X_L = \omega L \tag{2.37}$$

Here, the phase angle is $\varphi_L = \frac{\pi}{2}$ due to the Euler relationship of $e^{j\frac{\pi}{2}} = j$. In other words, the current lags the voltage by 90°.
Furthermore, other helpful frequency-dependent complex parameters can be extracted from recorded impedance data, including the admittance Y^*, permittivity ε_r^*, modulus M^*, elastance S^*, and dielectric

loss (see Equation 2.10):

$$Y^* = \frac{1}{Z^*} \tag{2.38}$$

$$\varepsilon_r^* = \frac{1}{j\omega C_0 \cdot Z^*} \tag{2.39}$$

$$M^* = j\omega C_0 \cdot Z^* \tag{2.40}$$

$$S^* = \frac{M^*}{C_0} = j\omega \cdot Z^* \tag{2.41}$$

with the vacuum permittivity C_0. S^* can essentially be regarded as the modulus but neglects component dimensions. Particular attention needs to be paid to the complex modulus and elastance since both parameters emphasize the capacitance, which is helpful for comparing the electrical response of manufactured MLCCs.

After defining all necessary quantities for the evaluation of impedance data, the electrical response of a material will be described in terms of equivalent circuits. On the one hand, a charge transport process comprises resistance against the transport itself, i.e., a resistor R can be used. On the other side, additional charge separation will occur concurrently, which can be interpreted as a capacitor C.[193] The complex impedance Z^*_{total} of a parallel RC-circuit can be calculated according to Kirchhoff's rules, which also apply to AC complex impedance, and is expressed by the complex admittance:[93]

$$Z^*_{total} = \frac{1}{Y^*_R + Y^*_C} = \frac{1}{\frac{1}{R} + j\omega C} = \frac{R}{(\omega RC)^2 + 1} - j\frac{\omega R^2 C}{(\omega RC)^2 + 1} \tag{2.42}$$

with complex admittance of a resistor Y^*_R and capacitor Y^*_C. As it was demonstrated by Equations 2.38-2.41, various entities allow a variety of different representations. However, the by far most conventional one is the Nyquist plot. The real part Z' is plotted on the abscissa, while the imaginary part Z'' is plotted on the ordinate (Figure 2.15). At the intersection between, the semicircle and real axis the DC resistance R can be read out. Further, each measurement point belongs to a specific frequency while ω increases counterclockwise on the semicircle. The peak value of Z'' corresponds to ω_{max} and is defined subsequently.

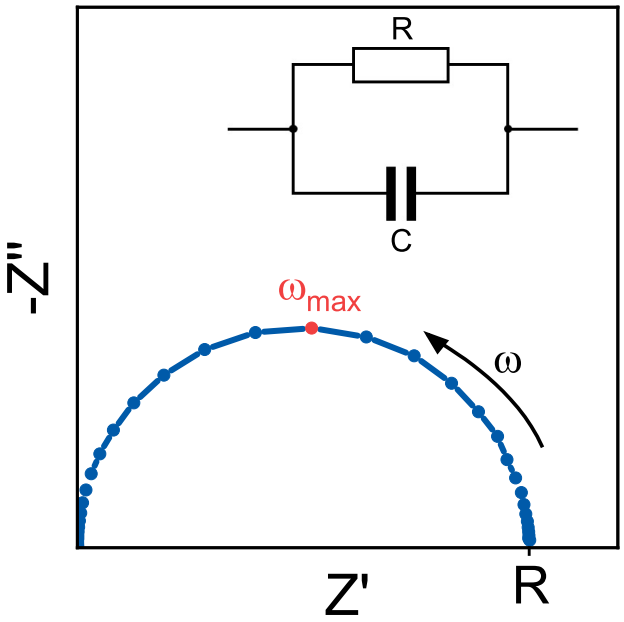

Figure 2.15: Schematic Nyquist plot of a single RC-element with the real part Z' on the x-axis and imaginary part $-Z''$ on the y-axis. The x-intercept marks the DC resistance R and angular frequency ω is increasing counterclockwise on the semicircle. The peak value of $-Z''$ corresponds to ω_{max}.

$$\omega_{max} = \frac{1}{\tau} = \frac{1}{R \cdot C} \tag{2.43}$$

ω_{max} is the peak frequency and is inversely proportional to the relaxation time $\tau = R \cdot C$ of an individual electrical response. Therefore, τ is a helpful parameter to obtain and compare capacitances. Due to the nature of a capacitor, the RC-element's capacitive part will get more conductive with increasing AC frequency. Ultimately, at high enough frequencies, the capacitor behaves like a shortcut. From the Nyquist plot, it can be deduced that real and imaginary impedance are zero (origin). The model described above is only valid for idealized materials so far. To be able to evaluate deviations from an ideal scenario, which is often the case for polycrystalline materials, a correction has to be applied. A constant phase element (CPE) can be employed that substitutes the capacitor. It essentially is a mixture of a resistance and capacitor emulating, therefore, different relaxation times. In the following equation a capacitive CPE can be expressed in terms of impedance Z^*_{CPE} where the width parameter α accounts for the correction:[194]

$$Z^*_{CPE} = \frac{1}{C_\alpha \cdot (j\omega)^\alpha}; 0 \leq \alpha \leq 1 \tag{2.44}$$

with the CPE parameter C_α. $\alpha = 0$ describes an ideal resistive, while $\alpha = 1$ features an ordinary capacitive response of the corresponding element.[193] The phase angle will be $-\alpha \cdot \frac{\pi}{2}$, resulting in a depression of the corresponding semicircle (see Figure 2.16).

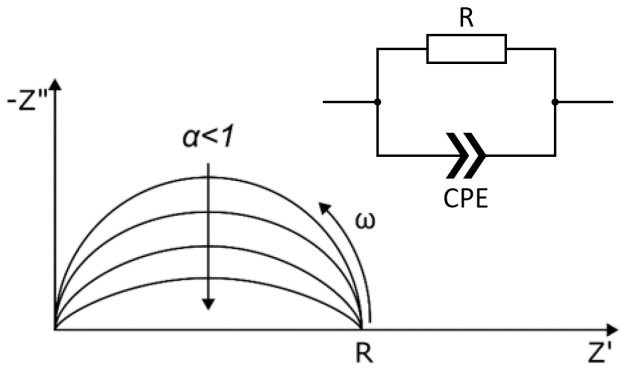

Figure 2.16: Depressed semicircle resulting from the correction by a CPE element. With increasing α the depression is progressing, adapted from Barsoukov.[193]

As seen in the latter Figure, with an increasing value of α, the semicircle starts to deviate more and more from a regular one.

As already mentioned above, a CPE can be used to fit a rather complex polycrystalline material. However, this does not mean the corresponding equivalent circuit matches the physical and electrical processes inside the material during AC bias. Further discrimination of a complex microstructure can be made if the relaxation times of specific regions, namely bulk and GBs, are so different to be able to separate them. Therefore, a model was developed in 1976 by Beekmans and Heyne.[195] It has been termed the brick layer model and can be understood as an idealized representation of a polycrystalline ceramic with defined grains and grain boundaries. Each element in the brick layer model is equivalent to a distinct physical region inside the material. The brick layer model is depicted in Figure 2.17 and demonstrates the response of the bulk, grain boundary, and electrode region. Though more realistic, it still treats the microstructure as an array of cubic grains separated by flat grain boundaries and connected by flat electrodes.[190,193,196]

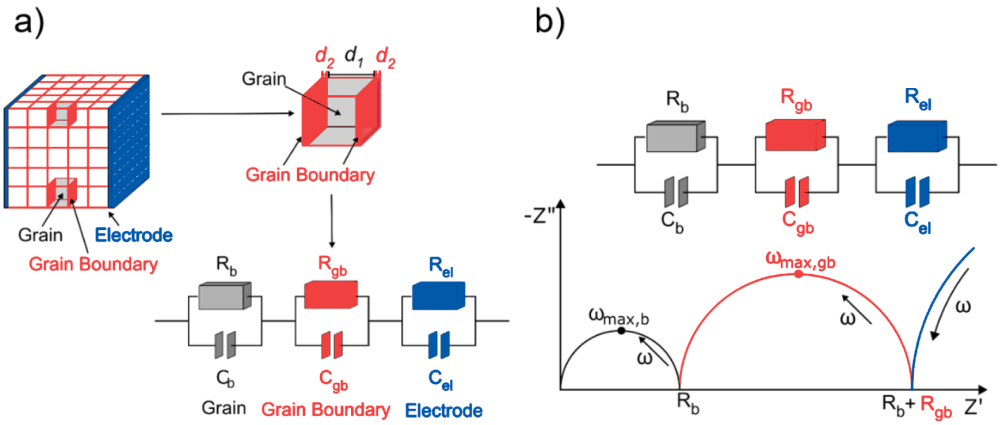

Figure 2.17: a) Brick layer model of an idealized polycrystalline ceramic with grains, grain boundaries, and two termination electrodes which can be converted into a series of RC elements, adapted from Song and Placido.[197] b) Schematic of an impedance spectrum with the typical response of each contribution.

Since this model assumes cube-shaped grains with defined distance d_1, flat grain boundaries with distance d_2, and two electrodes (Figure 2.17a), it handles every single grain, GB , or electrode equally. In turn, all responses can be merged into a single response, as shown by the equivalent circuit. In b) a typical impedance response of a polycrystalline ceramic displays a characteristic semicircle for each assigned region in the sample.
For instance, a typical value for the capacitance of grain boundaries is in the range of 10 nF - 10 pF.[190] Note that the quality of the sintered ceramic is of utmost importance for the electrical response, i.e., poorly sintered ceramics will exhibit lower capacitances. In comparison, properly sintered ones will exhibit higher capacitances.[198] In the work by Irvine et al., a table of capacitance values was published with the possible responsible responses (see Table 2.3).[190]

Table 2.3: Classification scheme for Class II dielectric capacitor materials.[10,76,78]

Capacitance (F)	Correlated response
10^{-12}	bulk
10^{-11}	minor secondary phase
10^{-11}-10^{-8}	grain boundary
10^{-10}-10^{-9}	bulk ferroelectric
10^{-9}-10^{-7}	surface layer
10^{-7}-10^{-5}	sample-electrode interface
10^{-4}	electrochemical reactions

Another interesting fact was already outlined in Figure 2.5, describing different electrical responses of LT- and HT-PNRs regarding impedance data. Only with the help of a modulus plot the relaxation of

PNRs in the matrix system could be revealed. It was stated by Zang et al. that this additional shoulder is linked to the interactions of PNRs.[108] However, they also conducted calculations with a single RC element. Nyquist plots obviously showed depressed semi-circles, but modulus plots revealed a second high capacitance response. This, in turn, means that two processes have to be present. Further, it may be a parallel process since only one response was detected in the Nyquist plots. This contradiction was investigated by Frömling et al. in 2022, who simulated various equivalent circuits emulating distinct physical responses and proposed different models like a grain boundary pathway or high permittivity inclusion model.[110] Interestingly, a parallel grain boundary pathway could explain the observed response of inhomogeneous electroactive materials in the same, or at least very similar, way as report by Zang et al. regarding a high capacitance response based on PNRs.

The quintessence is choosing an appropriate equivalent model to encircle and identify the physical mechanisms accurately. Therefore, Frömling et al. proposed a recipe for the evaluation of impedance-related data to rationalize underlying physical mechanisms:[110]

a) Determining a reasonable representation for the primary interest. Usually, capacitance, impedance, or admittance accounts for dielectrics/ferroelectrics, resistors, and conductors, respectively.

b) In general, possible parallel electrical responses may be detected using modulus or elastance representation.

c) If the peak frequencies of imaginary modulus and impedance converge, the corresponding response is purely conductive based on the coincidence of permittivity at very low and very high frequencies. Details about it can be read elsewhere.[110] The response of a Debye relaxation is seen in Figure 2.18a). In b), two peaks are detectable (I and II). I changes with temperature its height but is also affected by the temperature-dependent conductivity. Peak II is not shifted to higher frequencies due to higher temperatures, i.e., the interaction can be linked to a capacitive response.

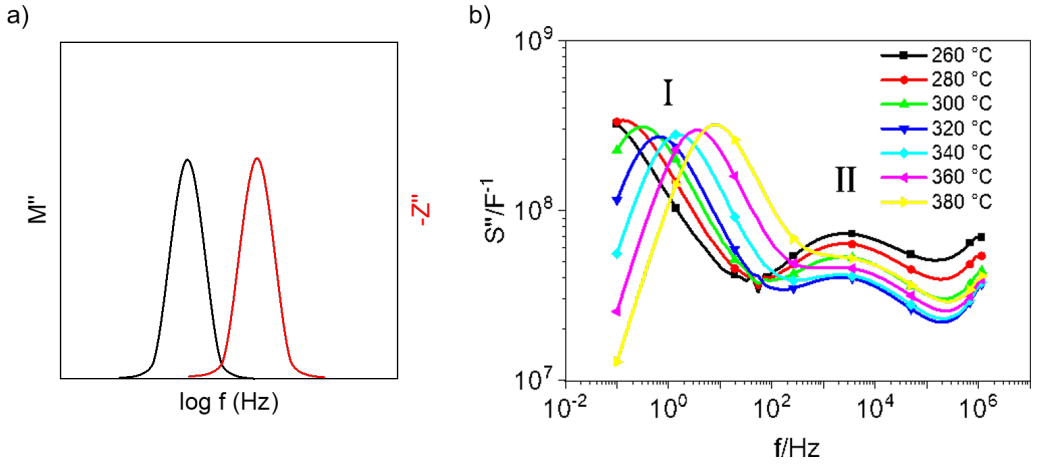

Figure 2.18: a) Schematic Debye response within the imaginary modulus and impedance representation and b) modulus plotted against frequency for pure NBT at varying temperatures exhibiting two characteristic peaks I and II, adapted from Frömling et al.[110]

d) After identifying respective mechanisms, it is necessary to attribute a physical model to them. For instance, a grain boundary pathway model or a high permittivity inclusion model can be used. Further, extracting values directly from impedance-related spectra may help to sort the contributions better. Equivalent circuits then may be used to rationalize the approximations made from the above steps.

e) Besides the qualification of recorded data, they must also be quantified regarding independent sample dimensions like permittivity, resistivity, and conductivity.

2.4.1 Equivalent Series Resistance & Inductance

After the main peculiarities of impedance spectroscopy, another related topic needs to be elucidated. So far, the AC resistance of different passive components has been described. Deviations from an ideal behavior were only rationalized with modifications of the equivalent circuits. Practical capacitors (and inductors), however, will always be accompanied by losses and cannot be considered perfect. These losses can be represented in an electric circuit using a simple resistance in series. This is called ESR. Likewise, all capacitors under real conditions within an electric circuit will inherently exhibit inductances due to leads, electrodes, and imperfections of the used materials. This can also be represented in an electric circuit using a simple inductance in series called ESL. The corresponding equivalent circuit is depicted in Figure 2.19. Additionally, dielectric losses are included in ESR, but the insulation resistance R_p is parallel to the capacitor element, which accounts for the leakage current.

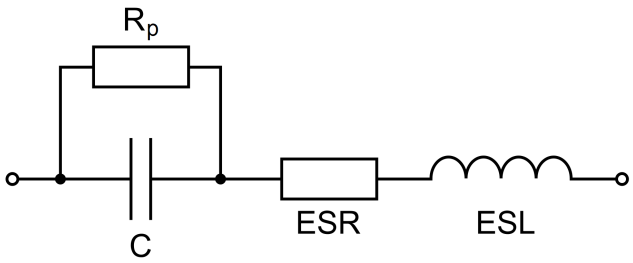

Figure 2.19: Equivalent circuit diagrams of a real capacitor with insulation resistance R_p parallel and ESR and ESL in series.

ESR and ESL stem from the fact that under real conditions, parasitic contributions (capacitive and inductive) will be present. They are always specified at certain frequencies since they are inevitably connected to AC conditions. In Equations 2.35 and 2.37, X_C (ESR) and X_L (ESL) are already derived numerically. The relation between both reactances, impedance, and resistance can be visualized via a complex plane diagram depicted in Figure 2.14b). Moreover, the magnitude of impedance can easily be calculated with the interrelationships from above:

$$|Z| = \underline{Z} = \sqrt{(X_L + X_C)^2 + R_S^2} \tag{2.45}$$

Additionally, the capacitor response is frequency-dependent. As shown in Figure 2.20, at low frequencies,

the impedance behaves capacitive. At the SRF ($X_C = X_L$), it behaves resistive and at high frequencies inductive. The self-resonant frequency f_{SRF} can be calculated by the following equation:[76,86]

$$f_{SRF} = \frac{1}{2\pi\sqrt{L \cdot C}} \tag{2.46}$$

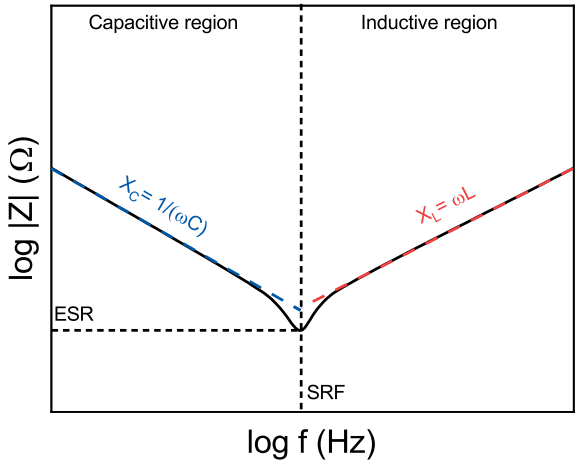

Figure 2.20: Schematic frequency-dependent impedance response of a capacitor.

2.5 MLCC Prototyping

In this last section of the theoretical background, the complete fabrication route of MLCCs will be elucidated since this is a crucial part of MLCC prototyping and the thesis. Each step will be described with emphasis on engineering issues, and decisive parameters will be given. Figure 2.21 features the essential processing steps in a successive order.

Nowadays, capacitors and multilayer ceramic capacitors, in particular, are irreplaceable passive components in almost every electronic device. There is ongoing demand for further miniaturization of such passive components.[10,87] For instance, the sheer number of MLCCs being installed in cell phones alone increased from roughly 100 to more than 1,000 from 2008 to 2018. Electric vehicles can contain more than 10,000 MLCCs.[81] How are all these small capacitors made? Glenn Howatt made the starting point with its publication in 1947 about fabricating thin ceramic sheets.[199] His method of producing thin ceramic plates was soon coined „tape casting“ and is the key step in manufacturing MLCCs.[64] This technique also enabled the miniaturization of capacitors by casting extremely thin tapes.[200] The industrial fabrication route, however, has not changed much in decades, which underlines the importance of this invention.

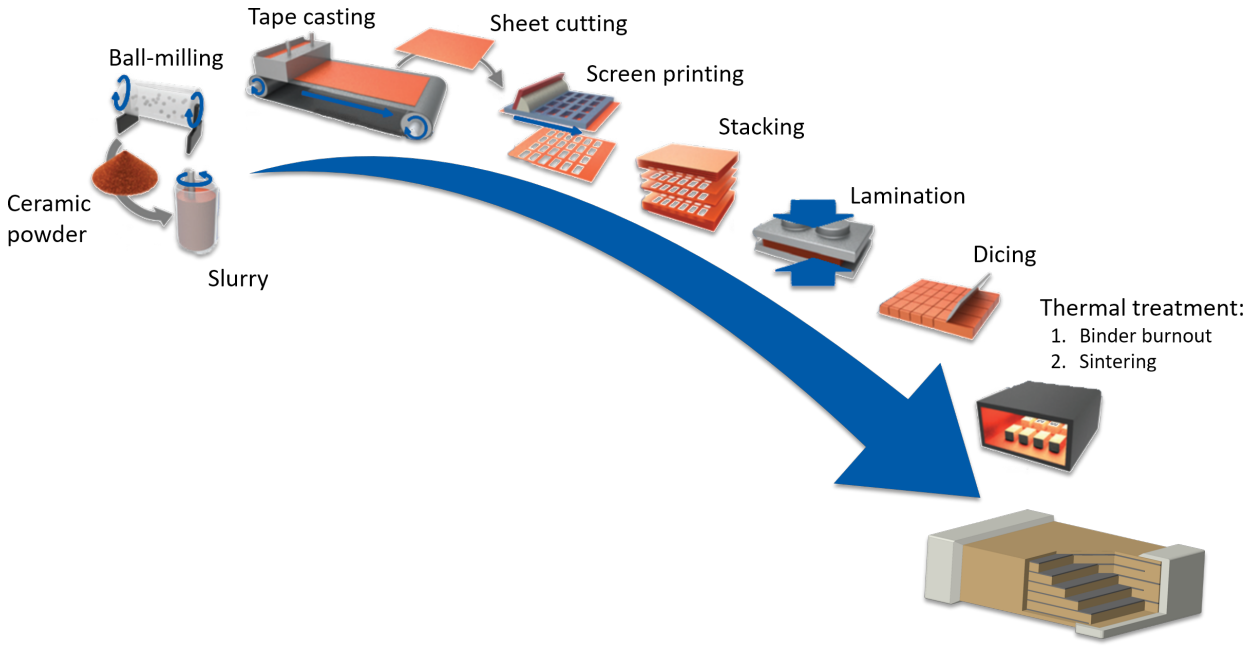

Figure 2.21: Schematic fabrication process of prototype MLCCs, adapted from Hong et al.[81]

For the following descriptions of each part of the MLCC fabrication, the textbook by Mistler and Twiname was taken into careful consideration:[64]

Ceramic powder:

This is maybe already the most crucial ingredient. Indeed, the processed powder is the only

remaining ingredient after all processing steps (excluding the electrode materials), which, to a large portion, defines the electrical properties of the final product. Everything else will be burnt out sooner or later. As the raw powder will highly affect the tape casting process, a thorough characterization is necessary. It includes an analysis of particle sizes, distribution, and morphology, along with surface area and powder density. For example, the surface area directly affects interactions with organic additives during slurry preparation. For tape casting, in particular, it is crucial as the amount of organics is proportional to the total powder area. Going one step further, an altered surface area can dramatically influence the sintering temperature-fired density relationship.[201] Nevertheless, how the green bulk density is generated is completely different compared to the conventional solid-state synthesis and powder processing routes. Only gravity and shrinkage of the organic system during drying create the packed density. Due to this unique densification process, controlling the particle size and distribution is vital. Nevertheless, coarser powders or larger particle sizes, respectively, require a higher driving force for the sintering process to yield a dense specimen. This is based on the higher surface energies of the particles. Such powder often exhibits a surface area between 5 and 10 m^2/g and a rather narrow particle size distribution.

Therefore, dispersion milling processes are necessary to primarily break down soft agglomerates to put the particle size distribution into a narrow range.[202] Still, a distribution of particle sizes is favorable so that smaller ones fit into interstices of larger particles. In reality, however, particles are irregularly shaped. Bridges between two bigger particles may form creating small voids and limiting the green density. An excellent particle size distribution is supposed to be in the range of 0.6-1.1 µm for d_{90} and 0.1-0.2 µm for d_{10}.[64] This yields a relation between the largest and smallest particles of roughly 6:1. However, the distribution is highly dependent on the functional properties of the final ceramic. For instance, it was shown that with a 25:1 ratio, a packed density of 95% was obtained.[203]

Slurry:

In general, slurries contain a liquid, often called „vehicle“, which can be aqueous or non-aqueous. Likewise, binder, plasticizer, and other additives such as dispersants or homogenizers may be added. A microstructural slurry is schematically depicted in Figure 2.22(a). Every ingredient has a distinct purpose, and only a balanced combination will eventually result in the desired properties of the final component. Solvents are not only added to disperse the powder particles; they will also dissolve organic constituents like binder, plasticizer, or dispersants.[200] It is a necessary part to ensure a homogeneous slurry.[202] The binder, however, determines the strength and flexibility of obtained tapes after drying. They build a polymer chain network containing all other ingredients of the slurry.[65] Additionally, lamination behavior during processing and rheology of the slurry is highly influenced by the binder material.[200] The binder will decompose during the burnout, which is essential for particle-particle interactions during the sintering step.[204] Also residuals of the binder will deteriorate further processing. One of the most prominent binder materials is polyvinyl butyral (PVB), which can be burnt out completely in the presence of oxygen, such as in air.[66] Plasticizers

are added to the slurry mixture to impart plasticity and flexibility to the green tapes.[65,202] In turn, during drying, they can prevent crack formation and allow for machining of the tape, such as cutting or punching.[64,200] Last but not least, there are plenty of additives that can be added for different reasons. Within this thesis, only dispersants will be covered as they also represent a central component of the slurry. Essentially, dispersants are key to wetting behavior, dispersion of solid content, high density, deagglomeration, and sedimentation.[64,200] Their generic appearance is displayed in Figure 2.22(b), with typical polymer chains protruding from the ceramic particle. One part of the molecule attaches to the ceramic particle's surface, and the remaining part forms a more or less solvated layer. Particle-particle interactions are now inhibited by the effect of steric hindrance.[65,205] It will promote the dispersion of ceramic particles.

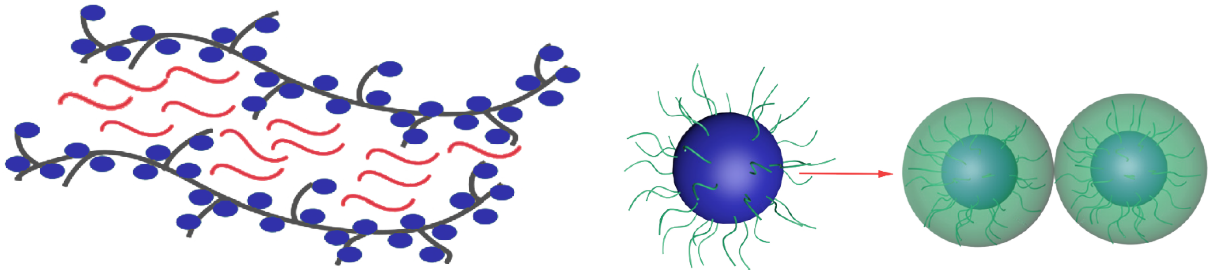

(a) Prototypical slurry with powder particles (purple) attached to the binder (black network chains). The molecules of the plasticizer (red) are located in between the binder chains.

(b) Polymer chains of the dispersant (green) attach to the powder particles, creating a steric hindrance (green spheres).

Figure 2.22: Schematic of a prototypical slurry with the most important ingredients, adapted from Ren et al.[65]

Note that an optimum amount of solid content and amount of organics and additives cannot be predicted because the interactions between each ingredient are rather complex. It has to be determined experimentally. Nevertheless, efforts have been made, and the solid content may be maximized to achieve a higher packed density.[206] This is going to affect the rheology as well as the processing of cast tapes. The green density or packed density can be calculated according to the following equation:[204]

$$\text{packing density} = \frac{\text{volume of solids}}{\text{total volume of arrangement (solids + voids)}} \tag{2.47}$$

Processing:

After the slurry preparation, the primary step of the MLCC fabrication is conducted. It is called doctor blading or tape casting, where thin ceramic sheets are obtained. Details about the equipment can be found elsewhere and will not be covered in this work.[64] Regardless of the equipment, the process parameters are significant. Before the tape is cast, a de-airing step may be necessary to remove bubbles from the slurry, which could be trapped during mixing. Casting itself will depend on several parameters like temperature, casting speed, doctor-blade height, substrate, and airflow.[64]

Further processing of cast tapes is in no way less important than the tape casting itself. To avoid any decline of desired and final properties of the MLCCs, high precision during sheet cutting, screen printing, stacking, and dicing is required. Otherwise, it could result in a mismatch of alternatively stacked inner electrodes and, hence, lowering the active area in between inner electrodes.[200] Note that the preparation and screen printing of electrode paste can be considered another branch of research and will, hence, only be outlined in this thesis. The lamination step follows the stacking step and will contain decisive parameters, too. The procedure for lamination of green tape cast sheets was patented in 1965 by Gyurk.[207] Only three parameters were described: temperature, pressure, and time. The temperature is dependent upon all organic additives in the green tape. The final glass transition temperature T_g of the compound determines the minimum and maximum lamination temperatures that can be applied. Depending on the number of layers and final thickness, an appropriate time has to be chosen to heat the entire green stack uniformly. Sufficient pressure is necessary to provide intimate contact between the different layers. During the application of pressure, distortion of the laminate must be avoided; otherwise, the final dimensions might be changed. The lamination step consists of an uniaxial and an isostatic pressing step schematically represented in Figure 3.1. After a complete lamination, the green MLCCs must only be diced before the final thermal treatment follows. Dicing will only be covered shortly in the Experimental Methodology in Chapter 3.

Thermal treatment:

The thermal treatment of MLCCs in this work involves a two-step process: binder burnout and sintering. In general, the removal of organic additives is called pyrolysis or binder burnout, where a thermal decomposition and evaporation of all organic ingredients will take place. During firing, organic components must be removed completely before densification reaches an advanced stage.[66] Any carbonized material trapped within the ceramic structure may alter the final properties of the capacitor component. The success of the binder burnout depends on the atmosphere, burnout time, and temperature. The same accounts for the second step, the actual sintering step, where densification sets in. Details about the sintering mechanics can be found elsewhere.[208,209] The neck formation for this kind of ceramics is of utmost significance. Ingredients and ratios have to be picked and selected so that the resulting green density is sufficiently high to allow for full densification during the sintering step.[67] Moreover, another limiting factor in this work is the co-firing process with the inner electrode material. A co-firing process includes the sintering of two (or more) different materials, and phase transition temperatures of the materials need to be considered. Ag/Pd is the material of choice. In Figure 2.23, the phase diagram of the Ag/Pd alloy is depicted. As a 70/30 ratio of Ag/Pd will be chosen for the preparation of MLCCs (highlighted in blue in Figure 2.23), a maximum sintering temperature of 1170 °C can be extracted from the calculated phase diagram by Karakaya and Thompson.[48]

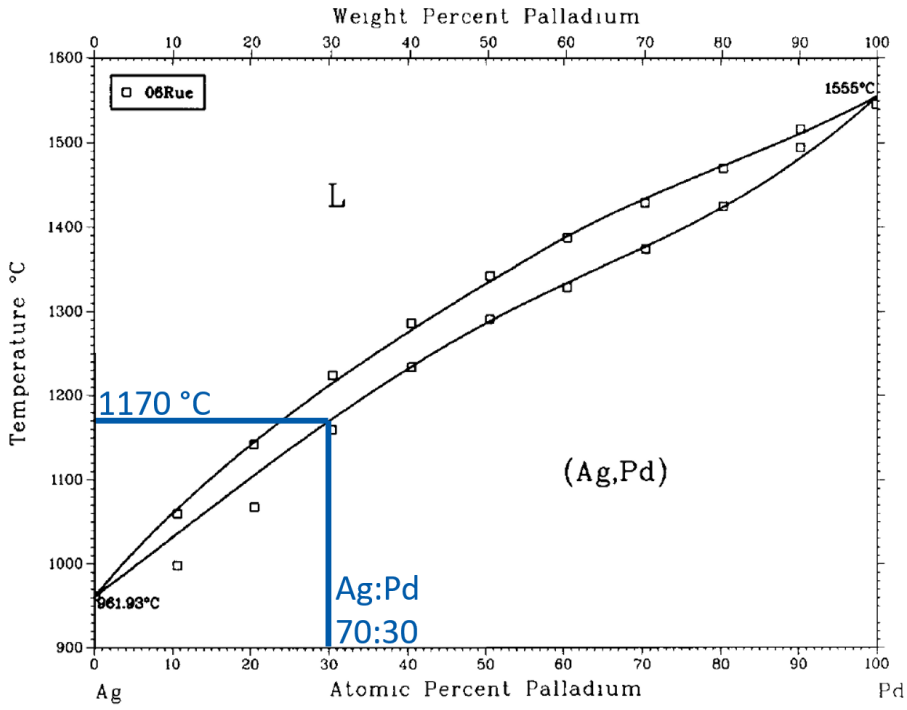

Figure 2.23: Calculated phase diagram of Ag/Pd with selected experimental data from Ruer[210], adapted from Karakaya and Thompson.[48]

After the thermal treatment, electrodes need to be deposited for electrical contact. It is achieved by applying outer electrodes or terminations to two sides of the MLCCs, which connect inner electrodes. The termination process is the last step to prepare the samples for electrical testing and operation. Dmitrieva et al. have demonstrated the importance of the electrode material(s), but this is also out of the scope of this thesis.[211] It is more about the prototyping of MLCCs with a focus on the dielectric material and interactions between the electrode material but not the influence of (different) outer electrodes.

3 Experimental Methodology

Within this chapter, necessary information will be given concerning the MLCC fabrication route and capacitor sample preparation. Subsequently, all measurement techniques and experimental conditions used for structural and electrical characterization will be described shortly. The last section about reliability and electrical fatigue will be handled separately, i.e., all techniques and experimental conditions used for the electroformation and dielectric breakdown strength parts will be given at once.

3.1 Processing and Sample Preparation

The MLCC components were prepared according to the MLCC fabrication route displayed in Figure 2.21. Details of each preparation step will be given below. Two types of slurries and two types of MLCCs were prepared during this work. Different equipment and techniques were used and will be mentioned here. The terminology of the slurries and MLCCs are as follows:

- A-slurry and A-MLCC
- Ω-slurry and Ω-MLCC

The Ω-MLCC will also be called prototype MLCC. The Ω-slurry and Ω-MLCC are referred to the fabrication with optimized conditions. In addition to the two types of MLCCs, laminates were fabricated according to the processing route of the A-MLCC. Only the screen printing step was skipped here, i.e., laminates did not contain Ag/Pd electrodes.

3.1.1 Powder Preparation

For the MLCCs and bulk reference samples used in this work, starting powder of $0.99[0.8(0.94Na_{0.5}Bi_{0.5}TiO_3\text{-}0.06BaTiO_3)\text{-}0.2CaZrO_3]\text{-}0.01BiAlO_3$ (NBT-BT-CZ-1BA) was prepared via the solid state synthesis route. Details about the powder and bulk reference sample preparation can be found elsewhere.[29,121] The bulk reference pellets had a thickness of 0.2 mm and a diameter of about 8 mm.

3.1.2 Slurry Preparation

Two different slurries were prepared from the aforementioned powder. The calcined and sieved powder for the Ω-MLCCs was additionally milled in a planetary mill (PM400, Retsch GmbH, Germany) to yield

smaller particles size with a threshold of $d_{90} < 1\,\mu m$. Therefore, the milling time was set to 2 h at 220 rpm within a direction reversal after 15 min each. For both slurries, the solvent and dispersant were mixed and added to an yttria-stabilized zirconia (YSZ) milling container filled with the corresponding ceramic powder and 10 mm YSZ milling balls. The initial slurries were mixed for 2 h at 110 rpm. After supplying the different plasticizers to the slip and mixing it for additional 30 min at 110 rpm, the binder was added. The finished slurries were then mixed for 24 h at 110 rpm. The ingredients, their weight, and the weight percentage of each slurry for the A-MLCC and Ω-MLCC are specified in Table 3.1:

Table 3.1: List of ingredients for the A-MLCC and Ω-MLCC.

	A-MLCC			Ω-MLCC		
	Component	Weight (g)	Weight percentage (%)	Component	Weight (g)	Weight percentage (%)
Ceramic powder	NBT-BT-CZ-1BA	12.00	59.00	NBT-BT-CZ-1BA	25.00	60.75
Solvent 1 Solvent 2	Ethanol (40%) methyl ethyl ketone (MEK) (60%)	6.04	29.70	1-Butanol	12.50	30.38
Homogenizer	Cyclohexane	0.17	0.84	/		/
Dispersant	Oleic acid	0.05	0.25	Solsperse™ M387	0.15	0.36
Plasticizer	polyethylene glycol (PEG)	1.04	5.11	Acetyltributylcitrate (ATBC)	1.30	3.16
Binder	PVB Butvar® B-98	1.04	5.11	PVB Mowital® LP BX 860	2.20	5.35

3.1.3 Tape Casting

A-MLCC:

The A-slurry was cast with 0.8 m/min with a doctor blade gap height of 250 µm onto a polyethylene terephthalate (PET) substrate. The cast slurry was dried at room temperature in air for 5 h. As a result, green tapes with a width of 10 cm and length of roughly 50 cm could be obtained. The thickness was about 60 µm.

Ω-MLCC:

The prototype slurry was cast with a lab-scale tape caster (Laboratory Tape Casters L-Series, KEKO Equipment Ltd., Slovenia) onto a PET substrate. The gap height of the doctor blade was set to 300 µm. The temperature was set to 25 °C, and the slurry was cast with a speed of 0.8 m/min. Drying was achieved in a closed chamber without airflow for 2 h. An approximate thickness of 65 µm could be achieved after drying. Tapes roughly 20 cm in width and 200 cm in length were produced.

3.1.4 Sheet Cutting

A-MLCC:

The dried green tapes were cut into $60 \times 100\,mm^2$ green sheets.

Ω-MLCC:

The dried green tapes were cut into sheets with similar dimensions as above with a laser cutter (LPKF ProtoLaser S, LPKF Laser & Electronics AG, Germany). Additional marks were cut for aligning the green sheets during stacking.

3.1.5 Screen Printing

A-MLCC:

Two different silver-palladium pastes were used for screen printing (EL44–040 and EL44-111, Ferro Corporation, OH, USA). The paste was screen printed manually with a squeegee at constant speed and force. An individual inner electrode had a dimension of 8×8 mm^2. Further marks and framing helped to cut the green sheets into individual green layers with printed inner electrodes.

Ω-MLCC:

Only the Ag/Pd paste EL44-040 was used for the Ω-MLCCs. The green sheets were semi-automatically screen printed (C1010, Aurel s.p.a., Italy) and had dimensions of 5×5 mm^2.

3.1.6 Stacking, Lamination, and Dicing

A-MLCC:

In total, ten green layers with inner electrodes and one green layer without inner electrode were stacked alternatively to form a green MLCC with nine active layers. Likewise, green MLCCs with only a single active layer were produced by stacking two green layers with inner electrodes and three layers without inner electrode. The green sheets had to be cut manually a second time with a custom-made cutting tool. The marks and framing from the screen printing step were used to align and cut the green sheets as precisely as possible. Afterwards, the green stacks were uniaxially pressed (RC106, Enerpac, WI, USA) at 25 MPa for 10 s and subsequently cold isostatically pressed (KIP 100E, Paul-Otto Weber GmbH, Germany) at 100 MPa for 3 min and room temperature as demonstrated in Figure 3.1. Both green MLCCs had dimensions of 12×12 mm^2 with a thickness of about 640 µm for the green MLCCs with nine active layers and 290 µm for the green MLCCs with one active layer.

Ω-MLCC:

The green MLCCs prepared here had only five green layers with inner electrodes and one green layer without inner electrode. Obtained green stacks were uniaxially pressed (PW 40, Paul-Otto Weber GmbH, Germany) at 20 kN for 1 h. Subsequently, warm isostatic pressing was conducted at 55 °C for 15 min (Avure Autoclave Systems, Inc., USA). Hereafter, the resulting green stacks were diced into 6×6 mm^2 green MLCCs (CM-15, KEKO Equipment Ltd., Slovenia) with a final green thickness of approximately 380 µm.

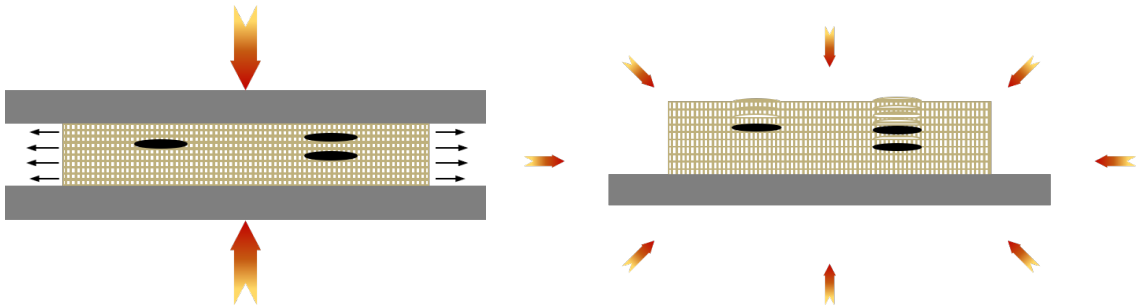

(a) Uniaxial pressing (b) Isostatic pressing

Figure 3.1: Schematic representation of an uniaxial and isostatic pressing step for green laminates, adapted from Fraunhofer IKTS.[200] Defects in the laminates will disappear during uniaxial pressing as the material flow is horizontal. When pressed isostatically, defects may cause small bumps on the surface of the laminate.

3.1.7 Thermal Treatment

Both A-MLCCs and Ω-MLCCs were handled in the same manner and prepared via a two-step heating process, as represented in Figure 3.2. Therefore, the laminated green stacks were placed in a closed rectangular crucible sandwiched between two porous alumina plates. It prevented deformation and bending during the thermal treatment. Sacrificial powder was added inside the crucible, inhibiting the evaporation of volatile species. The first heating step was the binder burnout step to remove all organic components. The samples were heated to 600 °C with a heating rate of 0.5 K/min. After 5 h at 600 °C, the actual sintering step was initiated. With a heating and cooling rate of 5 K/min, the brown MLCCs were co-fired at 1100 °C for 2 h. Bulk reference samples were sintered solely at 1100 °C for 2 h. The heating and cooling rates were identical (5 K/min). Even so, sacrificial powder was added to the crucibles.

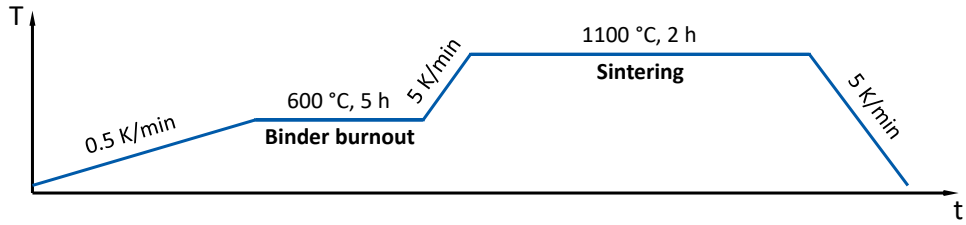

Figure 3.2: The thermal treatment of capacitor components comprises a two-step heating process. The first step is the binder burnout, and the second step is the actual sintering step.

3.1.8 Applying Terminations

Lastly, the sintered MLCCs have to be terminated. Two sides of the capacitor were ground to uncover the inner electrodes. The sides were sputter coated (K950X Turbo Evaporator, Quorum Technologies, UK) with Pt for 8 min at 40 mA to form terminations of roughly 120 nm thickness. The bulk reference samples had to be ground to a thickness of about 0.2 mm to guarantee isotropic properties by removing

the so-called sinter skin. Subsequently, Pt electrodes with a diameter of about 5 mm were sputtered on both sides of the pellet. Using this approach, sparking over the edge could be inhibited. A further annealing step of all samples and capacitors at 600 °C for 2 h with heating and cooling rates of 5 K/min was performed to equilibrate oxygen vacancies in the dielectric.[212]

3.2 Characterization

All characterization techniques being used for the evaluation of slurries and capacitor components in this work will briefly be described here. All important parameters are specified. However, details about the fundamentals of a corresponding method will not be given.

3.2.1 Structural Characterization

3.2.1.1 Scanning Electron Microscopy and Energy-Dispersive X-ray Spectroscopy

Cross-sectional micrographs of laminates and MLCCs were obtained by a high-resolution field-emission scanning electron microscopy (SEM) (JSM-7600F, JEOL, Japan) in the COMPO mode combining secondary electrons (SEs) and backscattered electrons (BSEs) to highlight both information of the topography and elemental composition around the surface. Acceleration voltages of 20 kV were applied. Points of interest, line scans, and mappings were investigated by energy-dispersive X-ray spectroscopy (EDX) (X-Max80, Oxford Instruments, UK) to reveal the elemental distribution, formation of secondary phases and any migration of inner electrodes' constituents at the dielectric-inner electrode interface. Therefore, cross-sections of the laminates and capacitors were ground, polished, and sputter-coated with gold or carbon, respectively. Before sputter coating, samples for the grain size analysis were thermally etched at 1050 °C for 4 min to reveal the grains by slight thermal decomposition of the grain boundaries. These samples were coated with gold for 4 min at 40 mA. The average grain size was calculated using the linear intercept method and software LINCE (version 2.4.2b, Sergio Luis dos Santos e Lucato, Technical University of Darmstadt, Germany). All other samples for investigations towards porosity, secondary phases, migration, and elemental distributions were not thermally etched but sputtered with carbon (1 pulse at 25 A).

3.2.1.2 Rheology

Slurries containing only the ceramic powder, 1-butanol, and different amounts of oleic acid were used for the rheological investigations to obtain an optimum amount of dispersant. Small amounts of slurries of about 10 cm^3 were produced in the same way as described in Subsection 3.1.2 without adding plasticizer and binder. Shear rates of up to 200 1/s were set at the rheometer (Physica MCR 301, Anton Paar GmbH, Germany). The shear rates started at 10 1/s up to 200 1/s and went down again to 10 1/s. The residual slurries were further used for sedimentation tests, where sedimentation was visually checked after 24 h.

3.2.1.3 Thermal Analysis

For thermogravimetric analysis (TGA) and differential scanning calorimetry (DSC) measurements (STA 449 F3 Jupiter, Netzsch-Gerätebau GmbH, Germany), the MLCC components were heated to 1200 °C with a heating rate of 2 K/min in air. The green MLCCs were put into an Al_2O_3 crucible. The cooling rate was set to 30 K/min.

3.2.1.4 Archimedes' Principle

Bulk samples and laminates were weighed according to the Archimedes' principle. Details about the procedure can be found elsewhere.[121] To calculate relative densities, the obtained Archimedes density was divided by the theoretical density of NBT-BT-CZ-1BA. The values were taken from Hoang et al.[29]

3.2.1.5 Particle Size Distribution

The ceramic powder was first dispersed in ethanol with an ultrasonic disperser for 3 min before a few drops of the dispersion were poured into the particle sizer (Saturn DigiSizer 5200, Micrometrics Instrument Corporation, GA, USA). The ethanol was first measured as the background. It was taken into account to add just enough drops to maintain an optimal obscuration rate within the measurement chamber.

3.2.2 Electrical Characterization

3.2.2.1 Permittivity and Dielectric Loss

Frequency- and temperature-dependent permittivity, as well as dielectric loss, were recorded using two different setups at $\frac{1}{\sqrt{2}}\,V_{rms}$. The first setup employed an LCR meter (4284A Precision LCR-Meter, Hewlett Packard, USA) and allowed for data collection at high temperatures ranging from RT - 500 °C. The heating and cooling rates were set to 5 K/min. At 500 °C, the temperature was held for 20 min to ensure thermal equilibration of the capacitors. Notably, all A-MLCCs and bulk samples with sintering aids were exclusively measured within this high-temperature range. To facilitate these measurements, the setup was connected to a box furnace (LE4/11/R6, Nabertherm GmbH, Germany). For low-temperature data acquisition, the range spanned from -115 to 50 °C (same cooling rate). It was performed using a Novocontrol Alpha-A High Performance Frequency Analyzer and a Quatro Cryosystem (Novocontrol Technologies, Germany). The response of the samples was measured at constant frequencies: 100 Hz, 1 kHz, 10 kHz, 100 kHz, and 1 MHz.

3.2.2.2 Impedance Spectroscopy

For temperature-dependent impedance spectroscopy, a comprehensive analysis was conducted using an MFIA Impedance Analyzer (Zurich Instruments, Switzerland) with a frequency range from 1 Hz to 5 MHz. The measurements were performed at an amplitude of 0.1 V_{rms}, covering the temperature range from room temperature up to 500 °C under atmospheric conditions. Throughout the experimental process, the complex impedance was recorded in 50 °C steps across the entire frequency range during both the heating and cooling cycles. The heating and cooling rates were maintained at 5 K/min, and a holding time of 20 min was implemented to guarantee thermal equilibration of the samples at each temperature step. Just as in the previous setup, the same box furnace was utilized. Subsequent to data acquisition, the analysis and data fitting procedures were carried out using the RelaxIS software (version 3.0.20.19, rhd instruments, Germany). To determine the TCC, the same frequency analyzer used for

dielectric permittivity measurements was employed, covering a frequency range of 1 Hz to 5 MHz. The temperature span for this particular investigation extended from RT to 600 °C. Concurrently, ESR and SRF investigations were also conducted. In this case, however, the temperature was held constant at room temperature, and the maximum frequency was 10 MHz.

3.2.2.3 Capacitance-Voltage Measurements and Polarization Response

In-depth investigations concerning the electric field and temperature stability of the samples were conducted using a combination of capacitance/permittivity and polarization loop measurements. To achieve this, a TF Analyzer 2000 (aixACCT Systems GmbH, Germany) was employed, enabling the application of maximum electric fields of up to 200 kV/cm and temperatures ranging from RT to 200 °C. The temperature settings were divided into 25 °C steps. Throughout the experiments, the bulk reference samples and prototype MLCCs were subjected to different temperature ranges. The bulk reference samples were exposed to temperatures up to 200 °C, whereas the MLCCs were limited to a maximum temperature of 150 °C. The applied electric fields resulted in an amplitude of 936 V for the prototype MLCCs, considering an approximate thickness of 46.8 µm. Correspondingly, the electric fields for the bulk reference sample with a thickness of 0.19 mm resulted in an applied voltage of 3824 V. The voltage was applied as a step function with a base waveform of 1 Hz in unipolar mode, while the small signal waveform was adjusted to 1 kHz and 50 V, keeping the current range within 1 mA. To ensure statistical reliability, 1000 repetitions were recorded, with 500 averages taken for each measurement. For the polarization loops, identical temperatures and electric fields were considered. However, the frequency was adjusted to 1 Hz, and the current range was set to 100 µA. To maintain a consistent and controlled environment during the experiments, all samples were fully submerged in silicone oil (AK200, Wacker), inhibiting bypassing over the surface.

3.3 Reliability and Electrical fatigue

The experimental methodology of the samples investigated towards electroformation and dielectric breakdown strength may substantially differ from the methodology elucidated before regarding the MLCCs and reference bulk samples. Consequently, the sample preparation and characterization will be explained in the two following subsections.

3.3.1 Electroformation

3.3.1.1 Sample Preparation

Powders of $Na_{0.5}Bi_{0.501}TiO_3$ ($NB_{0.501}T$) and $Na_{0.5}Bi_{0.501}Fe_xTi_{1-x}O_3$ ($NB_{0.501}T$-Fe) (x=0, 0.001, and 0.003) were prepared via the solid-state synthesis method. Details about the powder synthesis can be found elsewhere.[148] The prepared powders have been uniaxially pressed into 10 mm pellets with a pressure of 25 MPa for 10 s and cold isostatically pressed at 200 MPa for 3 min. The same presses as in Subsection 3.1.6 were used. The samples were sintered at 1150 °C for 2 h with a heating rate of 5 K/min. The samples were ground to a thickness of 0.2 mm. Electrical experiments were conducted on samples with three different types of electrode arrangements, as illustrated in Figure 3.3:

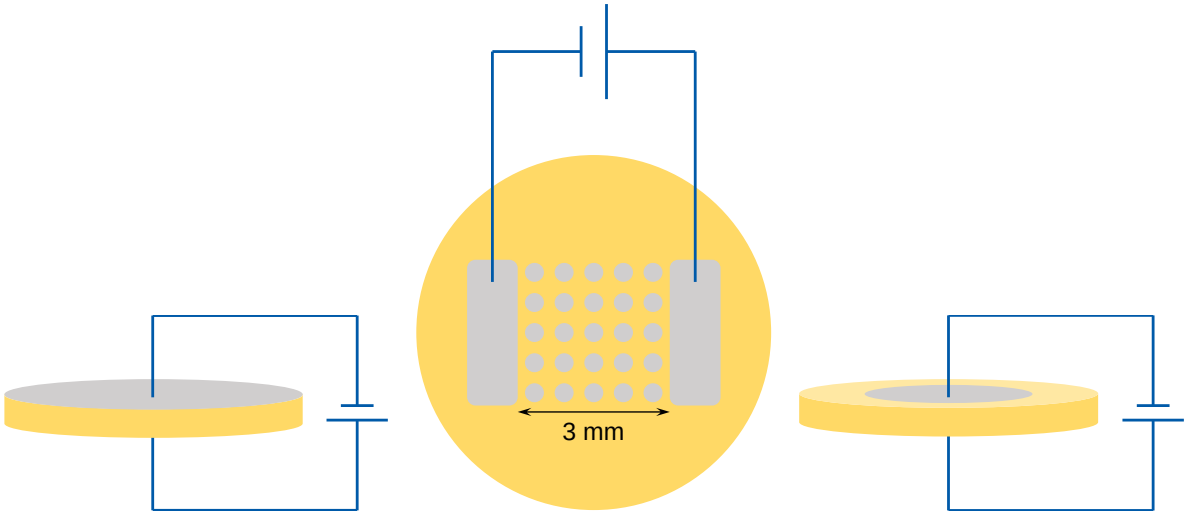

(a) Full Pt-electrode coverage of top and bottom surfaces.

(b) Rectangular surface electrodes for applying high fields and round microelectrodes for local resistance probing.

(c) Electrode arrangement covering partly top and bottom surfaces

Figure 3.3: Schematics of the electrode arrangement on the sample surfaces for high-field experiments, redrawn from Ren et al.[148]

The electrode configuration shown in Figure 3.3(a) and Figure 3.3(c) was established using Pt-paste and subsequent burning in at 1100 °C for 1 h. Covering only a small part of the surface allows a voltage drop in the sample instead of a possible surface pathway. The electrode arrangement in Figure 3.3(b) was

applied similarly to the procedure explained in Subsection 3.1.8.

3.3.1.2 Electrical and Structural Characterization

For DC experiments, a Keithley 2450 source measuring unit (Tektronix, OR, USA) was utilized, measuring the electrical response at 250 °C and 200 V. This results in an electric field of 10 kV/cm. The resistance degradation of NBT-based laminates was recorded slightly different. The laminates had a thickness of 0.25 mm. The top and bottom surfaces of the laminates were sputtered with a mask consisting of a small hole with a diameter of 250 µm. The previously used Keithley 2450 was connected to a microprobe setup (MPS150, Cascade Microtech GmbH, Germany), further connected to the top and bottom electrodes. The course of resistance of the laminates was monitored at an applied constant voltage of 210 V for 32 h at 350 °C.
The Novocontrol Alpha-A impedance analyzer recorded changes in impedance at 1 V amplitude and a frequency range of 0.1 Hz to 1 MHz with an additionally applied DC-bias of 150 V. Local resistance differences due to the application of high electric fields were investigated by the same equipment. The electrode arrangement in Figure 3.3(b) was used, while the microelectrodes had a diameter of about 100 µm. The electric field was applied to the rectangular electrodes, and local resistance changes could be recorded at the microelectrodes due to the stoichiometry polarization in the electroformed regions. Color changes of the surface were qualified by an optical microscope (PSM1000, Motic, Hong Kong).
X-ray photoelectron spectroscopy (XPS) spectra were obtained using a PHI 5700 spectrometer (Physical Electronics, Inc., MN, USA), which is part of the Darmstadt integrated system for materials research (DAISY-MAT).[213]

3.3.2 Dielectric Breakdown Strength

3.3.2.1 Sample Preparation

Barium titanate laminates were manufactured by the tape casting route with processing steps following the work by Fulanović et al.[114] For the slurry, the same recipe as for the A-MLCCs was used (Table 3.1). Likewise, further procedure was conducted as described before in Subsection 3.1.1 for the A-MLCCs. However, the sheets were not screen printed but stacked as 12 × 12 mm² green laminates. The laminates were further cut into 6 × 6 mm² pieces. The same route was chosen for the NBT-BT-CZ-1BA laminates, produced with the slurry used for the prototype MLCCs (Table 3.1).
After fabricating the green stacks, indents were created onto the surface of the sample by a custom-built indenting device, as it is depicted in Figure 3.4(a). The device is equipped with a (1) micrometer screw, (2) a transducer, (3) an indenting ball tip with a diameter of 1 mm, which can be moved under load control with a precision of ± 2.5 µm, and (4) an additional thermocouple socket to ensure a constant temperature during the indentation process.

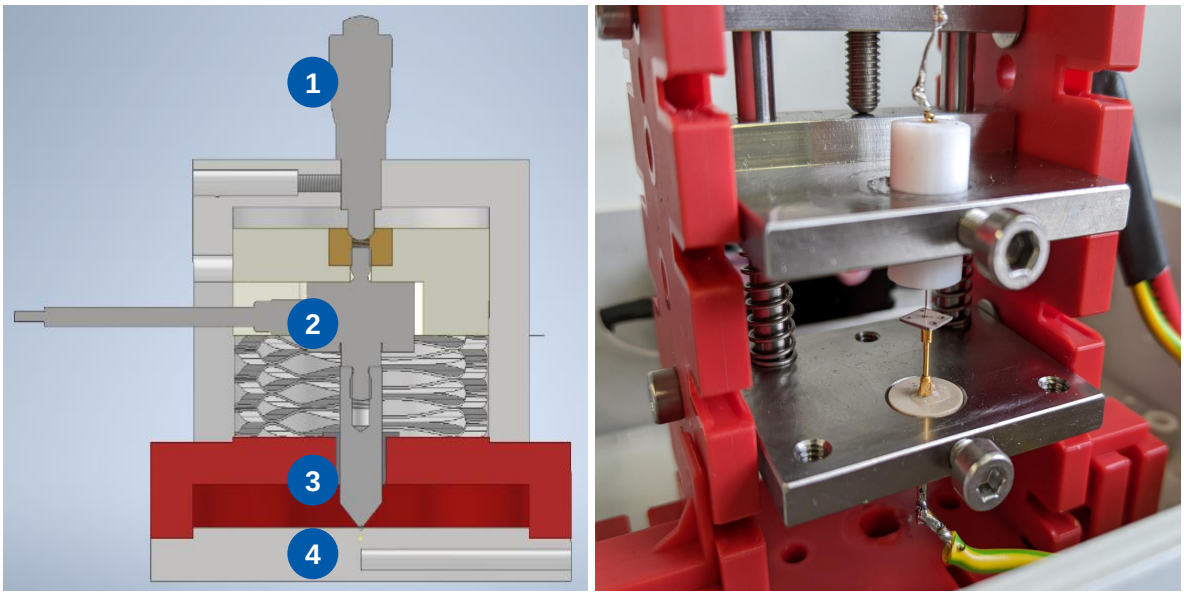

(a) Cross-sectional schematic of the indenting device with (1) micrometer screw, (2) transducer, (3) indenting tip, and (4) thermocouple socket.

(b) Measurement setup with a mounted sample between the top and bottom electrode. The thin top electrode helped to contact the surface within the indent.

Figure 3.4: Preparation and measurement setup for the indented laminates, adapted from Gehringer et al.[73]

Temperatures between RT and 120 °C were considered for indentations to evaluate the optimal temperature for plastic deformation of $BaTiO_3$. Instead, for the NBT-BT-CZ-1BA laminates, a temperature range between 40 °C and 110 °C was chosen. The temperature was adjusted by a heating plate (RCT basic, KA Werke GmbH & Co. KG, Germany). The transducer was connected to a data acquisition machine (MGCplus AB22A, Hottinger Baldwin Messtechnik, Germany) to capture the forces and the contact point between the indent tip and the laminates. After positioning the laminates below the indent tip, the indentation device was closed and heated up to the desired temperature. After 5 min of equilibration, the micrometer screw was screwed down to create indents with green thicknesses of 100, 200, 300, 400, and 500 µm. The indentation rate was set to 1-2 min per indent. Five indents per green laminate (Figure 3.5(b)) were prepared, resulting in 170 and 85 indents for the BT and NBT-BT-CZ-1BA laminates, respectively. An average distance of at least 1 mm between each indent prevented interference from neighboring deformations.

After indentation, the laminates were heat treated in a chamber furnace (HT 10/18, Nabertherm GmbH, Germany). Therefore, the green laminates were sandwiched in an alumina crucible between two porous alumina plates to prevent deformation and bending during the sintering step. Additional sacrificial powder of the corresponding ceramic powder inhibited the evaporation of volatile species. The thermal treatment is equal to the treatment of the MLCCs (c.f. Figure 3.2). Hence, the NBT-based indented laminates were sintered via a two-step heat treatment. The BT laminates, however, experienced a three-step heat treatment (c.f. Figure 3.5). The binder burnout step remained the same, but an additional

two-step sintering process reduced abnormal grain growth.[214] The temperature was first elevated to 1300 °C with a holding time of 1 h. The second sintering step was at 1200 °C for 8 h. A sufficiently dense microstructure with small grain sizes and a rather unimodal grain size distribution could be achieved.

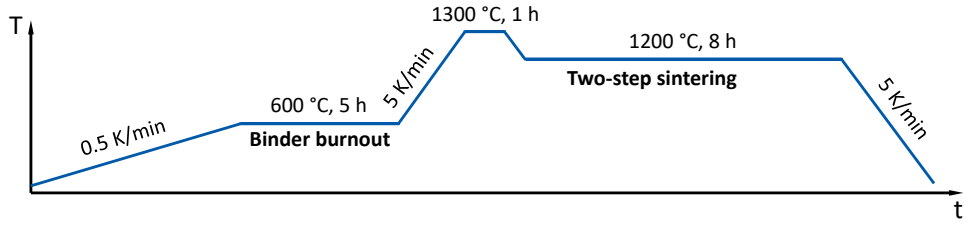

(a) The thermal treatment of BT laminates comprises a three-step heating process including a two-step sintering process to reduce abnormal grain growth.

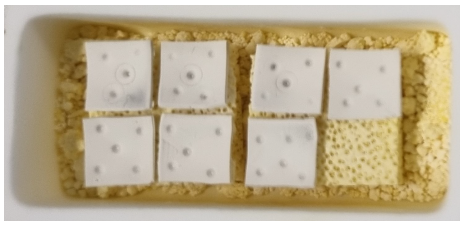

(b) Green laminates placed inside the crucible with sacrificial powder and one of the porous alumina plates below.

Figure 3.5: Schematic of the thermal treatment of BT laminates and green laminates exemplarily shown before the thermal treatment.

Contacting the indents is the last step during the sample preparation. Therefore, the top and bottom sample surfaces will be sputtered with Pt with the same equipment as in Subsection 3.1.8. It is essential to remove the sputtered layer on the top surface outside of the indent to avoid arcing over the surface or edge. The surface was ground with fine SiC grinding paper (4000) to entirely remove the sputtered layer on the surface of the sample and reduce surface deformations. The remaining Pt was present only within the indent pit, forming an arch-shaped top electrode.

3.3.2.2 Structural and Electrical Characterization

Depth profiles were performed with a laser confocal microscope (LEXT OLS4100, Olympus, MA, USA) to correlate the indent surfaces before and after sintering.
Sintered laminates were also cut in the center of the indent to contrast the microstructure below the indent and in the bulk. The cross-sections were investigated by SEM. Furthermore, electrical analysis was conducted with a custom-built high-voltage (HV) setup, as depicted in Figure 3.4(b). The voltage was supplied by an HV amplifier (Trek 20/20C, Advanced Energy, CO, USA). The signal was generated with the help of a data acquisition card (National Instruments, TX, USA) and controlled by a LabVIEW program. The samples were fixed between a gold-coated thin top and gold-coated bottom electrode of

the experimental setup, which is visualized in Figure 3.6. Silicone oil on the top of the samples' surface inhibited possible arcing over the edge.

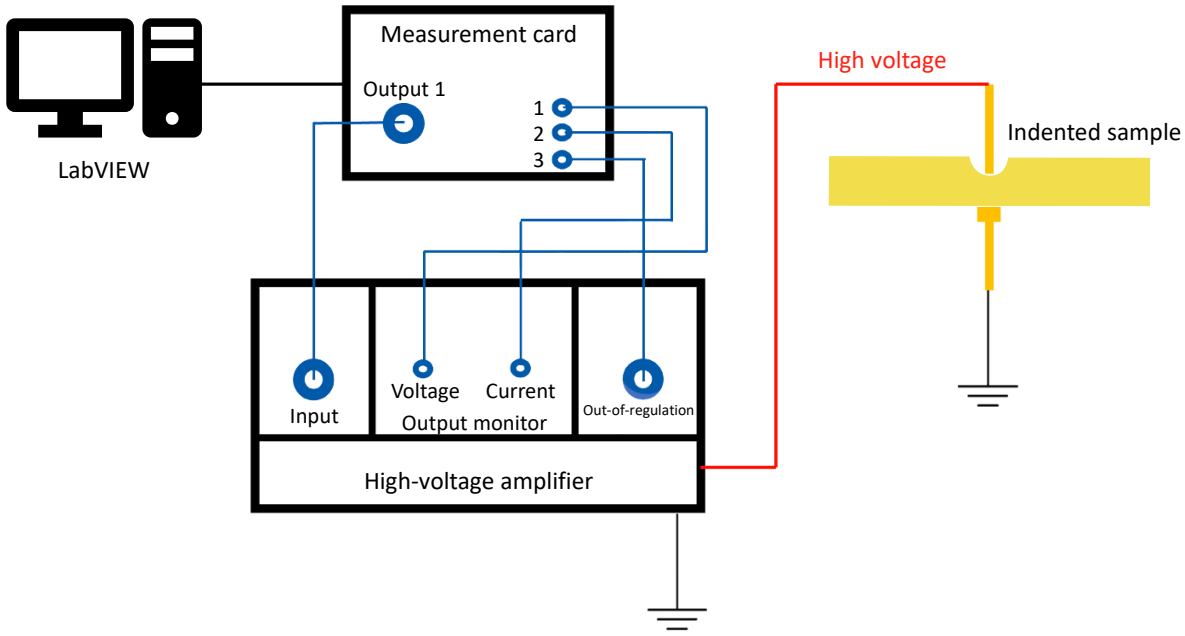

Figure 3.6: Schematic of the experimental setup for the breakdown measurements.

The card is used for the signal generation of up to 10 V, further amplified by a factor of 2000. The output of the amplifier is connected to the pin of the custom-built HV setup, which is in contact with the top electrode and positioned in the center of the indent. The bottom electrode of the sample is grounded. The output signal of the amplifier is connected to the first and second inputs of the measurement card, which are the applied voltage and current, respectively. An additional out-of-regulation function helped to identify the correct breakdown voltage. A signal is constantly generated until a breakdown event takes place. After that, the signal stops, and the card stops generating a signal for the amplifier. It will break the circuit, and the high voltages are turned off.

For the BT laminates, 75 indents were used to evaluate the thickness dependence. Therefore, samples with green indent depths ranging from 100-500 µm were chosen, resulting in 15 indents per individual indent thickness. Different active volumes were investigated with 55 indents by having tip diameters of 0.5 mm (15 indents), 1 mm (15 indents), and 3 mm (25 indents). Another 40 indents were utilized for different voltage ramps ranging from 5-5000 V/s with one order of magnitude steps, i.e., ten indents per voltage ramp. Electric fields of up to 30 kV/mm were experimentally probed.

For the NBT-based laminates, 85 indents were used for evaluating the thickness dependence. Here, electric fields close to 90 kV/mm were experimentally probed.

A finite element method has been utilized with COMSOL software (COMSOL Multiphysics ver. 5.6, COMSOL Inc., Sweden) and a 2D axial simulation module with a triangular element mesh. A constant electrical conductivity σ of 10^{-7} S/m as well as a permittivity ε_r of 1679 were assumed for the calculations

of BT.[161,215] Within the simulation, the bottom electrode was always set to ground and the top electrode to high electrical potential. Similar to the laminates, the ground electrode covered the complete bottom side. Regarding disk-shaped samples, the parallel top and bottom electrodes were fixed, partially covering the surfaces by leaving a 1 mm electrode-free rim. To this end, the electric field distribution was described by the following equations sustaining the current conservation:

$$J = \sigma \cdot E \tag{3.1}$$

with the current density J. The nominal electric field was adjusted to 30 kV/mm, and the electric displacement D was determined by:

$$D = \epsilon_0 \cdot \epsilon \cdot E \tag{3.2}$$

4 Results and Discussion

First, A-MLCCs will be characterized regarding the slurry, (micro-)structural aspects, dielectric, and impedance-related properties. This is followed by four influencing factors, which not only have a significant influence on the microstructure of the capacitors but also the final electrical properties. As will be seen, structure-property relationships are of tremendous importance for the prototype fabrication of MLCCs. The slurry composition, shaping processes, sintering conditions, and electrode material will be covered step by step (Figure 4.1). After each part, a short conclusion will be drawn, including an outlook on what can be improved further. The know-how gained from the characterization of A-MLCCs and all influencing factors will be used to prepare optimized Ω-MLCCs. Therefore, the structure of the results part will give deep engineering insights into prototyping lead-free MLCCs. The experimental proof of concept of NBT-based capacitors with Ag/Pd inner electrodes will be acknowledged.

Prototype MLCCs will be characterized to evaluate their suitability as a capacitor for high-temperature and power electronics applications. It will address structural insights, defect chemical viewpoints, dielectric and energy storage properties, impedance, and related properties. Comprehensive studies on capacitors tested under industrially relevant environments will emphasize key benefits. Further, the complex defect chemistry of NBT-based ceramics under temperature and voltage stress will be evaluated. Together with investigations on the dielectric breakdown behavior of prepared MLCCs, valuable information about the reliability will be highlighted.

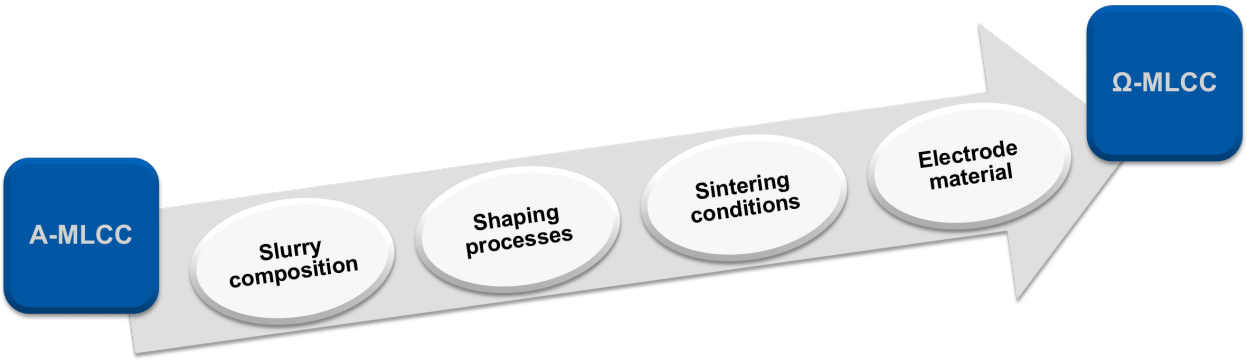

Figure 4.1: Schedule of prototyping MLCCs.

4.1 Characterization of A-MLCCs

The characterization of fabricated A-MLCCs serves as a starting point for this work. The composition of the slurry will be provided, and contributions to the microstructure will be discussed. Secondly, a structural characterization, including defects of the component and microstructure and chemical interactions between dielectric and inner electrode material, is followed. Subsequent electrical characterization of high-temperature dielectric properties and impedance spectroscopy will complete this section.

4.1.1 Slurry Composition

A slurry for the tape casting process was produced based on initial knowledge, and this composition was also published by Fulanović et al.[114] The composition of this slurry is shown in Table 4.1, including weight, weight percentage, specific density, volume, and volume percentage of each ingredient.

Table 4.1: Slurry composition for the A-MLCC, including the weight, weight percentage, specific density, volume, and volume percentage per ingredient.

Type	Component	Weight (g)	Weight percentage (%)	Spec. density (g/cm³)	Volume (cm³)	Volume percentage (%)
Ceramic powder	NBT-BT-CZ-BA	12.00	59.00	5.691	2.11	52.25
Solvent 1 Solvent 2	Ethanol (40%) MEK (60%)	6.04	29.70			
Homogenizer	Cyclohexane	0.17	0.84			
Dispersant	Oleic acid	0.05	0.25	0.89	0.06	1.39
Plasticizer	PEG	1.04	5.11	1.124	0.93	22.93
Binder	PVB Butvar® B-98	1.04	5.11	1.1	0.95	23.43

Essentially, two columns in the table are of high importance for the final quality of the tape, which is the weight percentage and the volume percentage after drying. This is also the reason why solvent 1 and 2 and the homogenizer are left blank as they basically do not contribute to the green density of the tape. A roughly 30% weight ratio of solvent was likely suitable to form a decent slurry and subsequent tapes.[64] Within these considerations, the solvent is meant to evaporate completely. However, a small residual amount of solvent may be inside the dried tapes. After the drying step, this results in a volume percentage of about 52% for the ceramic powder and the remaining part for the organic additives. The weight percentage of the ceramic powder also corresponds roughly to the actual green sheet density of the tape, as it is further considered that all organic additives will be burnt out during the binder burnout process.[204] The binder burnout process leaves behind a very rigid and brittle structure comprising the ceramic powder only. There is slight shrinkage to be expected during binder burnout.[216] The higher the porosity, the higher the surface energy. The surface energy will be reduced during sintering and corresponding neck formation.[208] However, to start densification, a sufficiently high green density needs to be present in order to initiate diffusion and mass transport. The microstructure obtained with the previous slurry will be determined subsequently, but higher green densities or volume percentages of solid loading are favored to get dense ceramics.

4.1.2 Structural Characterization

In Figure 4.2, cross-sectional SEM micrographs of A-MLCCs with 9 active layers and 1 active layer are depicted. Two types of electrode pastes were used first to figure out the most suitable paste for NBT-based dielectrics. On the one side, A-MLCCs in Figure 4.2(a) and Figure 4.2(b) contain inner electrodes with ZrO_2 as filler. On the other side, A-MLCCs in Figure 4.2(c) and Figure 4.2(d) have inner electrodes with $BaTiO_3$ as filler. Several distinctive structural defects will impede the final properties of the devices in terms of both electrical and mechanical properties. First of all, all prepared A-MLCCs exhibit a rather porous microstructure. Delamination of passive layers is present at the A-MLCC with only a single active layer and BT as a filler (Figure 4.2(d). Also, partial delaminations can be identified for all prepared capacitors. A-MLCCs with BT as filler exhibit much more discontinuities of inner electrodes. Regarding ZrO_2 as a filler, almost no discontinuities are visible. Fillers are added to adapt the coefficient of thermal expansion (CTE) of the dielectric and electrode material, preventing further defects.[217,218] The comparison here is sufficient to conclude that Ag/Pd inner electrode paste with a ZrO_2 is more suitable. Discontinuities can result in cracks or delamination during the operation of MLCCs.[219] For further processing, only the paste with ZrO_2 filler will be used. The question remains if there are detrimental interactions between Ag/Pd paste with BT filler and the NBT-BT-based matrix. Besides discontinuities, high porosity, and slight delamination, other bigger voids can be spotted. This will all diminish the final density of the components. Density measurements are usually conducted by the simple Archimedes' principle. It is, however, not viable for co-fired ceramics because the densities of the electrode material and ceramic will be different. An algorithm that counts the area of pores within a particular area of the dielectric was established by Patrick Breckner and could be applied to SEM micrographs with high contrast. It was now possible to estimate the final density of MLCCs by using this algorithm. It turned out that MLCCs with 9 active layers, on average, have a relative density of 91-92% with an error of 0.4%, and MLCCs with only a single layer have a slightly higher relative density of 93-95% with an error of 1.0%. As a dense ceramic is considered beyond relative densities of 95%, A-MLCCs are not fully dense.[220] They will likely also exhibit an open porosity or interconnected pores, which have a crucial influence on electrical properties.[221] Taking into account that bulk reference samples were sintered under the same conditions and yielded relative densities of 96-97%, other parameters than the sintering step have to be considered to further lower the porosity. Albeit, A-MLCCs with only a single layer tend to have slightly higher densities, which could indeed be the reason that thermal energy distributes better in smaller components. Another thought would be that evaporation of gaseous phases (organic residuals and Bi_2O_3) is promoted with thinner structures and open porosity.

Nevertheless, the flatness of inner electrodes seems to be acceptable compared to other manufactured MLCCs, e.g., the work by Jia et al.[117] Also, the individual sheet thickness of each layer appears to be homogeneous and could be estimated to be about 45 µm.

So far, the preparation of A-MLCCs lacks reproducibility. It is almost impossible to achieve defect-free microstructures with a negligible amount of structural defects. Too many parameters are adjusted simultaneously to draw any conclusion about what has to be improved. However, further characterization

of the A-MLCCs is required to fully understand what needs to be done to improve and optimize the processing and other previously mentioned parameters of MLCC fabrication.

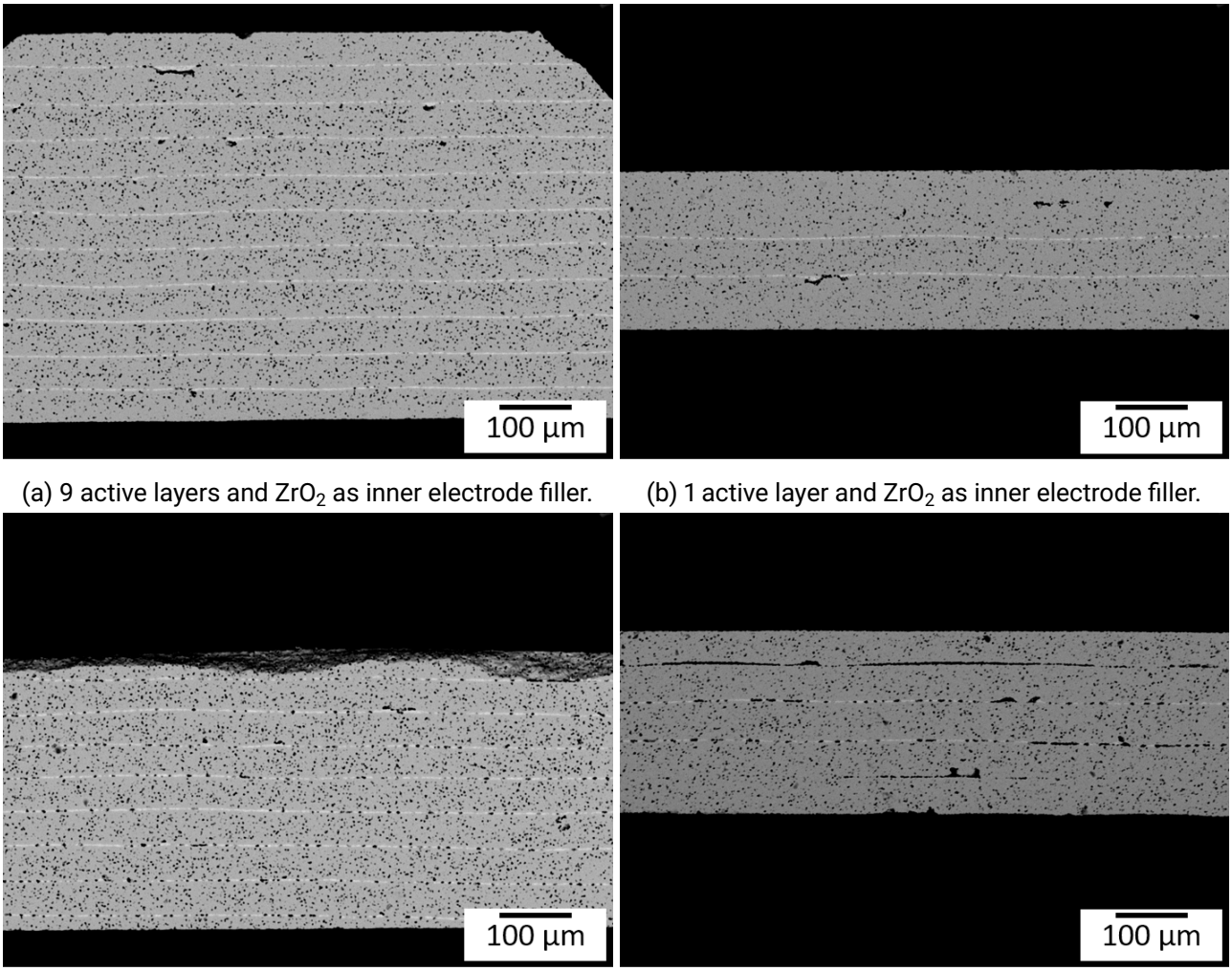

(a) 9 active layers and ZrO_2 as inner electrode filler.

(b) 1 active layer and ZrO_2 as inner electrode filler.

(c) 9 active layers and $BaTiO_3$ as inner electrode filler.

(d) 1 active layer and $BaTiO_3$ as inner electrode filler.

Figure 4.2: Cross-sectional SEM micrographs of A-MLCCs with different amounts of active layers and Ag/Pd inner electrodes.

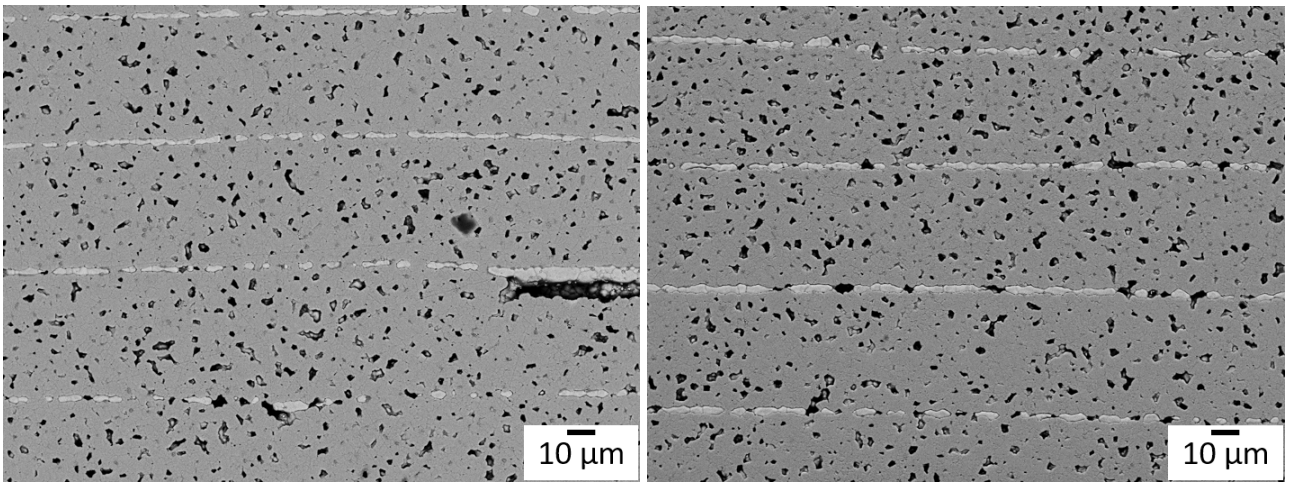

(a) 500x magnification and ZrO_2 as inner electrode filler. (b) 500x magnification and $BaTiO_3$ as inner electrode filler.

Figure 4.3: Magnified SEM micrographs of A-MLCCs with different types of structural defects like pores, discontinuities, and delamination.

In Figure 4.3, A-MLCCs with ZrO_2 and $BaTiO_3$ filler are depicted at 500x magnification. In Figure 8.1, in the supplementary material, the microstructure of the dielectric material is shown at 2500x magnification. Magnified images reveal further essential information on the pore shape and porosity. The pores rather have an angular shape, which could be rationalized by insufficient sintering conditions and the incorporation of gaseous phases.[222] Bulk reference samples were sintered at 1100 °C and 120 min sintering time. The dielectric processed here is the same. This was the reason also to choose the same conditions. Additionally, the binary system Ag and Pd in the ratio of 70/30 can only be sintered up to temperatures of 1160-1170 °C.[47,48] Harsher sintering conditions than for the bulk reference, i.e., longer time and higher temperatures, could be a solution and might be worth looking at. However, as the range between the sintering temperature and the melting point of 70/30 Ag/Pd is relatively small, it is assumed that optimization of sintering conditions will be challenging. Another reason could be an insufficient binder burnout step or the type of organic additives in general. For the organics, especially the binder and plasticizer chosen for A-MLCCs, air/oxygen is required to decompose the polymers fully.[65,66] As binder and plasticizer have a considerable share of the green A-MLCCs' volume (about 46%), an incomplete binder burnout step may result in solid or gaseous residues. It may affect the amount of pores.

4.1.2.1 Stacking Mismatch

Not only will porosity interfere with electrical properties, but also other factors during processing, such as stacking mismatch during the stacking of screen-printed green sheets. Due to limitations of the equipment and manual alignment, a precision of down to a few 100 µm could be achieved. A custom-made aligning device that helped to stack all individual sheets. Mismatch during stacking of individual green sheets can severely decrease final capacitance. The overlap of inner electrodes is constrained, and the active area is much smaller than an ideal alignment. However, determining the correct active area can be problematic

and comparisons to bulk or other MLCCs inaccurate. According to Equation 2.3, the area is substantial to the overall capacitance. During stacking, the sheet thickness is not altered at all. In Figures 4.4 and 4.5, stacking mismatch is visible. Figure 4.4(a) depicts lateral shifted inner electrodes. The area of an ideal overlap is indicated in red. In Figure 4.4(b), an even more drastic shift of stacked green sheets, especially at the edges, is perceived. The stacked green sheets seem to bend during the heat treatment. An additional top-view image with an optical microscope reveals further stacking mismatch of A-MLCCs (see Figure 4.5). Not only on the edges (magnified part), but also stacked inner electrodes are not aligned well. This can be seen within the marked red area. The mismatch seen in the figures here is about 2-5%. It will inhibit the final performance, but it will be discussed and optimized later in Section 4.3. Aligning the green sheets is important for successfully preparing MLCCs and their related capacitance.

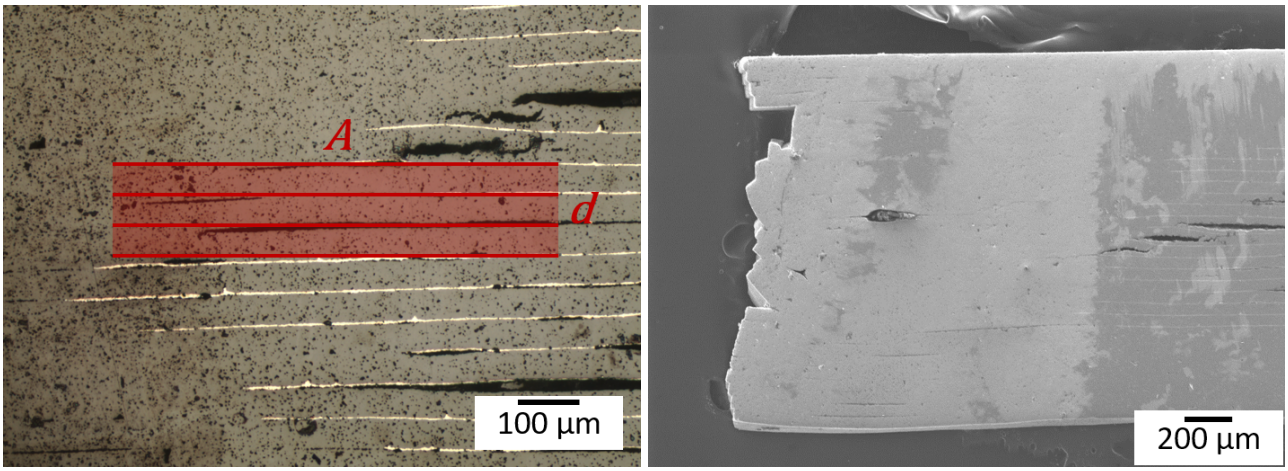

(a) Optical image of an A-MLCC with severe stacking mismatch of individual sheets. Indicated in red is the area of an ideal overlap of inner electrodes.

(b) SEM image demonstrating severe stacking mismatch at the outer edges of the sintered A-MLCC.

Figure 4.4: Optical and SEM images with severe stacking mismatch of the sintered A-MLCC.

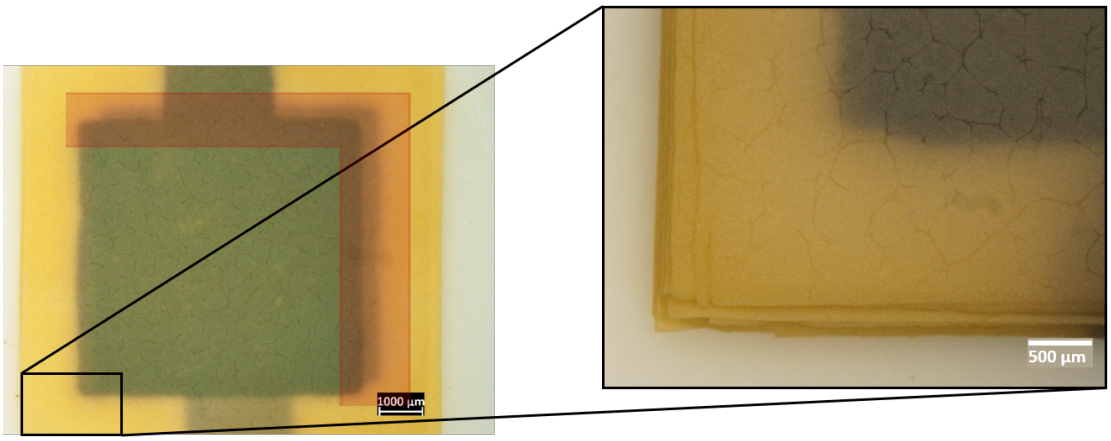

Figure 4.5: Stacking mismatch seen from a top view of a sintered A-MLCC. The red area marks a stacking mismatch of alternatively stacked inner electrodes, which can be identified by a shift towards the upper right and different shadings. The inset demonstrates the mismatch at the edges of the MLCCs. The layers were not well-aligned during stacking.

4.1.3 Dielectric Properties

In this subsection, the dielectric properties of prepared A-MLCCs will be sorted and compared to a reference bulk sample with Pt outer electrodes prepared by the common solid-state processing route. In comparison, helpful insights between MLCC and bulk can be gathered. The MLCC fabrication route is fairly different from the shaping process of bulk samples. Even the thermal treatment is different. In Figure 4.6, the bulk reference response of a) relative permittivity and d) dielectric loss against temperature (RT-500 °C) is shown with frequencies ranging from 0.1 kHz to 1 MHz in one order of magnitude steps. Figure 4.6b) and e) depict an A-MLCC with 9 active layers, whereas c) and f) an MLCC with only a single active layer. The approximate densities between MLCCs with 9 and 1 active layers were different. The bulk samples only serve as a reference to compare obtained results with actual A-MLCCs. Dielectric properties of it will not be described again but are summarized in Table 4.2. Additionally, the bulk reference sample exhibits highly similar properties compared to the bulk samples prepared by Hoang et al.[29]

The A-MLCC with 9 active layers (Figure 4.6b) and e)) exhibits much lower relative permittivities than the bulk. A maximum ε_r' of 322 at 150 °C at 1 kHz could be recorded. The dielectric loss is likewise worse. For example, the loss is already at 2% at temperatures of about 315 °C. Even the characteristic frequency dispersion is quite different; i.e., frequencies above 100 kHz already exceed the regime of low dielectric loss. This response is also reflected in the A-MLCC with only 1 active layer. Permittivity is, however, already enhanced, reaching a maximum value of 499 at 150 °C and 1 kHz. The dielectric loss is still relatively low since it surpasses 2% beyond 323 °C. The microstructure will have a significant effect on the dielectric properties, and the response of MLCCs shown in Figure 4.6 is an excellent example. For both A-MLCCs, the porosity of the dielectric appears to be high. Hence, they are considered not dense. It was shown by Hirata et al. that dielectric properties are indeed affected by porosity in BT.[223]

They suppose that, on the one side, a correlation between permittivity and density/porosity is somewhat tricky. Conversely, they claim that dielectric loss tends to be interrelated with the density/porosity. This seems to be true as the porosities of both A-MLCCs are in the same range, but the MLCC with 9 active layers has a lower relative permittivity. Nevertheless, the aforementioned stacking mismatch and perhaps also interactions between the inner electrode material and the dielectric could prevail over the dielectric properties. It was demonstrated by Schuetz et al. that Ag can segregate during the thermal treatment and can be incorporated into the NBT host lattice. This can drastically lower resistivity and increase losses.[47]

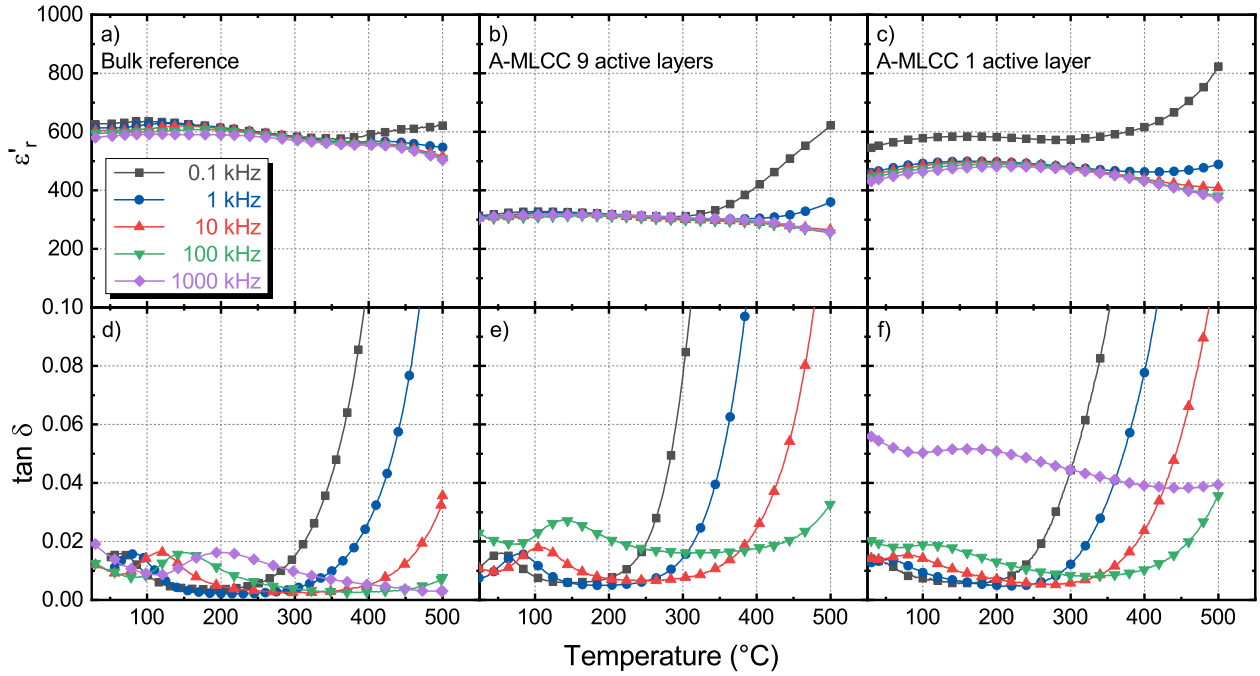

Figure 4.6: Dielectric properties of bulk NBT-BT-CZ-1BA (a) and d) as the reference) and a MLCC with 9 (b) and e)) and 1 (c) and f)) active layers, respectively.

Table 4.2: Comparison of dielectric properties determined at 1 kHz between bulk reference and A-MLCCs with 9 and 1 active layers.

Sample	Bulk	MLCC 9 active layers	MLCC 1 active layer
ε_r'(max)	629	360	500
ε_r'(150 °C)	625	322	499
$\Delta T(\varepsilon_r' \pm 15\%)$ (°C)	-81 - >500	RT - >500	RT - >500
$\Delta T(\tan\delta \leq 0.02)$ (°C)	-67 - 385	RT - 315	RT - 323
$\Delta T(\varepsilon_r' \pm 15\%; \tan\delta \leq 0.02)$ (K)	452	295	303

4.1.4 Impedance Spectroscopy

The impedance of the bulk sample in Figure 4.7a) is in the same range as published by Hoang et al.[29] In Figure 4.7b) and c), Nyquist plots of A-MLCCs with 9 and 1 active layer at 500 °C are depicted, respectively. The A-MLCC with 9 active layers has a drastically lower resistivity than the bulk reference. Permittivity data from the previous subsection indicated that something during processing was odd. Further, a high time constant at 630 Hz in combination with low capacitance, points towards a very conductive capacitor. These findings coincide well with the microstructure of the corresponding MLCC. A higher amount of pores contributes to overall conductivity.[224] Besides a slightly higher relative density, a similar response is found for the single-layered MLCC. The electrical conductivity is supposed to be lower, too. This is reflected in the Nyquist plot in Figure 4.6c). Compared to the A-MLCC with 9 active layers, it has a higher resistivity. As structural defects are present, it cannot keep up with bulk reference samples. The impedance emphasizes the component's resistance and hints towards undesired leakage currents.

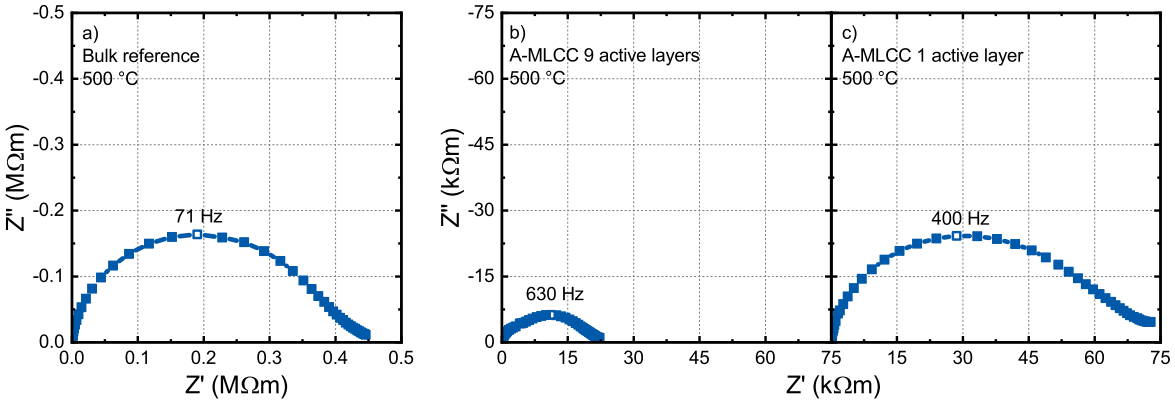

Figure 4.7: Nyquist plots of bulk (a) bulk NBT-BT-CZ-1BA and A-MLCCs with (b) 9 and (c) 1 active layers, respectively. Data was taken at 500 °C and each ω_{max} is marked with the corresponding frequency.

The complex modulus highlights the capacitances of processes involved in the overall response. Figure 4.8 shows the imaginary modulus against the frequency from 400-550 °C in 50 °C steps. PNRs are claimed to be present in this capacitor material.[29,34,35] Interestingly enough, Zang et al. revealed a second response within the modulus representation, which could be attributed to the presence of PNRs.[108,109] However, this response should disappear for NBT-BT-based materials at around 420 °C.[110] The response of the bulk reference in Figure 4.8 at 400 °C perhaps depicts a second response at the right side of the peak (dark brown). With increasing temperature, however, it vanishes completely. Only a shift of modulus peaks towards higher frequencies with increasing temperature can be identified. This is common and signifies a lowered capacitance. The maximum imaginary part of the modulus $M''_{max} = \frac{C_0}{2C}$ hardly changes within increasing frequency for all samples.[110] Taking into account the maximum frequency $f_{max} = \frac{1}{2\pi RC}$, derived from Equation 2.43, an increase in conductivity can be rationalized. A similar trend can be spotted for the A-MLCCs with 9 and 1 active layers in Figure 4.8b) and c), respectively. However, the peak modulus values of the A-MLCC with 9 active layers are slightly higher than the bulk. This aligns

with a lower capacitance measured and agrees well with previous results. A second sharp response between 1-10 MHz is seen and refers to the SRF and will be retaken into account in Subsection 4.6.4.1. The A-MLCC with 1 active layer seems to have a higher normalized capacitance than the A-MLCC with 9 active layers. Again, this is in accordance with previous results.
Impedance data and modulus representations can be considered very helpful to characterize the manufactured MLCCs properly. They contain and reveal application-oriented insights of utmost importance for the prototype MLCCs. Note that for the modulus responses in Figure 4.8b) and c), artifacts were measured between 10^3 and 10^5 Hz and were likely caused by an error in the measurement setup.

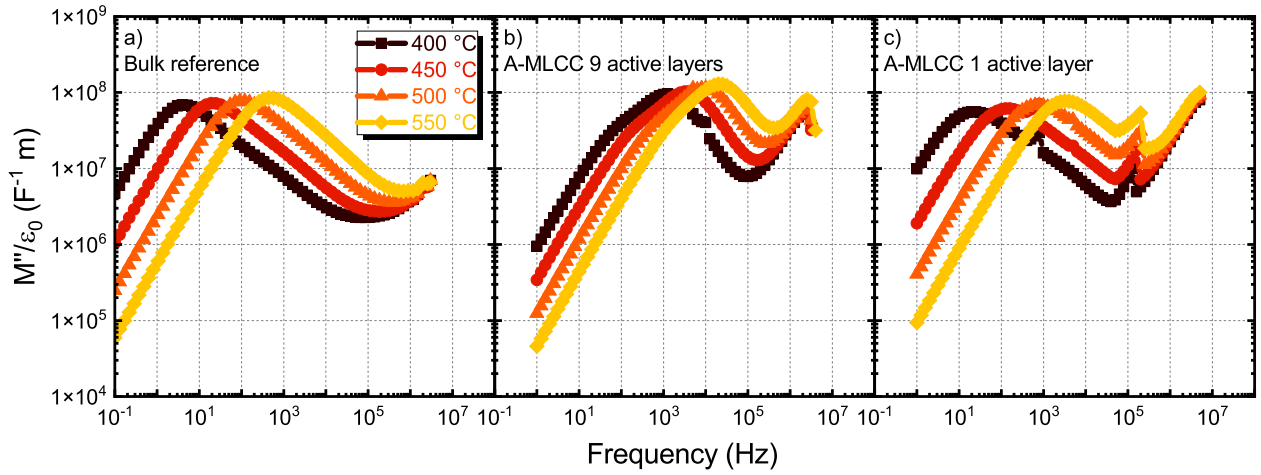

Figure 4.8: Modulus plots of bulk NBT-BT-CZ-1BA ((a) as the reference) and an MLCC with 9 (b) and 1 (c) active layers, respectively, at increasing temperatures from 400-550 °C.

4.1.5 Conclusion

In this section, prepared A-MLCCs were analyzed and evaluated. It could be demonstrated that the MLCC fabrication, in general, is feasible, and numerous parameters manipulate the final dielectric properties of the components. First, obtained A-MLCCs could not be sintered with a density above 95%, and a considerable stacking mismatch of individual layers was observed. This is reflected in the high-temperature properties and especially the dielectric loss of the prepared multilayers. Compared to the bulk reference, dielectric loss is beyond 2% already around 320 °C. Pores will detrimentally affect reliability, fatigue, degradation, and mechanical properties.
To address the issue of rather high porosities, the slurry composition for the preparation of MLCCs will be investigated first. The amount of organic additives affects not only the microstructure but also the final properties of the components, as outlined in Section 2.5.

4.2 Slurry Composition

Table 4.1 depicts the slurry composition that was used for the A-MLCCs. To increase the green sheet density and promote densely sintered samples, a high solid content is desirable.[205] High solid contents are in the range of 60 wt% and are considered to be the best trade-off with respect to flexibility, stability, processability, and high fired densities.[131] Remarkably, higher solid contents are possible, but processing will be much more complicated as higher solid loadings will make the tapes extremely brittle.[64]
Therefore, the dispersant was investigated first. A dispersant is understood to be a molecular compound capable of preventing agglomeration of dissolved particles for a certain period of time by attaching to them.[200] This is achieved by the attachment of the polymer chains to the ceramic particles, which sterically prevents the agglomeration of the individual particles. This prevents direct attachment, i.e., the direct contact of two ceramic particles. A huge variety of dispersants are known from literature, including oleic acid.[64] Sedimentation and rheology experiments were conducted to deduce the optimal amount of dispersant. Such experiments were only done with oleic acid as the dispersant. Therefore, slurries consisting of the ceramic NBT-BT-CZ-BA, solvent, and different amounts of oleic acid were prepared. The weight percentages are 0.1, 0.32, 1, and 2 wt% of the slurry. The sedimentation behavior is depicted in Figure 4.9a) and was recorded after 24 h of sedimentation. As can be seen, at 0.1 and 0.32 wt%, separated phases are present. The solid content of the slurry sedimented while a mixture of oleic acid and solvent remained at the surface. No sedimentation can be detected at or above 1 wt% of dispersant. This, in turn, clearly indicates that the optimal amount of dispersant for this slurry composition is between 0.32 and 1 wt% oleic acid. Further rheologic measurements of the same slurries in Figure 4.9b) do not confirm the key finding from the previous finding. Regarding the viscosity, an optimal amount of dispersant is found when the viscosity exhibits a local minimum.[65] It can be assumed that lower viscosities, in general, are preferred. This is not the case, as evidence was provided that the slurry with only 0.1 and 0.32 wt% is unstable. When plotting the viscosity against the amount of dispersant at the characteristic shear rates 10 and 100 1/s, no minimum turning point within the range of 0.1-2 wt% can be detected. It contradicts Figure 4.9a) where a clear separation between a stable slurry and sedimentation was observed. Ultimately, a slightly higher amount of dispersant was found to be most suitable, which amounts to 0.36 wt%, so sedimentation may be excluded, but viscosity is still rather low.

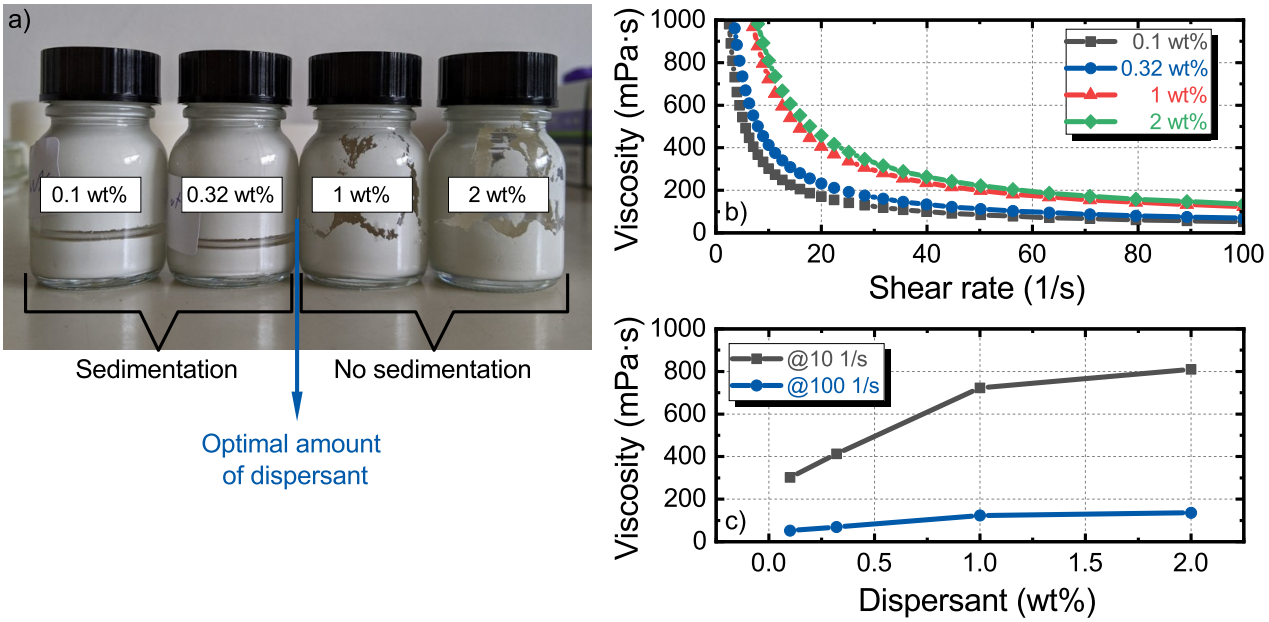

Figure 4.9: a) Sedimentation experiments of a slurry with the NBT-BT-CZ-BA, 1-butanol, and different amounts of oleic acid only. The duration of the experiment was 24 h, and the sedimentation behavior of all slurries was checked visually. b) Rheology measurement by plotting the viscosity against the shear rate of the same slurries. c) Viscosity plotted against the dispersant in wt% at different shear rates.

Oleic acid is a monounsaturated fatty acid that is relatively resistant to oxidation compared to polyunsaturated fatty acids.[225] This is because it has only one double bond, which is located near the center of the carbon chain, making it less susceptible to be attacked by reactive oxygen species. However, like all fats, oleic acid can still undergo oxidation when exposed to heat, light, and air, leading to changed functionality. It can only be assumed that the functionality of oleic acid was altered, and proper dispersion could not be guaranteed, which led to the decision to change the type of dispersant. Dispersants are preferred, which are characterized by excellent stability and cannot be decomposed by external influences. Experiments during this work have demonstrated that Solsperse™ M387 from the Lubrizol Corporation exhibits benefits compared to the dispersant used for the A-MLCC. This dispersant was suggested by K. Makarovič (personal communication, September 10, 2021). According to the product data sheet, the non-aqueous and high-performance dispersant promotes higher solid loading and particle size reduction.[226] Further, it seems that the dispersant effectively supports the separation of individual particles in the slurry through steric hindrance. A prolonged shelf life of the dispersant indicates a higher oxidation-resistance. Using this dispersant also contributed to a higher solid loading of ceramic particles. Since the binder and plasticizer have the highest share of weight percentage, adapting the type and amount of these additives could help to increase solid loading or the green sheets' density, respectively. In general, the binder crucially determines the arrangement of the ceramic particles and other organics during the slurry production step, as schematized in Figure 2.22(a). It serves as a temporary network that promotes the processability of the green sheets. According to the product data sheet, PVB Butvar® B-98

has a molecular weight of 40,000-70,000 g/mol.[227] Higher molecular weights will result in more viscous slurries with a higher glass transition temperature and increased fracture strain of the dried tapes.[200] More flexible tapes are beneficial to green stack processing. During mixing the A-slurry, it was found that the PVB Butvar® B-98 did not readily dissolve in the slip. It was relatively coarse-grained, which seemed adverse for a homogeneous slurry. For the Ω-slurry, a different PVB was used instead. The binder material Mowital® LP BX 860 was very fine-grained powder and easily soluble in the slip. According to the technical data sheet, this kind of PVB not only serves as a binder but also as a dispersant to disperse further and separate the ceramic particles even more.[228] It is optimized for ceramic tape cast materials as a temporary binder for ceramic applications. In comparison to the Butvar® PVB, they have similar specifications. The average molecular weight of the Mowital® PVB is comparable to the PVB used for the A-slurry and amounts to 50,000-60,000 g/mol. Even the hydroxyl content is almost the same; hence, the processability of both binder materials can be considered similar at first glance. Only the fact that the volatile content of the Mowital® PVB is about twice as low as that of the Butvar® PVB (2.5% and 5%) is different.[227,228] It could be helpful to obtain green stacks with higher densities. As both binder materials have similar specifications, the amount of binder was only slightly changed from 5.11 wt% to 5.35 wt% to maintain a certain degree of processability. Nevertheless, the improved solubility of the Mowital® PVB, because of the fine-grained powder, has proven advantageous. It ensured excellent homogenization of the entire Ω-slurry. The resulting network was distributed much more evenly than with the Butvar® PVB. But this binder was not suited for dissolution in ketones like MEK and cyclohexane that was used for the A-slurry.[228] Therefore, the solvent system had to be changed, too.

1-butanol was compatible with the new binder material.[228] Using 1-butanol, as opposed to solvents used for the A-MLCC (ethanol and MEK), also offered an advantage. 1-butanol, compared to ethanol at a vapor pressure of 1 bar, has a much higher boiling temperature, which is 117.4 °C for 1-butanol and 78 °C for ethanol.[229] In practical terms, substances with a high vapor pressure tend to evaporate more quickly, while substances with a low vapor pressure tend to evaporate more slowly. Due to the slower evaporation, the Ω-slurry has more time for uniform sedimentation after casting. Compared to the solvent system used for the A-slurry, the fast evaporation may lead to the formation of cavities due to restricted sedimentation and uneven packing. Even without the homogenizer cyclohexane, the Ω-slurry resulted in a more homogeneous film, improving the processing and lamination of individual sheets.[64] Additionally, this led to an improvement in the microstructure, as the dried film was more densely packed due to the improved sedimentation. Ceramic powder particles were now closer together. Throughout the tape casting experiments, it was found that a solvent (system) weight percentage of about 30% is reasonable to obtain rather viscous slips still. The weight percentage of the solvent system of the A-slurry (30.54 wt%) was hardly changed compared to the solvent used for the Ω-slurry (30.38 wt%).

As the plasticizer of the A-slurry has another considerable share of 5.11 wt%, adapting this type or amount of binder could also promote higher green sheet densities. During the preparation of the slurry or storage of the sheets cast with PEG, it was found that water was superficially attached to the surface. PEG exhibits a hygroscopic nature.[230] It became noticeable during stacking. A small water film on the surface of the sheets can make stacking difficult under certain circumstances. Individual green

sheets were basically glued together. In addition, water molecules that are attached to the surface will evaporate during the thermal treatment of the green stacks, leaving behind open structures. This, in turn, deteriorates the final properties of the MLCC by disturbing the degree of lamination and changing the fired density. By the use of ATBC, on the other hand, water did not attach to the green sheets' surface. This chemical was suggested by K. Makarovič (personal communication, September 30, 2021). ATBC is just not hygroscopic as it does not have any polar functional groups that are capable of hydrogen bonding with water molecules.[231] ATBC, therefore, does not exhibit a strong affinity for water and also does not absorb it from the surrounding environment. This plasticizer did not impair the final density of the component. Another important fact is the potentially remaining residues after the binder burnout. As the plasticizer is an organic compound, it will decompose at certain temperatures and atmospheres. For the A-slurry, PEG was used as the plasticizer material. It was shown that under N_2 atmosphere, roughly 1% of the plasticizer would remain.[232] All samples and MLCCs were sintered in air. This, in turn, means that it is quite likely to have residues within the green tape after binder burnout. During sintering, they will evaporate and may leave back voids, diminishing final densities. However, findings about the thermal degradation of organic additives and ATBC suggest that a complete decomposition and evaporation can happen under the right conditions.[233,234] This would mean a complete mass loss of ATBC during binder burnout. The thermal degradation of both A-MLCCs and Ω-MLCCs will later be evaluated (Figure 4.10). In the end, the amount of ATBC was reduced from 5.11 wt% (PEG) to 3.16 wt% to increase the solid content of the Ω-slurry further. Flexibility and processability were still given at a weight percentage of 3.16%.

In Table 4.3, the developed slurry composition and the amount of ingredients for the Ω-slurries are summarized and contrasted to the A-slurry composition:

Table 4.3: Comparison of ingredients for the slurry composition of A-MLCCs and Ω-MLCCs.

	A-MLCC		Ω-MLCC	
	Component	Weight percentage (%)	Component	Weight percentage (%)
Ceramic powder	NBT-BT-CZ-1BA	59.00	NBT-BT-CZ-1BA	60.75
Solvent 1 Solvent 2	Ethanol (40%) MEK (60%)	29.70	1-Butanol	30.38
Homogenizer	Cyclohexane	0.84	/	/
Dispersant	Oleic acid	0.25	Solsperse™ M387	0.36
Plasticizer	PEG	5.11	ATBC	3.16
Binder	PVB Butvar® B-98	5.11	PVB Mowital® LP BX 860	5.35

The green density of Ω-MLCCs could likely be enhanced, too. The approximate green density of the ceramic in the green stack can be estimated by calculating the volume percentage of the ceramic powder. Besides weight and weight percentages, specific density and volume are necessary to calculate the volume percentage as given in Table 4.4:

Table 4.4: Slurry composition for the prototype MLCC, including the weight, weight percentage, specific density, volume, and volume percentage per ingredient.

Type	Component	Weight (g)	Weight percentage (%)	Spec. density (g/cm³)	Volume (cm³)	Volume percentage (%)
Ceramic powder	NBT-BT-CZ-BA	25.00	60.75	5.691	4.39	56.48
Solvent	1-Butanol	12.50	30.38			
Dispersant	Solsperse™ M387	0.15	0.36	1.02	0.15	1.89
Plasticizer	ATBC	1.30	3.16	1.05	1.24	15.92
Binder	PVB Mowital® LP BX 860	2.20	5.35	1.1	2.00	25.71

It is further assumed that the solvent is completely evaporated during the drying step of the cast tape. Thus, it can be excluded for the estimation. All other species are still inside the dried green tape and will contribute to the overall weight and volume. Further considerations are that no volatile species of the ceramic powder are evaporating. Taking all approximations into account, a volume percentage that is equal to the green density of the ceramic of 56.48% could be calculated. To further approve the estimation of green density, a thermal analysis, depicted in Figure 4.10, is consulted. An A-MLCC green stack (red) and an Ω-MLCC green stack (blue) were measured by TGA and DSC. On the left and right side of the graph, the mass loss and the DSC signal are shown, respectively. The upper two graphs correspond to the mass loss, and the lower two ones to the DSC signal. The mass loss of the A-MLCC is slightly higher and can be quantified to roughly 15% up to 600 °C, the binder burnout temperature. The mass loss for Ω-MLCC is only about 13% up to the same temperature. As explained before, the slurry composition was optimized toward slightly higher solid content while keeping the mechanical properties of the green tapes constant. Thus, the difference in mass loss in Figure 4.10 is acknowledged by the difference in slurry compositions. Both weight percentages for all organic additives are in the same range as the mass loss. The DSC signals feature insights about the amount of heat absorbed or released by a sample as it is heated or cooled under controlled conditions. They can reveal important information about a material's thermal behavior and indicate endothermic and exothermic reactions, such as the melting point of a substance and the stability of a material under different conditions.[235] Different exothermic peaks can be identified according to the mass losses of both green stacks. Allocating each peak to the corresponding organic additive would be out of the scope of this thesis. All the organic constituents start to decompose above 200 °C up to about 400 °C, which is in good agreement with literature values.[229] Interestingly, the peaks for the Ω-MLCC green stack are much less pronounced and tend to be superimposed compared to the other green stack. It could be rationalized by the fact that the decomposition temperatures of the dispersant, plasticizer, and binder are in the same range. Beyond 600 °C, no severe change of mass was recorded. This underlines that the binder burnout conditions of 5 h at 600 °C are chosen appropriately and are enough to decompose organic additives in the new Ω-MLCC green stack completely. Nevertheless, an endothermic reaction starts to appear above 850 °C, much more pronounced for the A-MLCC compared to the Ω-MLCC. Schuetz et al. demonstrated that dissolution of Bi_2PdO_4 and melting of Bi_2O_3 take place at corresponding temperatures.[47] It will later be discussed in Section 4.5. As the overall functionality of the A-MLCC was restricted, the findings in Figure 4.10 align well with the previous results of this section.

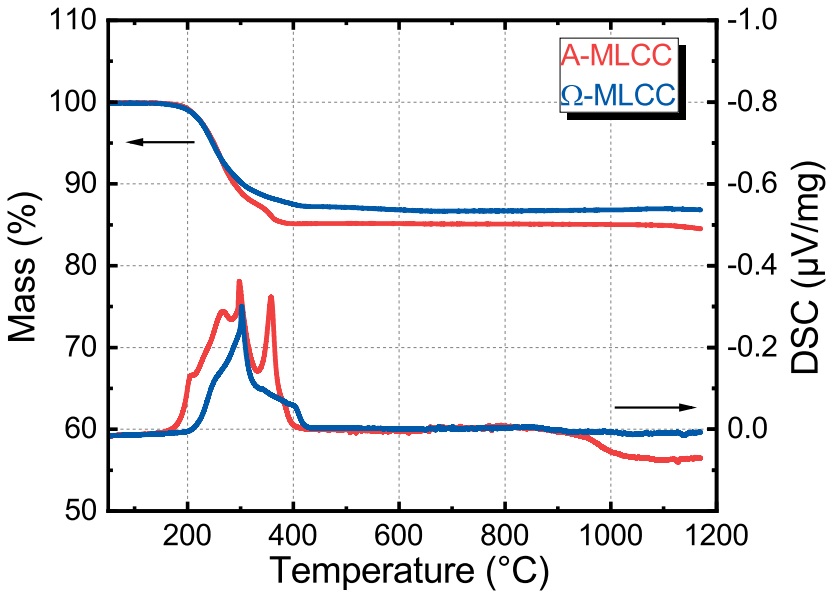

Figure 4.10: Thermal analysis of an A-MLCC Ω-MLCC green stack. The schematic represents the mass loss (left) and the heat flux (right) against the temperature.

4.2.1 Conclusion

The slurry composition was one of the most severe influencing factors regarding a high porosity within the A-MLCCs. It was empirically demonstrated that the ingredients for the A-slurry entailed huge manufacturing implications. The chosen ratio of ingredients and type of ingredients seemed to be responsible for the high porosity issues mentioned in the A-MLCC Section 4.1. An optimization concerning the weight percentages and the type of solvent, dispersant, plasticizer, and binder was conducted. A higher amount of dispersant and a lower amount of plasticizer ensured a higher solid loading for the Ω-slurries. A different solvent was helpful to slow down the evaporation and enhance the sedimentation behavior. The final composition is summarized in Table 4.4. Changed ingredients not only contributed to improved processability of the Ω-slurry but also to an enhanced green density. Lastly, TG-DSC measurements confirmed the complete decomposition of organic additives.
However, there is another influencing factor that impacts the final microstructure and properties of the components. According to the schedule in Figure 4.1, optimized shaping processes can contribute to increased properties and prolonged stability.

4.3 Shaping Processes

The reviewed shaping processes in this section include ball-milling of calcined ceramic powder, tape casting, sheet cutting, screen printing, stacking, lamination, and dicing. Note that ball-milling does not belong to the shaping process of green structures. Since it can be beneficial for shaping green sheets, it will also be investigated in this section. The optimization of shaping processes is based on engineering aspects, but it is equally important for a successful MLCC fabrication.

Milling, in general, contributes to a reduction of average particle size, as reported by Malič et al. in 2018.[236] An average particle size of 1 µm is desirable for advanced ceramics, as noted by Carter and Norton in 2007.[131] The use of polyamide milling containers has been proven successful not only by empirical observations but also by Salmang et al.[237] The calcined ceramic powder for the A-MLCC was only milled once, which yielded a rather multi-modal particle size distribution as seen in Figure 4.11. The red bars and graph correspond to the ceramic powder used for the A-MLCC, while the blue bars and graph correspond to the calcined powder used for the Ω-MLCC. The characteristic parameters of a particle size distribution, including the percentiles d_{10}, d_{50}, and d_{90}, are listed in Table 4.5. These parameters indicate that 10%, 50%, or 90% of all particles are below the corresponding particle size.

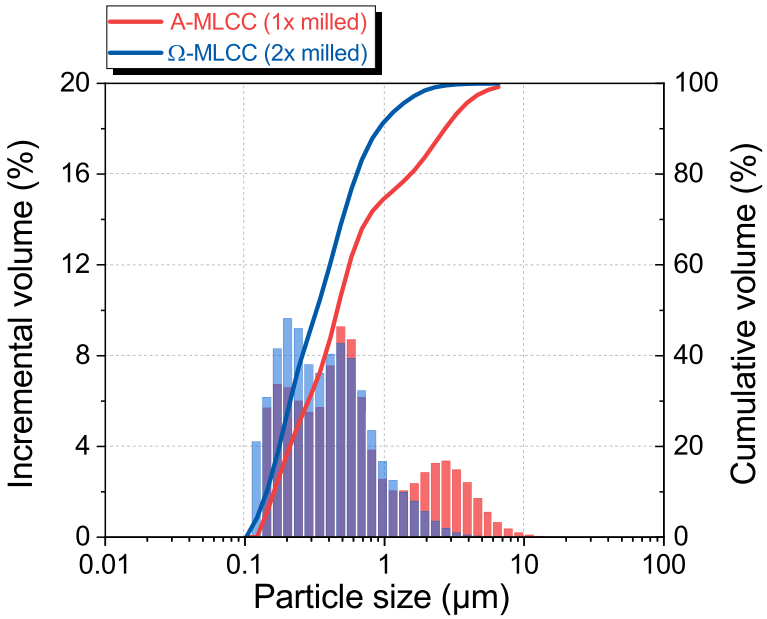

Figure 4.11: Particle size distribution of the powder used for the A-MLCC (red) and Ω-MLCC (blue). The powder for Ω-MLCCs was milled twice. The incremental (bars) and cumulative (lines) volumes are plotted against the particle size.

Table 4.5: Characteristic parameters of the particle size distribution of the ceramic powders used for the A-MLCC and Ω-MLCC. Percentiles are given at 10%, 50%, and 90%.

	Weighted arithmetic mean particle size (µm)	Modal distribution	d_{10}	d_{50}	d_{90}
A-MLCC	1.63	tri-modal	0.16	0.46	2.72
Ω-MLCC	0.76	bi-modal	0.14	0.32	0.92

First, the weighted arithmetic mean particle size, also known as the mean value, of both powders is quite different. Also, the modal distribution of the powder has changed positively. After the first milling, a tri-modal distribution is evident. Two local maxima are in the range between 0.1-1 µm, but a third one is visible between 2-3 µm. Bi- or multi-modal particle size distributions, for example, are not favored as they can exsolve during storage and will result in heterogeneous packing densities of the slurry during drying.[237] Coarse particles will start to densify at higher temperatures compared to small ones. This will lead to a lower final density of the component as the sintering temperature remains the same. Especially large particles can be identified as a vulnerability since they contribute to a higher porosity in the final component.[131] The material of the milling container for the second ball-milling step of the calcined powder for the Ω-MLCC was changed to zirconia. A higher energy input and changed kinetics during milling by the altered material and a prolonged milling time can be assumed. Longer milling times will not only decrease the particle size but probably also narrow the particle size distribution. Ultimately, the second powder exhibits a slightly bi-modal distribution between 0.1-1 µm. A significant reduction in particle sizes could be achieved. This is also reflected in the particle size distributions of both powders and can be identified by the percentiles. Taking the d_{90} percentile into consideration, a value below 1 µm is highly beneficial (S. Drnovšek, personal communication, September 3, 2021). The d_{90} value of the powder for A-MLCC was 2.72 µm, whereas for the Ω-MLCC powder, it is only 0.92 µm. This is a significant decrease and can be quantified by the width of particle size distribution.[64] It can be deduced from the previously mentioned percentiles and is explained in the following equation:

$$\text{Width of particle size distribution} = \frac{d_{90} - d_{10}}{d_{50}} \tag{4.1}$$

Taking the percentiles from Table 4.5 into account, a width of 5.57 for the A-MLCC powder and 2.44 for the Ω-MLCC powder is obtained. This translates to a more than two times lower width of the ceramic powder for the prototype MLCCs. Since the particle size distribution is another crucial parameter to obtaining MLCCs with high final densities, the powder used for Ω-MLCCs will contribute to a better microstructure.[205] Although not quantified, the sintering temperature of the dielectric could likely be reduced. However, the set temperature remained constant at 1100 °C.

The tape casting process for the green prototype MLCCs was performed under much more controlled conditions at a temperature of 25 °C without airflow. Airflow can cause center cracking in the cast slurry due to fast drying.[64] This phenomenon is illustrated in the supplementary information in Figure 8.3.

Slower evaporation of 1-butanol helped to form a more uniform green structure. It can be assumed that the lowered particle size and improved particle size distribution were beneficial for more dense sedimentation of the ceramic particles during drying. Screen printing of the green tapes for A-MLCCs was done manually with a squeegee, and a completely homogeneous distribution of the electrode paste could not be assured. Regarding the prototype MLCCs, the screen printing was done semi-automatically. After positioning the green sheets, the squeegee was driven automatically with fixed parameters to ensure uniform distribution of metal pastes. The sheet cutting process was performed using a laser cutter, and the utilization of fixpoints was found to be extremely helpful in aligning each tape perfectly. Otherwise, stacking mismatch, as seen in Figure 4.4 and Figure 4.5, can occur, which is detrimental to the final properties, particularly the capacitance. Sheet cutting for the A-MLCCs was done by hand with a custom-made cutting tool, which only had a precision of down to a few 100 µm. Before lamination, the green stacks for Ω-MLCCs were put under vacuum to remove entrapped air. The change of plasticizer from PEG to ATBC likely inhibited the superficial accumulation of water on the green sheets. The stacked green sheets were uniaxially pressed at 20 kN for 1 h, and isostatically pressed at 55 °C for 15 min and 20 MPa. The green stack already seemed to be interconnected after uniaxial pressing. It was found that prolonged times would initiate a rearrangement of polymer molecules, which would join with the polymer network from adjacent sheets. It turned out that evacuation of the green stack and subsequent uniaxial and warm-isostatic pressing are of tremendous importance for a microstructure without delamination.[200] All of that contributed to a perfect lamination of electrodes and ceramic layers, as seen later in Figure 4.20. Compared to the procedure for the A-MLCCs, stacking and lamination of the green prototype MLCCs were performed under more advanced conditions and with much higher precision. For example, if gaseous phases or water are entrapped during stacking and pressing, it may lead to bubbling. It will deteriorate the microstructure and the final properties.[200] Eventually, an automated cutting device guaranteed precise green Ω-MLCCs.

4.3.1 Conclusion

In this section, various shaping processes were reviewed, including ball-milling, tape casting, sheet cutting, screen printing, stacking, lamination, and dicing. The additional milling step of the calcined powder for the Ω-slurry was particularly critical as it reduced the average particle size and narrowed the particle size distribution. A d_{90} value of 0.92 µm was achieved, and the width of particle size distribution was two times lower than for the powder for the A-slurry. A better sedimentation behavior was concluded, which may be a hint towards enhanced densities of the prototype MLCCs. The tape casting process must also be performed in a drying chamber without air flow and at a constant substrate temperature of 25 °C to prevent flaws. Thus, center cracking could be inhibited, and slower evaporation of 1-butanol aided in shaping a more uniform green structure. Sophisticated equipment is crucial as every step of the shaping processes could be performed with higher precision and better reproducibility. Only by an advanced laser cutting system stacking mismatch, as observed in the A-MLCCs, could be prevented.
Besides the slurry preparation and shaping processes, the subsequent thermal treatment of the green

MLCCs is another influencing factor during the MLCC fabrication. The ceramic will be co-fired with Ag/Pd electrodes, which could result in interactions between both materials if not adjusted properly. Likewise, inappropriate sintering conditions deteriorate the dielectric properties of the ceramic.

4.4 Sintering Conditions

A sintering optimization scheme can be helpful to facilitate a more dense microstructure. Higher temperatures or longer times will increase the rate of densification, while heating rates and particle sizes will affect the rate of densification.[208,238] This has to be exercised cautiously as temperatures of 1100 °C are already close to the limit of 70/30 Ag/Pd electrodes, and (partial) melting could be initiated.[47,48] To investigate also harsher sintering conditions of the ceramic, the screen printing step during the fabrication will be neglected. Instead of MLCCs with inner electrodes, only samples without inner electrodes will be manufactured. These samples are referred to as laminates, and the approach is represented in Figure 4.12. The rest of the manufacturing follows the same route. Five green sheets will be stacked to a laminate. The samples can be considered as bulk samples; they are simply made by the MLCC fabrication route. The effect and interactions of co-firing Ag/Pd electrodes with NBT-based ceramics will be covered in the next Section 4.5. The thermal treatment to optimize the sintering conditions and its evaluation was done with the help of Giorgio De Checchi who was an Advanced Research Lab (ARL) student within the scope of this doctoral thesis.

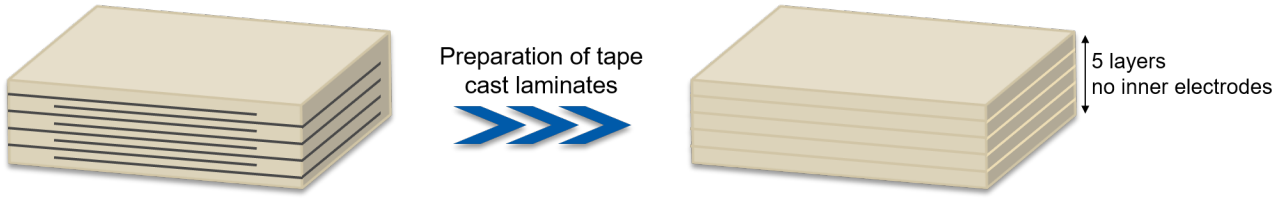

Figure 4.12: Laminate approach to exclude the influencing factor of co-firing electrodes during sintering. Laminates will be prepared the same way as MLCCs, only without screen printing of inner electrodes.

Figure 4.13 details SEM micrographs of laminates sintered under various sintering conditions. All micrographs were taken at 1000x magnification to compare pore sizes and distribution. The sample in Figure 4.13(a) was sintered at 1100 °C and 120 min. This condition is used for the reference bulk samples and seems to be a proper condition for the solid-state fabrication route of bulk samples.[29] The samples in Figure 4.13(b) and 4.13(c) were sintered at 1130 °C and 80 min or 120 min, respectively. For the last sample, a two-step sintering approach was chosen, which is meant to be very beneficial for smaller grain sizes but higher densities.[239,240] Porosities and densities of the laminates were analyzed and are confronted in Table 4.6. Relative densities were either determined by the Archimedes' principle or via the same algorithm used in Subsection 4.1.2, which can be applied to SEM micrographs. Hence, mean porosities, densities, and errors could be calculated. The laminate sintered under 1100 °C for 120 min in Figure 4.13(a) exhibits a porous structure. Some pores seem to be interconnected as they are comparably large in comparison to other pores. The shape of pores is quite unique, and its angular shape may indeed be the reason for insufficient sintering time.[222] With increasing energy input, the microstructure in Figure 4.13(b) improved, i.e., porosity is lower compared to the previous sintering condition. The pores still

tend to be interconnected with rather angular shapes. Figure 4.13(c) comprises a decent microstructure of the corresponding laminate, which was attained by a sintering temperature of 1130 °C and 120 min sintering time. A lower porosity and higher densification can be spotted compared to previous sintering conditions. Eventually, the two-step sintering condition in Figure 4.13(d) yields a similar porosity in contrast to the laminates sintered at 1130 °C and 80 or 20 min, respectively. A single large pore can be identified. This is considered a stark hint towards trapped gaseous phases from residues during binder burnout. When taking Table 4.6 and Figure 4.14 into account, a clear trend can be concluded. Higher sintering temperatures and sintering times significantly contribute to the densification and coarsening of grains.

The sample sintered with the lowest energy input resulted in a density of about 87%, while a sintering condition of 1130 °C and 180 min already resulted in a density of about 94%. The average density peaks at 120 min at 1130 °C and amounts to 96%. The two-step sintering process is not as successful as the previous sintering condition, with an average density of about 94%. It can be deduced that increasing sintering times and temperatures will enhance the final densities of the laminates. Interestingly, all determined values have a similar error in the range of 2-3%. The increase in grain size was not considered here. By longer and harsher sintering conditions, material diffusion will be accelerated and prolonged. This is why the shape of pores appears to be different for laminates sintered at higher temperatures and longer times. Still, a balance between temperature and time has to be found to avoid coarsening of the grains.

Corresponding dielectric properties of the laminates are displayed in the supplementary material in Figure 8.2. Essentially, the maximum permittivity increases with increasing relative density, but no correlation between relative density and dielectric loss is present. For all sintering conditions, the dielectric loss at 1 kHz is above 2% below 300 °C.

Table 4.6: Comparison of determined final densities of samples being sintered at different sintering conditions.

Sintering condition	Mean porosity (%)	Mean density (%)	Max. error (%)
1100 °C and 120 min	13.3	86.7	2.2
1130 °C and 80 min	6.4	93.6	2.6
1130 °C and 120 min	4.0	96.1	2.1
1200 °C and 10 min + 1050 °C and 60 min	6.2	93.8	3.4

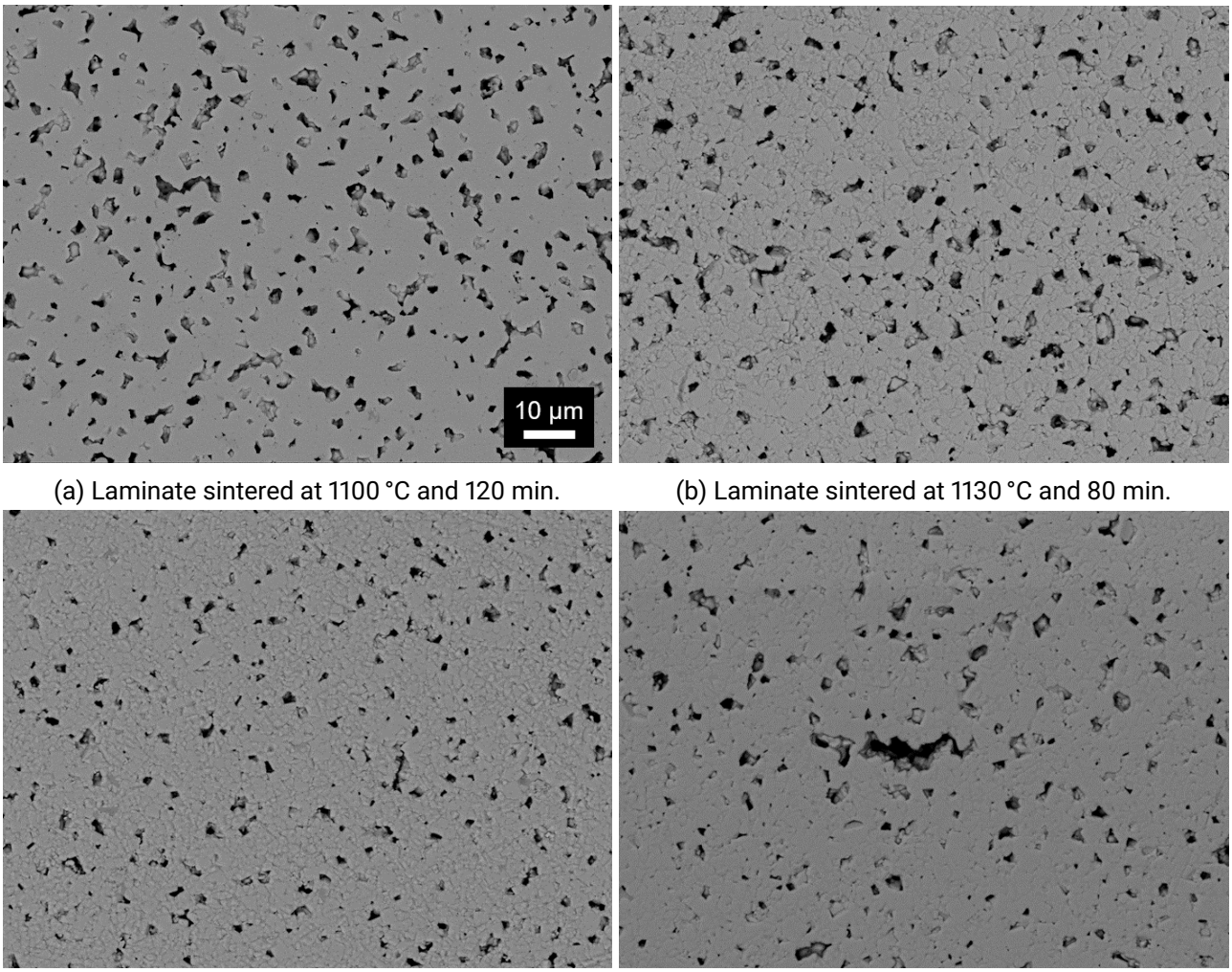

(a) Laminate sintered at 1100 °C and 120 min.

(b) Laminate sintered at 1130 °C and 80 min.

(c) Laminate sintered at 1130 °C and 120 min.

(d) Laminate sintered as a two-step sintering process first at 1200 °C and 10 min and second at 1050 °C and 60 min.

Figure 4.13: SEM micrographs of laminates sintered under different sintering conditions. All micrographs were taken at 1000x magnification.

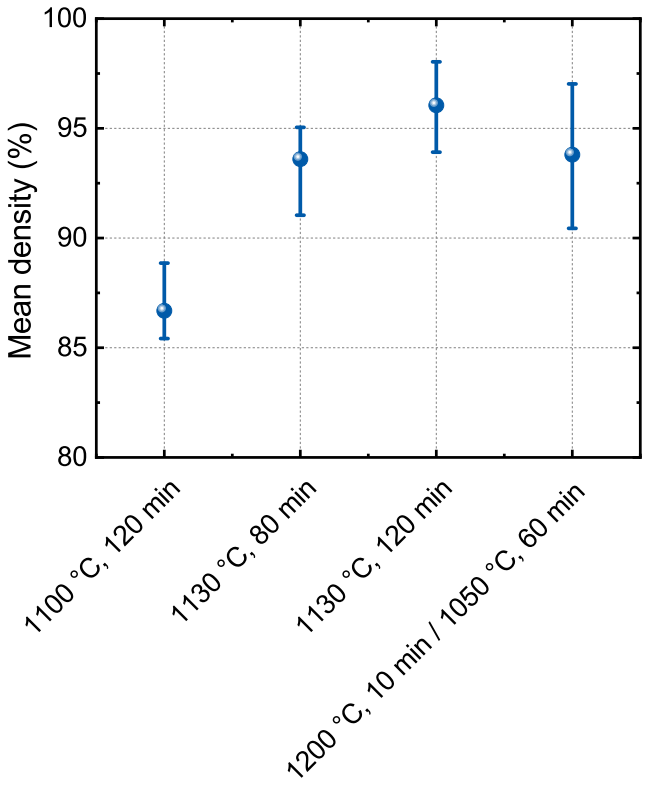

Figure 4.14: Average density of laminates sintered at different sintering conditions, including error bars.

In theory, the green sheets contain a distinct amount of organic additives. Since plasticizer and binder are needed in a decent amount, they severely contribute to the volume of the dried green sheet. In the A-slurry, they have a share of more than 46% of the volume (Table 4.1). The organic additives are represented in Figure 4.15 as red curved lines. During slurry preparation, an ideal dispersion of the ingredients is targeted. The dispersion is dependent on the mixing procedure, the components, and the interactions between them.[64,65] Local agglomeration may still be observed if an inappropriate slurry composition was chosen. After the binder burnout, all organic additives are meant to be removed from the now extremely fragile and porous green stack. Considering nearly half of the dried volume consists of organic additives, big voids may remain. During binder burnout, the additives are likely to undergo several phase transitions. As it was seen in Figure 4.10, the decomposition is initiated between 250-400 °C. According to Fu and Roosen, organic additives will start to melt at 250 °C.[216] The principle of shrinkage during binder burnout is due to capillary forces, which can be high at these temperatures. Pores in the green stack may be filled by molten organics. It pulls the ceramic particles together, resulting in a slightly denser structure. As the organic additives start to decompose, a phase transformation from liquid to gas can be expected.[216] This will slightly blow up the green stack and reduces the shrinkage. Further densification is not expected as no mass transport mechanisms are supposed to be activated at temperatures of 600 °C.[209] The residual voids from organic additives still reduce the potential area of ceramic particle-particle interfaces, which are necessary to form necks. In this hypothesis, it is proposed that a lower amount of these interfaces

will diminish the mass transport and densifying diffusion mechanisms during the actual sintering step. As a result, the sintered laminates will keep a high porosity, as highlighted in Figure 4.15. Based on this hypothesis, lower porosities of the Ω-MLCCs can be expected. Dried tapes of Ω-slurry only contained about 42 vol% of binder and plasticizer.

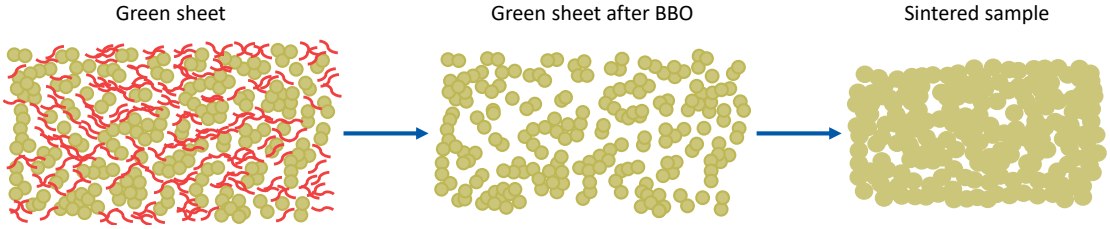

Figure 4.15: Hypothesis for relatively low green sheet density of NBT-based laminates and A-MLCCs. Organic additives are schematically depicted in red. After binder burnout, a brittle and porous ceramic structure remains, which cannot densify as anticipated.

4.4.1 Conclusion

In this section, a possible optimization of sintering conditions was contemplated. A new approach with laminates was established. Instead of MLCCs with inner electrodes, laminates without inner electrodes were prepared. By excluding possible migration, formation of secondary phases, or melting of the electrode material, the focus could be put on the sintering of the ceramic dielectric. A higher energy input in terms of longer sintering times and higher sintering temperatures facilitated reaching sufficiently high final densities of laminates. The laminate sintered at 1130 °C for 120 min exhibited a mean density of 96%. Despite this, the laminates still do not exhibit dielectric properties, which are in the same range as the bulk reference sample. This holds true for the dielectric loss in particular. For all sintering conditions, the dielectric loss at 1 kHz was above 2% below 300 °C. Ultimately, the optimization scheme of sintering conditions was not viable for the laminates prepared by the A-slurry. A hypothesis for the remaining high porosity was constructed, as shown in Figure 4.15. A possible cause for the porosity could be identified. It is assumed that the share of organic additives (almost 50%) in the dried tape is inappropriate and may result in a preferably high amount of voids after the binder burnout. However, the Ω-slurry would presumably yield higher densities of the corresponding MLCCs.
According to Figure 4.1, the electrode material and sintering aids will be investigated as the last influencing factor on the fabrication of prototype MLCCs.

4.5 Electrode Material and Sintering Aids

As mentioned earlier in Chapter 1, another exciting part of the prototyping is the co-firing process of the NBT ceramic and Ag/Pd electrodes. The co-firing process can be quite challenging since melting or oxidizing the electrode material must be inhibited. Migration of electrode material also has to be suppressed; otherwise, this could have a tremendous effect on the defect chemistry. In turn, the final properties and the reliability of prepared MLCCs may be deteriorated. This will be covered in the following.

EDX measurements were conducted on the cross-sections of an MLCC sample sintered at 1130 °C for 120 min, as shown in Figure 4.16. This sintering condition was found to be most appropriate for achieving high densities of laminates, as demonstrated in previous Section 4.4.

4.5.1 EDX Investigations

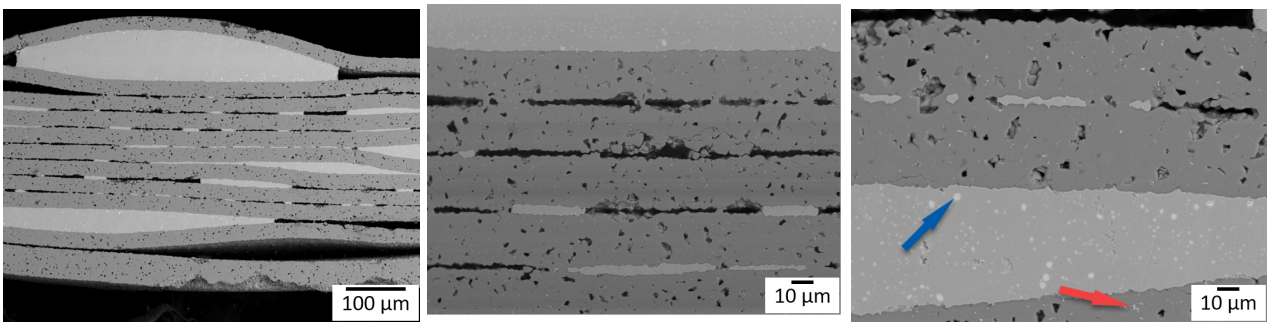

(a) Molten Ag/Pd contracted and agglomerated on different spots, leaving back voids.

(b) Heavy interactions with the matrix material can be spotted within the agglomerated Ag/Pd electrode.

(c) Close-up of voids where molten Ag/Pd retracted. The blue and red arrows correspond to the EDX spectra in Figure 4.17(a) and Figure 4.17(b), respectively.

Figure 4.16: SEM micrographs reveal heavy interactions between the matrix and electrode material. The MLCC was sintered at 1130 °C, and the dielectric layer thickness was around 21 µm.

According to the phase diagram by Karakaya and Thompson in Figure 2.23, 70/30 Ag/Pd electrode paste could bear temperatures of up to 1170 °C before melting. However, the inner electrodes appear to be melted completely. Taking into account a possible wrong calibration of the sintering furnace and slight temperature deviations, this is a remarkable finding. The molten Ag/Pd left behind empty voids of the former inner electrode structure. The voids in Figure 4.16(b), are actually not empty but probably filled with an atmosphere consisting of different ingredients of inner electrode, dielectric material, and surrounding air. Diffusion might be promoted by thin dielectric layers, which had a thickness of roughly 21 µm. This melting has to be correlated with interactions between the ceramic and inner electrode material. At interfaces in Figure 4.16(c), brighter spots inside the electrode material can be seen. Also brighter spots close to the interface within the dielectric are visible. This is a stark indication of very

heavy reactions. It needs to be figured out what was formed during the sintering step. Figure 4.17(a) shows a spectrum of bright white spot within the inner electrode from Figure 4.16.

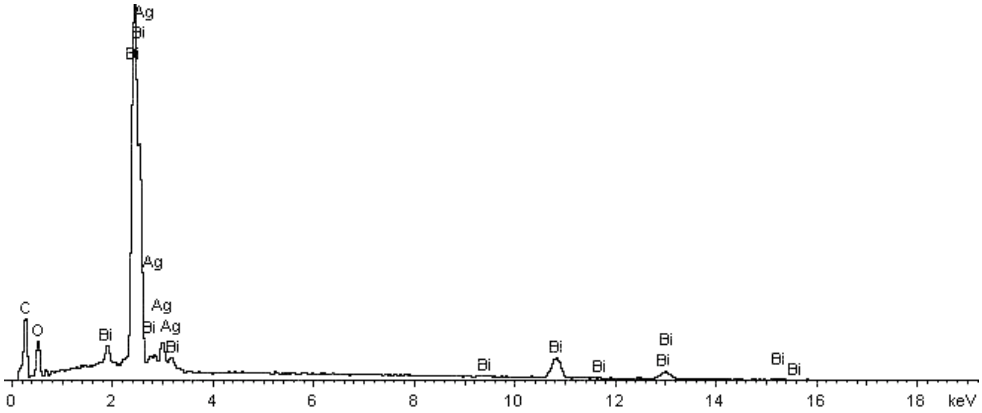

(a) EDX spectrum of a bright white spot (blue arrow) within the inner electrode in Figure 4.16(c). Marked elements are C, O, Bi, and Ag. Energies were recorded up to 20 keV.

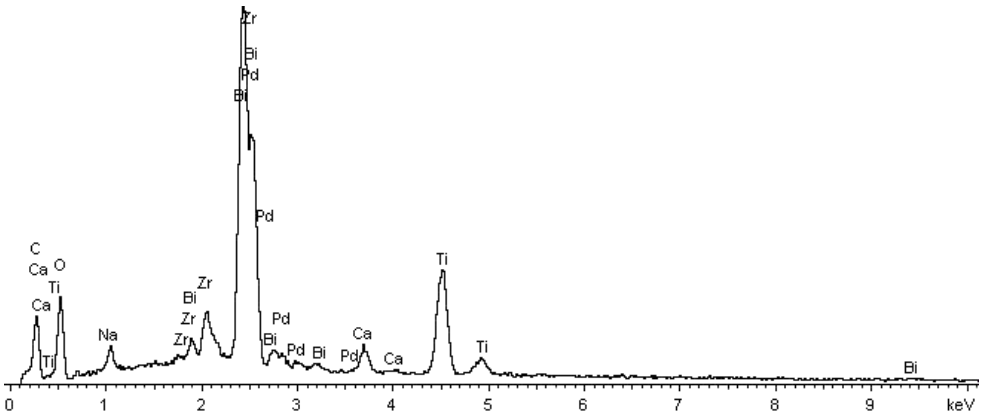

(b) EDX spectrum of a bright white spot (red arrow) within the matrix material and close to the inner electrode in Figure 4.16(c). Marked elements are C, O, Ca, Ti, Na, Zr, Bi, and Pd. Energies were recorded up to 10 keV.

Figure 4.17: EDX spectra of spots of heavy reactions between matrix NBT and electrode material.

It reveals a clustering of Bi and Ag elements. An Ag_xBi_y alloy could have formed due to lower melting temperatures of Bi. Bismuth will drastically lower the melting temperature of this alloy.[241] As there is also a small oxygen peak detected, gaseous or liquid Bi_2O_3 may have migrated toward the inner electrodes and formed the Ag_xBi_y alloy. Carbon is only monitored due to the sputtering process, which makes the surface conductive and does not mask the characteristic energies of other species. Figure 4.17(b) is within the dielectric but close to the metal-electrode interface. Evidence of Pd can be provided here in the matrix. The matrix is detected by the numerous amount of different peaks corresponding to the NBT-BT-CZ-BA dielectric material. It is quite interesting that Pd was found outside the actual inner electrode. A reason for this could be the delamination seen in A-MLCCs. The MLCCs were sintered in air, which is present in the voids/pores resulting from the delamination. It was stated that whenever the

evaporation of Ag was possible, segregation of Ag/Pd occurred.[47] On the one side, by the dissolution of Ag/Pd, silver can be incorporated in bismuth-based materials to at least 1%. Although not detected, Ag could be present in the dielectric. It may be masked by more pronounced peaks. Assuming that Ag will occupy the bismuth vacancies (Equation 4.2), which are present due to the evaporation of Bi_2O_3 during sintering, as illustrated in Equation 2.18, a further increase of oxygen vacancies can be expected. Additional oxygen vacancies will have a detrimental influence on the dielectric properties, particularly under high-temperature conditions.[41,45,130,242] Likewise, the incorporated Ag can act as acceptor doping, impairing the stability of the capacitor during operation.[55,56] Steiner et al. have proven that the conductivity increased by orders of magnitude at only small acceptor dopant concentrations of 1 mol% in NBT.[44] This could lead to leakage currents and accelerated electrical fatigue. Another possibility is the formation of a defect dipole $(Ag''_{Bi} - V_O^{\bullet\bullet})^x$ between an oxygen vacancy and the acceptor. While temporarily trapped at sufficiently high dopant concentrations and low temperatures, oxygen vacancies could almost migrate freely through the ceramic at high temperatures.[46] This can further impair dielectric loss at high operating conditions. However, solid solutions of NBT seem to be much more resistant. The conductivity of NBT-6BT doped with 1 mol% Fe still showed low dominating electronic conductivity.[44] Because the dielectric ceramic for the MLCCs is also based on a solid solution of NBT-6BT and further developed by CZ and BA to immobilize the oxygen vacancies, it can be deduced that the effect of possible acceptor doping by Ag and the formation of additional oxygen vacancies is diminished. The consequences of simultaneously applying high voltages and temperatures are unknown yet, but this could further limit the application of NBT-based MLCCs with Ag/Pd inner electrodes. It will be elucidated in Section 4.7.

$$Ag_2O \rightarrow 2Ag''_{Bi} + 2V_O^{\bullet\bullet} + O_O^x \tag{4.2}$$

$$Ag_xPd_y(s) + \frac{1}{2}O_2 \rightarrow Ag(s) + PdO(s) \qquad (300-835\,^\circ\mathrm{C}) \tag{4.3}$$

$$PdO(s) + Bi_2O_3(s) \rightarrow Bi_2PdO_4(s) \qquad (350-835\,^\circ\mathrm{C}) \tag{4.4}$$

$$Bi_2PdO_4(s) \rightarrow Pd_xBi_y(s) + Bi_2O_3(l+g) + \frac{1}{2}O_2 \qquad (>835\,^\circ\mathrm{C}) \tag{4.5}$$

On the other side, by the dissolution of Ag/Pd, bismuth palladate (Bi_2PdO_4) could have formed.[47] Interestingly, similar reactions could be seen in lead-based and Bi-based systems.[243,244] Pd was oxidized within a temperature range between 300-835 °C, as seen in Equation 4.3. In a range between 350-835 °C, palladium oxide reacted with bismuth oxide to Bi_2PdO_4 regarding Equation 4.4. They also found that bismuth palladate dissolves again beyond 835 °C into a palladium bismuth alloy, Bi_2O_3, and oxygen (Equation 4.5). It could have been detected by EDX measurements, which is incorporated into the matrix as a secondary phase. This could either point toward bismuth palladate itself or the remaining Pd_xBi_y alloy. Additional formation of gaseous Bi_2O_3 could further increase the concentration of $V_O^{\bullet\bullet}$, according to Equation 2.18. It is very important to note that upon cooling, the sintered samples again will reach the temperature regime where the formation of Bi_2PdO_4 is promoted. Therefore, it may be present again,

although it was dissolved at sintering temperatures of 1100 °C.
Ultimately, suppressing the aforementioned reactions with the NBT matrix and the migration of electrode material is essential.

4.5.2 Utilization of Sintering Aids

One approach to suppress the reactions between NBT and electrode material seen in Figure 4.16 is the utilization of sintering aids. A good selection of sintering aids can effectively lower sintering temperatures while final properties remain identical to samples prepared without sintering aids. However, sintering aids can act as dopants as they may diffuse into the lattice during sintering and occupy different sites depending on their charge.[68] This is another way how the defect chemistry of the NBT matrix can be manipulated, as it was already outlined in Subsection 2.2.4.1. It is important to know the ionic radii of possible cations that can be occupied. According to their relative charge, aliovalent ions will be regarded as acceptors or donors.
CuO was chosen because evidence was provided that it drastically lowers the sintering temperatures of NBT-based ceramics and corresponding MLCCs.[49,50,68] Despite potentially acting as an acceptor dopant, the ultimate goal is a low-cost MLCC, which is only feasible with BMEs. If migration of electrode material is supposed to occur, the Cu will likely substitute the Ti atom on a B-site of the NBT host lattice, see Equation 2.19. Additional oxygen vacancies are induced, which can deteriorate the high-temperature dielectric properties. The mobility of oxygen vacancies will be increased at high temperatures and limit low dielectric loss to lower temperatures.[46]
Another promising contender as a sintering additive is Li_2CO_3.[51,69,245,246] In contrast to CuO, lithium carbonate will first decompose to Li_2O at around 600 °C and subsequently substitute a Na atom on the A-site as schematized in the following equation:

$$Li_2CO_3 \xrightarrow{600\,^{\circ}C} Li_2O \rightarrow 2Li_{Na}^{x} + O_O^{x} \tag{4.6}$$

No additional oxygen vacancies are induced to comply with charge neutrality. Adding Li to the system is considered as isovalent doping. It is assumed that the high-temperature dielectric properties of the final sample are not altered when adding Li_2CO_3.
For the investigations undertaken in this section, only bulk samples prepared by the solid-state processing route were analyzed. Figure 4.18a) details different amounts of sintering aids (Li_2CO_3 in red and CuO in blue) in mol% added to the calcined powder. Relative densities of samples sintered at 1100 °C with no sintering aids, 0.25 and 0.5 mol% CuO, as well as 0.5 and 1 mol% Li_2CO_3 are displayed. Compared to adding no sintering aids, a clear upward trend of relative density can be identified with the addition of sintering aids. Relative densities of 98-99% were achieved, while for CuO, relative densities are the highest. However, the results were obtained at the reference sintering temperature. In Figure 4.18b), the relative densities of all sintering aids are plotted against the sintering temperature. With lower sintering temperatures, the final density tends to be lower as well. For sintering temperatures of 1030 °C, the achieved microstructures of the samples cannot be regarded as dense. The relative densities are always

below 95%. Nevertheless, at 1050 °C, all samples exhibit densities above 95%. Again, the copper oxide sintering aid will promote higher densities than lithium carbonate. The dielectric properties of samples sintered at 1050 °C are presented in Figure 4.19. The relative permittivity of both samples does not change a lot compared to the bulk reference sample (black, no aids), which was sintered at 1100 °C. This is not the case for the dielectric loss. As can be seen, the CuO sample has a low dielectric loss below 2%, only up to temperatures of about 315 °C. As outlined before, this is reasonable and follows the theory. Additional oxygen vacancies will get mobile at elevated temperatures and enhance the dielectric loss. For the case of Li_2CO_3, no change in dielectric properties compared to the reference sample can be detected. This is in very good agreement with defect chemical considerations before. Isovalent doping will not change the defect chemistry of the NBT matrix. Hence, dielectric properties are supposed to remain unchanged. This is only valid if the amount of doping is lower than the solubility limit of the sintering aids. Keeping the sintering temperature at 1100 °C and adding Li_2CO_3 would increase the final density of the MLCCs without affecting the dielectric properties.

Although it is out of the scope of this thesis, the ultimate goal would be the utilization of BMEs instead of Ag/Pd or Pt. This would lower the production costs for an MLCC dramatically. Considering today's prices for 70/30 Ag/Pd in Figure 1.2, the prices for the electrode material copper would be lowered by a staggering factor of about 1,500. Except for the costs for the electrode material, other costs would roughly remain the same. Sintering in reducing atmosphere is likely to be more expensive compared to conventional sintering in air.[247] Obviously, there is a huge driving force to utilize base metal electrodes. This would imply the use of sintering aids or a combination of several sintering aids. Yesner et al. demonstrated that the sintering temperature of NBT-based ceramics could be lowered to 900 °C, enabling the co-firing with copper inner electrodes.[52] However, the oxygen partial pressure must be balanced to prevent oxidization of the electrodes and reduction of the NBT ceramic. This seems to be one of the most intricate challenges. Further, the electrical properties are supposed to be affected when adding sintering aids due to incorporation into the matrix as dopants or the formation of secondary phases.[49,51,68]

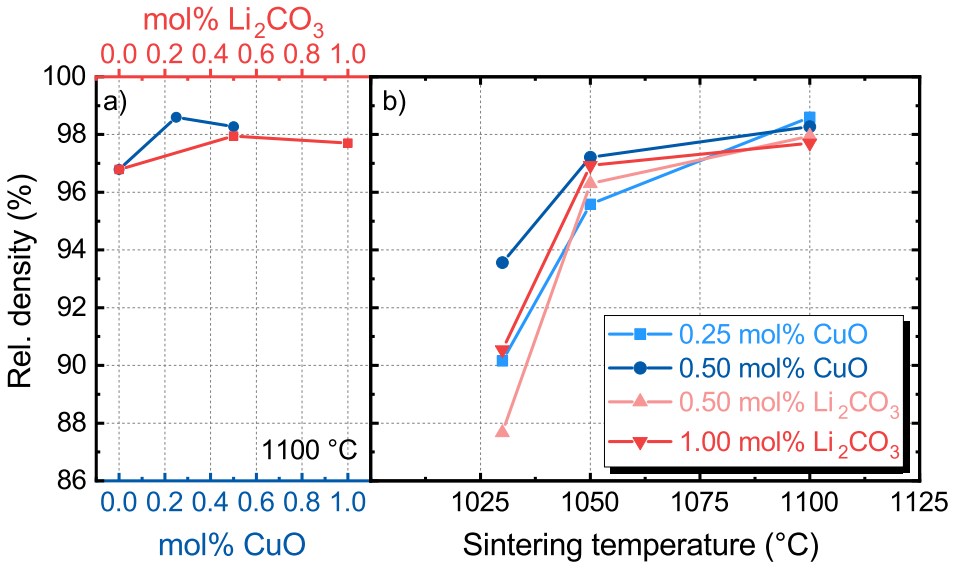

Figure 4.18: Relative densities of CuO and Li_2O_3 sintering aids plotted against their a) mol% and b) sintering temperature.

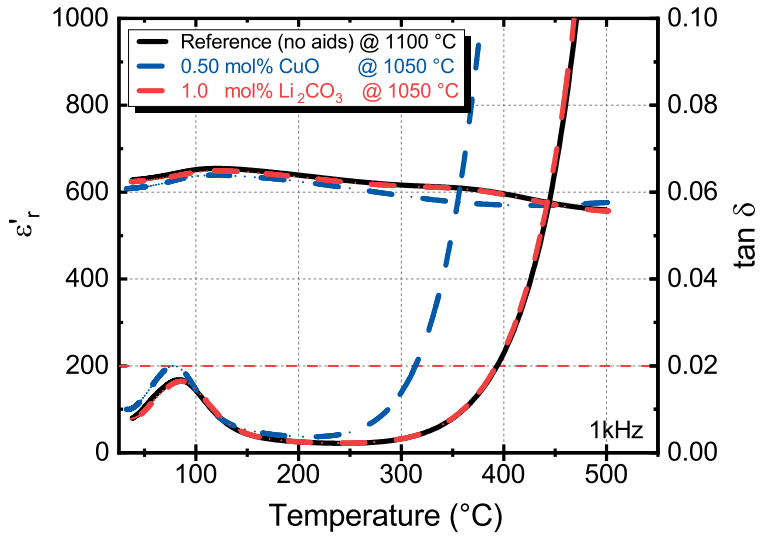

Figure 4.19: Dielectric properties (ε_r and $\tan\delta$) of bulk samples with sintering aids plotted against temperature at 1 kHz. Both samples with sintering aids were sintered at 1050 °C and the reference sample with no aids at 1100 °C.

4.5.3 Conclusion

It was shown that severe reactions between the inner electrode and the ceramic can occur. Sintering temperatures of 1130 °C, close to the melting temperature of 70/30 Ag/Pd electrodes, are critical. Dissolution and segregation of the metal electrodes were evidenced by SEM micrographs and corresponding EDX measurements. Likewise, secondary phases around the electrode-dielectric interface were found. Due to

the complex defect chemistry of NBT-based materials, the migration of Ag likely causes the formation of $(Ag_{Bi}^{''} - V_O^{\bullet\bullet})^x$ defect dipoles as well as further increase the $\left[V_O^{\bullet\bullet}\right]$ concentration. This would limit the high-temperature operational window of the capacitors. 0.5 mol% Li_2CO_3 lowered the sintering temperature by 50 °C down to 1050 °C. Thereby, dielectric properties were not affected. Choosing sintering aids that act as isovalent doping is an elegant way to maintain the dielectric properties but lower the firing temperature. However, the approach of adding sintering aids to the MLCC's dielectric is out of the scope of this thesis. The findings, nevertheless, could pave the way for the utilization of copper inner electrodes for future experiments to manufacture low-cost lead-free prototype MLCCs. It is concluded that suppressing the migration of electrode material and reactions between dielectric and electrodes is key for a reliable operation of the capacitors. This can be achieved by keeping the sintering temperature of the Ω-MLCCs at 1100 °C, even without sintering aids.

4.6 Characterization of Prototype MLCCs

In this section, findings from previous sections are digested and evaluated to prepare and characterize Ω-MLCCs. This section also provides the main findings of this work. Detailed measurements of dielectric and energy storage properties follow the microstructural characterization. Impedance spectroscopy and an insight into application-related ESR and ESL data complete this section.

4.6.1 Microstructural Characterization

Figure 4.20 presents cross-sectional micrographs of the MLCC obtained by SEM. At 250x magnification in Figure 4.20(a), the MLCC shows extremely homogeneous dielectric layers and inner electrodes. The dielectric layer thickness is approximately 47 µm, while the electrodes have an average thickness of about 3.5 µm. Notably, the second electrode from the top appears to be thicker compared to the others, which could be rationalized by different pressures of the squeegee and locally changed conditions on the green sheets during the manufacturing process. The machine was operated semi-automatically, and no apparent difference in applying the electrode paste could be detected during this process. A single inner electrode roughly has a dimension of 4.08×4.08 mm after sintering. The dielectric material features a dense microstructure with a porosity of about 3%. Compared to the A-MLCCs (Figure 4.2 and Figure 4.3) with final densities of about 93-95%, the microstructural appearance of the prototype MLCCs looks substantially improved. The average grain size of the dielectric material is 2.9 ± 0.3 µm. The optimized sedimentation behavior due to different equipment could be one of the reasons for less porosity. Both dielectric layers and silver-palladium inner electrodes exhibit excellent flatness and continuity with homogeneous thicknesses. It seems that the findings throughout the sections about the slurry composition and shaping processes facilitated a homogeneous microstructure with low density. For example, the lowered particle size distribution, with a d_{90} of 0.92 µm, and the changed slurry composition could have reduced the grain sizes of the final dielectric. Combined with the revised slurry composition and better dispersion of ceramic particles, a smaller and narrower but still slightly bi-modal particle size distribution is one of the critical factors for obtaining higher final densities.[240,248] Bi-modal and narrow distributions depress the enlargement of original pores but support uniform densification. The second milling step helped to decrease the particle size and increase the total surface energy of the calcined powder, intensifying the driving force for densification.[65,67]

At 500x magnification in Figure 4.20(b), pores and their structure are emphasized. Angular pores cannot be detected, suggesting that the chosen sintering temperature of 1100 °C is appropriate, as outlined in Section 4.4. Disproportional big pores are also not visible. This can be rationalized by an improved dispersion of the ingredients in the slurry. Agglomerations of organic additives likely were avoided.

At first glance, the microstructure points towards a suppression of interactions between the dielectric and inner electrodes. It was stated that whenever the evaporation of Ag was possible, segregation of Ag/Pd occurred.[47] This was also claimed before to be one of the reasons for severe interactions between the dielectric and the electrode material of A-MLCCs. The perfect lamination inhibited air to be present

close to the electrode material and may reduced the segregation of Ag. However, EDX investigations are necessary to prove that substantial migration or diffusion of electrode material into the ceramic could be prevented.

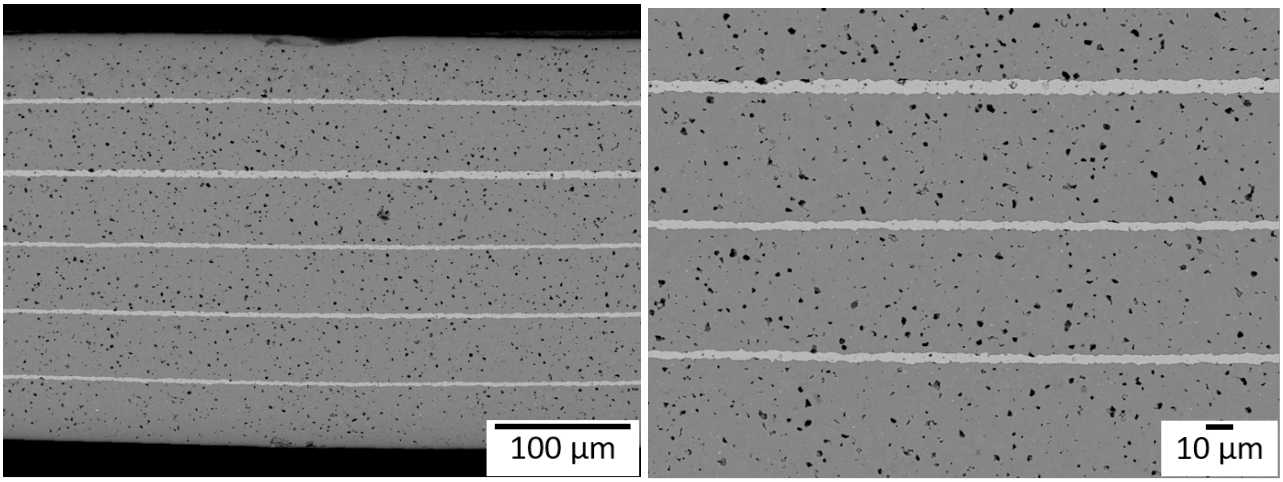

(a) 250x magnification (b) 500x magnification

Figure 4.20: SEM micrographs of the prototype MLCC at different magnifications.

4.6.1.1 EDX Investigations

In Equations 4.3-4.5 it was demonstrated that bismuth-based materials may react with silver-palladium alloys. Even more, secondary phases can form at the interfaces between the dielectric and inner electrodes.[47] Thorough element-specific EDX analyses were conducted to detect any interaction, which is displayed in Figure 4.21. Every single element within the layered structure was analyzed, i.e. Na, Bi, Ti, Ba, Ca, Ag, Pd, Zr, Al, and O. The mappings depict no migration or dissolution of Ag or Pd into the bulk material after sintering. Since the content of Al is, in general, extremely low, the detected counts are also very weak. Note that migration cannot be excluded entirely; the concentrations of Ag and Pd may be below the limit of detection of the corresponding EDX device.

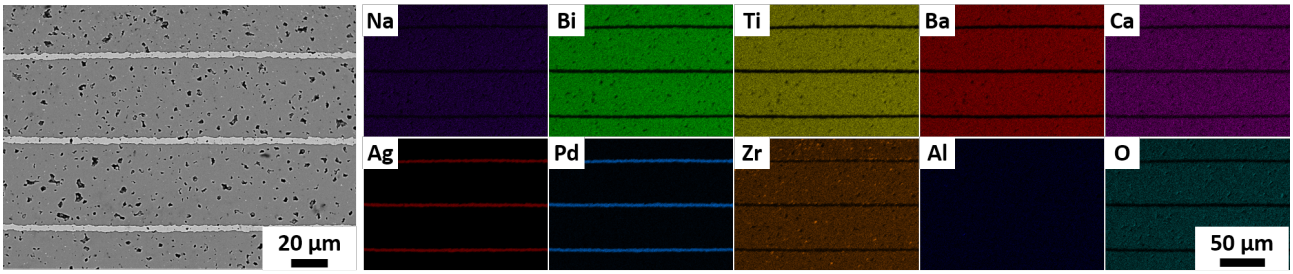

Figure 4.21: Cross-sectional SEM micrograph at which the corresponding EDX mapping was recorded. EDX images of the equivalent spot provide the distribution of all elements (Na, Bi, Ti, Ba, Ca, Ag, Pd, Zr, Al, O) comprised in the dielectric and inner electrode.

Besides an EDX mapping, local line scans were performed on the cross-section of the MLCCs. The line scan in Figure 4.22(a) confirms that only a negligible amount of inner electrode material migrated. Here, the atomic ratio is contrasted to an arbitrary position of the line scan, which coincides with the x-axis of the plot. Palladium in black and silver in blue were only detected at the corresponding site of the inner electrodes. The detected counts for Ag sum up to a ratio slightly higher than 22%, while for Pd, the atomic ratio is about 10%.
Another EDX line scan was performed in a higher magnified region where only a single inner electrode was imaged. The detected atomic ratio of the corresponding electrode site is also slightly off of the nominal 70/30 Ag/Pd composition. However, this is within the measurement errors of a common EDX. The Ag atomic ratio amounts to roughly 68%, and the Pd ratio to about 32%. Despite slight deviations of the nominal composition, no secondary phases at the interfaces were found.

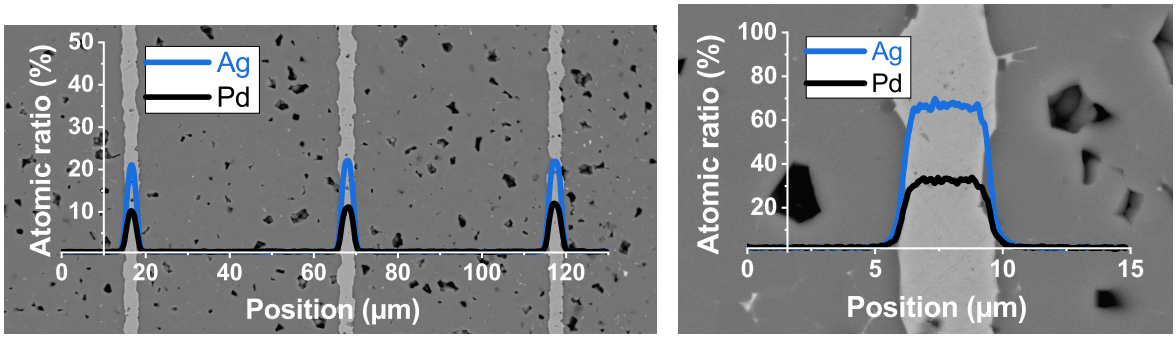

(a) EDX line scan with three electrodes.

(b) EDX line scan with one electrode.

Figure 4.22: EDX line scans at arbitrary cross-sectional positions of the prototype MLCC.

On top of the EDX mapping and line scans, spots near the interface between the inner electrode and ceramic were investigated. Each site of the EDX spots is visualized in Figure 4.23. The corresponding element distribution is contrasted in Table 4.7. Again, every element consisting of the dielectric and inner electrode was monitored.
In spectrum 1, no material of the NBT matrix could be detected. Since the spot was roughly 1 µm off the interface, no contamination was expected. The nominal ratio is slightly off, which is, however, negligible. Spectrum 2 was taken at an adjacent ceramic grain to the interface. This grain should, in principle, have the same composition as the bulk NBT-BT-CZ-1BA material. Indeed, the atomic weight percentages detected confirm that only bulk is present without Ag or Pd.
The site of spectrum 3 points to a bright spot between two bulk grains. In comparison to the nominal stoichiometry, a relatively high amount of bismuth was monitored. Bismuth oxide already starts to melt at around 824 °C.[249] Due to this low melting point, a tiny liquid phase of excess bismuth may partially coat individual grains and concentrate at triple points.[131] This results in a bismuth-rich phase, shown here with an atomic% of bismuth of about 15%. The same phenomena can be identified in the work of Hoang et al. and Steiner and do not impair the properties of the MLCC components compared to the bulk reference samples.[29,121]

Lastly, spectrum 4 represents a darker spot inside the bulk regime of the ceramic. It is located between several bulk grains, likely with the same stoichiometry as in spectrum 2. The darker spot, however, seems to be another third phase in the ceramic bulk. It contains a high amount of zirconium, about 24%. Further, no barium and aluminum could be detected. The origin of this zirconium-rich phase may be due to contamination by the YSZ milling container and milling balls. Likely, it will not deteriorate the dielectric properties of the capacitor component.
All investigations with respect to EDX mappings, line scans, and spots corroborate previous findings that no or only a negligible amount of silver or palladium has migrated into the bulk material. Compared to Figure 4.16 and the A-MLCCs, severe reactions between both materials could be suppressed. The optimization of the shaping processes helped to obtain such microstructures.

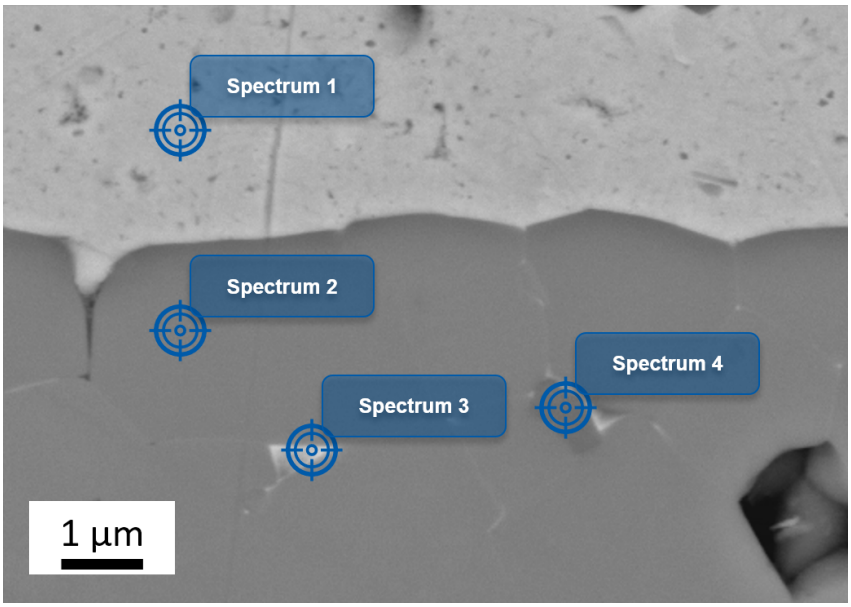

Figure 4.23: SEM micrograph at the Ag/Pd-dielectric interface of the prototype MLCC with marked EDX spots for analysis of the element distribution.

Table 4.7: Element distribution of recorded elements at four corresponding spectra at the Ag/Pd-dielectric interface of the prototype MLCC. The distribution is given in atomic%.

Element	Na	Bi	Ti	Ba	Ca	Ag	Pd	Zr	Al	O
Spectrum 1						62.91	37.09			
Spectrum 2	7.18	8.51	15.71	1.42	4.19			4.06	0.45	58.48
Spectrum 3	5.40	14.80	17.16	1.08	4.25			4.37	0.60	52.35
Spectrum 4	1.91	3.55	5.11		1.29			24.15		64.00

4.6.2 Dielectric Properties

The dielectric properties are essential for gauging the overall performance of the capacitor component. Temperature- and frequency-dependent permittivity and dielectric loss are displayed in Figure 4.24a) and b), respectively. The measurements were taken within a frequency range between 0.1 kHz and 1 MHz, but only data up to 100 kHz is depicted. Upon initial observation, the relative permittivity appears to be quite stable concerning temperature and frequency. The temperature ranged from -115 °C to 500 °C. Considering the permittivity at 1, kHz, the MLCC components exhibit a huge operational window of 615 K. This highlights their ability to withstand extreme conditions without significantly compromising their energy storage capabilities. The upper temperature limit is probably much higher. The measurement conditions were set to a maximum temperature of 500 °C. The upper plot suggests a T_m of about 100 °C, which fits the bulk reference material in Figure 4.6a). Furthermore, a notable temperature-independent permittivity plateau is observed between roughly -100 and 400 °C with a permittivity between 500-600, which corresponds to the bulk reference sample's response. Moving to Figure 4.24b), the dielectric loss is plotted against temperature and different frequencies. Similar to the bulk reference sample and the reported dielectric properties from Hoang et al.,[29] the low-temperature and high-temperature phase transitions of the PNRs are visible. Enhanced loss values at 100 kHz are likely related to the SRF of the MLCC component, as the frequency of 100 kHz is already approaching the SRF region. In Figure 2.20, it can be seen that the ESL will start to have a more pronounced effect on the losses at high frequencies. At high frequencies, the impedance response behaves inductively. This behavior is influenced by factors such as the leads, type, and dimensions of the electrodes, as well as the overall geometry of the capacitor. The comparison with bulk samples reveals that the losses are higher for the MLCC components, which may be attributed to the higher SRF of the bulk pellets compared to the SRF of the MLCC samples. Consequently, the enhanced peak of the high-temperature PNRs phase transition at 150 °C and 100 kHz could be caused by the lowered SRF in the MLCC components.

From Figure 4.24, it can be extracted that the relative permittivity and tan δ are highly promising with respect to high-temperature applications. Higher densities or lower porosities tend to result in lower dielectric loss, as claimed by Hirata et al.[223] However, only the data at 1 kHz are often related to industrial applications and will be considered subsequently.[10] The frequency-dependent behavior of the MLCC component will be evaluated later in Figure 4.28.

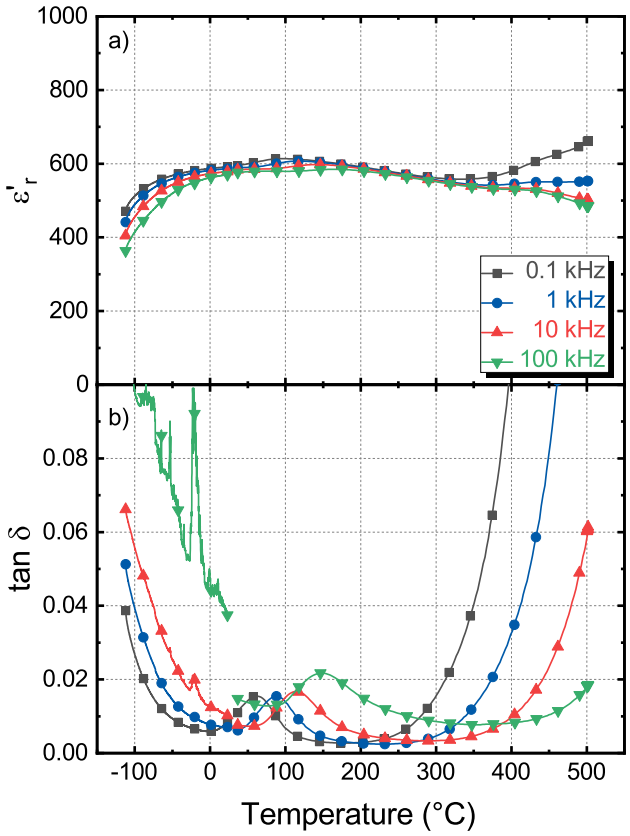

Figure 4.24: Dielectric properties of the prototype MLCC comprising a) relative permittivity and b) tan δ plotted against the temperature.

Figure 4.25 contrasts the temperature-dependent dielectric properties of the Ω-MLCC (blue), A-MLCC (red), and the bulk reference sample (gray) regarding ε_r and tan δ at 1 kHz. Characteristic dielectric parameters determined at this frequency are listed in Table 4.8 and represented as a bar plot in Figure 2.7. Maximum permittivities ε_r'(max), the relative permittivity at 150 °C (ε_r'(150 °C)), the resulting temperature range with permittivity deviations less than 15% from the nominal value ε_r'(150 °C) $T_{range}(\varepsilon_r' \pm 15\%)$ in °C, the temperature range with dielectric loss smaller or equal to 2% $T_{range}(\tan\delta \leq 0.02)$ in °C as well as the actual key parameter, which is the overlapping temperature range of stable permittivity and low dielectric loss $\Delta T(\varepsilon_r' \pm 15\%; \tan\delta \leq 0.02)$, in K are specified. The shaded area in red in Figure 4.25a) indicates variations of the relative permittivity in the range of ±15% (marked only for the Ω-MLCC), whereas the red dashed line in Figure 4.25b) corresponds to the limit of dielectric loss to be considered low, which is ≤ 2%.

In general, the overall dielectric properties neatly resemble the bulk reference sample. In the range of 0-450 °C, slight deviations in ε_r' can be explained by different conditions during heating and cooling cycles. Besides, the dielectric loss of the prototype MLCC matches even better with the bulk sample; only minor variations at elevated temperatures of close to 400 °C are apparent. The high-temperature regime is slightly off. This can be rationalized by the mobilization of oxygen vacancies.[46] It could be a result of a

slight incorporation of Ag into the NBT lattice, which is described in Equation 4.2.[47] The Ag would act as an acceptor dopant when substituting Bi on the A-site, increasing the oxygen vacancy concentration. The mobilization of additional vacancies and the detaching of $V_O^{\bullet\bullet}$ from the $(Ag_{Bi}^{''} - V_O^{\bullet\bullet})^x$ defect associate may be the reason. However, compared to the dielectric loss of the A-MLCC, the contribution of oxygen vacancies at high temperatures is quite low. Differences in the fired density between the Ω-MLCCs and bulk samples could likewise rationalize minor deviations at high temperatures.

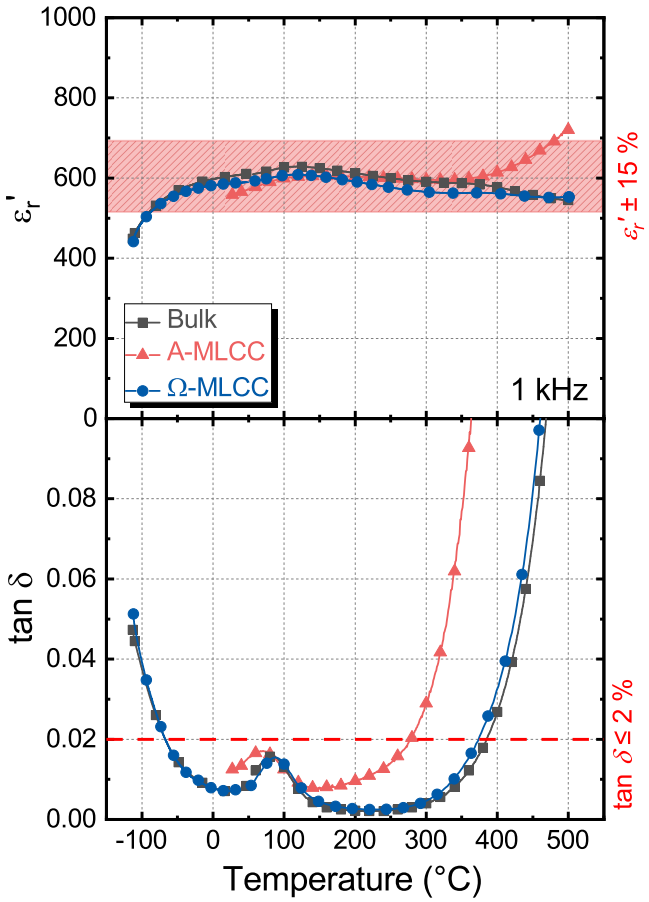

Figure 4.25: Characteristic dielectric properties, comprising a) relative permittivity and b) tan δ, of the Ω-MLCC (blue) and A-MLCC (red) in comparison with the reference bulk sample (gray) and plotted against the temperature.

Transferring the outstanding dielectric properties of the bulk samples to the MLCCs is one of the major achievements of this doctoral thesis. As seen in the results part before, it was extremely challenging to manufacture proper MLCC components. These findings result from an integral approach of analyzing and improving almost every manufacturing step within the MLCC fabrication route. Not only processing parameters but also different sintering conditions and the adapted slurry composition contribute to this impressive result. So far, it seems that the possible migration of electrode material does not have a significant role during the application of high temperatures. Compared to the A-MLCCs, Ω-MLCCs are superior in terms of dielectric properties. This was obtained by the knowledge gained from before. These

findings were essentially the starting point for an in-depth characterization of the MLCC components towards a high-temperature power electronics application.

Table 4.8: Comparison of dielectric properties determined at 1 kHz between the bulk reference, Ω-MLCC, and A-MLCC.

Sample	Bulk	Ω-MLCC	A-MLCC
ε_r'(max)	629	609	720
ε_r'(150 °C)	625	604	605
$\Delta T(\varepsilon_r' \pm 15\%)$ (°C)	-81 - >500	-89 - >500	<RT - 481
$\Delta T(\tan\delta \leq 0.02)$ (°C)	-67 - 385	-67 - 375	<RT - 278
$\Delta T(\varepsilon_r' \pm 15\%; \tan\delta \leq 0.02)$ (K)	452	442	>258

To further rank the applicability of the prepared MLCCs towards high-temperature and energy storage applications, the EPC (c.f Equation 2.8) is considered. It is a figure of merit for an easy comparison between different components.[84] In Figure 4.26(a), the EPC is plotted against the applied electric field and temperature. Applied electric fields of up to 200 kV/cm and temperatures from 25-125 °C are depicted. As a result of this representation, relative changes opposed to zero-field values are emphasized. Strikingly, the EPC for all temperatures and the highest electric field does not fall below 15%. At 125 °C and 200 kV/cm, prototype capacitors demonstrate an approximate decrease of EPC of only 13%. Considering that very demanding conditions are present, the relatively small decrease in EPC showcases the universal applicability of the manufactured lead-free prototype MLCCs.

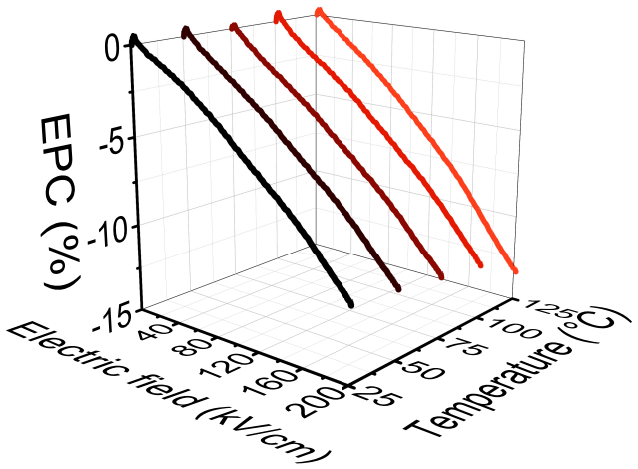

(a) Electric field permittivity coefficient with temperatures up to 125 °C.

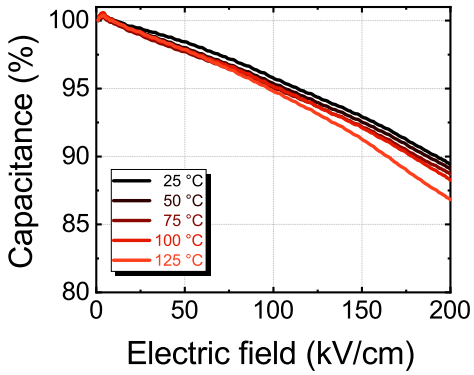

(b) Relative capacitance of the prototype MLCC with temperatures up to 125 °C.

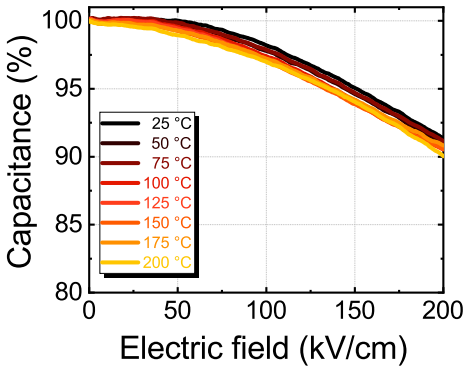

(c) Relative capacitance of the bulk reference sample with temperatures up to 200 °C.

Figure 4.26: Electric field permittivity coefficient (EPC) and relative capacitances of the prototype MLCC and bulk reference sample versus applied electric field.

In Figure 4.26(b), the relative capacitance is plotted against the electric field with temperatures ranging from 25-125 °C. This representation is similar to the EPC representation. Instead, the capacitance is not referenced to a zero-field capacitance value. This allows for direct hints regarding loss of capacitance at the corresponding temperature. It can be seen that at 125 °C and 200 kV/cm the loss of relative capacitance is about 13%. Within this representation, a more pronounced decline beyond 150 kV/cm and at 125 °C can be detected. Given the circumstances, a rapid degradation of dielectric properties may be the cause. When compared to the bulk reference sample in Figure 4.26(c), remarkable differences are apparent. The maximum temperature during the measurements could be elevated to 200 °C (yellow). The maximum applied electric field is 200 kV/cm, which relates to an applied voltage of about 3800 V. The thickness of the reference pellets is 0.19 mm. The small loss of capacitance of roughly 10% at maximum operating conditions is impressive. Considering such extreme conditions, the ceramic material NBT-BT-CZ-1BA appears to be a resilient dielectric. Such results may rank this capacitor material as one

of the most stable materials for high-temperature and power electronics applications.[11,84] The prototype MLCCs and bulk samples consist of an RFE dielectric material, which was already evidenced to exhibit a wide temperature-stable permittivity plateau.[29] The ferroelectric-relaxor phase transition temperature T_{F-R}, where rhombohedral LT PNRs are formed[135], got shifted to temperatures of about -100 °C for the NBT-6BT-20CZ material. Likewise, the formation of HT PNRs, which consist of both rhombohedral and tetragonal PNRs, got depressed at high levels of CZ content.[34,35] The increased CZ content enhances the degree of lattice disorder and reduces the correlation length between the polar nanoregions.[250,251] The findings above justify the dielectric response of the NBT-BT-CZ-1BA dielectric. High electric fields of up to 200 kV/cm were applied, and measurements were conducted in the temperature range between RT and 200 °C. Additionally, the T_{F-R} is far from the current operating conditions, and the transition from LT- to HT-PNRs is still depressed due to the $CaZrO_3$ content. Consequently, it can be expected that only other influences, aside from structural aspects of the dielectric ceramic, will affect the dielectric performance of the prototype capacitors. Such influences may arise from internal electrodes and corresponding leakage currents. It has been evidenced that the Schottky barrier of the dielectric-inner electrode interface affects occurring leakage currents at high electric fields.[252] Ag/Pd inner electrodes were used for the prototype MLCCs, while sputtered Pt was used for electrically contacting the bulk ceramics. Besides the effect of different work functions of Ag/Pd and Pt, the influence of increased temperature simultaneously with applied electric fields will certainly increase leakage currents.[84] The loss of relative capacitance of about 13% for the Ω-MLCC, nevertheless, underlines the paramount dielectric behavior of the ceramic material and contributes to the high versatility of the manufactured components.

The previous comparison is helpful in terms of the manufacturing parameters. MLCC components were produced via the MLCC fabrication route. It was outlined throughout this thesis that many synthesis parameters are not only interrelated but were also rather unknown before the start of this work. With respect to further optimizing the MLCC fabrication route, the actual prototype MLCCs may be prepared on a higher level of sophistication.

As mentioned earlier, there is a lack of information about the real-world operating conditions of capacitors used for high-temperature and power electronics applications. Nonetheless, testing conditions from commercially available CeraLink® J-style low-profile capacitors (B58031U5105M062) from TDK Electronics AG can be deduced.[23] Those conditions will be referred to as reference conditions for the prototype capacitors. Specifications for the commercial MLCCs were taken at 25 °C and 400 V, the AFE to FE phase transition voltage.[16] This voltage translates to an electric field of about 82 kV/cm. Figure 4.27a) depicts the voltage dependence of the normalized capacitance with temperatures ranging from 25-150 °C in 25 °C-steps. Applied voltages of up to about 700 V (150 kV/cm) are monitored. Only a minor variation of normalized capacitance of $\leq \pm 7\%$ could be recorded within the maximum range of both voltage and temperature. By contrasting Figure 4.27a) and Figure 4.27b), tremendous differences can be spotted. The types of ceramic materials are mainly responsible for the differences. While the prototype MLCCs consist of an RFE material, the CeraLink® capacitor was prepared with a PLZT-based material and is considered to behave like an AFE material (c.f. Figure 2.6(c)).[16] Unlike the lead-based material, no switching field is required for the RFE prototype MLCCs. This aspect considerably confines

the operational window of the AFE capacitor regarding applied voltage and ambient temperatures. The synthesized prototype MLCCs, however, can be operated efficiently in a wide range between 0-150 kV/cm (up to about 700 V). Even higher fields with rather small deviations of capacitance are no hurdle, as found in Figure 4.26. This stability yields also the main advantage of those capacitors. Rated voltages do not have to be specified. The actual breakdown voltage has to be known, though. This will elucidated in Subsection 4.7.2. Comparing this response to the commercially available antiferroelectric MLCCs, this is a huge benefit and is founded on the different nature of AFE and the rather linear RFE processed in this work. It can be assumed that short-pulsed ripples and fluctuations do not deteriorate the dielectric properties at operating voltages around 700 V.[15] Such a broad electric field and voltage range make the prototype capacitor components versatile for manifold applications.

Figure 4.27c) displays the normalized capacitance of the prototype MLCC versus the temperature at different voltages based on the CeraLink® B58031U5105M062 data sheet.[23] Only for the zero-field condition, negative temperatures in °C were recorded. 400 V, 500 V, and the maximum voltage of 700 V were measured at temperatures between RT and 150 °C. A similar difference in normalized capacitance of $\leq \pm 7\%$ is visible. On the other hand, the commercial capacitor in Figure 4.27d) exhibits a strong voltage-dependent capacitance. Regarding the reference condition at 25 °C, the relative capacitance is about 55% at zero-field. At 400 V the capacitance is at 100%. With increasing the applied voltage to 500 V the capacitance decreases to about 80%. A universal applicability of such capacitors is not viable. These capacitors can only be used in a highly specified and narrow operational window.

Nevertheless, the Ω-MLCCs have their limits. Considering Figure 4.26 and Figure 4.27, it can be deduced that electric fields of up to 200 kV/cm simultaneously with temperatures up to 125 °C were feasible. Vice versa, electric fields of up to 150 kV/cm and temperatures up to 150 °C were recorded. Consequently, the operational limit is somewhere around these conditions. It was seen that the bulk ceramic (Figure 4.26(c)) can bear even higher temperatures at 200 kV/cm. The design of the capacitor as a whole is probably the weak spot and diminishes the maximum applied operating conditions.

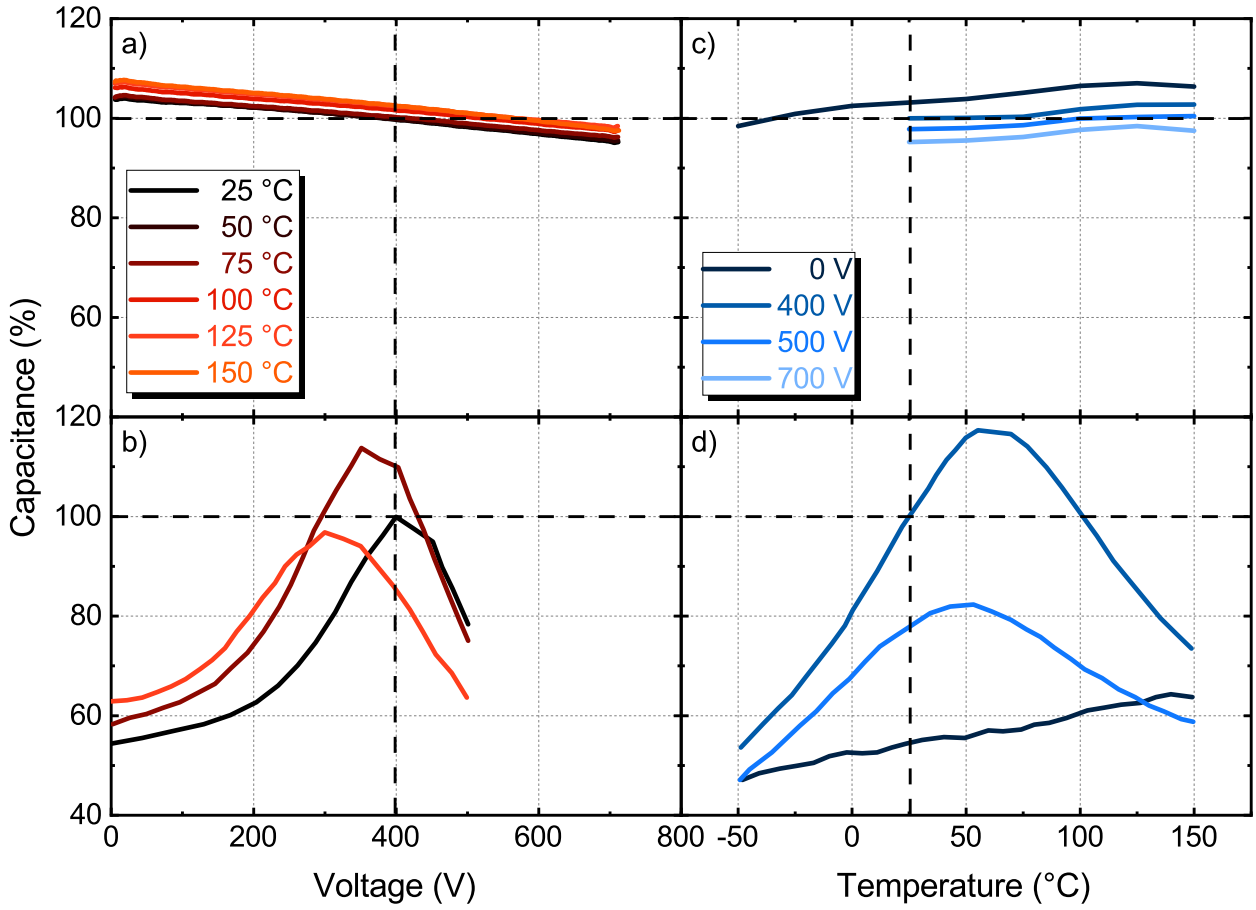

Figure 4.27: Comparison of the normalized capacitance against applied voltage and temperature between the prototype MLCC and a CeraLink® B58031I5105M062 capacitor. Normalized values were calculated from the capacitance at 25 °C and 400 V according to TDK Electronics AG (black dashed lines), while the figures of the CeraLink capacitor were adapted from TDK Electronics AG.[23]

For further comparison, not only voltage- and temperature-dependent relative capacitances are compared, but also the capacitance and its related geometries. Therefore, in Table 4.9, the prototype is subdivided into four active and 80 active layers. This would be in rough correlation with the CeraLink® capacitor. Since this thesis serves as a proof of concept of manufacturing lead-free NBT-based MLCCs with Ag/Pd inner electrodes, only a small amount of four active layers were chosen for the manufacturing process. With a thickness of 46.8 µm, an electrode area of 16.7 mm², a capacitance of 7.5 nF, a volumetric efficiency of 2.4 µF/cm³ is obtained. Extrapolating this to the approximate design of the CeraLink® capacitor, 80 active layers would be most appropriate. By reducing the thickness of dielectric layers to 23.5 µm, the nominal capacitances between both would roughly match. Both assumptions would translate the volumetric efficiency into staggering a 9.6 µm/cm³. This is almost doubled compared to a value of 4.9 µF/cm³ for the CeraLink® MLCC.

The prototype MLCC already displayed superior normalized capacitances with respect to applied voltage

and temperature compared to the CeraLink® capacitor. This extrapolation further contributes to the benefits of a lead-free NBT-based MLCC for high-temperature and power electronics applications. Note that this is only an extrapolation and was not experimentally confirmed.

Table 4.9: Comparison of capacitance, related geometries, and resulting volumetric efficiency of the Ω-MLCC with extrapolation of 80 active layers and the CeraLink® capacitor.

	Prototype MLCC		CeraLink® capacitor[23]
	4 active layers	80 active layers	
Capacitance (nF)	7.5	300	350 ±20%
Electrode area (mm²)	16.7	16.7	
Thickness (µm)	46.8	23.5	
Volumetric efficiency (µF/cm³)	2.4	9.6	4.9

So far, the paramount stability of prototype MLCCs compared to high electric fields and temperatures has been discussed and rationalized. Besides the application in high-temperature power electronics, there is also growing demand for capacitors with high frequency stability in fast-switching wide-bandgap semiconductors in electric vehicles, 5G base stations, or DC-link power electronic converters.[3,15,22] In Figure 4.28, the temperature-dependent frequency stability of the prototype MLCCs' TCC is plotted against the applied frequency from 1 Hz to 5 MHz. The ±15% tolerance is marked in gray. With increasing temperature, starting at 50 °C, the TCC of the MLCC is declining slowly. However, at 100 °C, the TCC is enhanced by a few percent. This can be attributed to the T_m peaking at around 100 °C and was depicted in Figure 4.24. Further heating of the sample is followed by a steady loss of TCC until a temperature between 300 °C and 400 °C. With temperatures beyond 400 °C the reduction of TCC is extraordinarily high. It surpasses the -15% tolerance at 500 °C. This translates to a frequency-stability up to temperatures between 400 °C and 500 °C. Note that the peak at around 5 MHz is related to the SRF of the capacitor component. The SRF is later described in Figure 4.31. As the SRF is the frequency where capacitive and inductive reactance are equal, it is linked to the ESR (see Equations 2.45-2.46). The ESR is temperature-dependent and is commonly lowered with elevated temperatures.[76,253,254] Hence, the self-resonant frequency is conditioned by the temperature.[76,99,255]

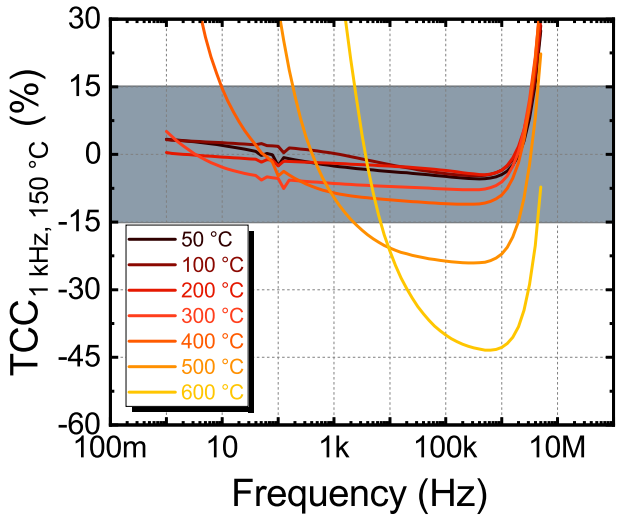

Figure 4.28: Temperature-dependent frequency stability of the Ω-MLCCs' TCC at 1 kHz and 150 °C. Marked in gray is the area with ±15% tolerance.

4.6.3 Energy Storage Properties

Besides dielectric properties, which were evaluated in the previous subsection, the temperature-dependent energy storage properties are highly important for a successful application as a capacitor component for high-temperature and power electronics. In Figure 4.29(a), a P-E loop at room temperature is depicted with a bipolar electric field of up to ±280 kV/cm. Voltages are marked on the top of the graph. A slim polarization loop can be spotted, indicating the relaxor behavior as already figured out for the capacitor material itself by Hoang et al.[29] With an applied field of 280 kV/cm, a polarization of about 17 µC/cm² was recorded. Compared to other capacitor materials and capacitors, this is still in a well-acceptable range. Polarization values in the range between 10-25 µC/cm² were achieved at similar electric fields, according to several publications from 2022.[11,84,256]

Temperature-dependent P-E loops are depicted in Figure 4.29(b) with temperatures ranging from RT to 125 °C and electric fields of up to ±200 kV/cm. The maximum polarization is 14 µC/cm² for a temperature of 125 °C and 200 kV/cm. A slight increase in maximum polarization values with enhanced temperatures and a higher loss is apparent. As T_m is around 100 °C, increased polarization values can be rationalized by approaching this temperature. The rather harsh conditions, 125 °C and an electric field of 200 kV/cm or 936 V, will inescapably enhance the lost energy. As a result, the polarization loops slightly open up.

In Figure 4.29(c) the energy density (black) and energy efficiency (blue) are presented at room temperature and electric fields of up to 320 kV/cm. A recoverable energy density W_{rec} of 2.7 J/cm³ and an efficiency η of 86% were monitored. The maximum applied electric field does not correspond to the breakdown field (c.f. Subsection 4.7.2).

For better comparability with literature values, the energy densities and efficiencies for different applied electric fields (100, 150, and 200 kV/cm) are plotted against the temperature ranging from 25-150 °C in Figure 4.29(d). Even under maximum operating conditions of 200 kV/cm and 125 °C or 150 kV/cm

and 150 °C, the energy efficiency does not fall below 66%. At moderate conditions of 100 kV/cm and 125 °C, however, the energy efficiency is about 90%. The temperature ranges with efficiency ≥ 80% and efficiencies at the maximum temperature are summarized in Table 4.10.

For the utilization as high-temperature power electronics capacitors, it is essential to apply high electric fields as rated voltages easily can go up to several hundred volts.[257] However, according to Xiao et al., rated voltages for capacitor applications with temperatures of 230-250 °C are only in the range of up to 100 V.[5] Introduced prototype MLCCs could likely go beyond these temperatures. It was already shown in Figure 4.25 that dielectric properties are stable up to temperatures of about 400 °C. By applying only voltages in the range of 100 V, the overall performance and energy efficiencies would be enhanced compared to high fields. It has to be kept in mind that the prototype MLCCs are considered for the application of both high temperatures and electric fields. Inevitably, a balance between high energy storage properties and stable high-temperature dielectric properties has to be found. The manufactured capacitors in this work are supposed to be operated in a wide range of rated voltages and are rather universally applicable.

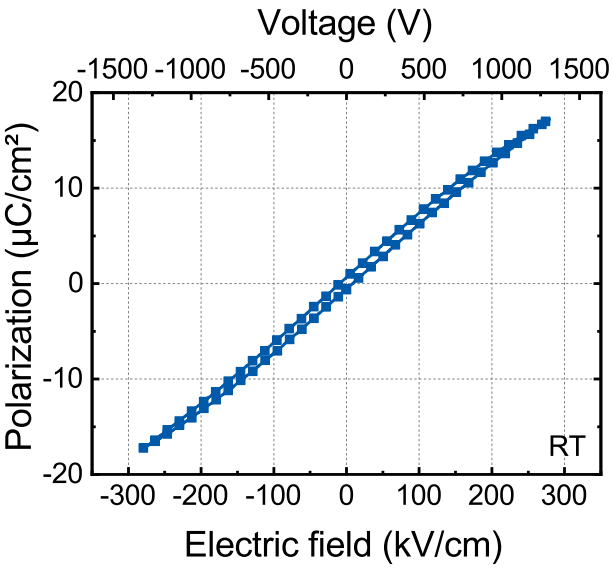

(a) P-E loop up to electric fields of ±280 kV/cm.

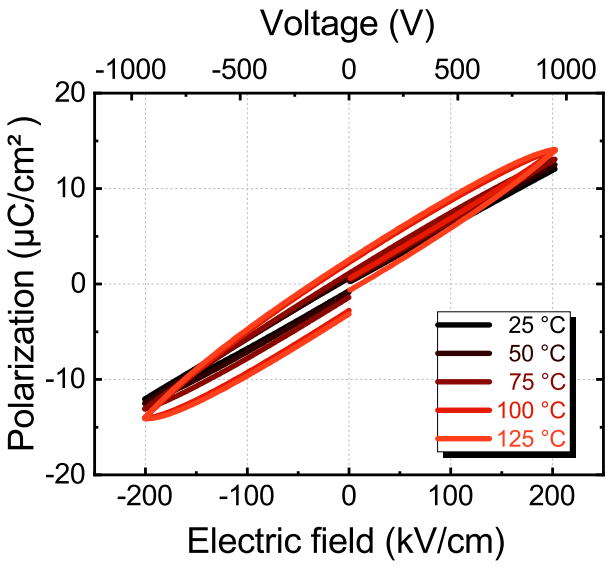

(b) P-E loop from RT-125 °C up to electric fields of ±200 kV/cm.

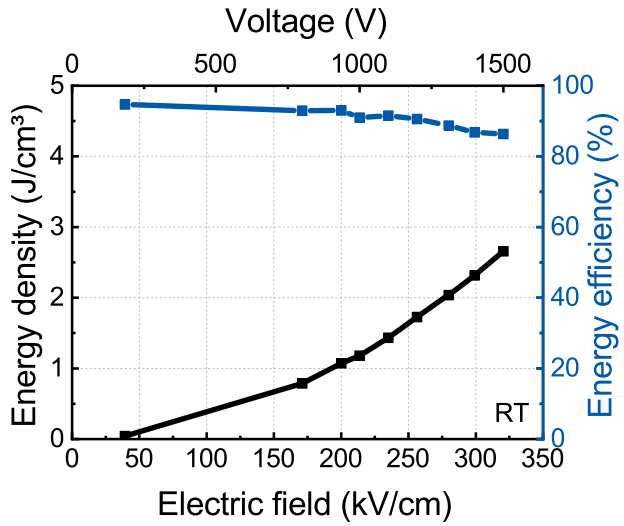

(c) Energy density and efficiency of the corresponding P-E loop measurement at RT and positive electric fields up to 320 kV/cm.

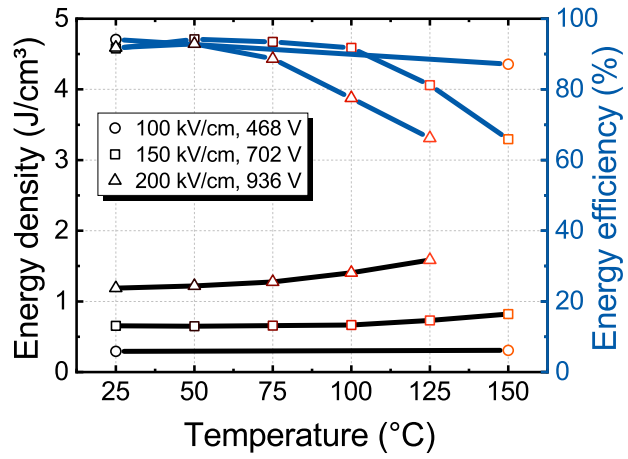

(d) Energy densities and efficiencies at different temperatures and applied electric fields.

Figure 4.29: Obtained P-E loops and calculated energy storage properties of the Ω-MLCCs at temperatures from RT-150 °C and electric fields from -280 to 320 kV/cm in different steps.

Table 4.10: Comparison of efficiencies at different conditions (temperature and electric field) where the efficiency is at least 80% and the efficiency at the maximum temperature.

Electric field (kV/cm)	T_{max} (°C)	$T_{range}(\eta \geq 80\%)$ (°C)	$\eta(T_{max})$ (%)
100	150	25-150	87
150	150	25-126	66
200	125	25-94	66

4.6.4 Impedance

Figure 4.30(a) expresses a fitted Nyquist plot at 400 °C with an inset of a fitted semicircle at 500 °C. The response for both temperatures is close to an ideal resistive behavior. The values for resistivity resemble the values of bulk samples obtained by Hoang et al. very well.[29] At 400 °C, only a single semicircle was recorded with an approximate DC resistivity of about 11 MΩm and an ω_{max} of 2 Hz, translating to an RC constant of 0.5 s. In contrast, the resistivity of the prototype MLCC is 0.34 MΩm at the x-axis intercept and exhibits an ω_{max} of 79 Hz. The progression of ω_{max} and DC resistivity is apparent at both temperatures. With decreasing temperatures, although 400 °C already approaches the operational window of the MLCCs, the RC constant will increase. It can be expected that the resistivity within the operational window is extremely high, indicating a resistive behavior. Furthermore, this points towards a high resilience against the migration of oxygen vacancies at elevated temperatures as they may lead to the formation of ion-conductive pathways.[212] Conductivity measurements would be necessary to identify a possible contribution by oxygen vacancies. It still seems that the proposed incorporation of Ag into the NBT lattice is negligible. In Figure 4.30(b), the complex modulus is plotted against the frequency at temperatures ranging from 400-550 °C in 50 °C-steps. By comparing these results with the bulk reference sample in Figure 4.8, almost no changes can be identified. The increase of the maximum frequency for each temperature is according to the reference bulk sample and just denotes an increasingly conductive behavior with increasing temperature.

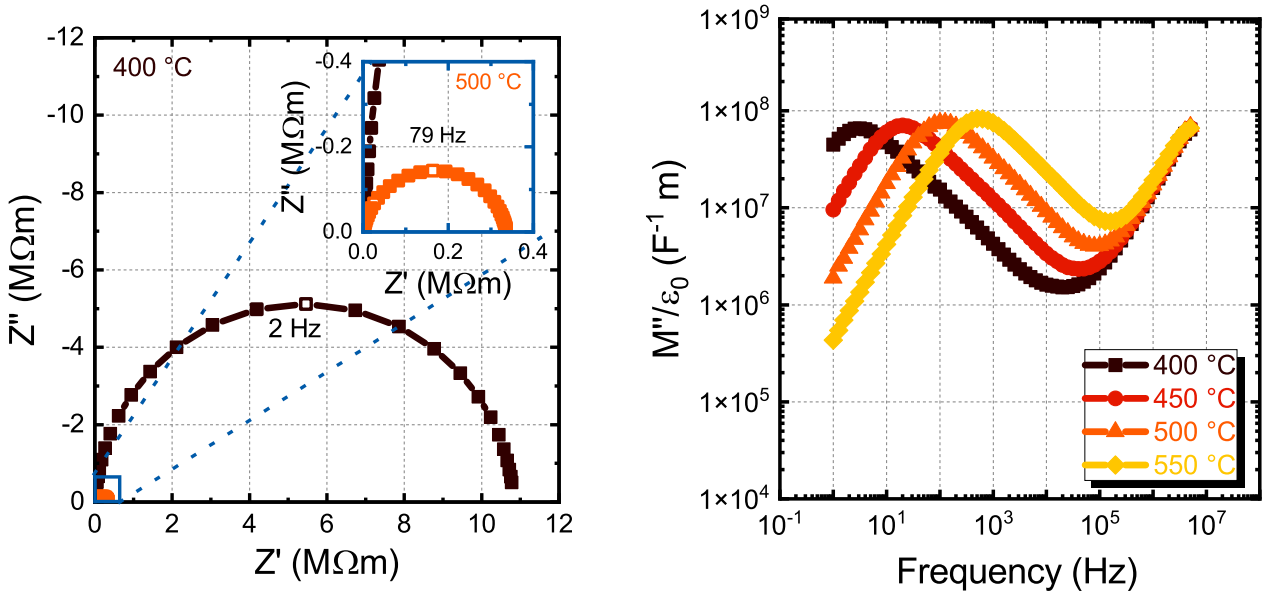

(a) Nyquist plots of the Ω-MLCC at 400 °C and 500 °C (inset).

(b) Modulus plot of the Ω-MLCC with temperatures ranging from 400-550 °C.

Figure 4.30: Nyquist and modulus representations of the Ω-MLCC at different temperatures.

4.6.4.1 ESR and ESL

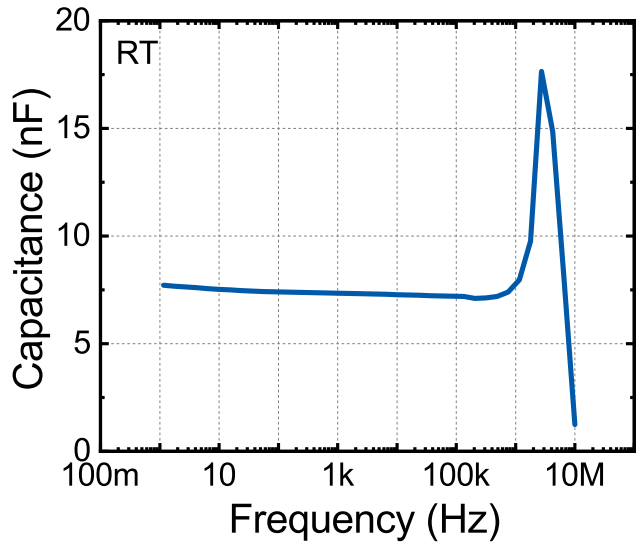

Figure 4.31: Frequency-dependent capacity of the Ω-MLCC plotted at room temperature. The peak is indicating the self-resonant frequency SRF.

Within the upper representation, the frequency-dependent capacity of the prototype MLCC was measured at room temperature. At first glance, a rather constant capacitance of 7.5 nF from 1 Hz to about 1 MHz can be noted. The SRF could be resolved at around 3 MHz in this graph, as the maximum frequency

was 10 MHz. The capacitance is sharply decreases due to the annihilation of capacitive and inductive reactances. According to Equation 2.45, only the ESR will remain. This can perfectly be seen in the following Figure 4.32. At around 3 MHz, the black curve (total impedance) and the blue dashed curve intercept, marking the value for the ESR at the SRF. Moreover, values of the ESR and ESL at either 1 kHz or 1 MHz were obtained from the graph or calculated with the help of Equation 2.13 and are summarized in Table 4.11. This table also contains reference values from the TDK capacitor component.[23] The values for ESR and ESL of the prototype MLCCs were extracted at 0 V_{DC}, 0.5 V_{RMS} (AC), and room temperature. For better comparison between the CeraLink® capacitors and the prototype MLCCs, an equal capacitance was considered according to Table 4.9. Extrapolating to 80 layers and taking into account only half of the layer thickness was done to reach a similar nominal capacitance of about 300-350 nF for both capacitors. It can be seen that the ESR at 1 kHz is about 3 Ω for both. At 1 MHz, the equivalent series resistances are comparable with values of 0.06 and 0.012 Hz for the prototype MLCC and CeraLink®, respectively. It underlines the competitiveness of the manufactured MLCCs with already existing commercial MLCCs. Nevertheless, the difference in ESL is more pronounced. While a comparison with the TDK capacitor is impossible at 1 kHz, a high ESL of 82.4 nH can be approximated at 1 MHz. This is in stark contrast to the commercial MLCC which exhibits a small ESL of 3 nH at the respective frequency. It is a clear sign of an adverse structural design of the prototype MLCCs. The manufactured MLCCs were not fabricated with respect to certain case sizes since the focus of this thesis to prepare lead-free NBT-based MLCCs with Ag/Pd inner electrodes is of major importance. As this work can be seen as a proof of concept, no emphasis was given on specific case sizes for better comparison between other capacitors. However, the ESL values are merely governed by the component's design, namely the type of electrodes, electrode sizes, terminations, and leads.[76,94]

It can be concluded that one of the future outlooks is the preparation of case size-specific capacitors for distinct applications, e.g., utilization of the prototype MLCCs within power electronics of electric vehicles.

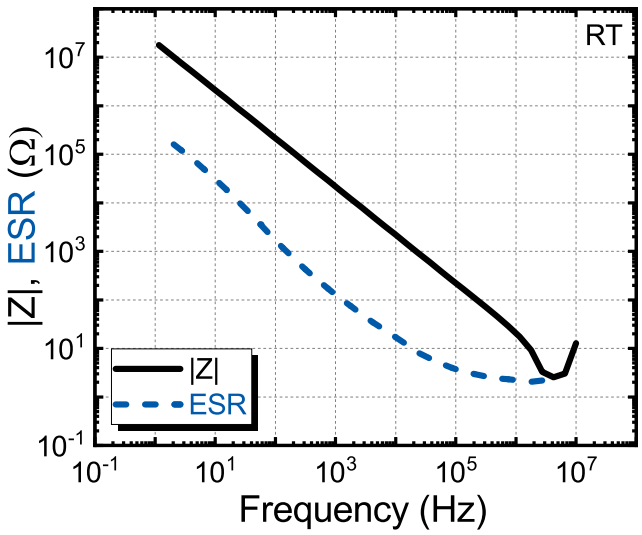

Figure 4.32: Total impedance and ESR measurement of the Ω-MLCC at ambient temperature. The SRF is located at the minimum of the total impedance.

Table 4.11: Comparison of obtained ESR and calculated ESL values of the Ω-MLCC with extrapolation to 80 active layers and the CeraLink® specifications. All values were obtained at V_{DC} = 0 V, V_{AC} = 0.5 V_{RMS}, and room temperature.

	Ω-MLCC		CeraLink®[23]
	4 active layers	80 active layers	
ESR at 1 kHz (Ω)	~140	3.21	3
ESR at 1 MHz (Ω)	2.22	0.06	0.012
ESL at 1 kHz (H)	3.76	0.08	
ESL at 1 MHz (nH)	323	82.4	3

4.7 Reliability and Electrical Fatigue

After characterizing the MLCCs, the performance of NBT-based capacitors and the material itself has to be assessed concerning reliability and electrical fatigue. It is vital to prepare multilayers with outstanding durability. By applying high electric fields and high temperatures, the capacitor components may alter and experience accelerated electrical fatigue. Eventually, this can result in component failure. Failure modes have to be investigated and evaluated to develop prevention strategies, risk profiles, and reliability predictions. This will significantly reduce qualification and validation efforts for later industrial utilization. Within this work, particular emphasis will be given to the electroformation and resistance degradation mechanisms of NBT-based materials in the sense of investigating bulk samples with different arrangements of electrodes. Applying high voltages accompanied by elevated temperatures can be challenging for MLCCs under continuous operation.[258] It was stated that acceptor doping of NBT-based materials can drastically increase the material's conductivity and accelerate degradation.[44,46] Ag can be incorporated in the NBT host lattice, acting as an acceptor dopant.[47] Like in Equation 2.20, acceptor dopants can form tightly bound defect couples in NBT-based ceramics with induced oxygen vacancies.[44] In Section 4.5, it was proposed that a $(Ag''_{Bi} - V_O^{\bullet\bullet})^x$ defect dipole could be formed in the MLCCs. The question needs to be addressed whether electrical properties depend on acceptor dopant concentrations under high voltages and elevated temperatures. It was already outlined that the non-linear dependence of ionic conductivity on acceptor defect or bismuth vacancy concentration, respectively, is based on differences in defect associate formation energy.[46]

Besides electroformation, the reliability of capacitors is a challenge that requires attention. This is especially true in power conversion applications, such as renewable energy and electric vehicles, where voltage peaks can be critical.[13] Hence, the actual DBS, as another failure mode of capacitor components, needs to be investigated. The DBS, defined as the field at which the conductivity of an insulating material rapidly grows by several orders of magnitude,[92] has to be known to specify limits of the capacitor components regarding applied voltages.

4.7.1 Electroformation of NBT-based Ceramics

The investigations on electroformation and their evaluation were conducted with the assistance of Pengrong Ren. The following results were already partially published by Ren and Gehringer et al.[148] The procedure was illustrated in Subsection 3.3.1.

In Figure 2.9(a) and Figure 2.12(a), it was already illustrated that with increasing Fe content, the material shifts from a highly resistive behavior with intrinsic electronic conductivity to an ionically conductive behavior at 1 mol% Fe.[44] In Figure 4.33(a), Nyquist plots of pure and doped NBT of 0.1 and 0.3 mol% Fe are monitored. While the temperature was 700 °C, only a single semicircle for all compositions can be observed. This tends to be the case for dominant electronic conduction, as no severe electrode polarization or grain boundary response is detectable.[25,44,46] It would be a feature of prevalent oxygen ionic conductivity. Nevertheless, the resistivity is slightly decreased with increased Fe content.

To answer the questions of how NBT-based materials behave under high electric fields and elevated temperatures and how the dependency on acceptor dopant concentration affects the electrical response of the samples, an electrode configuration depicted in Figure 3.3(a) is applied to bulk samples. The samples were heated to 250 °C, and an electric field of 10 kV/cm was used. This is represented in Figure 4.33(b). The measurement was stopped when the current increased to a current cut-off value specified by the instrument. After a tiny rise in resistivity of all three samples in the beginning, a gradual degradation of resistivity is followed. A final transition into a highly conductive state is induced. It needs to be pointed out that the complete switching could not be recorded due to the instrument's current limit. Remarkably, the extent of the drop in resistivity is highly dependent on the acceptor dopant concentration. A non-linear change with time results in an order of magnitude lower resistivity during the electroformation experiment with increasing Fe concentration. While the 0.3 mol% Fe-doped NBT was highly conductive after around 300 s, it took more than 1250 s to degrade pure NBT. A stoichiometry polarization can most likely be linked to the induced effects. In turn, this mechanism is reversible. Compared to the capacitor material NBT-BT-CZ-BA, the NBT and NBT-Fe materials are much more prone to electrodegradation. The durability against harsh electric fields and high temperatures of prototype multilayers was already demonstrated in Section 4.6.

At low electric fields, oxygen vacancies do not considerably contribute to the conductivity. At high fields, however, migration of vacancies leads to an uneven distribution, inducing a stoichiometry polarization. Figure 4.33(c) depicts an Arrhenius plot of the NBT-Fe-0.003 sample after performing the resistance degradation experiment. The black line with higher conductivity corresponds to the condition within about 10 min of cooling down from 250 °C without an electric field. The gap in this curve stems from constantly changing electrical properties since the sample equilibrates here. Hence, no proper impedance data could be obtained. By further lifting the temperature, the conductivity values slowly approach the values of the untreated material.[148] Upon further cooling and heating cycles after degradation, congruent data confirms the re-establishment of a low-conductive defect chemistry.

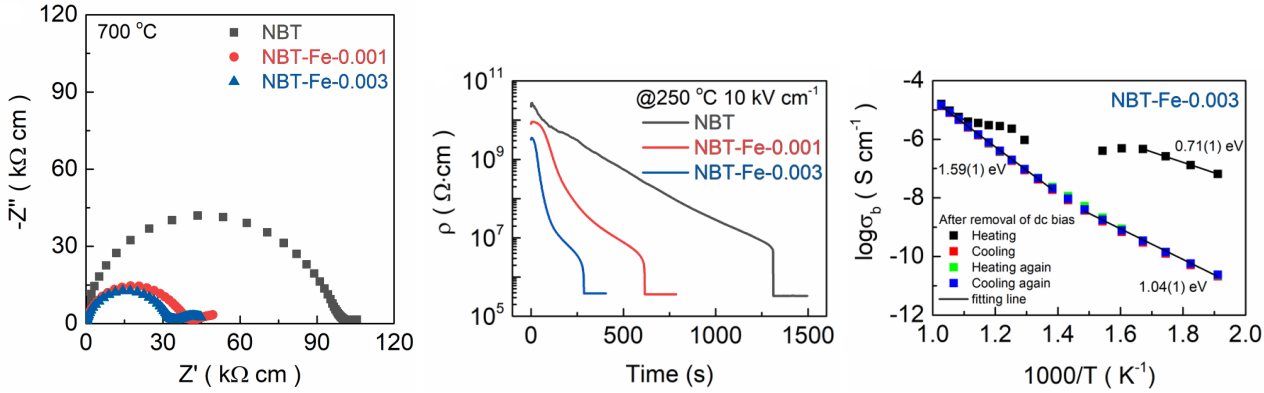

(a) Impedance response of NBT and differently doped NBT-Fe at 700 °C.

(b) Resistance degradation experiments for NBT and differently doped NBT-Fe at DC bias.

(c) Arrhenius-plots of the NBT-Fe-0.003 sample after degradation. Further heating and cooling cycles demonstrate the equilibration of the ceramics' defect chemistry.

Figure 4.33: Electrical response of pure NBT (gray) and NBT doped with 0.1 (red) and 0.3 mol% (blue) Fe and with electrode arrangements as depicted in Figure 3.3(a), adapted from Ren and Gehringer et al.[148]

With the help of bias-dependent impedance spectroscopy, underlying conductive processes' changes due to electroformation could be resolved. Such data can be evaluated using modulus values, which were previously introduced by Bayer et al.[150] By using complex elastance data (c.f. Equation 2.40 and Equation 2.41), the imaginary parts of the elastance are plotted against the frequency of three different samples, namely NBT, NBT-Fe-0.001, and NBT-Fe-0.003. This is displayed in Figure 4.34. All measurements were conducted at 250 °C and 7.5 kV/cm. The scales on the x-axes are different, as well as the recorded time after each measurement point. Regardless, there is one peak in the graphs, which moves to higher frequencies with time. The time frame is extremely different depending on the acceptor concentration. As only a single semicircle could be detected beforehand, $S''_{max} = 1/C$.[190] The peak values barely change for all of the samples. According to the maximum frequency $f_{max} = \frac{1}{2\pi RC}$, an increase in f_{max} is accompanied by a decrease in resistance. Hence, it is a measure of rising conductivity.[150] The time necessary for the resistance degradation is longer compared to Figure 4.33(b). It is rationalized by the lower applied electric fields of only 7.5 kV/cm.

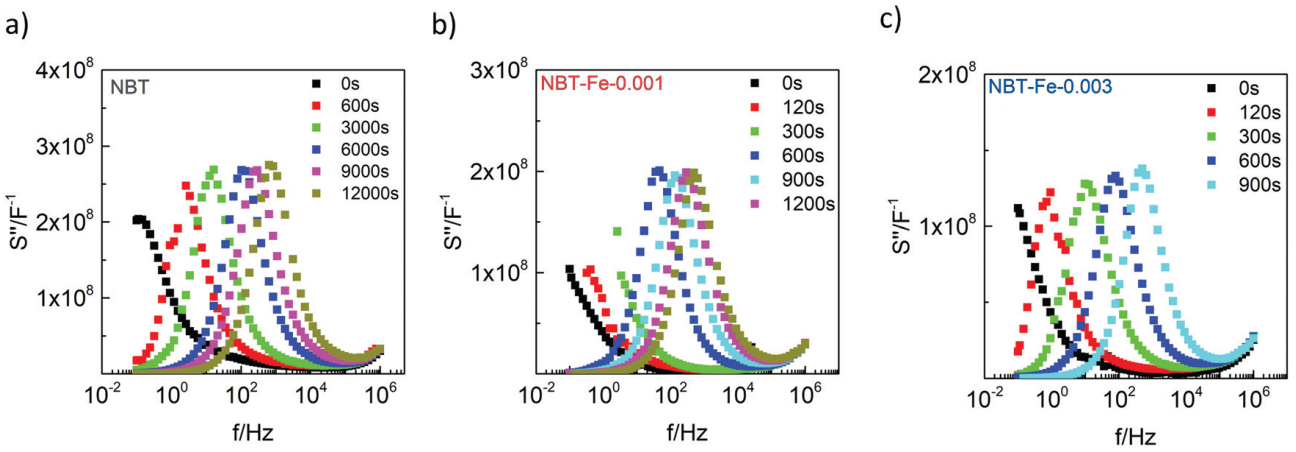

Figure 4.34: Imaginary parts of the elastance of pure NBT and NBT doped with 0.1 and 0.3 mol% Fe at 250 °C and an electric field of 7.5 kV/cm, adapted from Ren and Gehringer et al.[148] Take note of the different times and dimensions on the y-axes.

The electrode configuration in Figure 3.3(b) is helpful in probing local resistance and color changes during stoichiometry polarization of the sample.[259] A voltage of 200 V was applied to the outer surface electrodes of the NBT-Fe-0.003 bulk sample at a temperature of 280 °C. The voltage was the maximum voltage of the instrument and is equivalent to an applied electric field of 0.67 kV/cm. In Figure 4.35(a), the resistance was probed at 1 V. After this, 200 V were applied for 3 h, during which the resistance decreased by two orders of magnitude, as shown in Figure 4.35(b). In the inset, a blackened front evolved from the anode during the experiment. It extended about 1.5 mm into the sample. Induced holes are trapped at the iron ion, which leads to a change in oxidation state from Fe^{3+} to Fe^{4+}.[260–263] Therefore, the electrocoloration process is attributed to the presence of the iron dopant and can be visualized. After annealing at 800 °C for 6 h, the initial value of the resistance is established, which is depicted in Figure 4.35(c). Likewise, the sample color reverts, as seen in the inset.

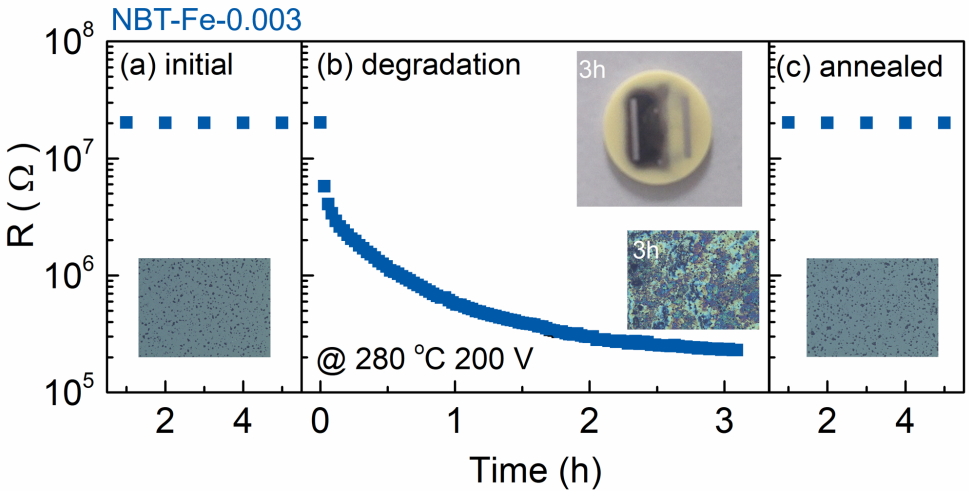

Figure 4.35: Resistance over time of the 0.3 mol% Fe-doped sample at different stages of the electroformation process and with insets of the corresponding state visualizing the electroformation process, adapted from Ren and Gehringer et al.[148] (a) Before the electroformation process, probed at 1 V. (b) Change in resistance from the degradation process at 280 °C and 200 V with an inset marking the blackened front after 3 h. (c) Restored initial resistance after annealing the sample at 800 °C.

Furthermore, local investigations on the resistance after electroformation were performed by impedance spectroscopy and with microelectrodes in between two large electrodes. This is schematically shown in Figure 4.36(a). The resistance in this configuration of electrodes is now measured against the large electrode (spot 0), formerly the anode.

Electrode 1 (black), 2 (red), and 3 (green) experienced a blackening of the ceramic material below. The impedance data is plotted in the inset in Figure 4.36(b). Apparently, a second semicircle was obtained and is probably the result of a Schottky barrier formation. Electrode 4 (blue) resided in the light region and exhibited the highest resistance compared to the other electrodes. It is two orders of magnitude higher than in the anode region. The impedance declines again at electrode 5 (purple). This is in contrast to $SrTiO_3$ and $BaTiO_3$.[264] The conduction band energy of NBT is about 1 eV higher than $SrTiO_3$ and $BaTiO_3$, which can rationalize the lack of significant electron conduction in the cathode region of electroformed NBT. The mixing of the occupied Bi 6s orbitals with the O 2p valence band states is responsible for this.[265] It can be quite common that energy levels of defects in different compounds are aligned. Consequently, oxygen vacancies may be deep donors in NBT and cannot induce electrons into the conduction band. Similarly, this can be seen in PZT.[266]

For in-depth analysis of defect chemical changes in the regions of interest, XPS investigations were conducted between the electrodes at position A (dark brown), B (brown), and C (light brown). The plot shows the intensity at each position versus the binding energy, as displayed in Figure 4.36(c). Note that position A was measured again after annealing. Each position can be spotted in Figure 4.36(a). At position A (anode region), the sodium peak is very high, while Ti and Bi signals are below the limit of detection. However, the latter signals evolve at position B and reach a maximum at position C close to

the cathode. The intensity of the sodium signal behaves vice versa; it decreases from anode to cathode. After annealing the sample, the XPS spectra of different positions cannot be discerned anymore. Only region A after annealing is depicted in this plot. A re-occurrence of the bismuth and titanium signal is noted, but also a reduced signal of the sodium compared to the initial position A. The electroformation process seems much more complex and is an integral part of the reversible stoichiometry polarization process. To gain a deeper understanding, the same XPS measurement was performed on the polished backside. The distinctive coloring could be seen here as well. This raises the question of whether this process also extends to the bulk and not only to the surface. Measurements according to Ren et al. revealed that within the bulk, the XPS signals are similar to the non-electroformed surface.[148] In the bulk, a sodium-rich phase can only be formed at grain boundaries. However, the respective phase may not be detectable due to the limit of detection of the XPS.

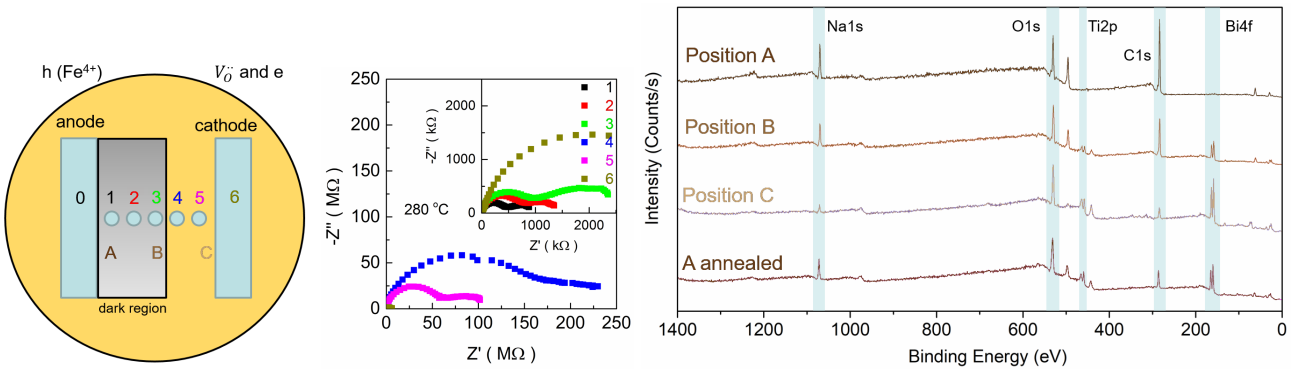

(a) (b) (c)

Figure 4.36: a) Schematic electroformation process, b) impedance plots at the corresponding micro-electrodes 1-6, and c) XPS spectra of the corresponding positions A-C, adapted from Ren and Gehringer et al.[148]

It must be figured out if this stoichiometry polarization mechanism is dominant at or close to the surface. By utilizing an electrode arrangement as depicted in Figure 3.3(c), the major voltage drop will be in the bulk of the samples. Taking into account Figure 4.37(a), enormous differences are striking. The response of pure NBT and NBT-Fe-0.001 was recorded, but the time scale is completely different. Also, in comparison to Figure 4.33(b), the differences are drastic. For fully electroded samples, severe degradation was observed already after a few hundred seconds. Instead, partially electroded samples of NBT and NBT-Fe-0.001 show severe degradation after a few thousand seconds. This points towards a fast process at the surface and a slow process in the bulk. Similar results were obtained for NBT-BT and NBT-BT-Fe-0.01, as depicted in Figure 4.37(b). For these samples, the electrode configuration from Figure 3.3(a) was used, thus full surface coverage. Again, the electrodegradation is much faster compared to the Fe-doped sample. The NBT-BT samples were less mechanically stable with a thickness of 200 µm, which rationalizes the current jump after 4000 s. It can be concluded that differences are similar to the low field conductivity, but processes are slower than for pure NBT.

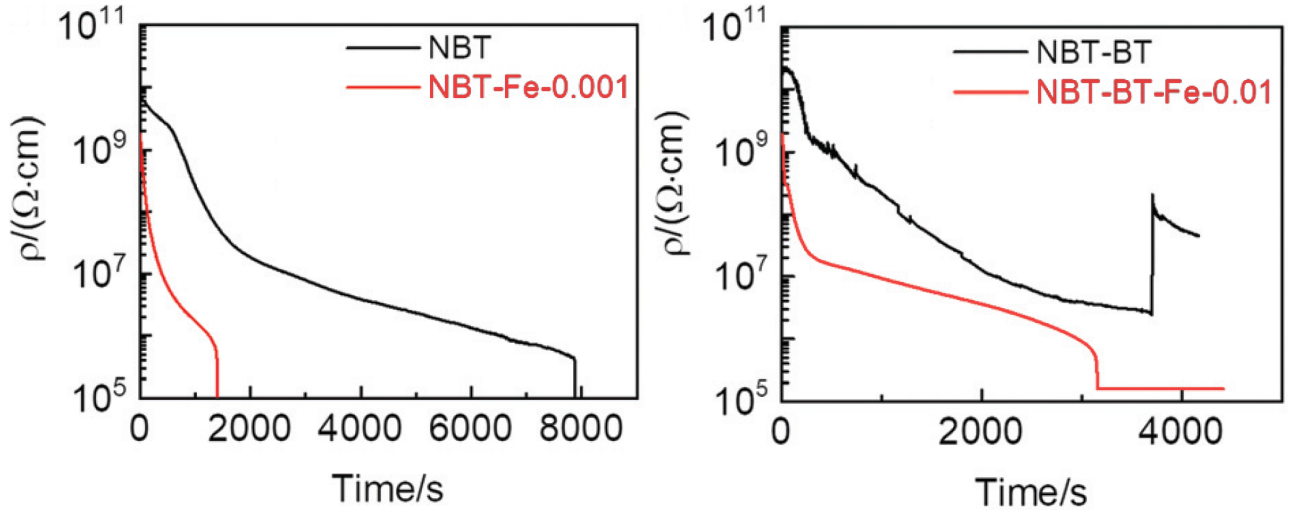

(a) NBT and doped NBT with 0.1 mol% Fe and electrode configuration from Figure 3.3(c).

(b) NBT-BT and doped NBT-BT with 1 mol% Fe and electrode configuration from Figure 3.3(a).

Figure 4.37: DC resistance degradation of NBT and NBT-BT bulk samples with different electrode configurations, adapted from Ren and Gehringer et al.[148].

Resistance degradation over time was additionally performed on an NBT-BT-CZ-BA laminate. The electrode configuration used in Figure 3.3(c) was considered. The conditions were quite different, though. The applied field was 8.4 kV/cm, kept constant for 32 h at around 350 °C. The electric field was limited by the maximum voltage of the instrument. Although these conditions are quite demanding, the resistance degradation in Figure 4.38 indicates considerable stability. The resistivity is plotted in blue and the current in gray against the time in hours. Higher temperatures for the NBT-BT-CZ-BA laminates were applied, which would explain the lowered resistivity already at the start of the experiment in comparison to previous measurements. Further, the degradation over time is much slower. Note that small electrodes, covering the surface only partially, were used for the laminates here. For the solid solution NBT-BT-CZ-1BA, it can be expected that the time scale for severe degradation is orders of magnitudes higher. Even after 32 h, the resistivity dropped by only two orders of magnitude and approached a value of about 10^7 Ωcm. It underlines the stability against high electric fields and temperatures, as already discussed in the previous section. The addition of BA seems to trap oxygen vacancies effectively. However, only laminates were investigated here. For future work, studying the resistance degradation of MLCCs would further contribute to unveiling the complex electrodegradation mechanisms of NBT in combination with the migration of Ag/Pd electrode material.

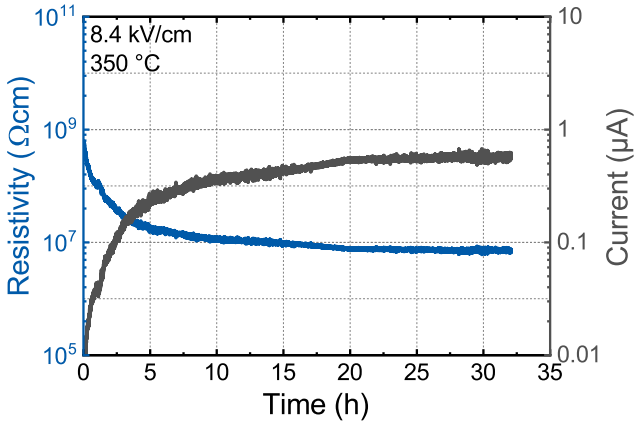

Figure 4.38: DC resistance degradation of a prototype NBT-BT-CZ-1BA laminate at 210 V (8.4 kV/cm) and 350 °C for 32 h. The resistance degradation and current are plotted against time.

In previous research, no concentration dependence on other Al- or Fe-doped perovskites like $SrTiO_3$ could be determined.[140,262] In the case of NBT and NBT-BT, the grain boundary potential barrier could influence the process. An overall rise in current but only a small change in time to reach a severe degradation was observed in recent models describing the electroformation process of STO.[262] Thus, the response of NBT and its solid solutions is unique. With regards to model evaluations explaining the underlying mechanism qualitatively, the following defect equilibria are usually taken into consideration:[147,261,262]

$$O_O^x \rightleftharpoons \frac{1}{2}O_2 + V_O^{\bullet\bullet} + 2e' \tag{4.7}$$

$$\text{nil} \rightleftharpoons e' + h^{\bullet} \tag{4.8}$$

$$Fe_{Ti}^X \rightleftharpoons Fe_{Ti}' + h^{\bullet} \tag{4.9}$$

$$\tag{4.10}$$

Equation 4.9 describes the oxidation state change of Fe, which results in a blackening due to hole injection at the anode. However, the creation of oxygen vacancies, charge neutrality, and the hole trapping reaction of iron are not enough to quantitatively elucidate the stoichiometry polarization of NBT. Acceptor dopants can form tightly bound defect couples in ferroelectric materials as displayed in Equation 2.20. Evidence was provided for the high influence of defect complex formation with respect to the acceptor dopant concentration dependence of conductivity in the low-field regime.[44,46] The increase in acceptor concentration in NBT has a relevant impact on the content of mobile oxygen vacancies, even at low dopant concentrations. However, this does not significantly change the electronically dominated conductivity at low acceptor concentrations. The sensitivity to high fields, on the other hand, can change remarkably, making the system non-linearly dependent on acceptor concentration and electric field.
This still does not explain the surface degradation and composition changes measured by XPS, which suggests that the surface-related process differs from the one in the bulk or at least an order of magnitude

slower. The Schottky equilibrium in Equation 4.11 must not be neglected and is formulated for sodium. It can also be formulated with Bi or Ti for NBT. Using this equation, the observed effects can now be rationalized.

$$2Na_{Na}^{X} + O_{O}^{x} \rightleftharpoons 2V'_{Na} + V_{O}^{\bullet\bullet} + Na_2O \tag{4.11}$$

Previous studies did not claim any significant contribution from these cations towards diffusion in sodium bismuth titanate. Thus, ionic conductivity only was attributed to the oxygen sublattice.[41,44,46] At a high sodium chemical potential, the formation of a Na-rich secondary phase was provided. Thus, it seems that the system exerts a Na-rich phase towards the surface or grain boundaries. Additional sodium and oxygen vacancies in the bulk remain, which is expressed by Equation 4.11. A schematic of this process is illustrated in Figure 4.39. The oxygen chemical potential is modified at the triple-phase boundary. By incorporating oxygen, the chemical potential may be increased. It is unknown whether this increase in oxygen chemical potential leads to severe phase instability with precipitation of a sodium-rich secondary phase.

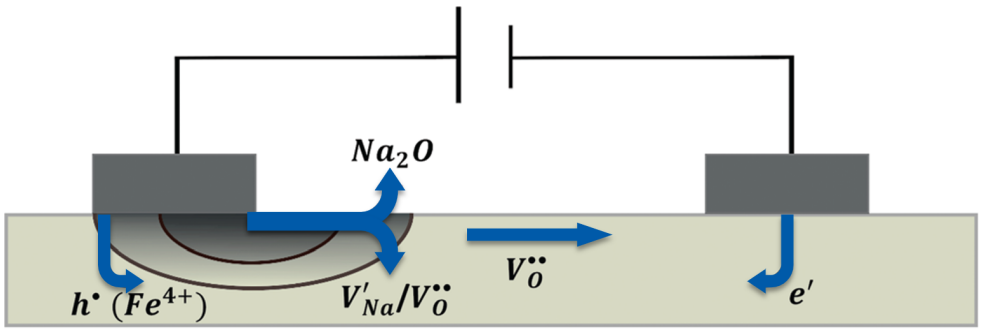

Figure 4.39: Model surface electroformation process of NBT, adapted from Ren and Gehringer et al.[148]

The results detail essential information on resistance degradation and electroformation processes of NBT and NBT-based ferroelectric ceramics. Likely, a high amount of ferroelectric and dielectric properties of NBT and its solid solutions are affected by the surface pathway. This could eventually lead to degradation already during the poling process or application in devices. Further investigations would have to be conducted to diminish or even prevent degradation through the surface pathway. As NBT ceramics and their defect chemistry are highly complex, it is essential to analyze contributing processes to clarify the electroformation process thoroughly.

For high-temperature and high-field capacitor materials and MLCCs, focus has to be given to reducing the oxygen vacancy concentration as much as possible. Such defects would detrimentally affect low-field dielectric properties and dielectric loss. Additionally, they would also lead to pronounced high-field degradation of electrical properties. Ultimately, NBT-based ceramics and its solid solutions seem less prone to fast degradation. Future work is necessary to identify a significant contribution of migrated electrode material to the resistance degradation of MLCCs. Nevertheless, the obtained results provide a profound basis for developing optimization strategies of reliability to alleviate electrical fatigue during

the long-term operation of NBT-based MLCCs.

4.7.2 Dielectric Breakdown Strength

In the first part, the novel indentation method will be assessed, and indents and the microstructure will be inspected. The prototypical material BT was used for the following investigations. After assessing this technique and its influences on the DBS, measurements will be conducted with the actual prototype MLCCs. The preparation of indented samples for DBS measurements and evaluation thereof was done with the help of Rizabek Bolat and Wanja Fichera, who were master and bachelor students, respectively, within the scope of this doctoral thesis. Additionally, Lovro Fulanović helped to develop and evaluate this indentation method. The following results were already partially published by Gehringer et al.[73] The procedure was described in Subsection 3.3.2.

4.7.2.1 Robustness of Setup and Inspection of Indents

First of all, the robustness of the indentation setup has to be assessed. This is a novel technique to indent green ceramic bodies. Before evaluating several parameters affecting the DBS, the novel indentation method has to be assessed. Several indentation procedures were performed in the range of RT-120 °C. The quality of the sample and the indent itself is highly affected by the applied temperature and the slurry composition used for individual sheets. A temperature range of 60-70 °C was found suitable for BT to enable viscoplastic flow.[184] The green bodies consist of solid ceramic particles and a mixture of organic phases. By empirical observations, it was revealed that below 60 °C, deformation and cracking of the samples occurred. It is in good accordance with the glass transition temperature of PVB, which is around 53-70 °C (depending on the purity).[267] Beyond 120 °C, delamination and bubbling were observed. Therefore, an optimal temperature is 60-70 °C for achieving viscoplastic flow. This could be improved by the forces that were applied throughout the indentation process. Adjusting a moderate indentation rate of 250 µm/min, a relaxation of the applied load close to zero happened after about 30 s.
Regarding the inspection of indents, Figure 4.40(a) outlines a three-dimensional topography of a 100 µm deep green indent. The z-direction is color-coded and vividly visualizes a highly symmetric spherical shape of the indent. The indent was mapped after sintering and was quantified by a final indent depth of approximately 50 µm. Figure 4.40(b) displays a line depth-profile of the same indent with an inset. The line profile was taken from the center of the indent in the y-direction and scanned across the x-direction, as shown in the schematic inset. Then, the mean surface height of the sample was calculated by averaging the surface heights of all areas without indents. The sintered indent depth results from the difference between the bottom of the indent and the averaged surface height. The correlation between green and sintered indent depth is presented in Figure 4.40(c). The sintered indent depth is not related to the sample's thickness used for the electrical characterization later. Evidence was found for the linear relation between green and sintered indent depths and is expected for indentations imprinted within the viscoplastic regime of such a green stack.[184] While a 100 µm green indent resulted in a final sintered indent depth of about 50 µm, a green indent depth of 500 µm ended up with a final depth of 388 µm

after sintering. Additionally, the extent of plastic deformation seems equal for all indentation procedures. The load-monitored indenting device displayed similar forces not exceeding 7 N during the indentation. This is corroborated by a goodness of fit of 0.96. The robust method only has an error of about 13 µm and can, therefore, be used for indenting green stacks for dielectric breakdown measurements.

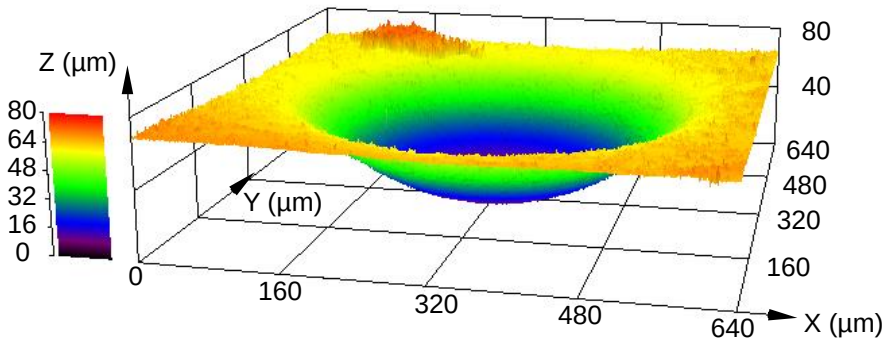

(a) Three-dimensional topography of the indent taken with the help of a laser confocal microscope.

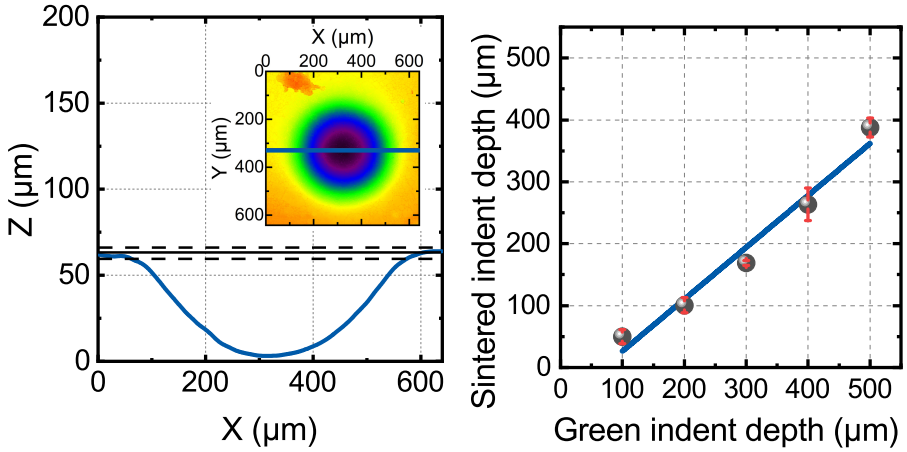

(b) Depth profile of a 100 µm indent with an inset of the top-view of the indent.

(c) Relation between sintered and green indent depth.

Figure 4.40: Topographical evaluation of a 100 µm indent, adapted from Gehringer et al.[73]

4.7.2.2 Microstructural Evaluation

Already Tunkasiri et al. found that the DBS of BT is severely governed by its microstructure.[268] Not only the movement of charge carriers is affected by the porosity,[224] but also the grain size and grain size distribution affect the actual breakdown behavior.[269,270] Lastly, the distribution and location of pores and their shape will also manipulate the breakdown behavior.[156,178,188] In Figure 4.41, the cross-section of a 390 µm sintered indent depth sample is visualized. The spherical and symmetric shape catches the eye. It seems that there are, on the one side, no microcracks and, on the other side, no pores larger than 5 µm. The thickness below the indent was determined to be 130 µm. By thermal etching, as seen in the inset, microstructural changes due to the indentation process can be revealed. An average grain

size of 5.4 µm was calculated, while the area below the indent has a porosity of 3.6%. Typically, smaller intragranular pores, along with larger intergranular pores, are visible. A comparison between the area below the indent and the bulk was anticipated to reveal differences in the microstructure. This was achieved by analyzing the pore and grain sizes and their respective distributions. For the bulk region, an area far apart from the indent was selected. An average grain size of 12.3 µm with a porosity of 4.5% was ascertained for the bulk area of all measured samples.

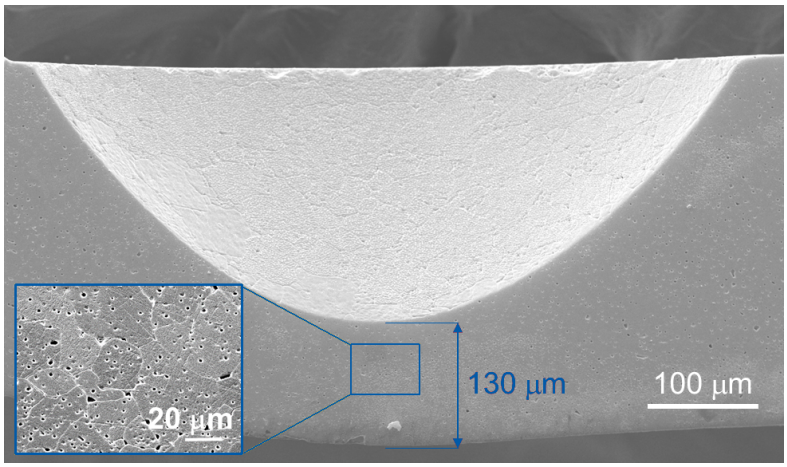

Figure 4.41: SEM micrograph of the cross-section with a sintered indent depth of about 390 µm revealing the final sample thickness at the lowest point of about 130 µm, adapted from Gehringer et al.[73] The inset presents a thermally etched surface underneath the indent at higher magnification.

In Figure 4.42(a), normalized grain sizes and in Figure 4.42(b), normalized pore sizes are indicated by different percentiles (d_{10}, d_{50}, d_{90}) as a function of sintered indent depth. Red and blue lines refer to the bulk area and area below the indent, respectively. The corresponding histograms are found in the supplementary information in Figures 8.4-8.6. Normalized grain sizes for all percentiles of the area below the indent differ by +70% (170 µm) to -10% (390 µm) compared to the bulk. There is no clear tendency as a function of indent depth, as shown in 4.42(a). Nevertheless, the most significant difference in grain sizes appears to lie in the higher percentage of small grains below the indent. Since only small forces were applied to the green microstructure below the ball pin, a slight rearrangement and local compaction of this area may still occur. This is expressed in 4.42(b). Compared to the corresponding bulk area, all percentiles and all individual sintered indent depths are reduced by an average of close to 10%. In Figures 8.4-8.6, the reduction of grain and pore size distributions aids the hypothesis of a local rearrangement and partial densification during the actual indentation process.[240,271]
If small changes in local microstructure are contemplated due to viscoplastic indentation, the altered values of d_{90} need to be treated with much more attention. As the dielectric breakdown, similar to mechanical fracture, obeys the weakest link scenario, the number of large pores will play a decisive role.[92] Above d_{90}, the amount of large pores decreases between 52% and 61% for the different indent depths compared to the bulk. In consequence, a twice lower probability of breakdown under the indent

can be assumed in contrast to the bulk. This is because the largest pores are presumed to be the weakest link.[187,270] Furthermore, the change of pore size from d_{50} to d_{90} is 30%. According to Cai et al., this would decrease the DBS by about 10% if the largest defect is the pronounced influence.[156] The changes in the microstructure at the potential breakdown site are considered insignificant compared to the variations in the electric field from the center to the edge of the electrode on flat surfaces.[179]

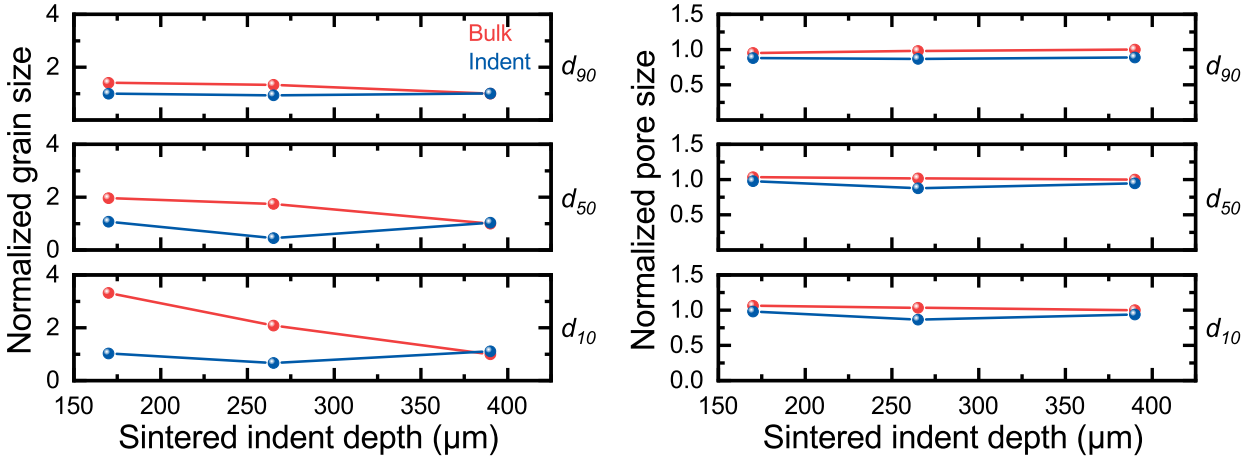

(a) Normalized grain sizes

(b) Normalized pore sizes

Figure 4.42: Normalized grain and pore sizes of d_{10}, d_{50}, and d_{90} percentiles versus sintered indent depth (170, 265, and 390 µm), adapted from Gehringer et al.[73] Red lines correspond to the bulk, and blue lines represent the area below the indent.

4.7.2.3 DBS Evaluation of Laminates and MLCCs

Figure 4.43 features two calculated FEM models of a rotationally symmetrical a) disk-shaped sample with partially covered surface electrodes on both top and bottom and b) an indented sample with a thickness below the indent of 0.2 mm. Here, the top electrode only covers the surface of the indent. The nominal electric field was taken as 30 kV/mm. The below calculations reveal a maximum field of 79 kV/mm at the edges of the electrodes of the disk-shaped sample. This is in accordance with concentrations of electric fields at the electrode edges of MLCCs. However, the electric fields were 3-5x larger compared to the nominal field used here.[181,272,273] This is in stark contrast to the concentration of electric field for an indented sample. A considerably lower maximum field of 38 kV/mm could be determined. It needs to be stressed that this difference outweighs microstructural changes from the bottom of the electrode to the bulk by far. Ultimately, the breakdown spot is at the center of the indent or the lowest thickness, respectively. Figure 4.43b) focuses on the distribution of the field along the surface of the indentation. The calculations promote that corresponding electrode edge effects are with this configuration of electrodes much less likely to have an external influence when such kinds of samples are tested. It allows localizing the breakdown event better by defining the site of the highest field concentration. Tani et al. made similar conclusions, too.[180] A slightly curved top surface will cause a breakdown within the center and

with higher DBS values compared to values obtained from disk-shaped samples and flat surfaces. They, however, assign it to the strain mismatch between active (with electrode) and passive sample volume, which provides tensile stresses of 20 MPa for a typical soft PZT material solely during poling.[274]

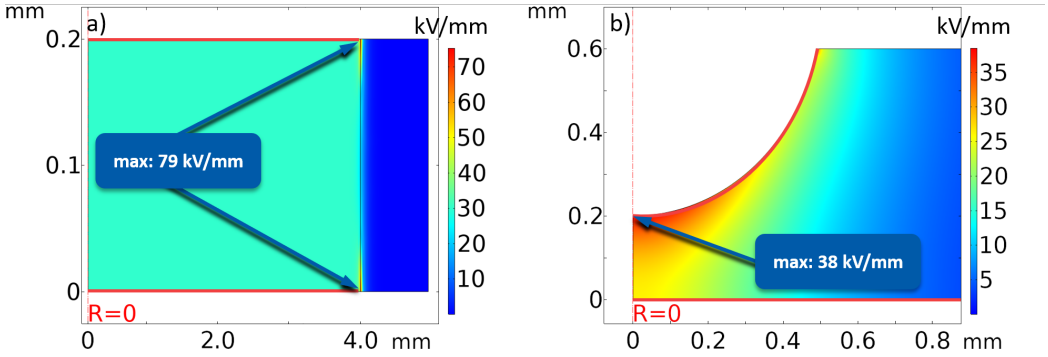

Figure 4.43: FEM model of the distribution of the electric field of a) a disk-shaped sample versus b) a sample with indent, adapted from Gehringer et al.[73] The nominal electric field was set to 30 kV/mm. All samples are rotationally symmetrical; hence, they are plotted in only one direction, starting from R = 0. The top and bottom electrodes are emphasized in red.

After successfully approving the robustness of this novel indentation method, further evaluation of the dielectric breakdown strength in terms of electrical investigations is required. Hence, the DBS will be opposed to the active volume below the electrodes, the thickness of the sample below the indent, and the voltage ramp during the actual measurement. The findings are illustrated in Figure 4.44. In a) a micrograph of the cross-sectioned breakdown site showcases a typical large pore caused by melted material residuals and material removal.[176] The detection of the actual breakdown channel can be quite tedious, but various researchers have already performed it. They similarly investigated cross-sections as well as chemical changes at the breakdown site.[30,275–277] The samples prepared in this work bear advantages compared to flat samples. The indentation predetermines the breakdown site and allows for better localization of the breakdown event. The found breakdown channel in 4.44a) confirms the expectations experimentally. The highest concentration of electric field is at the center of the indent, and the breakdown will occur at this spot, as shown by the FEM calculations in Figure 4.43. However, that does not guarantee the breakdown will always happen there. It can also occur in the vicinity of the indent's center. Better localization of the breakdown site would be evident since a distortion by the height difference due to the curvature of the indent would distort the DBS value.

In the following, a quantification of breakdown probability is attempted with the help of contrasting the DBS for different indent diameters and their respective active volumes, as shown in Figure 4.44b). The active volumes ranged from 0.08-1.13 mm^3 and 0.5-3 mm indent diameter, respectively, and demonstrated no difference in the actual value for the DBS. This can be identified as a strong indication of a breakdown occurring predominantly in the center of the indent. A larger active volume consequently results in a larger length of electrode edge. Thus, a higher probability of finding a defect on the edge or in the volume is present. Investigations by Mieller confirm such a hypothesis for disk-shaped samples.[176] The results obtained in this work, however, reveal that the active volume does not have a crucial impact on

DBS for the indented samples. It implies a measuring method that is rather independent of such extrinsic influence. In fact, a lack of correlation between active volume and DBS could be showcased in BT-based commercial MLCCs.[163]

The thickness dependence of the dielectric breakdown strength is provided in Figure 4.44c). A clear trend of reduced DBS with larger thicknesses is apparent. Obtained DBS values correlate well with literature for a comparable thickness and microstructure.[161] Neusel et al. rationalize the thickness dependence as a consequence of space charge injection and not the distribution of defects in the active volume.[278] In contrast, Stark et al. propose a relation between size dependence and DBS due to electric field inhomogeneities related to the length of the electrode edge.[179] Anyways, a good agreement with the DBS $\propto 1/\sqrt{d}$ could empirically be determined by the fit in Figure 4.44c). The exact local specimen thickness is accessible because all determined breakdowns were localized. This is also utilized to display different error sizes to account for the fact that breakdown spots occur at locally varying specimen thicknesses. Increasing thicknesses of the area below the indent can be translated into smaller differences between the sample height. Hence, the error is also reduced with thickness. It is likely to obtain a larger error at small thicknesses than larger ones, as visualized in Figure 4.44c) at a thickness of 0.14 mm.

The last parameter to be tested is the voltage ramp, as represented in a log-scale in Figure 4.44d). With higher voltage ramps, the DBS is significantly increased. Vice versa, lower voltage ramps and, hence, lower DBS values may correlate with enhanced probabilities of a thermal breakdown.[90,279]

More specifically, by increasing the voltage ramp or reducing the time of applied electric field, the thermal diffusion of the heat gain from locally grown conductivity is suppressed. A higher voltage ramp, thus, leads to a higher dielectric breakdown strength. It has to be taken into account that according to ASTM D149 the voltage ramp may be adjusted to initiate a breakdown between 10-20 s.[280] This finding is important for ferroelectrics, and also high-temperature and power electronics applications as high-field permittivity or polarization vs. electric field properties are frequency or voltage ramp-dependent, respectively.

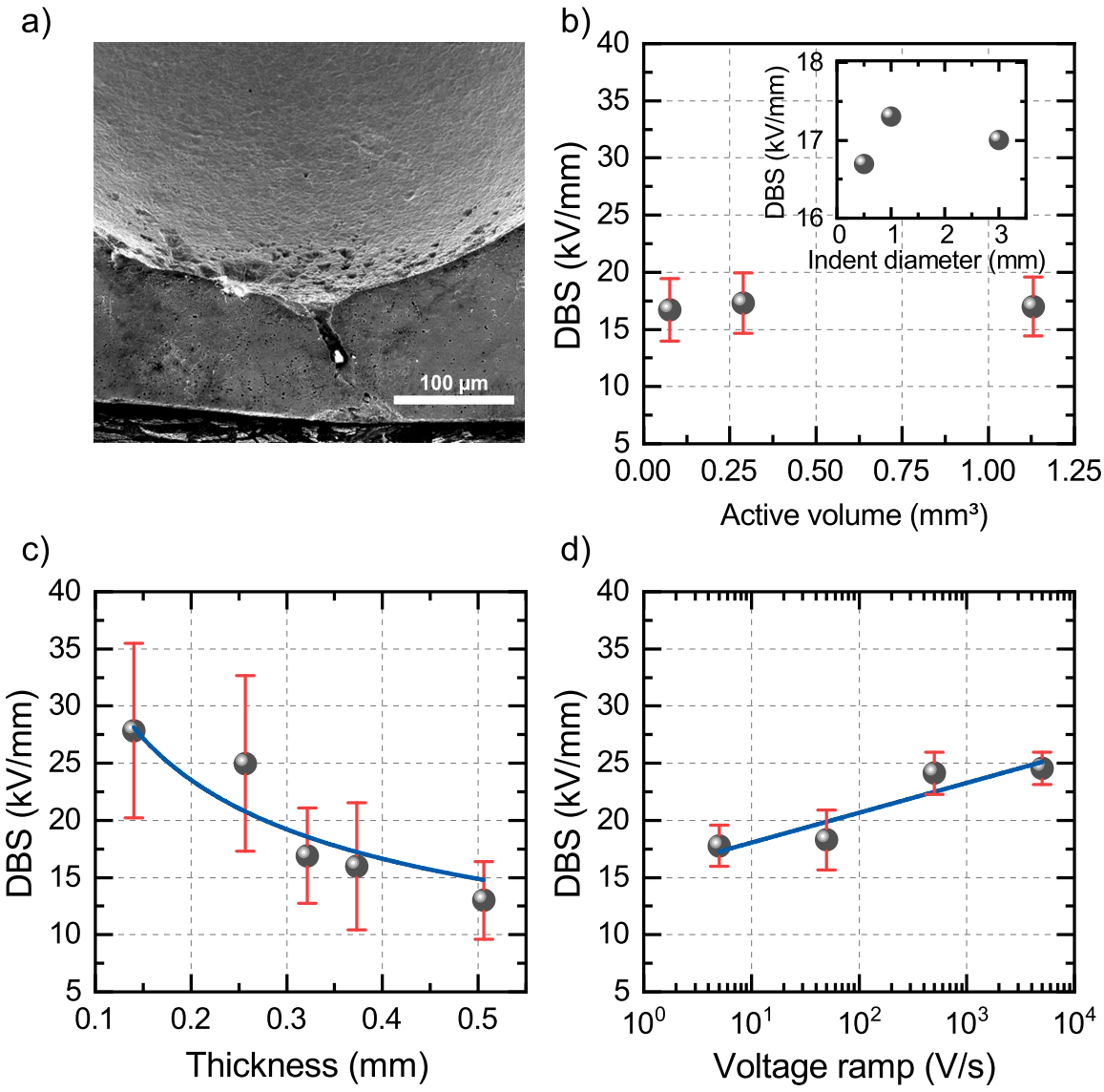

Figure 4.44: a) Micrograph of a breakdown site, which demonstrates that the breakdown channel was formed at the thinnest part of the sample, plotted DBS against b) the active volume (indent diameter in the inset), c) the thickness, and d) the voltage ramp, adapted from Gehringer et al.[73] The blue dashed fit in c) is according to $1/\sqrt{\text{thickness}}$ and a voltage ramp of 50 V/s was applied. In d) a fixed thickness of 0.33 mm was used and the blue dashed line is a guide to the eye only.

A novel, efficient, and fast method to prepare arch-shaped indents on the surface of ceramic green stacks was successfully developed. Not only experimental results but also FEM calculations ascertain that well-known electrode edge effects can be eliminated. It further focuses on the probability of a breakdown to the thinnest part of the sample, i.e., in the center of the indent. This method was then validated by DBS measurements of $BaTiO_3$ regarding sample thickness, volume, and voltage ramp.

With the approved indentation method and gained knowledge throughout this work, a transfer to the

actual NBT-based MLCCs is required. For real-world applications, it is essential to know not only the truly intrinsic DBS of the dielectric material but also the capacitor as a component. It would be of greatly beneficial to specify limits and operational windows to increase reliability during operation. Figure 4.45(a) features the thickness-dependence of NBT-BT-CZ-BA laminates, which is according to the $1/\sqrt{\text{thickness}}$ relation. Extrapolation to the actual layer thickness of 47 µm suggests an extreme DBS of around 65 kV/mm. Note that only laminates were tested. The range of error increased with decreasing thickness. A single breakdown event could be recorded at an electric field of about 90 kV/mm. However, it is unclear why such high electric fields could be applied. The indents were created according to the work by Gehringer et al.[73] Such high extrapolated values underline the robustness of the prepared NBT-BT-CZ-BA material, but also of the laminate and MLCC preparation route. Figure 4.45(b) displays the Weibull modulus of Ω-MLCCs. Thus, the complete component design, dimensions, and inner electrodes significantly contribute to the obtained Weibull parameters. While a Weibull modulus of 10.5 is considered sound,[281] the DBS value cannot compete with the extrapolated value of 65 kV/mm. Nevertheless, a remarkable value of 34.4 kV/mm was determined by measuring 11 prototype MLCCs. In comparison to NBT- and BT-based MLCCs with either Ag/Pd or Pt inner electrodes and comparable layer thicknesses, it can be deduced that 34 kV/mm is slightly higher than the average DBS value of 32 kV/mm.[11,116,117,282] The range was between 12 and 45 kV/mm. Compared MLCCs were also listed in Figure 2.8. Note that the layer thicknesses of compared MLCCs are always thinner (30-42 µm). This encourages the stability of prepared prototype MLCCs, which exhibit a slightly higher thickness of about 47 µm. The obtained value of 34.4 kV/mm is close to the maximum electric field of 32 kV/mm applied during hysteresis measurements at room temperature in Figure 4.29(a). This correlation once again supports the robustness of the prepared prototype MLCCs. Likely, the improvements in the slurry composition and shaping processes of green laminates/stacks contributed to the obtained Weibull parameters. For example, small grain sizes and lower porosities facilitate high dielectric breakdown strengths.[156,269,283] However, breakdown sites could mainly be detected close to the edges of inner electrodes, indicating a weak spot in the component design. Considering future designs of MLCCs, the appearance of the inner electrodes needs to be considered. This adjustment would likely enhance the reliability of such capacitors.

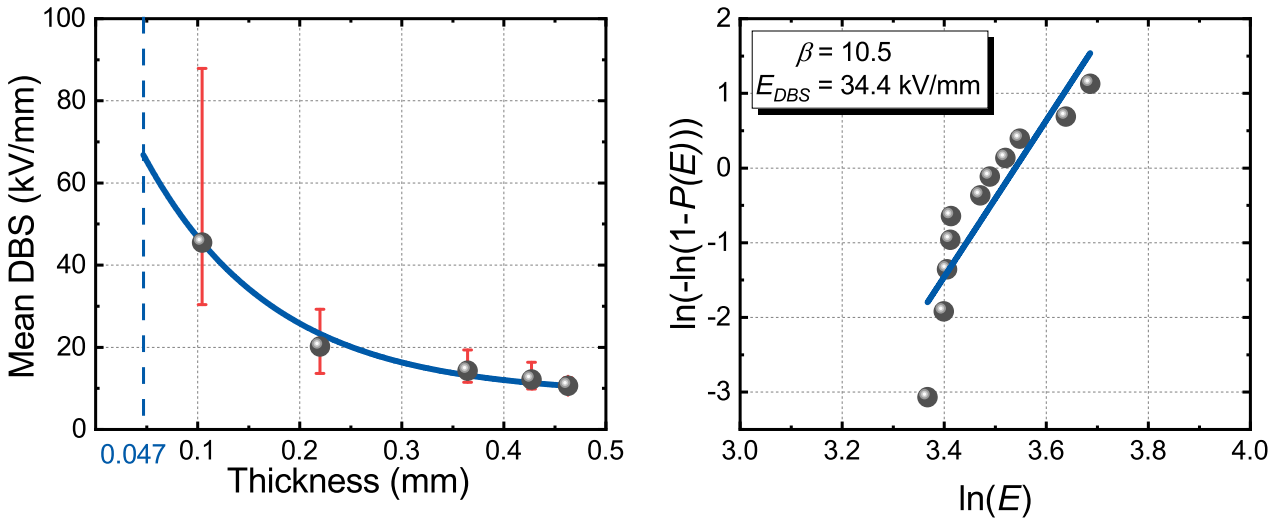

(a) Thickness-dependence of DBS of indented NBT-BT-CZ-BA laminates with extrapolation to the actual layer thickness of the Ω-MLCCs.

(b) Established failure probability of the Ω-MLCCs with Weibull parameters attached.

Figure 4.45: Thickness-dependence of DBS of indented NBT-BT-CZ-BA laminates and Weibull probability of the Ω-MLCCs.

5 Conclusion and Outlook

With this work, a pivotal proof of concept for the fabrication of $Na_{0.5}Bi_{0.5}TiO_3$-based MLCCs with Ag/Pd inner electrodes, specifically tailored for the demanding field of high-temperature and power electronics applications, could be provided. The findings have unveiled a remarkably versatile and stable prototype capacitor that holds immense promise for the future. These MLCCs have not only showcased their viability but also have the potential to alleviate a substantial burden when it comes to industrial validation. A systematic approach to improving the four designated influencing factors (slurry composition, shaping processes, sintering conditions, and electrode material) was the basis of this work. The capacitors' performance regarding capacitance, voltage tolerance, ripple current handling, low dielectric loss, capacitance stability across a broad range of temperatures, and cost-effectiveness have gained significant advancements.

Initially, prepared MLCCs exhibited a rather porous structure with a relative density lower than 95% and considerable stacking mismatch of individual layers. This was reflected in the high-temperature properties and especially the dielectric loss. Compared to the bulk reference, the dielectric loss was beyond 2% already around 320 °C. Lower porosities are necessary to increase the reliability of prepared prototype MLCCs.

The slurry composition was one of the most severe influencing factors contributing to high porosities. The chosen ratio of ingredients and type of ingredients seemed to be responsible for it. The increased amount of a different dispersant and lowered amount of a different plasticizer allowed for higher solid loading. Additionally, a solvent with a slower evaporation rate enhanced the sedimentation behavior. Good processability of the adapted slurry could be maintained while the green density of the sheets and stacks could be raised. To this end, TG-DSC investigations revealed complete decomposition of the changed organic additives.

In addition, various shaping processes were reviewed. An additional milling step of the calcined powder decreased the d_{90} value to 0.92 µm, which helped to improve the sedimentation behavior further. To prevent cracking and promote more uniform green tapes, a drying chamber without air flow and at a constant substrate temperature of 25 °C was beneficial during tape drying. Ultimately, advanced equipment for sheet cutting, screen printing, stacking, lamination, and dicing was necessary to obtain green MLCCs without stacking mismatch but with excellent lamination. These findings stress the importance of process engineering and its contribution to the final performance of manufactured MLCCs.

The thermal treatment as an additional influencing factor was investigated. Although the ceramic would be co-fired with Ag/Pd inner electrodes, they were excluded for this part. By preparing laminates, harsh

sintering conditions were adjusted without risking interactions arising from the electrodes. This indeed helped to reach sufficiently high relative densities of 96% when sintered at 1130 °C for 120 min. However, these laminates still did not exhibit acceptable dielectric properties. The dielectric loss was above 2% already below 300 °C. Since the share of organic additives in the dried green tape was close to 50% before adapting the slurry composition, it was hypothesized that this leads to a considerable amount of voids during the binder burnout. Thus, densification during the sintering step was less pronounced.
Furthermore, co-firing the green MLCCs revealed heavy interactions between the ceramic and Ag/Pd electrodes. It was concluded to keep the sintering temperature at 1100 °C and 120 min. When sintering at 1130 °C, close to the melting point of 70/30 Ag/Pd, dissolution and segregation of metal electrodes were evidenced by SEM and EDX investigations. Secondary phases around the electrode-dielectric interface were found. It is believed that due to the possible migration of Ag into the NBT matrix, the formation of $(Ag_{Bi}^{''} - V_O^{\bullet\bullet})^x$ defect dipoles accompanied by an increase of oxygen vacancies could take place. Adding 0.5 mol% Li_2CO_3 as a sintering aid was a viable approach to lower the sintering temperature to 1050 °C while keeping the desired dielectric properties. Nevertheless, suppressing possible migration of electrode material and reactions between the dielectric and electrodes was considered a key factor for reliable capacitors. This is achieved by keeping the sintering temperature for the prototype MLCCs at 1100 °C, even without sintering aids.
The gained knowledge and experience from prior optimization of processing steps of the MLCC fabrication route were put together to prepare prototype MLCCs as the main part of this work. Microstructural investigations have unveiled a homogeneous microstructure. Notably, a significant reduction of porosity was achieved to 3%. The dielectric layers and the Ag/Pd inner electrodes exhibited excellent flatness without delamination. Through EDX measurements, evidence was provided that segregation and dissolution of Ag/Pd were suppressed. Possible diffusion of Ag or Pd appeared to be drastically reduced. Manufactured NBT-based prototype MLCCs showcased an impressive operational window. They could be operated in a temperature range from -67 to 375 °C and applied voltages of up to 1.5 kV with only slight variations of capacitance and low dielectric loss. At voltages of about 1 kV and temperatures of 125 °C, the capacitance was reduced by only 13%. Temperature-dependent P-E loops confirmed the impressive stability of the capacitors. An efficiency of 87% was realized at 500 V and 150 °C. In terms of stability against voltage and temperature, they are superior compared to commercially available capacitors for high-temperature power electronics applications. The highly resistive behavior at elevated temperatures, confirmed by impedance investigations, suggested a high resilience against the migration of oxygen vacancies.
Investigations on reliability and electrical fatigue shed light on the degradation mechanisms of NBT and NBT-based materials. Electroformation was evidenced to be non-linearly dependent on the oxygen vacancy or acceptor concentration, respectively. Even differences between bulk and surface processes were detected and rationalized. Although NBT-based materials exhibit a complex defect chemistry, the prototype laminates and MLCCs seem to be quite resistant against degradation under harsh operating conditions. On the other side, a novel, fast, and efficient method to prepare green laminates with arch-shaped indents was developed. With the help of this method, the dielectric breakdown behavior could be elucidated in more detail. Electrode edge effects affecting the dielectric breakdown strength

could be eliminated, and the breakdown event localized. Extrinsic influences were narrowed down with this new approach. The failure probability of prototype MLCCs was quantified with the help of a Weibull distribution. It revealed a substantial dielectric breakdown strength of 344 kV/cm, which is considered rather high with respect to a layer thickness of 47 µm.
For future development, it needs to be stressed that co-firing electrodes with ceramics is a challenging but mandatory task. Especially for complex lead-free perovskites, the defect chemistry has to be investigated. Diffusion and migration of electrode material can be one of the most critical impacts and severely lower the reliability of prepared components. By using the aforementioned approach, considerable suppression of interactions between the dielectric and electrode material was achieved. However, the type of electrode material may be the most important aspect of an economic MLCC fabrication. The production costs of an MLCC co-fired with base metal electrodes like copper could lower the costs significantly. Therefore, a huge driving force to replace precious metals is evident. This thesis explained how sintering aids, Li_2CO_3 in particular, can lower the sintering temperature. Ultimately, this could facilitate the use of base metals. However, BMEs would need reducing atmosphere to prevent oxidation. Vice versa, reducing NBT-based materials would inherently increase the oxygen vacancy concentration. Added sintering aids could also influence the dielectric properties by incorporating into the host lattice. The sensitivity of NBT-based ceramics regarding changes in defect chemistry could detrimentally affect electrical properties during operation under harsh conditions. The findings about electrodegradation and dielectric breakdown provided a sound basis for the development of optimization strategies of reliability. They further contributed to the understanding of electrical fatigue of prototype MLCCs. Manufacturing NBT-based MLCCs with BMEs is a challenging task for future work, though. This thesis has given the starting point for it. All of the above considerations will, ultimately, pave the way for the utilization of economical NBT-based multilayer ceramic capacitors for high-temperature and power electronics applications.

6 Declaration of Competing Interest

Maximilian Gehringer, An-Phuc Hoang, and Till Frömling have filed a patent application under number DE 102022114964 A1.

7 Acknowledgments

First and foremost, I would like to express my sincere gratitude to Dr. Till Frömling, who supervised me through all stages of being a student in the working group of NAW. I am incredibly thankful for the fruitful scientific discussions during my PhD. Your deep perspective on defect chemistry and your industrial perspective on the project were invaluable and helped me to master the challenges of this work. Whether writing publications or patent applications, supervising students, or ordering needed lab equipment, your feedback was always appreciated. I honestly enjoyed the social climate in our project group and your very kind supervision.

Further, I want to thank Prof. Jürgen Rödel for giving me the opportunity to pursue my PhD in his research group NAW. Your continuous scientific feedback and assistance, particularly at the beginning of my PhD, were precious. Your concise directives were helped to guide the group through Corona and keep up the working atmosphere.

I would like to express my deep gratitude to Dr. Lovro Fulanović for not only sharing and solving the same issues concerning tape casting and further processing but also for his extremely valuable advice during my research. I truly enjoyed our discussions about science but also the large amount of spare time activities shared.

I want to acknowledge Prof. Andreas Klein for allowing me to be somewhat part of the FLAME project and for hosting the FLAME-inars, which were often related to my work. My thanks go to him and Prof. Anke Weidenkaff for their time and for being in the committee.

A special thanks goes to Prof. Barbara Malič for being in the committee and supervising me during my research stay at the K5 Electronic Ceramics Department at the Jožef Stefan Institute in Ljubljana, Slovenia. I genuinely appreciated every discussion with you about science, research, and life. Without the experience gained during this time, this work would not have been possible.

A very, very big thank you goes to Gila Völzke, Daniel Isaia, and Patrick Breckner for keeping the working group running and for having very open and personal conversations with them. Without their administrative and technical support, the working group would not work as it does.

Another big thank you goes to An-Phuc Hoang for her continuous support from the beginning of my studies until the very end of my PhD and after work. Having you as a colleague and very close friend in the project was very relieving during tough times. It was a pleasure to work with you.

I also would like to thank Daniel, Andi, and my office mate Michi for their valuable time during the PhD and also apart from it.

In addition, I want to thank the entire NAW for their support and the comfortable and motivational working atmosphere. Thank you for all the amusing spare time activities we had. I would like to express my gratitude to all my (former) colleagues: Ahmad, Alex, Changhao, Fangping, Hamed, Jurij, Kuan, Lei, Lukas, Maohua, Maryam, Mehrzad, Mihail, Oliver, Peter, Qaisar, Sabrina, Shuang, Sophie, Wolfgang, and Xufei.

Furthermore, I want to express my appreciation to my bachelor's student, Wanja Fichera, ARL student, Giorgio De Checchi, and master's student, Rizabek Bolat, for giving me the opportunity to supervise you.

Thank you, Silvo Drnovšek and Andrej Debevec, for introducing me to the equipment and enabling me to research during my research stay independently. Thank you, Brigita Kmet, for your time at the SEM investigating prepared laminates and MLCCs.

An exceptional thanks goes to Dr. Kostja Makarovič for his very helpful hints and advice regarding the slurry preparation and tape casting. It was a pleasure going on a scuba dive at night with you. Thank you also for showing me the industrial plants of tape casting and the manufacture of capacitors.

Another warmhearted thanks goes to Dr. Matej Šadl, who organized our hike to the top of Mount Triglav. I am deeply grateful for my charming office mate, Oana Andreea Condurache, during the research stay. Thank you for all the scientific discussions and your advice on how to handle Slovene. Thank you Barbara, Danjela, Lia, Maja, Matic, Maria, Mirela, Mojca, Sabi, Samir, Tina, and the above colleagues and friends from K5 for the enjoyable time at work but also the spare time in Ljubljana and Slovenia.

Thank you so much, Constanze, for your exuberant and ongoing support during the last few years and your patience, especially during hard times.

Last, I want to thank my parents, Gabriele and Friedbert, for their love and help throughout my life. This is concise but by far the biggest thank you.

8 Supplementary Material

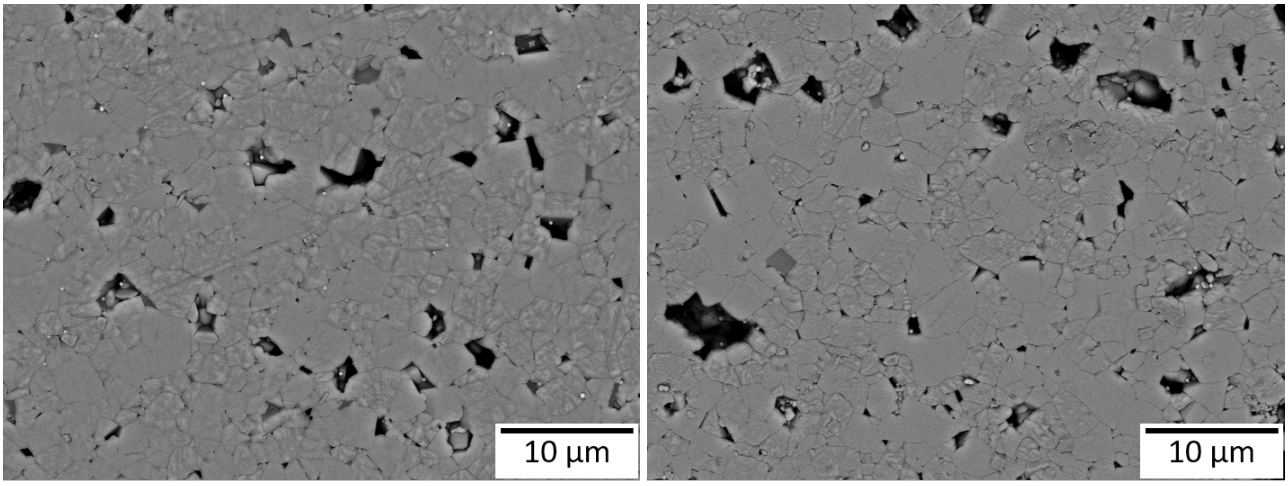

(a) 2500x magnification and ZrO_2 as inner electrode filler.

(b) 2500x magnification and $BaTiO_3$ as inner electrode filler.

Figure 8.1: Magnified SEM micrographs of the A-MLCCs' dielectric.

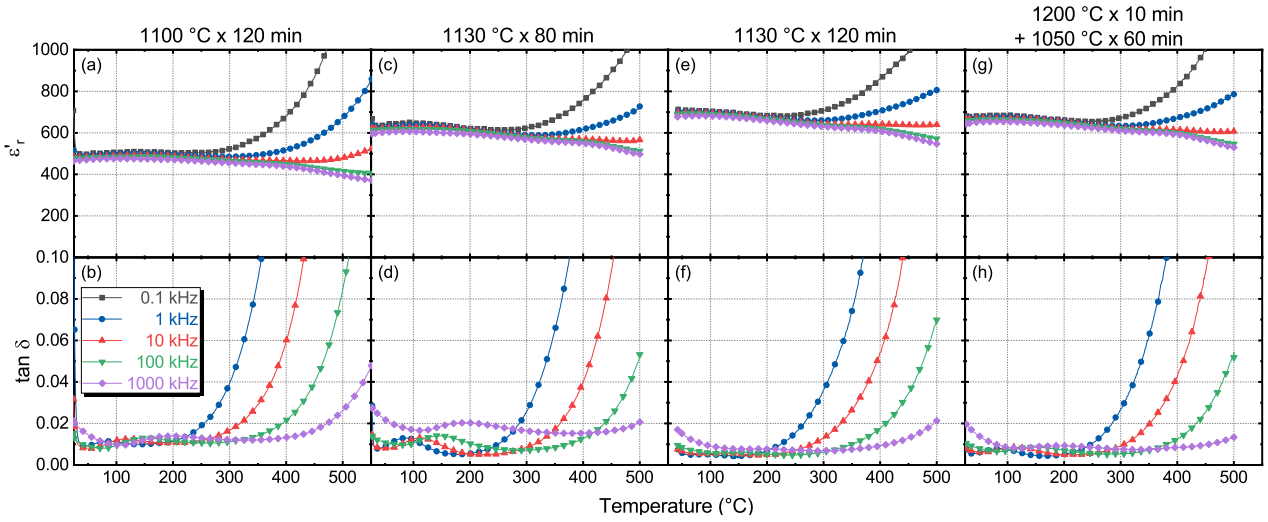

Figure 8.2: Dielectric properties of NBT-based laminates sintered at different sintering conditions. The first sample (a) and (b) was sintered at 1100 °C for 120 min, the second sample (c) and (d) at 1130 °C for 80 min, the third sample (e) and (f) at 1130 °C and 120 min, and the forth sample (g) and (h) as a two-step sintering process at 1200 °C for 10 min first and subsequently at 1050 °C for 60 min.

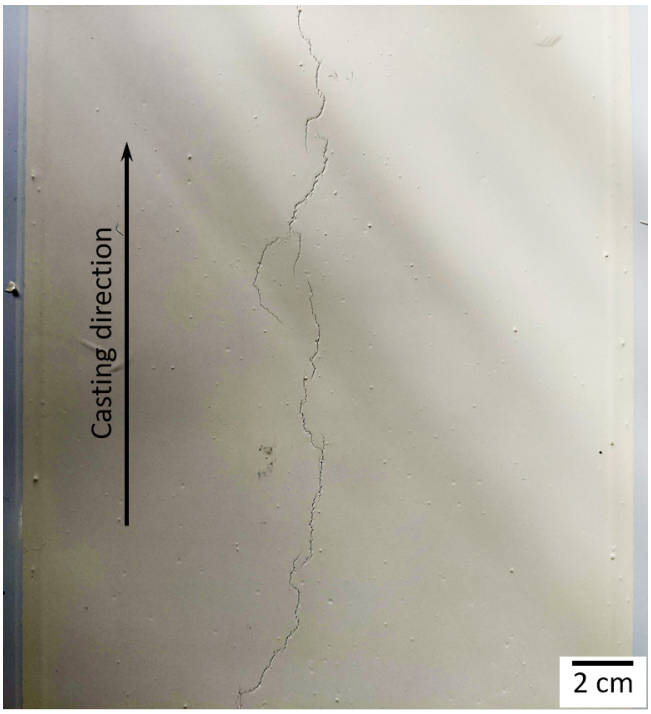

Figure 8.3: Dried green tape exhibiting typical center cracking along the casting direction.

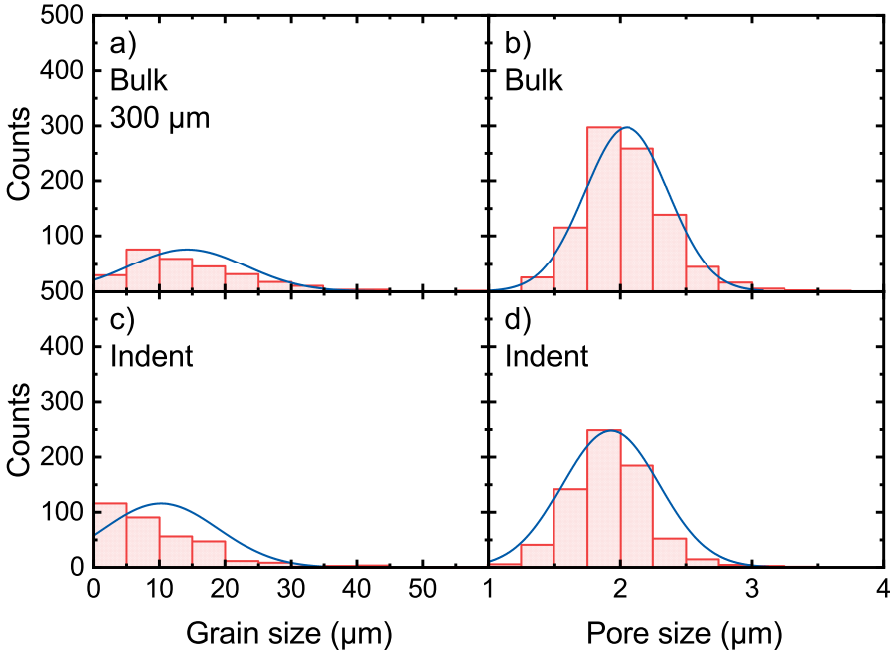

Figure 8.4: Histograms of grain and pore size exemplary shown for 170 µm sintered indent depth. a) and b) correspond to the grain and pore size of the bulk. c) and d) represents the grain and pore size of the area below the indent.

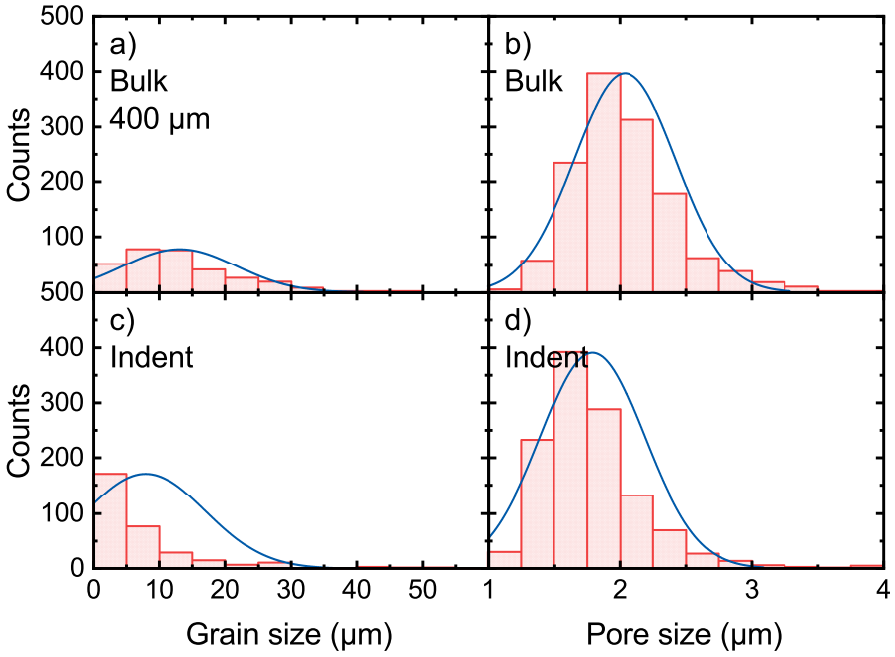

Figure 8.5: Histograms of grain and pore size exemplary shown for 265 µm sintered indent depth. a) and b) correspond to the grain and pore size of the bulk. c) and d) represents the grain and pore size of the area below the indent.

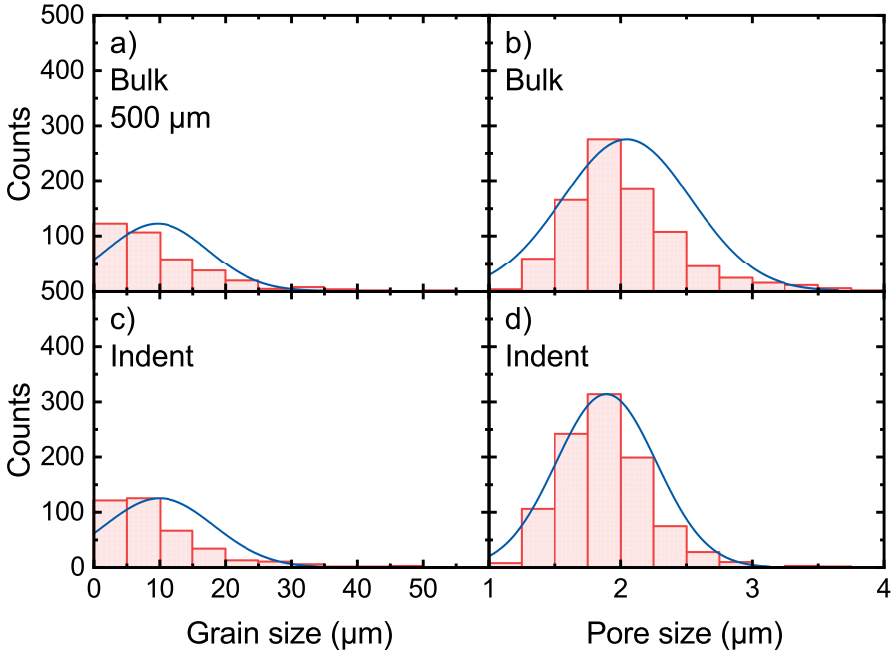

Figure 8.6: Histograms of grain and pore size exemplary shown for 390 µm sintered indent depth. a) and b) correspond to the grain and pore size of the bulk. c) and d) represents the grain and pore size of the area below the indent.

Bibliography

[1]I. Dincer and C. Acar, “A review on clean energy solutions for better sustainability”, International Journal of Energy Research **39**, 585–606 (2015).

[2]S. Chu, Y. Cui, and N. Liu, “The path towards sustainable energy”, Nature Materials **16**, 16–22 (2017).

[3]G. Wang, Z. Lu, Y. Li, L. Li, H. Ji, A. Feteira, D. Zhou, D. Wang, S. Zhang, and I. M. Reaney, “Electroceramics for High-Energy Density Capacitors: Current Status and Future Perspectives”, Chemical Reviews **121**, 6124–6172 (2021).

[4]Q. Li, F.-Z. Yao, Y. Liu, G. Zhang, H. Wang, and Q. Wang, “High-Temperature Dielectric Materials for Electrical Energy Storage”, Annual Review of Materials Research **48**, 219–243 (2018).

[5]Y. Xiao, Z. Zhang, M. S. Duraij, T. G. Zsurzsan, and M. A. Andersen, “Review of High-Temperature Power Electronics Converters”, IEEE Transactions on Power Electronics **37**, 14831–14849 (2022).

[6]S. Lande, “Supply and demand for high temperature electronics”, HITEN 1999 - 3rd European Conference on High Temperature Electronics, 133–135 (1999).

[7]C. Buttay, D. Planson, B. Allard, D. Bergogne, P. Bevilacqua, C. Joubert, M. Lazar, C. Martin, H. Morel, D. Tournier, and C. Raynaud, “State of the art of high temperature power electronics”, Materials Science and Engineering B: Solid-State Materials for Advanced Technology **176**, 283–288 (2011).

[8]S. Yang, A. Bryant, P. Mawby, D. Xiang, L. Ran, and P. Tavner, “An industry-based survey of reliability in power electronic converters”, IEEE Transactions on Industry Applications **47**, 1441–1451 (2011).

[9]J. Falck, C. Felgemacher, A. Rojko, M. Liserre, and P. Zacharias, “Reliability of Power Electronic Systems”, IEEE Industrial Electronics Magazine **12**, 24–35 (2018).

[10]A. Zeb and S. J. Milne, “High temperature dielectric ceramics: a review of temperature-stable high-permittivity perovskites”, Journal of Materials Science: Materials in Electronics **26**, 9243–9255 (2015).

[11]X. Liu, Y. Hou, B. Song, H. Cheng, Y. Fu, M. Zheng, and M. Zhu, “Lead-free multilayer ceramic capacitors with ultra-wide temperature dielectric stability based on multifaceted modification”, Journal of the European Ceramic Society **42**, 973–980 (2022).

[12]X. Guo, Q. Xun, Z. Li, and S. Du, “Silicon Carbide Converters and MEMS Devices for High-temperature Power Electronics: A Critical Review”, Micromachines **10**, 406 (2019).

[13]J. Watson and G. Castro, “A review of high-temperature electronics technology and applications”, Journal of Materials Science: Materials in Electronics **26**, 9226–9235 (2015).

[14]P. Yousefian and C. A. Randall, “Power Electronic Devices and Components Quality assessment and lifetime prediction of base metal electrode multilayer ceramic capacitors : Challenges and opportunities”, Power Electronic Devices and Components **6**, 100045 (2023).

[15]H. Wang and F. Blaabjerg, “Reliability of capacitors for DC-link applications in power electronic converters - An overview”, IEEE Transactions on Industry Applications **50**, 3569–3578 (2014).

[16]G. F. Engel, “Material requirements for power and high temperature multilayer ceramic capacitors (MLCC)”, in Imaps/acers 11th international conference and exhibition on ceramic interconnect and ceramic microsystems technologies, cicmt 2015, April 2015 (2015), pp. 21–28.

[17]H. Ogihara, C. A. Randall, and S. Trolier-Mckinstry, “High-energy density capacitors utilizing 0.7 baTiO3-0.3 BiScO3 ceramics”, Journal of the American Ceramic Society **92**, 1719–1724 (2009).

[18]Huiqing Wen, Weidong Xiao, Xuhui Wen, and P. Armstrong, “Analysis and Evaluation of DC-Link Capacitors for High-Power-Density Electric Vehicle Drive Systems”, IEEE Transactions on Vehicular Technology **61**, 2950–2964 (2012).

[19]H. Wang, M. Liserre, F. Blaabjerg, P. de Place Rimmen, J. B. Jacobsen, T. Kvisgaard, and J. Landkildehus, “Transitioning to Physics-of-Failure as a Reliability Driver in Power Electronics”, IEEE Journal of Emerging and Selected Topics in Power Electronics **2**, 97–114 (2014).

[20]D. Tan, L. Zhang, Q. Chen, and P. Irwin, “High-Temperature Capacitor Polymer Films”, Journal of Electronic Materials **43**, 4569–4575 (2014).

[21]J. Both, “The modern era of aluminum electrolytic capacitors”, IEEE Electrical Insulation Magazine **31**, 24–33 (2015).

[22]P. Zhao, Z. Cai, L. Wu, C. Zhu, L. Li, and X. Wang, “Perspectives and challenges for lead-free energy-storage multilayer ceramic capacitors”, Journal of Advanced Ceramics **10**, 1153–1193 (2021).

[23]TDK Electronics AG, *Capacitors for fast-switching semiconductors - Low profile (LP) series B58031U5105M062*, 2019.

[24]J. Rödel, W. Jo, K. T. Seifert, E. M. Anton, T. Granzow, and D. Damjanovic, “Perspective on the development of lead-free piezoceramics”, Journal of the American Ceramic Society **92**, 1153–1177 (2009).

[25]J. Koruza, A. J. Bell, T. Frömling, K. G. Webber, K. Wang, and J. Rödel, “Requirements for the transfer of lead-free piezoceramics into application”, Journal of Materiomics **4**, 13–26 (2018).

[26]L. Yang, X. Kong, F. Li, H. Hao, Z. Cheng, H. Liu, J. F. Li, and S. Zhang, “Perovskite lead-free dielectrics for energy storage applications”, Progress in Materials Science **102**, 72–108 (2019).

[27]A. Zeb, Y. Bai, T. Button, and S. J. Milne, “Temperature-Stable Relative Permittivity from -70°C to 500°C in (Ba0.8Ca0.2)TiO3-Bi(Mg0.5Ti0.5)O3-NaNbO3 Ceramics”, Journal of the American Ceramic Society **97**, edited by W. Jo, 2479–2483 (2014).

[28]P. Ren, J. Wang, J. He, Y. Wang, H. Yuan, Y. Hao, T. Frömling, Y. Wan, Y. Shi, and G. Zhao, "Ultrawide Temperature Range with Stable Permittivity and Low Dielectric Loss in (1-x)[0.90Na0.5Bi0.5TiO3-0.10BiAlO3]-xNaNbO3 System", Advanced Electronic Materials **1901429**, 1–9 (2020).

[29]A.-P. Hoang, S. Steiner, F. Yang, L. Li, D. C. Sinclair, and T. Frömling, "Reducing dielectric loss in Na0.5Bi0.5TiO3 based high temperature capacitor material", Journal of the European Ceramic Society **41**, 2587–2595 (2021).

[30]M. Chen, Y. Pu, and L. Zhang, "Novel NBT-based relaxor ferroelectric ceramics with excellent discharge performance and high-temperature stability", Journal of Materials Science: Materials in Electronics **32**, 23540–23553 (2021).

[31]G. A. Samara, "The relaxational properties of compositionally disordered ABO 3 perovskites", Journal of Physics: Condensed Matter **15**, R367–R411 (2003).

[32]V. V. Shvartsman and D. C. Lupascu, "Lead-free relaxor ferroelectrics", Journal of the American Ceramic Society **95**, 1–26 (2012).

[33]A. Pramanick and S. Nayak, "Perspective on emerging views on microscopic origin of relaxor behavior", Journal of Materials Research **36**, 1015–1036 (2021).

[34]M. Acosta, J. Zang, W. Jo, and J. Rödel, "High-temperature dielectrics in CaZrO3-modified Bi1/2Na1/2TiO3-based lead-free ceramics", Journal of the European Ceramic Society **32**, 4327–4334 (2012).

[35]M. Höfling, S. Steiner, A. P. Hoang, I. T. Seo, and T. Frömling, "Optimizing the defect chemistry of Na1/2Bi1/2TiO3-based materials: Paving the way for excellent high temperature capacitors", Journal of Materials Chemistry C **6**, 4769–4776 (2018).

[36]T. R. Shrout and S. J. Zhang, "Lead-free piezoelectric ceramics: Alternatives for PZT?", Journal of Electroceramics **19**, 111–124 (2007).

[37]J. Rödel, A. B. Kounga, M. Weissenberger-Eibl, D. Koch, A. Bierwisch, W. Rossner, M. J. Hoffmann, R. Danzer, and G. Schneider, "Development of a roadmap for advanced ceramics: 2010-2025", Journal of the European Ceramic Society **29**, 1549–1560 (2009).

[38]K. Uchino, J. H. Zheng, Y. H. Chen, X. H. Du, J. Ryu, Y. Gao, S. Ural, S. Priya, and S. Hirose, "Loss mechanisms and high power piezoelectrics", Journal of Materials Science **41**, 217–228 (2006).

[39]M. Li, M. J. Pietrowski, R. A. De Souza, H. Zhang, I. M. Reaney, S. N. Cook, J. A. Kilner, and D. C. Sinclair, "A family of oxide ion conductors based on the ferroelectric perovskite Na0.5Bi0.5TiO3", Nature Materials **13**, 31–35 (2014).

[40]I. T. Seo, S. Steiner, and T. Frömling, "The effect of A site non-stoichiometry on 0.94(NayBix)TiO3-0.06BaTiO3", Journal of the European Ceramic Society **37**, 1429–1436 (2017).

[41]F. Yang, M. Li, L. Li, P. Wu, E. Pradal-Velázquez, and D. C. Sinclair, "Defect chemistry and electrical properties of sodium bismuth titanate perovskite", Journal of Materials Chemistry A **6**, 5243–5254 (2018).

[42]T. Frömling, S. Steiner, A. Ayrikyan, D. Bremecker, M. Dürrschnabel, L. Molina-Luna, H.-J. Kleebe, H. Hutter, K. G. Webber, and M. Acosta, “Designing properties of (Na 1/2 Bi x)TiO 3 -based materials through A-site non-stoichiometry”, Journal of Materials Chemistry C **6**, 738–744 (2018).

[43]K. Reichmann, A. Feteira, and M. Li, “Bismuth Sodium Titanate based materials for piezoelectric actuators”, Materials **8**, 8467–8495 (2015).

[44]S. Steiner, I. T. Seo, P. Ren, M. Li, D. J. Keeble, and T. Frömling, “The effect of Fe-acceptor doping on the electrical properties of Na1/2Bi1/2TiO3 and 0.94 (Na1/2Bi1/2)TiO3–0.06 BaTiO3”, Journal of the American Ceramic Society **102**, 5295–5304 (2019).

[45]L. Koch, S. Steiner, A. P. Hoang, A. J. Klomp, K. Albe, and T. Frömling, “Revealing the impact of acceptor dopant type on the electrical conductivity of sodium bismuth titanate”, Acta Materialia **229**, 117808 (2022).

[46]L. Koch, S. Steiner, K. C. Meyer, I. T. Seo, K. Albe, and T. Frömling, “Ionic conductivity of acceptor doped sodium bismuth titanate: Influence of dopants, phase transitions and defect associates”, Journal of Materials Chemistry C **5**, 8958–8965 (2017).

[47]D. Schuetz, W. Krauss, J. Albering, C. Kurta, and K. Reichmann, “The chemical interaction of silver-palladium alloy electrodes with bismuth-based piezomaterials”, Journal of the American Ceramic Society **93**, 1142–1147 (2010).

[48]I. Karakaya and W. T. Thompson, “The Ag-Pd (Silver-Palladium) system”, Bulletin of Alloy Phase Diagrams **9**, 237–243 (1988).

[49]C. W. Ahn, S. Nahm, J. Ryu, K. Uchino, S. J. Yoon, S. J. Jung, and J. S. Song, “Effects of CuO and ZnO Additives on Sintering Temperature and Piezoelectric Properties of 0.41Pb(Ni1/3Nb2/3)O3-0.36PbTiO3-0.23PbZrO3 Ceramics”, Japanese Journal of Applied Physics, Part 1: Regular Papers and Short Notes and Review Papers **43**, 205–210 (2004).

[50]C. Groh, K. Kobayashi, H. Shimizu, Y. Doshida, Y. Mizuno, E. A. Patterson, and J. Rödel, “High-Temperature Multilayer Ceramic Capacitors Based on 100-x(94Bi1/2Na1/2TiO3-6BaTiO3)-xK0.5Na0.5NbO3”, Journal of the American Ceramic Society **99**, 2040–2046 (2016).

[51]N. J. Donnelly, T. R. Shrout, and C. A. Randall, “Properties of (1-x)PZT-xSKN Ceramics Sintered at Low Temperature Using Li2CO3”, Journal of the American Ceramic Society **91**, 2182–2188 (2008).

[52]G. Yesner, M. Kuciej, and A. Safari, “Low temperature sintering of Bi0.5Na0.5TiO3 based ceramics”, 2015 Joint IEEE International Symposium on the Applications of Ferroelectric, International Symposium on Integrated Functionalities and Piezoelectric Force Microscopy Workshop, ISAF/ISIF/PFM 2015, 21–23 (2015).

[53]L. Gao, H. Guo, S. Zhang, and C. Randall, “Base Metal Co-Fired Multilayer Piezoelectrics”, Actuators **5**, 8 (2016).

[54]T. Frömling, A. Schintlmeister, H. Hutter, and J. Fleig, "Oxide ion transport in donor-doped Pb(ZrxTi1-x)O 3: The role of grain boundaries", Journal of the American Ceramic Society **94**, 1173–1181 (2011).

[55]H. Ossmer, C. Slouka, L. Andrejs, P. Blaha, G. Friedbacher, and J. Fleig, "Electrocoloration of donor-doped lead zirconate titanate under DC field stress", Solid State Ionics **281**, 49–59 (2015).

[56]L. Andrejs and J. Fleig, "Resistance degradation in donor-doped PZT ceramic stacks with Ag/Pd electrodes: I. Phenomenology of processes", Journal of the European Ceramic Society **33**, 779–794 (2013).

[57]L. Andrejs, H. Oßmer, G. Friedbacher, J. Bernardi, A. Limbeck, and J. Fleig, "Conductive AFM and chemical analysis of highly conductive paths in DC degraded PZT with Ag/Pd electrodes", Solid State Ionics **244**, 5–16 (2013).

[58]L. Andrejs, H. Oßmer, G. Friedbacher, and J. Fleig, "Resistance degradation in donor-doped PZT ceramic stacks with Ag/Pd electrodes: II. Distribution of conduction paths", Journal of the European Ceramic Society **33**, 1165–1176 (2013).

[59]N. Iwagami, H. Nagata, I. Sakaguchi, and T. Takenaka, "Diffusion behavior of Ag electrodes into (Bi1/2Na1/2)TiO3 ceramics", Journal of the Ceramic Society of Japan **124**, 644–647 (2016).

[60]E. Sapper, A. Gassmann, L. Gjødvad, W. Jo, T. Granzow, and J. Rödel, "Cycling stability of lead-free BNT-8BT and BNT-6BT-3KNN multilayer actuators and bulk ceramics", Journal of the European Ceramic Society **34**, 653–661 (2014).

[61]T. Raymond, D. Wilson, and B. Clifford, *Platinum perspectives*, tech. rep. (World Platinum Investment Council, London, 2021).

[62]*Electroplating Edelmetallpreise | Umicore, URL: https://mds.umicore.com/de/electroplating/aktuelles-medien/edelmetallpreise, October 14, 2023*.

[63]*Copper Prices | MacroTrends, URL: https://www.macrotrends.net/1476/copper-prices-historical-chart-data, October 14, 2023*.

[64]R. E. Mistler, *Tape Casting - Theory and Practice* (The American Ceramic Society, 2000).

[65]L. Ren, X. Luo, and H. Zhou, "The tape casting process for manufacturing low-temperature co-fired ceramic green sheets: A review", Journal of the American Ceramic Society **101**, 3874–3889 (2018).

[66]L. A. Salam, R. D. Matthews, and H. Robertson, "Pyrolysis of polyvinyl butyral (PVB) binder in thermoelectric green tapes", Journal of the European Ceramic Society **20**, 1375–1383 (2000).

[67]R. K. Nishihora, P. L. Rachadel, M. G. N. Quadri, and D. Hotza, "Manufacturing porous ceramic materials by tape casting—A review", Journal of the European Ceramic Society **38**, 988–1001 (2018).

[68]W. Jo, J. B. Ollagnier, J. L. Park, E. M. Anton, O. J. Kwon, C. Park, H. H. Seo, J. S. Lee, E. Erdem, R. A. Eichel, and J. Rödel, "CuO as a sintering additive for (Bi1/2Na1/2)TiO3-BaTiO3- (K0.5Na0.5)NbO3 lead-free piezoceramics", Journal of the European Ceramic Society **31**, 2107–2117 (2011).

[69]T. H. Chung and K. W. Kwok, “Low-temperature-sintered Pr-doped 0.93(Bi0.5Na0.5)TiO3-0.07BaTiO3 multifunctional ceramics with Li2CO3 sintering aid”, Journal of Alloys and Compounds **737**, 317–322 (2018).

[70]J. Glaum and M. Hoffman, “Electric fatigue of lead-free piezoelectric materials”, Journal of the American Ceramic Society **97**, 665–680 (2014).

[71]J. Rödel and G. Tomandl, “Degradation of Mn-doped BaTiO3 ceramic under a high d.c. electric field”, Journal of Materials Science **19**, 3515–3523 (1984).

[72]M. Gehringer, A.-P. Hoang, L. Fulanović, K. Makarovič, B. Malič, and T. Frömling, “Prototyping Na0.5Bi0.5TiO3-based multilayer ceramic capacitors for high-temperature and power electronics”, Journal of the European Ceramic Society **43**, 6122–6129 (2023).

[73]M. Gehringer, R. Bolat, D. Isaia, J. Rödel, and L. Fulanović, “Evaluation of dielectric breakdown of BaTiO3 by novel indentation method”, Journal of the European Ceramic Society **42**, 5652–5658 (2022).

[74]Z. Yan, “Microstructure evolution during sintering of multilayer ceramic capacitors: nanotomography and discrete simulations”, PhD thesis (2014), p. 166.

[75]M. Reisch, *Elektronische Bauelemente* (Springer Berlin Heidelberg, Berlin, Heidelberg, 2007).

[76]L. Stiny, *Passive elektronische Bauelemente* (Springer Fachmedien Wiesbaden, Wiesbaden, 2019).

[77]TDK Electronics AG, *Technical Guide - CeraLink Capacitors*, 2021.

[78]Electronic Components Industry Association (ECIA), *Ceramic Dielectric Capacitors Classes I, II, III and IV - Part I: Characteristics and Requirements - EIA-198-1*, 2002.

[79]R. R. Grzybowski and F. P. McCluskey, “High temperature performance of polymer film capacitors”, High-Temperature Electronics, 711–716 (1998).

[80]R. W. Johnson, “The changing automotive environment: High-temperature electronics”, Advanced Packaging **13**, 40 (2004).

[81]K. Hong, T. H. Lee, J. M. Suh, S. H. Yoon, and H. W. Jang, “Perspectives and challenges in multilayer ceramic capacitors for next generation electronics”, Journal of Materials Chemistry C **7**, 9782–9802 (2019).

[82]Y. Fu, Y. Hou, B. Song, H. Cheng, X. Liu, X. Yu, M. Zheng, and M. Zhu, “Construction of lead-free dielectrics for high temperature multilayer ceramic capacitors and its inner electrode matching characteristics”, Journal of Alloys and Compounds **903**, 163995 (2022).

[83]Y. Wan, F. Cao, J. Song, N. Hou, P. Ren, F. Yan, X. Lu, M. Ma, K. Song, and G. Zhao, “High-temperature dielectric properties of Bi0.5Na0.5TiO3–NaNbO3–Sr0.8Na0.4Nb2O6 ceramics”, Ceramics International **48**, 13041–13046 (2022).

[84]C. Zhu, Z. Cai, L. Guo, Y. Jiang, L. Li, and X. Wang, “Simultaneously Achieved Ultrastable Dielectric and Energy Storage Properties in Lead-Free Bi 0.5 Na 0.5 TiO 3 -Based Ceramics”, ACS Applied Energy Materials **5**, 1560–1570 (2022).

[85]T. Schulz, V. Veerapandiyan, M. Deluca, and J. Töpfer, “Synthesis and properties of lead-free BNT-BT-xCZ ceramics as high-temperature dielectrics”, Materials Research Bulletin **145**, 111560 (2022).

[86]M. Ellis and T. Williams, “Voltage Coefficient of Capacitance”, The EMC Journal (2013).

[87]L. Wu, Y. Huan, X. Wang, C. Li, Y. Luo, and T. Wei, “A combinatorial improvement strategy to enhance the energy storage performances of the KNN–based ferroelectric ceramic capacitors”, Journal of Materials Science **57**, 15876–15888 (2022).

[88]A. G. Cockbain and P. J. Harrop, “The temperature coefficient of capacitance”, Journal of Physics D: Applied Physics **1**, 302 (1968).

[89]Q. Xu, X. Huang, and H. Liu, “Dielectric and energy-storage properties in Bi0.5Na0.5TiO3-BaTiO3-AgNbO3 ternary perovskite compounds”, Journal of Materials Science: Materials in Electronics **31**, 10512–10520 (2020).

[90]J. J. O’Dwyer, “Dielectric breakdown in solids”, Advances in Physics **7**, 349–394 (1958).

[91]Y. Sun, C. Bealing, S. Boggs, and R. Ramprasad, “50+ Years of Intrinsic Breakdown”, IEEE Electrical Insulation Magazine **29**, 8–15 (2013).

[92]M. G. Cain, J. Tesař, and M. van Veghel, *Characterisation of Ferroelectric Bulk Materials and Thin Films*, edited by M. G. Cain, Vol. 2, Springer Series in Measurement Science and Technology (Springer Netherlands, Dordrecht, 2014).

[93]T. Harriehausen and D. Schwarzenau, *Moeller Grundlagen der Elektrotechnik* (Springer Fachmedien Wiesbaden, Wiesbaden, 2020).

[94]W. Matthes, *Embedded Electronics 1: Passive Bauelemente* (Elektror-Verlag, 2008), p. 382.

[95]G. Liu, S. Zhang, W. Jiang, and W. Cao, “Losses in ferroelectric materials”, Materials Science and Engineering R: Reports **89**, 1–48 (2015).

[96]Agilent Technologies, *Agilent Impedance Measurement Handbook A guide to measurement technology and techniques*, 4th Editio (Santa Clara, CA, 2009).

[97]H. L. Dang and S. Kwak, “Review of health monitoring techniques for capacitors used in power electronics converters”, Sensors **20**, 1–22 (2020).

[98]A. J. Moulson and J. M. Herbert, *Electroceramics* (Wiley, 2003).

[99]R. Waser, U. Böttger, and S. Tiedke, *Polar Oxides: Properties, Characterization, and Imaging* (WILEY-VCH Verlag GmbH & Co. KGaA, Weinheim, 2005), pp. 1–387.

[100]B. Jaffe and W. R. J. Cook, *Piezoelectric Ceramics* (Elsevier, 1971).

[101]A. K. Bain, *Ferroelectrics Principles and Applications*, Vol. 53, 9 (2013), pp. 1689–1699.

[102]R. E. Newnham, *Properties of Materials* (Oxford University Press, 2005).

[103]A. A. Bokov and Z. G. Ye, “Recent progress in relaxor ferroelectrics with perovskite structure”, Journal of Materials Science **41**, 31–52 (2006).

[104]R. A. Cowley, S. N. Gvasaliya, S. G. Lushnikov, B. Roessli, and G. M. Rotaru, “Relaxing with relaxors: A review of relaxor ferroelectrics”, Advances in Physics **60**, 229–327 (2011).

[105]C. W. Ahn, C. H. Hong, B. Y. Choi, H. P. Kim, H. S. Han, Y. Hwang, W. Jo, K. Wang, J. F. Li, J. S. Lee, and I. W. Kim, “A brief review on relaxor ferroelectrics and selected issues in lead-free relaxors”, Journal of the Korean Physical Society **68**, 1481–1494 (2016).

[106]L. E. Cross, “Relaxor ferroelectrics”, Ferroelectrics **76**, 241–267 (1987).

[107]D. H. Zhou, G. L. Hoatson, and R. L. Vold, “Local structure in perovskite relaxor ferroelectrics: High-resolution 93Nb 3QMAS NMR”, Journal of Magnetic Resonance **167**, 242–252 (2004).

[108]J. Zang, M. Li, D. C. Sinclair, W. Jo, and J. Rödel, “Impedance spectroscopy of (Bi 1/2 Na 1/2) TiO 3-BaTiO 3 ceramics modified with (K 0.5 Na 0.5) NbO 3”, Journal of the American Ceramic Society **97**, 1523–1529 (2014).

[109]J. Zang, M. Li, D. C. Sinclair, T. Frömling, W. Jo, and J. Rödel, “Impedance spectroscopy of (Bi 1/2 Na 1/2) TiO 3- BaTiO 3 based high-temperature dielectrics”, Journal of the American Ceramic Society **97**, 2825–2831 (2014).

[110]T. Frömling, Y. Liu, A. P. Hoang, M. Gehringer, S. Steiner, M. Zhuk, J. Glaum, and B. X. Xu, “Modulus spectroscopy for the detection of parallel electric responses in electroceramics”, Journal of Materiomics **8**, 556–569 (2022).

[111]X. Hao, “A review on the dielectric materials for high energy-storage application”, Journal of Advanced Dielectrics **03**, 1330001 (2013).

[112]S. I. Shkuratov and C. S. Lynch, “A review of ferroelectric materials for high power devices”, Journal of Materiomics **8**, 739–752 (2022).

[113]Y. Xu, Z. Yang, K. Xu, J. Tian, D. Zhang, M. Zhan, H. Tian, X. Cai, B. Zhang, Y. Yan, L. Guo, G. Wang, L. Lin, J. Fan, T. Wang, and Y. Tian, “Enhanced energy-storage performance in silver niobate-based dielectric ceramics sintered at low temperature”, Journal of Alloys and Compounds **913**, 165313 (2022).

[114]L. Fulanović, M.-h. Zhang, Y. Fu, J. Koruza, and J. Rödel, “NaNbO3-based antiferroelectric multilayer ceramic capacitors for energy storage applications”, Journal of the European Ceramic Society **41**, 5519–5525 (2021).

[115]C. Su, H. Hao, Q. Xu, Y. Lu, M. Appiah, C. Diao, M. Cao, Z. Yao, and H. Liu, “Manufacture and dielectric properties of X9R Bi-based lead-free multilayer ceramic capacitors with AgPd inner electrodes”, Journal of Materials Science: Materials in Electronics **27**, 6140–6149 (2016).

[116]L. Chen, H. Wang, P. Zhao, C. Zhu, Z. Cai, Z. Cen, L. Li, and X. Wang, “Multifunctional BaTiO 3 -(Bi 0.5 Na 0.5)TiO 3 -based MLCC with high-energy storage properties and temperature stability”, Journal of the American Ceramic Society **102**, 4178–4187 (2019).

[117]W. Jia, Y. Hou, M. Zheng, Y. Xu, X. Yu, M. Zhu, K. Yang, H. Cheng, S. Sun, and J. Xing, “Superior temperature-stable dielectrics for MLCCs based on Bi0.5Na0.5TiO3-NaNbO3 system modified by CaZrO3”, Journal of the American Ceramic Society **101**, 3468–3479 (2018).

[118]T. Kainz, B. Bitschnau, F. A. Mautner, and K. Reichmann, “Comparison of Lanthanum and Bismuth modification of lead Zirconate-Lead Titanate PZT-A structural and dielectric study”, Journal of the European Ceramic Society **36**, 507–514 (2016).

[119]Y. Xu, Y. Hou, B. Song, H. Cheng, M. Zheng, and M. Zhu, “Superior ultra-high temperature multilayer ceramic capacitors based on polar nanoregion engineered lead-free relaxor”, Journal of the European Ceramic Society **40**, 4487–4494 (2020).

[120]A. P. Hoang, S. Steiner, F. Yang, L. Li, D. C. Sinclair, and T. Frömling, “Reducing dielectric loss in Na0.5Bi0.5TiO3 based high temperature capacitor material”, Journal of the European Ceramic Society **41**, 2587–2595 (2021).

[121]S. Steiner, “Defect Chemistry of Sodium Bismuth Titanate and its Solid Solutions”, PhD thesis (2019).

[122]R. Dittmer, “Lead-Free Piezoceramics Ergodic and non-ergodic relaxor FE based on NBT”, PhD thesis (2013).

[123]G. Smolenskii, V. Isupov, A. Agranovskaya, and N. Krainik, “New Ferroelectrics of Complex Composition”, Soviet Physics Solid State **2**, 2651–2654 (1961).

[124]J. A. Zvirgzds, P. P. Kapostins, J. V. Zvirgzde, and T. V. Kruzina, “X-ray study of phase transitions in ferroelectric Na0.5Bi0.5TiO3”, Ferroelectrics **40**, 75–77 (1982).

[125]S. B. Vakhrushev, V. A. Isupov, B. E. Kvyatkovsky, N. M. Okuneva, I. P. Pronin, G. A. Smolensky, P. P. Syrnikov, and A. F. Ioffe, “Phase Transitions and Soft Modes in Sodium Bismuth Titanate”, Ferroelectrics **63**, 153–160 (1985).

[126]K. Roleder, A. Kania, and J. Suchanicz, “Time dependence of electric permittivity in Na0.5Bi0.5TiO3 single crystals”, Ferroelectrics **89**, 1–5 (1989).

[127]L. Li, M. Li, H. Zhang, I. M. Reaney, and D. C. Sinclair, “Controlling mixed conductivity in Na1/2Bi1/2TiO3 using A-site non-stoichiometry and Nb-donor doping”, Journal of Materials Chemistry C **4**, 5779–5786 (2016).

[128]I. P. Pronin, P. P. Syrnikov, V. A. Isupov, V. M. Egorov, N. V. Zaitseva, and A. P. Ioffe, “Peculiarities of phase transitions in sodium-bismuth titanate”, Ferroelectrics **25**, 395–397 (1980).

[129]A. Mishra, D. K. Khatua, A. De, B. Majumdar, T. Frömling, and R. Ranjan, “Structural mechanism behind piezoelectric enhancement in off-stoichiometric Na0.5Bi0.5TiO3 based lead-free piezoceramics”, Acta Materialia **164**, 761–775 (2019).

[130]F. Yang, P. Wu, and D. C. Sinclair, “Suppression of electrical conductivity and switching of conduction mechanisms in ‘stoichiometric’ (Na 0.5 Bi 0.5 TiO 3) 1-x (BiAlO 3) x (0 less than x less than 0.08) solid solutions”, Journal of Materials Chemistry C **5**, 7243–7252 (2017).

[131]C. Barry Carter and M. Grant Norton, *Ceramic materials: Science and engineering* (Springer, 2007), pp. 1–716.

[132]E. Aksel, E. Erdem, P. Jakes, J. L. Jones, and R. A. Eichel, "Defect structure and materials "hardening" in Fe2 O3 -doped [Bi0.5 Na0.5] TiO3 ferroelectrics", Applied Physics Letters **97**, 10.1063/1.3455888/166415 (2010).

[133]P. V. Lambeck and G. H. Jonker, "Ferroelectric domain stabilization in batio3 by bulk ordering of defects", Ferroelectrics **22**, 729–731 (1978).

[134]T. Takenaka, K.-i. M. Kei-ichi Maruyama, and K. S. Koichiro Sakata, "(Bi 1/2 Na 1/2)TiO3-BaTiO3 System for Lead-Free Piezoelectric Ceramics", Japanese Journal of Applied Physics **30**, 2236 (1991).

[135]W. Jo, S. Schaab, E. Sapper, L. A. Schmitt, H.-J. Kleebe, A. J. Bell, and J. Rödel, "On the phase identity and its thermal evolution of lead free (Bi1/2Na1/2)TiO3-6 mol% BaTiO3", Journal of Applied Physics **110**, 074106 (2011).

[136]J. E. Daniels, W. Jo, J. Rödel, and J. L. Jones, "Electric-field-induced phase transformation at a lead-free morphotropic phase boundary: Case study in a 93% (Bi0.5Na0.5) TiO 3 -7% BaTiO3 piezoelectric ceramic", Applied Physics Letters **95**, 2007–2010 (2009).

[137]E. Sapper, R. Dittmer, D. Damjanovic, E. Erdem, D. J. Keeble, W. Jo, T. Granzow, and J. Rödel, "Aging in the relaxor and ferroelectric state of Fe-doped (1-x)(Bi1/2Na1/2)TiO3-xBaTiO3 piezoelectric ceramics", Journal of Applied Physics **116**, 104102 (2014).

[138]L. Koch, "First-principles study of the defect chemistry and conductivity in sodium bismuth titanate", PhD thesis (Technische Universität Darmstadt, 2021), p. 250.

[139]J. E. Daniels, W. Jo, J. Rödel, D. Rytz, and W. Donner, "Structural origins of relaxor behavior in a 0.96 (Bi1/2 Na 1/2) TiO3 -0.04 BaTiO3 single crystal under electric field", Applied Physics Letters **98**, 2009–2012 (2011).

[140]R. Waser, T. Baiatu, and K.-H. .-. Härdtl, "dc Electrical Degradation of Perovskite-Type Titanates: I, Ceramics", Journal of the American Ceramic Society **73**, 1645–1653 (1990).

[141]A. Teverovsky, "Breakdown voltages in ceramic capacitors with cracks", IEEE Transactions on Dielectrics and Electrical Insulation **19**, 1448–1455 (2012).

[142]G. A. Schneider, "Influence of electric field and mechanical stresses on the fracture of ferroelectrics", Annual Review of Materials Research **37**, 491–538 (2007).

[143]Q. Y. Jiang and L. E. Cross, "Effects of porosity on electric fatigue behaviour in PLZT and PZT ferroelectric ceramics", Journal of Materials Science **28**, 4536–4543 (1993).

[144]Y. A. Genenko, J. Glaum, M. J. Hoffmann, and K. Albe, "Mechanisms of aging and fatigue in ferroelectrics", Materials Science and Engineering B: Solid-State Materials for Advanced Technology **192**, 52–82 (2015).

[145]R. M. Waser, "Electrochemical Boundary Conditions for Resistance Degradation of Doped Alkaline-Earth Titanates", Journal of the American Ceramic Society **72**, 2234–2240 (1989).

[146]R. Waser, T. Baiatu, and K.-H. .-. Härdtl, “dc Electrical Degradation of Perovskite-Type Titanates: II, Single Crystals”, Journal of the American Ceramic Society **73**, 1654–1662 (1990).

[147]T. Baiatu, R. Waser, and K.-H. .-. Härdtl, “dc Electrical Degradation of Perovskite-Type Titanates: III, A Model of the Mechanism”, Journal of the American Ceramic Society **73**, 1663–1673 (1990).

[148]P. Ren, M. Gehringer, B. Huang, A. P. Hoang, S. Steiner, A. Klein, and T. Frömling, “High field electroformation of sodium bismuth titanate and its solid solutions with barium titanate”, Journal of Materials Chemistry C **9**, 3334–3342 (2021).

[149]Y. Cao, J. Shen, C. Randall, and L.-Q. Chen, “ Effect of Ferroelectric Polarization on Ionic Transport and Resistance Degradation in BaTiO 3 by Phase-Field Approach ”, Journal of the American Ceramic Society **97**, 3568–3575 (2014).

[150]T. J. M. Bayer, J. J. Carter, J.-J. Wang, A. Klein, L.-Q. Chen, and C. A. Randall, “Determination of electrical properties of degraded mixed ionic conductors: Impedance studies with applied dc voltage”, Journal of Applied Physics **122**, 244101 (2017).

[151]M. Kubicek, S. Taibl, E. Navickas, H. Hutter, G. Fafilek, and J. Fleig, “Resistive states in strontium titanate thin films: Bias effects and mechanisms at high and low temperature”, Journal of Electroceramics **39**, 197–209 (2017).

[152]W. Zhang, C. Zhu, K. Hui, P. Zhao, and L. Guo, “A strategy to detect the effect of electrode defects on the electrical reliability in multilayer ceramic capacitors”, Materials Today Energy **27**, 101022 (2022).

[153]E. Kuffel, W. Zaengl, and J. Kuffel, *High Voltage Engineering Fundamentals*, 2nd (Elsevier, 2000).

[154]A. Von Hippel, “Electric Breakdown of Solid and Liquid Insulators”, Journal of Applied Physics **8**, 815–832 (1937).

[155]H. Fröhlich, “Theory of electrical breakdown in ionic crystals”, Proceedings of the Royal Society of London. Series A - Mathematical and Physical Sciences **160**, 230–241 (1937).

[156]Z. Cai, P. Feng, C. Zhu, and X. Wang, “Dielectric breakdown behavior of ferroelectric ceramics: The role of pores”, Journal of the European Ceramic Society **41**, 2533–2538 (2021).

[157]K. D. Schomann, “Zum elektrischen Durchschlag von keramischem Bariumtitanat und Barium-Strontium-Titanat”, Archiv für Elektrotechnik **56**, 223–227 (1974).

[158]N. Yoshimura, A. Ito, J. Funaki, and T. Ogasawara, “Effect of pore on electrical conduction and dielectric breakdown for dielectric ceramics.”, IEEJ Transactions on Fundamentals and Materials **108**, 155–161 (1988).

[159]D. Zheng, J. Swingler, and P. Weaver, “Current leakage and transients in ferroelectric ceramics under high humidity conditions”, Sensors and Actuators, A: Physical **158**, 106–111 (2010).

[160]G. A. Schneider, “A Griffith type energy release rate model for dielectric breakdown under space charge limited conductivity”, Journal of the Mechanics and Physics of Solids **61**, 78–90 (2013).

[161]C. Neusel and G. A. Schneider, “Size-dependence of the dielectric breakdown strength from nano- to millimeter scale”, Journal of the Mechanics and Physics of Solids **63**, 201–213 (2014).

[162]K. D. Schomann, “Electric breakdown of barium titanate: A model”, Applied Physics **6**, 89–92 (1975).

[163]A. D. Milliken, A. J. Bell, and J. F. Scott, “Dependence of breakdown field on dielectric (interelectrode) thickness in base-metal electroded multilayer capacitors”, Applied Physics Letters **90**, 2005–2008 (2007).

[164]F. Forlani and N. Minnaja, “Thickness Influence in Breakdown Phenomena of Thin Dielectric Films”, Physica Status Solidi (B) **4**, 311–324 (1964).

[165]J. F. Scott, M. Azuma, C. A. De Araujo, L. D. McMillan, M. C. Scott, and T. Roberts, “Dielectric breakdown in high-e films for ulsi drams: II. barium-strontium titanate ceramics”, Integrated Ferroelectrics **4**, 61–84 (1994).

[166]D. G. Park, H. J. Cho, K. Y. Lim, C. Lim, I. S. Yeo, J. S. Roh, and J. W. Park, “Characteristics of n+ polycrystalline-Si/Al2O3/Si metal-oxide-semiconductor structures prepared by atomic layer chemical vapor deposition using Al(CH3)3 and H2O vapor”, Journal of Applied Physics **89**, 6275–6280 (2001).

[167]W.-t. Li, D. R. Mckenzie, W. D. Mcfall, and Q.-c. Zhang, “Breakdown mechanism of Al 2 O 3 based metal-to-metal antifuses”, Solid-State Electronics **44**, 1557–1562 (2006).

[168]B. H. Lee, Y. Jeon, K. Zawadzki, W. J. Qi, and J. Lee, “Effects of interfacial layer growth on the electrical characteristics of thin titanium oxide films on silicon”, Applied Physics Letters **74**, 3143–3145 (1999).

[169]J. Kolodzey, E. A. Chowdhury, T. N. Adam, G. Qui, I. Rau, J. O. Olowolafe, J. S. Suehle, and Y. Chen, “Electrical conduction and dielectric breakdown in aluminum oxide insulators on silicon”, IEEE Transactions on Electron Devices **47**, 121128 (2000).

[170]H. S. Kim, D. C. Gilmer, S. A. Campbell, and D. L. Polla, “Leakage current and electrical breakdown in metal-organic chemical vapor deposited TiO2 dielectrics on silicon substrates”, Applied Physics Letters **69**, 3860–3862 (1996).

[171]A. Chin, Y. H. Wu, S. B. Chen, C. C. Liao, and W. J. Chen, “High Quality La203 and A1203 Gate Dielectrics with Equivalent Oxide Thickness 5-10A”, Symposium A Quarterly Journal In Modern Foreign Literatures, 16–17 (2000).

[172]P. Castro, C. J. Buchenauer, J. Gaudet, and E. Schamiloglu, “Studies of dielectric breakdown under pulsed power conditions”, Digest of Technical Papers-IEEE International Pulsed Power Conference, 978–981 (2007).

[173]S. A. Campbell, D. C. Gilmer, X. C. Wang, M. T. Hsieh, H. S. Kim, W. L. Gladfelter, and J. Yan, “MOSFET transistors fabricated with high permitivity tio2 dielectrics”, IEEE Transactions on Electron Devices **44**, 104–109 (1997).

[174]B. A. Baumert, L. H. Chang, A. T. Matsuda, T. L. Tsai, C. J. Tracy, R. B. Gregory, P. L. Fejes, N. G. Cave, W. Chen, D. J. Taylor, T. Otsuki, E. Fujii, S. Hayashi, and K. Suu, “Characterization of sputtered barium strontium titanate and strontium titanate-thin films”, Journal of Applied Physics **82**, 2558–2566 (1997).

[175]H. J. De Wit and C. Crevecoeur, “The dielectric breakdown of anodic aluminum oxide”, Physics Letters A **50**, 365–366 (1974).

[176]B. Mieller, “Influence of test procedure on dielectric breakdown strength of alumina”, Journal of Advanced Ceramics **8**, 247–255 (2019).

[177]P. K. Fischer and G. A. Schneider, “Influence of the experimental set-up and voltage ramp on the dielectric breakdown strength and breakdown site in borosilicate glass”, Journal of the European Ceramic Society **41**, 1332–1341 (2021).

[178]T. Zhang, J. Du, Y. Lei, Y. Cheng, W. Liu, X. Yi, J. Yin, and P. Yu, “Effect of pores on dielectric breakdown strength of alumina ceramics via surface and volume effects”, Journal of the European Ceramic Society **40**, 3019–3026 (2020).

[179]S. Stark, “On the size dependence of the dielectric breakdown strength of solid insulators at room temperature”, Journal of the European Ceramic Society **42**, 462–471 (2022).

[180]T. Tani, M. Asai, K. Takatori, and N. Kamiya, “Evaluation of Dielectric Strength with and Breakdown Shapes Behavior for PZT Ceramics Various of Electrodes”, Journal of the Ceramic Society of Japan **311**, 308–311 (1997).

[181]Z. Cai, X. Wang, and L. Li, “Phase-Field Modeling of Electromechanical Breakdown in Multilayer Ceramic Capacitors”, Advanced Theory and Simulations **2**, 1–7 (2019).

[182]E. Furman and L. E. Cross, “Dielectric Breakdown in PLZT 9.5/65/35 ceramics”, in (1990), pp. 87–106.

[183]P. H. Fang and W. S. Brower, “Temperature Dependence of the Breakdown Field of Barium titanate”, Physical Review (1959).

[184]J. Doh, S. H. Hur, and J. Lee, “Viscoplastic parameter identification of temperature-dependent mechanical behavior of modified polyphenylene oxide polymers”, Polymer Engineering and Science **59**, E200–E211 (2019).

[185]R. Gerson and T. C. Marshall, “Dielectric breakdown of porous ceramics”, Journal of Applied Physics **30**, 1650–1653 (1959).

[186]I. O. Owate and R. Freer, “Ac breakdown characteristics of ceramic materials”, Journal of Applied Physics **72**, 2418–2422 (1992).

[187]F. Gheorghiu, L. Padurariu, M. Airimioaei, L. Curecheriu, C. Ciomaga, C. Padurariu, C. Galassi, and L. Mitoseriu, “Porosity-dependent properties of Nb-doped Pb(Zr,Ti)O3 ceramics”, Journal of the American Ceramic Society **100**, 647–658 (2017).

[188]G. Dale, M. Strawhorne, D. C. Sinclair, and J. S. Dean, “Finite element modeling on the effect of intragranular porosity on the dielectric properties of BaTiO3 MLCCs”, Journal of the American Ceramic Society **101**, 1211–1220 (2018).

[189]B. D. Flinn, R. K. Bordia, A. Zimmermann, and J. Rödel, “Evolution of defect size and strength of porous alumina during sintering”, Journal of the European Ceramic Society **20**, 2561–2568 (2000).

[190]J. T. Irvine, D. C. Sinclair, and A. R. West, “Electroceramics: Characterization by Impedance Spectroscopy”, Advanced Materials **2**, 132–138 (1990).

[191]L. Papula, *Mathematik für Ingenieure und Naturwissenschaftler Band 2* (Springer Fachmedien Wiesbaden, Wiesbaden, 2015).

[192]L. Papula, *Mathematik für Ingenieure und Naturwissenschaftler Band 1* (Springer Fachmedien Wiesbaden, Wiesbaden, 2014).

[193]E. Barsoukov and J. R. Macdonald, *Impedance Spectroscopy Theory, Experiment, and Applications*, 2nd ed. (2005), p. 595.

[194]S. Holm, T. Holm, and Ø. G. Martinsen, “Simple circuit equivalents for the constant phase element”, PLoS ONE **16**, 1–12 (2021).

[195]N. M. Beekmans and L. Heyne, “Correlation between impedance, microstructure and composition of calcia-stabilized zirconia”, Electrochimica Acta **21**, 303–310 (1976).

[196]T. van Dijk and A. J. Burggraaf, “Grain boundary effects on ionic conductivity in ceramic GdxZr1-xO2-(x/2) solid solutions”, Physica Status Solidi (a) **63**, 229–240 (1981).

[197]S. Song and F. Placido, “The influence of phase probability distributions on impedance spectroscopy”, Journal of Statistical Mechanics: Theory and Experiment **2004**, P10018 (2004).

[198]P. G. Bruce and A. R. West, “The A-C Conductivity of Polycrystalline LISICON, Li(2+2x)Zn(1-x)GeO4, and a Model for Intergranular Constriction Resistances”, Journal of The Electrochemical Society **130**, 662–669 (1983).

[199]G. N. Howatt, R. G. Breckenridge, and J. M. Brownlow, “Fabrication of Thin Ceramic Sheets for Capacitors”, Journal of the American Ceramic Society **30**, 237–242 (1947).

[200]Fraunhofer IKTS, *Seminarunterlagen DKG-Seminar Foliengieß- und Schlitzdüsenverfahren*, Hermsdorf, 2019.

[201]E. M. Anderson, R. A. Marra, and R. E. Mistler, “Tape casting reactive aluminas”, American Ceramic Society bulletin **76**, 45–50 (1997).

[202]P. Kumar Panda and B. Sahoo, “Tape Casting Technique for Fabrication of Piezoelectric Ceramics and Other Multilayered Devices-A Review”, Advanced Materials Science and Technology **3**, 1–17 (2021).

[203]D. J. Shanefield, *Organic Additives and Ceramic Processing* (Springer US, 1995).

[204]M. N. Rahaman, *Ceramic Processing and Sintering*, 2nd (CRC Press, Dec. 2003), p. 875.

[205]J. Reed, *Principles of Ceramics Processing* (John Wiley & Sons, Ltd, 1995), pp. 1–323.

[206]D. Sarkar, *Ceramic Processing*, edited by D. Sarkar (CRC Press, Boca Raton : Taylor & Francis a CRC title, part of the Taylor & Francis imprint, a member of the Taylor & Francis Group, June 2019), pp. 12–26.

[207]W. J. Gyurk, *Methods for manufacturing multilayered monolithic ceramic bodies*, June 1965.

[208]S. J. L. Kang, *Sintering: Densification, grain growth and microstructure* (Elsevier Butterworth-Heinemann, 2005), pp. 1–265.

[209]R. M. German, *Sintering - From Empirical Observatins to Scientific Principles* (2016).

[210]R. Ruer, "On the Alloys of Palladium with Silver", Z. Anrog. Allg. Chem. **51**, 315–319 (1906).

[211]A. V. Dmitrieva, P. S. Gordiev, and I. Y. Gallai, "Investigation of the pastes for multilayer ceramic capacitors termination", Key Engineering Materials **822**, 885–891 (2019).

[212]J. H. Lee, G. J. Lee, A. P. Hoang, T. Frömling, T. L. Pham, J. S. Lee, and W. Jo, "Suppression of high-temperature dielectric loss by designed thermal annealing treatment in (Bi1/2Na1/2)TiO3 ceramics", Journal of the European Ceramic Society **42**, 1388–1395 (2022).

[213]A. Klein, "Interface Properties of Dielectric Oxides", Journal of the American Ceramic Society **99**, edited by D. J. Green, 369–387 (2016).

[214]T. Karaki, K. Yan, and M. Adachi, "Barium Titanate Piezoelectric Ceramics Manufactured by Two-Step Sintering", Japanese Journal of Applied Physics **46**, 7035–7038 (2007).

[215]N. S. Panwar and B. S. Semwal, "Study of electrical conductivity of barium titanate ceramics", Ferroelectrics **115**, 1–6 (1991).

[216]Z. Fu and A. Roosen, "Shrinkage of tape cast products during binder burnout", Journal of the American Ceramic Society **98**, 20–29 (2015).

[217]K. Reinhardt, C. Kretzschmar, R. Schmidt, and M. Eberstein, "Silver/palladium pastes for aluminium nitride applications", EMPC-2011 - 18th European Microelectronics and Packaging Conference, Proceedings, 2009–2014 (2011).

[218]V. Mussi Toschi, "Lead-free ferroelectric ceramics for multilayer ceramic capacitors.", PhD thesis (2019).

[219]Z. Yan, C. L. Martin, O. Guillon, D. Bouvard, and C. S. Lee, "Microstructure evolution during the co-sintering of Ni/BaTiO3 multilayer ceramic capacitors modeled by discrete element simulations", Journal of the European Ceramic Society **34**, 3167–3179 (2014).

[220]J. Koruza, "Sintering and phase transition behaviour of sodium niobate", PhD thesis (2013), p. 131.

[221]D. Kuscer, A. Kocjan, M. Majcen, A. Meden, K. Radan, J. Kovač, and B. Malič, "Evolution of phase composition and microstructure of sodium potassium niobate –based ceramic during pressure-less spark plasma sintering and post-annealing", Ceramics International **45**, 10429–10437 (2019).

[222]Y. Imanaka, *Multilayered Low Temperature Cofired Ceramics (LTCC) Technology*, Vol. 66 (Kluwer Academic Publishers, Boston, 2005), pp. 37–39.

[223]Y. Hirata, A. Nitta, S. Sameshima, and Y. Kamino, "Dielectric properties of barium titanate prepared by hot isostatic pressing", Materials Letters **29**, 229–234 (1996).

[224]T. Zeng, X. L. Dong, C. L. Mao, Z. Y. Zhou, and H. Yang, “Effects of pore shape and porosity on the properties of porous PZT 95/5 ceramics”, Journal of the European Ceramic Society **27**, 2025–2029 (2007).

[225]L. F. Voss, M. F. Bazerbashi, C. P. Beekman, C. M. Hadad, and H. C. Allen, “Oxidation of oleic acid at air/liquid interfaces”, Journal of Geophysical Research: Atmospheres **112**, 209 (2007).

[226]The Lubrizol Corporation, *Product Data Sheet Solsperse™ M387 Non-Aqueous Dispersant*, 2021.

[227]Eastman Chemical Company, *Technical Data Sheet polyvinyl butyral Butvar® B-98*, 2018.

[228]Kuraray Co. Ltd., *Technical Data Sheet polyvinyl butyral Mowital® LP BX 860*, 2010.

[229]W. M. Haynes, *CRC Handbook of Chemistry and Physics*, edited by W. M. Haynes, 95th (CRC Press, 2014), p. 2704.

[230]J. A. Baird, R. Olayo-Valles, C. Rinaldi, and L. S. Taylor, “Effect of Molecular Weight, Temperature, and Additives on the Moisture Sorption Properties of Polyethylene Glycol”, Journal of Pharmaceutical Sciences **99**, 154–168 (2010).

[231]H. Kim, M. Choi, Y. Ji, I. Kim, G. Kim, I. Bae, M. Gye, and H. Yoo, “Pharmacokinetic Properties of Acetyl Tributyl Citrate, a Pharmaceutical Excipient”, Pharmaceutics **10**, 177 (2018).

[232]N. S. Vrandečić, M. Erceg, M. Jakić, and I. Klarić, “Kinetic analysis of thermal degradation of poly(ethylene glycol) and poly(ethylene oxide)s of different molecular weight”, Thermochimica Acta **498**, 71–80 (2010).

[233]K. Aouachria, V. Massardier, M. T. Benaniba, and N. Belhaneche-Bensemra, “Evaluation of the effects of acetyl tributyl citrate as bio-based plasticizer on the physical, thermal, and dynamical mechanical properties of poly(vinyl chloride)/polymethyl methacrylate blends”, Journal of Vinyl and Additive Technology **25**, E73–E82 (2019).

[234]M. Erceg, T. Kovačić, and I. Klarić, “Thermal degradation of poly(3-hydroxybutyrate) plasticized with acetyl tributyl citrate”, Polymer Degradation and Stability **90**, 313–318 (2005).

[235]G. W. Ehrenstein, “Thermische Analyse”, in *Hanser* (Carl Hanser Verlag GmbH & Co. KG, München, May 2020).

[236]B. Malič, D. Kuščer, M. Vrabelj, and J. Koruza, “Review of methods for powder-based processing”, Magnetic, Ferroelectric, and Multiferroic Metal Oxides, 95–120 (2018).

[237]H. Salmang, H. Scholze, and R. Telle, “Band 3: Technologie von den Rohstoffen bis zur Hartbearbeitung”, in *Keramik* (De Gruyter, 2022).

[238]Z. Cai, C. Zhu, H. Wang, P. Zhao, L. Chen, L. Li, and X. Wang, “High-temperature lead-free multilayer ceramic capacitors with ultrahigh energy density and efficiency fabricated: Via two-step sintering”, Journal of Materials Chemistry A **7**, 14575–14582 (2019).

[239]S. Y. Ko and S. J. L. Kang, “Growth behavior of faceted Na1/2Bi1/2TiO3-BaTiO3 grains in single and two-step sintering”, Journal of the European Ceramic Society **36**, 1159–1165 (2016).

[240]L. Kang, “Consider for for Full Densification when Sintering”, Materials **13**, 3578 (2020).

[241]I. Karakaya and W. T. Thompson, “The Ag-Bi (Silver-Bismuth) System”, Journal of Phase Equilibria **14**, 525–530 (1993).

[242]F. Yang, A. R. West, and D. C. Sinclair, “Non-ohmic conduction in sodium bismuth titanate: The influence of oxide-ion conduction”, Physical Chemistry Chemical Physics **22**, 20941–20950 (2020).

[243]S. F. Wang and W. Huebner, “Interaction of Silver/Palladium Electrodes with Lead-and Bismuth-Based Electroceramics”, Journal of the American Ceramic Society **76**, 474–480 (1993).

[244]S. F. Wang and W. Huebner, “Interaction of Ag/Pd Metallization with Lead and Bismuth Oxide-Based Fluxes in Multilayer Ceramic Capacitors”, Journal of the American Ceramic Society **75**, 2339–2352 (1992).

[245]G. F. Fan, M. B. Shi, W. Z. Lu, Y. Q. Wang, and F. Liang, “Effects of Li2CO3 and Sm2O3 additives on low-temperature sintering and piezoelectric properties of PZN-PZT ceramics”, Journal of the European Ceramic Society **34**, 23–28 (2014).

[246]S. Guan, H. Yang, Y. Zhao, and R. Zhang, “Effect of Li2CO3 addition in BiFeO3-BaTiO3 ceramics on the sintering temperature, electrical properties and phase transition”, Journal of Alloys and Compounds **735**, 386–393 (2018).

[247]R. Mikkenie, “Materials development for commercial multilayer ceramic capacitors”, PhD thesis (University of Twente, 2011), p. 200.

[248]E. Liniger and R. Raj, “Packing and Sintering of Two-Dimensional Structures Made fro Bimodal Particle Size Distributions”, Journal of the American Ceramic Society **70**, 843–849 (1987).

[249]T. Atou, H. Faqir, M. Kikuchi, H. Chiba, and Y. Syono, “A New High-Pressure Phase of Bismuth Oxide”, Materials Research Bulletin **33**, 289–292 (1998).

[250]X. Dai, Z. Xu, and D. Viehland, “The spontaneous relaxor to normal ferroelectric transformation in La-modified lead zirconate titanate”, Philosophical Magazine B **70**, 33–48 (1994).

[251]R. Dittmer, W. Jo, D. Damjanovic, and J. Rödel, “Lead-free high-temperature dielectrics with wide operational range”, Journal of Applied Physics **109**, 3–8 (2011).

[252]S. Takeoka and Y. Mizuno, “Effect of Internal Electrode Materials in Multilayer Ceramic Capacitors on Electrical Properties”, Japanese Journal of Applied Physics **50**, 09NC06 (2011).

[253]S. Prasanth, M. H. M. Sathik, F. Sasongko, T. C. Seng, M. Tariq, and R. Simanjorang, “Online equivalent series resistance estimation method for condition monitoring of DC-Link capacitors”, 2017 IEEE Energy Conversion Congress and Exposition, ECCE 2017 **2017-Janua**, 1773–1780 (2017).

[254]M. Manofu, R. Voina, and C. Negrea, *Analysis of Multi-Layer Ceramic Capacitors used in Power Distribution Networks*, 2019.

[255]R. Horn, “Keramikkondensatoren steigern Leistungsdichte und Wirkungsgrad”, Elektronikpraxis Nr. 5 (2021).

[256]J. Joseph, Z. Cheng, and S. Zhang, “NaNbO3 modified BiScO3-BaTiO3 dielectrics for high-temperature energy storage applications”, Journal of Materiomics **8**, 731–738 (2022).

[257]H. Haag, “Dc Biased Equivalent Series Resistance Measurement and Loss Estimation in Ferroelectric Ceramic Capacitors Kurzreferat”, PhD thesis (University of Applied Sciences Vorarlberg, 2019), p. 73.

[258]Z. Pan, J. Ding, X. Hou, S. Shi, L. Yao, J. Liu, P. Li, J. Chen, J. Zhai, and H. Pan, “Substantially improved energy storage capability of ferroelectric thin films for application in high-temperature capacitors”, Journal of Materials Chemistry A **9**, 9281–9290 (2021).

[259]S. Rodewald, J. Fleig, and J. Maier, “Resistance Degradation of Iron-Doped Strontium Titanate Investigated by Spatially Resolved Conductivity Measurements”, Journal of the American Ceramic Society **83**, 1969–1976 (2004).

[260]C. Lenser, A. Kalinko, A. Kuzmin, D. Berzins, J. Purans, K. Szot, R. Waser, and R. Dittmann, “Spectroscopic study of the electric field induced valence change of Fe-defect centers in SrTiO3”, Physical Chemistry Chemical Physics **13**, 20779–20786 (2011).

[261]R. Merkle and J. Maier, “How Is Oxygen Incorporated into Oxides? A Comprehensive Kinetic Study of a Simple Solid-State Reaction with SrTiO3 as a Model Material”, Angewandte Chemie International Edition **47**, 3874–3894 (2008).

[262]J. J. Wang, H. B. Huang, T. J. Bayer, A. Moballegh, Y. Cao, A. Klein, E. C. Dickey, D. L. Irving, C. A. Randall, and L. Q. Chen, “Defect chemistry and resistance degradation in Fe-doped SrTiO3 single crystal”, Acta Materialia **108**, 229–240 (2016).

[263]J. N. Baker, P. C. Bowes, D. M. Long, A. Moballegh, J. S. Harris, E. C. Dickey, and D. L. Irving, “Defect mechanisms of coloration in Fe-doped SrTiO3 from first principles”, Applied Physics Letters **110**, 10.1063/1.4978861 (2017).

[264]S. Li, F. Chen, R. Schafranek, T. J. M. Bayer, K. Rachut, A. Fuchs, S. Siol, M. Weidner, M. Hohmann, V. Pfeifer, J. Morasch, C. Ghinea, E. Arveux, R. Günzler, J. Gassmann, C. Körber, Y. Gassenbauer, F. Säuberlich, G. V. Rao, S. Payan, M. Maglione, C. Chirila, L. Pintilie, L. Jia, K. Ellmer, M. Naderer, K. Reichmann, U. Böttger, S. Schmelzer, R. C. Frunza, H. Uršič, B. Malič, W.-B. Wu, P. Erhart, and A. Klein, “Intrinsic energy band alignment of functional oxides”, physica status solidi (RRL) - Rapid Research Letters **8**, 571–576 (2014).

[265]S. Li, J. Morasch, A. Klein, C. Chirila, L. Pintilie, L. Jia, K. Ellmer, M. Naderer, K. Reichmann, M. Gröting, and K. Albe, “Influence of orbital contributions to the valence band alignment of Bi 2O3, Fe2O3, BiFeO3, and Bi0.5Na0.5TiO3”, Physical Review B - Condensed Matter and Materials Physics **88**, 045428 (2013).

[266]R. Schafranek, S. Li, F. Chen, W. Wu, and A. Klein, “PbTiO3/SrTiO3 interface: Energy band alignment and its relation to the limits of Fermi level variation”, Physical Review B - Condensed Matter and Materials Physics **84**, 045317 (2011).

[267]M. Sônego, L. C. Costa, and J. D. Ambrósio, “Flexible thermoplastic composite of Polyvinyl Butyral (PVB) and waste of rigid Polyurethane foam”, Polímeros **25**, 175–180 (2015).

[268]T. Tunkasiri and G. Rujijanagul, “Dielectric strength of fine grained barium titanate ceramics”, Journal of Materials Science Letters **15**, 1767–1769 (1996).

[269]Z. Song, H. Liu, S. Zhang, Z. Wang, Y. Shi, H. Hao, M. Cao, Z. Yao, and Z. Yu, “Effect of grain size on the energy storage properties of (Ba0.4Sr0.6)TiO3 paraelectric ceramics”, Journal of the European Ceramic Society **34**, 1209–1217 (2014).

[270]Q. Jiang, E. C. Subbarao, and L. E. Cross, “Grain size dependence of electric fatigue behavior of hot pressed PLZT ferroelectric ceramics”, Acta Metallurgica Et Materialia **42**, 3687–3694 (1994).

[271]J. V. Biggers, T. R. Shrout, and W. A. Schulze, “Densification of PZT cast tape by pressing”, Am Ceram Soc Bull **58**, 516–518, 521 (1979).

[272]W. Qiu, Y. L. Kang, Q. H. Qin, Q. C. Sun, and F. Y. Xu, “Study for multilayer piezoelectric composite structure as displacement actuator by Moiré interferometry and infrared thermography experiments”, Materials Science and Engineering: A **452-453**, 228–234 (2007).

[273]W. G. Jiang, X. Q. Feng, and C. W. Nan, “Influence of residual thermal stresses and geometric parameters on stress and electric fields in multilayer ceramic capacitors under electric bias”, Journal of Physics D: Applied Physics **41**, 135310 (2008).

[274]M. Kamlah, “Ferroelectric and ferroelastic piezoceramics - Modeling of electromechanical hysteresis phenomena”, Continuum Mechanics and Thermodynamics **13**, 219–268 (2001).

[275]D. Zhan, Q. Xu, D. P. Huang, H. X. Liu, W. Chen, and F. Zhang, “Dielectric nonlinearity and electric breakdown behaviors of Ba0.95Ca0.05Zr0.3Ti0.7O3 ceramics for energy storage utilizations”, Journal of Alloys and Compounds **682**, 594–600 (2016).

[276]Y. J. Wu, Y. H. Huang, N. Wang, J. Li, M. S. Fu, and X. M. Chen, “Effects of phase constitution and microstructure on energy storage properties of barium strontium titanate ceramics”, Journal of the European Ceramic Society **37**, 2099–2104 (2017).

[277]T. Chen, R. Liang, Z. Zhou, K. Jiang, Z. Hu, and X. Dong, “Chemical interpretation, enhanced ferroelectric property and dielectric breakdown strength of CuO-added Sr2Nb2O7 ceramics”, Journal of the European Ceramic Society **38**, 3147–3153 (2018).

[278]C. Neusel, H. Jelitto, D. Schmidt, R. Janssen, F. Felten, and G. A. Schneider, “Thickness-dependence of the breakdown strength: Analysis of the dielectric and mechanical failure”, Journal of the European Ceramic Society **35**, 113–123 (2015).

[279]E. Gockenbach, “High Voltage Engineering”, in *Springer handbooks* (Springer Science and Business Media Deutschland GmbH, 2021), pp. 131–182.

[280]ASTM-D149, “Standard Test Method for Dielectric Breakdown Voltage and Dielectric Strength of Solid Electrical Insulating Materials at Commercial Power Frequencies”, ASTM **97**, 1–6 (2012).

[281]H. Salmang, H. Scholze, and R. Telle, “Band 2: Thermische, mechanische, tribologische, optische, elektrische und magnetische Eigenschaften”, in *Keramik*, 8th (De Gruyter, 2022).

[282]W. B. Li, D. Zhou, R. Xu, D. W. Wang, J. Z. Su, L. X. Pang, W. F. Liu, and G. H. Chen, "BaTiO3-Based Multilayers with Outstanding Energy Storage Performance for High Temperature Capacitor Applications", ACS Applied Energy Materials **2**, 5499–5506 (2019).

[283]Z. Cai, X. Wang, W. Hong, B. Luo, Q. Zhao, and L. Li, "Grain-size–dependent dielectric properties in nanograin ferroelectrics", Journal of the American Ceramic Society **101**, 5487–5496 (2018).